

Semi-circular Sweep Voltammetry for Electroanalysis

A thesis submitted for the degree of

Doctor of Philosophy

in Physical and Theoretical Chemistry

Yuanzhe Wang

Wadham College

Trinity Term 2021

Semi-circular Sweep Voltammetry for Electroanalysis

Yuanzhe Wang

Wadham College, University of Oxford

A thesis submitted for the degree of D.Phil. in Physical and Theoretical Chemistry

Trinity Term, 2021

Abstract

This thesis focuses on electroanalysis using semi-circular sweep voltammetry. This method is particularly developed for analytes which show significant difficulties when analysed using conventional voltammetry.

The fundamentals of electrochemistry and the principles of electrochemical methods are introduced in Chapter 1. Next, the theoretical aspects of semi-circular sweep voltammetry and the insights from related simulation studies are reviewed in Chapter 2. In Chapter 3, the generic experimental procedures used widely in the following chapters are described.

In the chapters, from Chapter 4 to Chapter 9, new, bespoke electrochemical methods for the detection of a range of target molecules are introduced with the focus on the electroanalytical applications of semi-circular sweep voltammetry the generation of new methodology for wider application. Chapter 4 considers the detection of the analyte piperine allowing comparative evaluation of semi-circular sweep voltammetry. In this chapter, the electrochemical behaviour of piperine at macro-and micro-electrodes are discussed. Semi-circular sweep voltammetry is used to maximise the analytical signal shown under conditions where high capacitive and solvent currents were present. The suggested electroanalytical method is validated in real samples following the establishment of a quick and simple improved extraction procedure of piperine from black pepper.

The electro-oxidation of phenol causes electrode passivation via electro-polymerisation making meaningful electroanalysis impossible. Chapter 6 investigates the passivating behaviour and develops an electroanalytical method for determining phenol using semi-circular sweep voltammetry by means of the introduction of a second species which reacts with phenol largely eliminating electro-polymerisation. The presence of the

second species prevents the passivation at low phenol concentrations and the semi-circular sweep voltammetry amplifies the signal from the unreacted phenol in the low concentration range.

In Chapter 5 and 7, the merits of using semi-circular sweep voltammetry for the selective detection of one or other component of a mixture containing two components with closely similar potentials which preclude their resolution in conventional voltammetry are discussed. Chapter 5 demonstrates proof of concept of the developed approach applying semi-circular sweep voltammetry for distinguishing and quantifying chlorophyll a and chlorophyll b in their mixtures and is then applied to real samples. Chapter 7 suggests the *generic* applicability of semi-circular sweep voltammetry and its advantages over other analytical voltammetry in terms of the voltammetric resolution and sensitivity of detection. The electrochemical reaction processes and the analytical indications are investigated specifically in the cases of biological mixtures of ascorbic acid and acetaminophen, glucose and ethanol, and hydroquinone and catechol.

Finally, Chapter 8 focuses on another important technique for – adsorptive stripping voltammetry and discusses the intrinsic limitations in the practical voltammetric detections. The possibility of employing semi-circular sweep voltammetry to overcome such limitations is also explored in this Chapter.

Acknowledgements

There are countless people have given me invaluable help during my DPhil study who made this thesis possible. First and foremost, I would like to profoundly thank my supervisor, Professor Richard Compton, for accepting me in his group and providing the best possible supervision throughout my DPhil. Thank you for the constructive feedbacks and guidance you have given in electrochemistry as well as the support and positive spirit you have brought in life especially during this unprecedentedly difficult time amid Covid. It has been an absolutely amazing experience to do research with you, which I believe, teaches me a lot about how to be a proper scientist. The idea of being 'frogs' instead of 'birds' in science would always be a motto that motivates me to go down the right path in the future not only research, but every aspect of life.

I would also like to give massive thanks to Dr. Lifu Chen, Dr. Korbua Chaisiwamongkhol, and Dr. Hatem Amin for your generous help and support in the first year. Thank you for helping me out with everything in fitting in DPhil working dynamics, running experiments, interpreting results, and even in deciphering RGC's handwriting. I could have never done this without your patience and advice.

To the whole RGC group, every one of you is a great pleasure to work with. Many thanks to Dr. Christopher Batchelor-McAuley and Jake for managing the lab and providing help to everyone when it is needed. To Grace, Ryan, Daisey, Yifei, Archana, Xin, Collin and many more, thank you for sharing your research idea and life hacks with me and being my mates both in and outside lab. The lovely memories with you of talking about food when polishing electrodes and the random chit-chats while enjoying ciders in the Oxford pubs will always stay with me.

Finally, enormous thanks must go to my family who always support me, give my much love and care during these three years. Having you by my side has made me strong, brave and tenacious. I also want to thank my friends in Oxford and China for bringing so much fun and support to me. To my flatmate GL and all my friends, your warm company and sweet words have always meant a great deal to me.

Contents

Abstract……...……...i

Acknowledgements……...…….……..iii

Contents……...…….……iv

Glossary……...…….……ix

Chapter 1 Fundamentals of Electrochemistry

1.1 Electrochemical Equilibrium……...…….……1

1.2 Electrode Kinetics ……...…….……...……..6

1.3 Faradaic and Non-Faradaic Processes……...…….……..12

1.4 Mass Transport ……...…….……...……16

1.4.1 Diffusion ……...…….…….....….....16

1.4.2 Convection …..…….……...…….……20

1.4.3 Migration ……...…….…….....…....….21

1.5 Electrochemical Cells……...…….……...…….…….……22

1.6 Macroelectrodes and Microelectrodes…….…….……...25

1.7 Some Electrochemical Techniques…….…….……..…..26

1.7.1 Cyclic and Linear Sweep Voltammetry…….…….....……27

1.7.1.1 Voltammetry at Macroelectrodes.…….....……..28

1.7.1.2 Voltammetry at Microelectrodes…….....……...32

1.7.2 Stripping Voltammetry…….……...……....34

1.7.2.1 Effect of Adsorption…….....…….....35

1.7.2.2 Voltammetry of Surface-Adsorbed Species…….....…….....37

1.7.3 Pulse Voltammetry…….……...…….....38

1.7.3.1 Differential Pulse Voltammetry…….……...…….....39

1.7.3.2 Square Wave Voltammetry…….……...…….....40

1.7.4 Chronoamperometry…….……...…….....42

1.7.5 The Nano-impact Method…….……...…….....…44

Bibliography……...…….……...…….45

Chapter 2 Semi-circular Sweep Voltammetry

2.1 Semi-circular Potential Wave ……...…….……...……...49

2.2 Applications of Semi-circular Sweep Voltammetry in Electroanalysis: Theory……51

Bibliography……53

Chapter 3 Experimental

3.1 Chemicals and Reagents ……...54

3.2 Electrochemical Instrumentation……56

Bibliography……57

Chapter 4 Electrochemical Quantification of Piperine in Black Pepper

4.1 Introduction……...59

4.2 Experimental…...……62

4.2.1 Chemicals and Reagents……62

4.2.2 Electrochemical Instrumentation and Methods…...62

4.2.3 Sample Preparation…..62

4.2.4 Analytical Procedures…..64

4.3 Results and Discussion ……..64

4.3.1 Electrochemical Study of Piperine……..65

4.3.1.1 Effect of Voltage Scan Rate……...66

4.3.1.2 Measurement of Number of Electrons Transferred and the Diffusion Coefficient. ……67

4.3.1.3 Possible Reaction Mechanism……69

4.3.2 Electrochemical Detection of Piperine ……72

4.3.2.1 Using Cyclic Voltammetry for the Detection of Piperine……73

4.3.2.2 Using Semi-circular Potential Sweep Voltammetry for Detection of Piperine……75

4.3.3 Analysis of a Real Sample ……80

4.4 Conclusions……84

Bibliography……85

Chapter 5 Selective Voltammetric Detection of Chlorophylls Using a Semi-circular Potential Wave

5.1 Introduction……..……...…….……...88

5.2 Experimental…...……...…….……91

5.2.1 Chemicals and Reagents……..…….……....91

5.2.2 Apparatus …..……..……..……..……..…..93

5.2.3 Analytical Procedures…..…….…..…..…....94

5.3 Results and Discussion ……...…….……..……..95

5.3.1 UV-vis Spectroscopic Examination of Chlorophylls……..……..….96

5.3.2 Electrochemical Behaviours of the Two Chlorophylls……...97

5.3.2.1 Effect of Voltage Scan rate ……..……..…….97

5.3.2.2 Adsorption on GC Electrode…….……..…..98

5.3.3 Detection of Chlorophyll a and b in Mixtures…....…….……...….103

5.3.3.1 Selective Detection in Standard Mixture Solutions..…….103

5.3.3.2 Detection in Real Samples……...……..……107

5.4 Conclusions…….……..109

Bibliography……...…….……...……...……110

Chapter 6 An Approach to the Electroanalysis of Electrode Passivating Analytes: The Determination of Phenol

6.1 Introduction……..……...…….……113

6.2 Experimental…...……...…….……...116

6.2.1 Chemicals and Reagents……...…...……..……...116

6.2.2 Apparatus.…..……..……...……..……..……...…117

6.3 Results and Discussion……...…….……...……..……117

6.3.1 Electrochemistry of Phenol ……...……..….118

6.3.2 Phenol Detection in the Presence of PAP……...……...….120

6.3.2.1 Electrochemistry of PAP…….……..…120

6.3.2.2 Phenol Detection in the Presence of PAP Using CV……...……123

6.3.3.3 Phenol Detection in the Presence of PAP Using SCV…….…....127

6.4 Conclusions…….……..132

Bibliography……...…….……...……...……133

Chapter 7 Semi-circular Sweep Voltammetry. Bio-analytical Applications

7.1 Introduction……..……...…….……137

7.2 Experimental…...……...…….……...…...139

7.2.1 Chemicals and Reagents……....…….……..……...139

7.2.2 Apparatus…..……..……...……..……...……..…140

7.2.3 Sample Preparation……..……...……..……...……..…141

7.3 Results and Discussion……...…….……..……...…….142

7.3.1 Ascorbic Acid and Acetaminophen ……..….143

7.3.1.1 Electrochemical Behaviours of Ascorbic Acid and Acetaminophen..143

7.3.1.2 The Determination of Acetaminophen in the Presence of Ascorbic Acid ……..……..……...……..145

7.3.1.3 Real Sample Analysis ……...……...…147

7.3.2 Glucose and Ethanol……...……...….150

7.3.2.1 Voltammetric Characterisation ……....……....….150

7.3.2.2 Simultaneous Determinations of Glucose and Ethanol...……152

7.3.3 Hydroquinone and Catechol……...…….……154

7.3.3.1 Electrochemical Behaviours of Hydroquinone and Catechol ……...154

7.3.3.2 Simultaneous Determinations of Hydroquinone and Catechol at a MWCNTs/GC Electrode…….…….……159

7.4 Conclusions…….……..162

Bibliography……...…….……...……...……163

Chapter 8 Optimising Adsorptive Stripping Voltammetry; Strategies and Limitations

8.1 Introduction……..……...…….……166

8.2 Experimental…...……...…….……...…...169

8.2.1 Chemicals and Apparatus ……...……..……...169

8.2.2 Voltammetry on Carbon Macroelectrodes……...…...…….…...…170

8.2.3 Nano-impact Experiments……...…….……..……...172

8.3 Results and Discussion…....…….……..……172

8.3.1 Electrochemical Behaviour of Fipronil……...…….…….173

8.3.2 Adsorption on Single Carbon Nanotubes: A Nano-impact Study……..…..179

8.3.3 Analytical Performances of Different Carbon Electrode Surfaces……..…183

8.4 Conclusions…….……..191

Bibliography……...…….……...……...……191

Chapter 9 Overall Conclusions …..……...…..……...…..196

Appendix A…...……...…..……...……..199

Appendix B…...……...…..……...……..202

Appendix C…...……...…..……...……..205

Appendix D…...……...…..……...……..207

Appendix E…...……...…..……...……..211

Appendix F…...……...…..……...……...215

Appendix G…...……...…..……...……..216

Glossary

Roman Symbols

Symbol	Meaning	Unit
a_j	activity of species j	mol m^{-3}
$a_{j,0}$	activity of species *j* at electrode surface	mol m^{-3}
A	area	m^2
A_0	potential sweep amplitude	V
c_j	concentration of species j	mol m^{-3}
c_j^*	bulk concentration of species j	mol m^{-3}
$c_{j,0}$	concentration of species *j* at electrode surface	mol m^{-3}
C_d	double layer capacitance	F m^{-2}
D_j	diffusion coefficient of species *j*	m^2 s^{-1}
E	potential applied at the working electrode	V
E_0	standard electrode potential	V
E_f^0	formal potential	V
E_{mid} / E_{centre}	mid-point of potential window	V
$E_{1/2}$	half-wave potential	V
ΔE_{pp}	peak-to-peak separation	V
ΔE_p	pulse height	V
ΔE_s	staircase height	V
F	Faraday constant ≈ 96485	C mol^{-1}
f	frequency	s^{-1}
G	Gibbs energy	J mol^{-1}
$\Delta G_0^\dagger$	standard Gibbs energy of activation	J mol^{-1}
$\Delta G_{ox}^\dagger$	Gibbs energies of activation of the oxidation	J mol^{-1}
$\Delta G_{red}^\dagger$	Gibbs energies of activation of the reduction	J mol^{-1}
I	current	A
I_p	peak current	A
I_{ss}	steady-state current	A
I_f	Faradaic current	A
I_c	capacitative current	A
J_j	flux of species j	mol m^{-2} s^{-1}

k^0	standard electrochemical rate constant	m s^{-1}
k_{ox}	oxidation rate constant	m s^{-1}
k_{red}	reduction rate constant	m s^{-1}
K	equilibrium constant	m^3 mol^{-1}
l	path length	m
m	mass	g
m_T	mass transport coefficient	m s^{-1}
M	molar mass	g mol^{-1}
n	number of electrons transferred	dimensionless
N_i	number of species j	dimensionless
N_A	Avogadro constant ≈ 6.022 × 1023	mol^{-1}
Q	charge	C
R	Universal Gas Constant ≈ 8.314	J K^{-1} mol^{-1}
$\boldsymbol{R}$	electrical resistance	Ω
r_e	electrode radius	m
T	absolute temperature	K
t	time	s
t_p	pulse time	s
v	potential scan rate	V s^{-1}
$x; y; z$	Cartesian coordinate	dimensionless
z_j	ionic charge of species j	dimensionless

Greek Symbols

Symbol	**Meaning**	**Unit**
α	reductive transfer coefficient	dimensionless
β	oxidative transfer coefficient	dimensionless
δ	diffusion layer thickness	m
ε	extinction coefficient	m^2 mol^{-1}
ε_0	permittivity of vacuum	C^2 J^{-1} m^{-1}
ε_r	dielectric constant	C^2 J^{-1} m^{-1}
η	overpotential $(E - E_f^0)$	V
γ	activity coefficient	dimensionless

λ	wavelength	m
κ	Debye length	m
μ	chemical potential	J mol^{-1}
μ_0	standard chemical potential	J mol^{-1}
$\overline{\mu}$	electrochemical potential	J mol^{-1}
τ	dimensionless time	dimensionless
ϕ	electric potential	V
ϕ_m	electric potential of the metallic electrode	V
ϕ_s	electric potential of the solution	V
ρ	density	g m^{-3}
θ	fractional surface coverage	dimensionless
Γ	surface coverage	mol m^{-2}

Abbreviations

Abbreviations	**Meaning**
AdsSV	adsorptive stripping voltammetry
AdsSCV	adsorptive semi-circular sweep voltammetry
AdsSWV	adsorptive square wave voltammetry
ASV	anodic stripping voltammetry
AA	ascorbic acid
AC	acetaminophen
BPPG	basal plane pyrolytic graphite
Britton–Robinson	B-R
CC	catechol
CB	carbon black

CE	counter electrode
Chl a	chlorophyll a
Chl b	chlorophyll b
CNT	carbon-nanotube
CSV	cathodic stripping voltammetry
CV	cyclic voltammetry
DPV	differential pulse voltammetry
EPPG	edge plane graphite
FIP	fipronil
GC	glassy carbon
GNP	graphene nano-platelet
Glu	Glucose
HOMO	highest occupied molecular orbital
HQ	hydroquinone
IHP	Inner Helmholtz Plane
ISV	insertive stripping voltammetry
LOD	limit of detection
LSV	linear sweep voltammetry
LUMO	lowest unoccupied molecular orbital
MWCNT	multi-walled carbon nanotube
OHP	Outer Helmholtz Plane
PAP	4-Amino-2,6-dichlorophenol
pAdsSV	prior-adsorptive stripping voltammetry
PBS	phosphate-buffered saline
PME	particle modified electrode
PZC	potential of zero charge
QI	quinone imine
RE	reference electrode
SCE	saturated calomel electrode
SCV	semi-circular sweep voltammetry

SHE	standard hydrogen electrode
SV	stripping voltammetry
SWV	square wave voltammetry
UV-vis	ultraviolet-visible spectroscopy
WE	working electrode

Chapter 1

Fundamentals of Electrochemistry

This chapter introduces the fundamental concepts and principles of electrochemistry and the electrochemical techniques employed in this thesis. Topics covered in this chapter include electrochemical equilibrium, electrode kinetics, Faradaic and non-Faradaic processes, mass transport, electrochemical cells, macro- and micro-electrodes and electrochemical techniques. These topics are essential for understanding the experiments and results in the next chapters and provide an overview of the underlying theories for the discussions.

1.1 Electrochemical Equilibrium

Electrochemical reactions involve chemical changes and transfer of electric charge across interfaces between two conducting phases. Consider the following case of a general one-electron reduction reaction, where a metallic electrode is inserted into a solution containing redox species A and B:

$$A_{(aq)} + e^-_{(metal)} \rightleftharpoons B_{(aq)} \tag{1.1}$$

The metal used here acts as an electron provider and acceptor aiding the electron transfer within the redox couple. A charge separation between the solution and electrode may be established at the point of equilibrium leading to a development of electrode potential at the metal relative to the solution. This can be understood by looking at the electron energy levels associated with the species participating in the potential determining equilibrium, as schematically shown in Figure 1.1. In the metallic electrode, the electrons form a conduction band, filling up the continuous energy levels to an energy maximum known

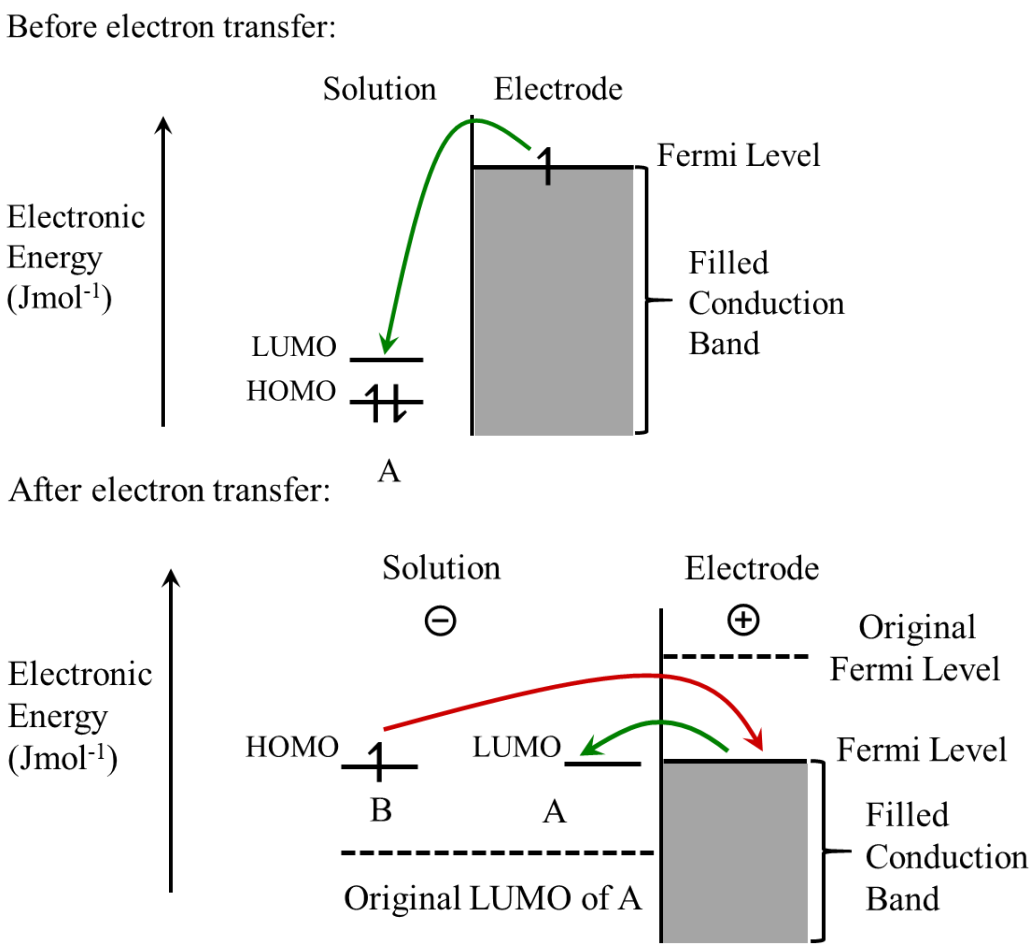


Figure 1.1 Illustration of energy levels of the ions in solution and the metallic electrode during establishment of electrochemical equilibrium between A and B[1].

as Fermi level. On the contrary, in the solution phase, the electronic energy levels of species A and B are discrete involving a vacant molecular orbital in A. From a thermodynamic aspect, considering the situation in which initially the Fermi level of the electrode is relatively higher than the lowest unoccupied molecular orbitals (LUMO) of A, the energy difference drives an energetically favourable transfer of electrons from the Fermi level to the LUMO of A, converting A to B in the solution phase. Such electron transfer allows the positive charge to build up on the electrode (metal) and corresponding negative charge in the solution, which causes the progressive drop of Fermi level of the electrode and the increase of energy levels of solution phase species. At the point when it becomes energetically favourable for the electron transfer from the highest occupied

molecular orbital (HOMO) of B to the metallic phase, the reverse oxidation reaction also occurs. The Fermi level ultimately reaches the position in between the LUMO of A and the HOMO of B, where the reaction rates of reduction and backward oxidation are matched and thus no net transfer of charge is observed. This corresponding to a dynamic equilibrium leading to a charge separation at the electrode/solution interface and the establishment of electrode potential on the metal[1, 3].

In the electrochemical equilibrium as discussed above, the chemical and electrical energies of all the involved entities must be balanced at the position of equilibrium. For a species *j*, the electrochemical potential, $\overline{\mu_j}$ is introduced:

$$\overline{\mu_j} = \mu_j + z_j F\phi \tag{1.2}$$

where μ_j and z_j are the chemical potential (J mol^{-1}) and the charge of species *j*, respectively, *F* is the Faraday constant (96485 C mol^{-1}) corresponding to the charge of one mole of electrons and ϕ is the potential (V) of the electrode (ϕ_M) or solution phase (ϕ_S) where the species *j* presents. For the equilibrium of reaction in Eqn. (1.1), given a constant temperature and pressure, the electrochemical potentials can be expressed as:

$$\overline{\mu}_A + \overline{\mu}_e = \overline{\mu}_B \tag{1.3}$$

Substituting Eqn. (1.2) into Eqn. (1.3):

$$(\mu_A + z_A F\phi_S) + (\mu_{e^-} - F\phi_M) = (\mu_B + z_B F\phi_M) \tag{1.4}$$

$$F(\phi_s - \phi_M) = \mu_B - \mu_A - \mu_{e^-} \tag{1.5}$$

The chemical potential term (μ_j) can be further expressed using:

$$\mu_j = \mu_j^0 + RT \ln \frac{c_j}{c_0} \tag{1.6}$$

where R is the universal gas constant (8.314 J K^{-1} mol^{-1}), T is the absolute temperature (K), c_j is the concentration of species j (mol m^{-3}) in solution and c_0 is the standard concentration of one molar (1 M).

Substituting Eqn. (1.6) into Eqn. (1.5) and rearranging Eqn. (1.5) gives:

$$\phi_M - \phi_S = \frac{\Delta\mu^0}{F} + \frac{RT}{F}\ln(\frac{c_A}{c_B}) \tag{1.7}$$

where:

$$\Delta\mu^0 = \mu_A^0 + \mu_{e^-} + \mu_B^0 \tag{1.8}$$

which is a constant at the given temperature and pressure.

Eqn. (1.7) is the *Nernst equation* applicable to a single electrode/solution interface. It quantitatively describes the position of the electrochemical equilibrium shown in Eqn. (1.1) and its dependency on the concentrations of the ions involved in the equilibrium. Note that the chemical potentials used in Eqn. (1.6) and (1.7) are associated with the species in solutions. For reactions involving an ideal gas, the gaseous pressure p_j (Pa) and the standard pressure p_0 is used to replace c_j and c_0. In the case of pure liquid or solid, the chemical potentials approximate to their standard chemical potentials; therefore no concentration term is present.

However, the *Nernst equation* in Eqn. (1.7) only applies to ideal solutions. For a concentrated solution of ion *j*, the activity (a_j) considering the non-ideality of solution due to ion-ion and ion-solvent interactions is introduced:

$$a_j = \gamma_j c_j \tag{1.9}$$

where γ_j is defined as the activity coefficient of species *j* which measures the extent of non-ideality of solution. Eqn. (1.7) is modified as:

$$\phi_M - \phi_S = \frac{\Delta\mu^0}{F} + \frac{RT}{F}\ln\left(\frac{a_A}{a_B}\right) \tag{1.10}$$

Note if A or B is a pure solid rather than a dissolved species then the amount present does not influence the potential corresponding to a formal definition of $a = 1$ for pure solids.

In practice, it is impossible to experimentally measure the absolute value of the quantity ($\phi_M - \phi_S$) associated with a single electrode/solution interface since the voltmeter measuring the potential difference has to be connected through a circuit which creates the second interface. To make this measurement feasible a second electrode is introduced into the solution so as to act as a 'reference electrode'[2]. Then the *difference* of the quantity ($\phi_M - \phi_S$) between two electrodes can be measured using the voltammeter as:

$$E = (\phi_M - \phi_S)_{test} - (\phi_M - \phi_S)_{reference} \tag{1.11}$$

where E is the potential difference (V) between the test and reference electrodes where the 'test electrode' refers to the interface of interest, namely the A/B couple in the above example. Classically, and by IUPAC definition, the electrode potentials (E) are measured using a standard hydrogen electrode (SHE) as the reference electrode. In particular, the standard electrode potential (E^0) of an arbitrary redox couple (A/B) is measured against SHE at the condition where the activities of the species involved (a_A and a_B) in the electrochemical equilibrium are unity. The Nernst equation incorporating the term E^0 can be expressed as:

$$E = E^0 + \frac{RT}{F}\ln\left(\frac{a_A}{a_B}\right) \tag{1.12}$$

The formal potential E_f^0 is defined as:

$$E_f^0 = E^0 + \frac{RT}{F}\ln\left(\frac{\gamma_A}{\gamma_B}\right) \tag{1.13}$$

E_f^0 breaks the thermodynamic generality of E^0 but reflects the experimentally meaningful parameters γ_A and γ_B which are dependent on the concentrations of all species present in the electrolyte that affect the ion activities, reflecting the nature of the supporting medium and avoiding the inconvenience of handling the activities which are usually unknown in many cases of interest. Therefore E^0 in Eqn. (1.12) is replaced by E_f^0 and the Nernst equation is expressed as:

$$E = E_f^0 + \frac{RT}{F}\ln\left(\frac{c_A}{c_B}\right) \tag{1.14}$$

Note that the electrode potential described in the Nernst equation above is established at a dynamic equilibrium which requires a fast rate of electron transfer. The kinetics with respect to the electrode process will be elaborated in the following section.

1.2 Electrode Kinetics

As discussed in the last section, *Nernst equation* applies to the reactions under the electrochemical equilibrium where 'fast kinetics' occurs. To describe the approach to the equilibrium and the dynamic maintenance of such state quantitatively, the kinetics of the electrochemical reactions needs to be considered. Looking back at the one-electron reduction reaction in Eqn (1.1), given the heterogeneous electron transfer rate of the forward and backward reactions are k_{red} and k_{ox} (m s^{-1}) respectively:

$$A_{(aq)} + e^-_{(metal)} \underset{k_{ox}}{\overset{k_{red}}{\rightleftharpoons}} B_{(aq)} \tag{1.15}$$

As the reactant A gets close to the electrode within the distance of 10-20 Å, the electrons are able to transfer between A and the electrode via quantum mechanical tunnelling. The electron transfer leads to the passage of net electrical current, I (A) through the electrode. I is determined by the equation:

$$I = -FA_{elec}\, j \tag{1.16}$$

where F is the Faraday constant and A_{elec} is the geometric area (m^2) of the electrode, j is the flux (mol m^{-2} s^{-1}) of reactant undergoing electrolysis, which represents the rate of the interfacial electrochemical reaction via:

$$j = k_{red} c_{A,0} - k_{ox} c_{B,0} \tag{1.17}$$

where $c_{A,0}$ and $c_{B,0}$ are the surface concentrations (mol m^{-3}) of reactants A and B representing the concentration within the electron tunnelling distance which are usually derived from the bulk concentrations[4].

The factors controlling the electrochemical reaction rates are predicted by the *Transition State Theory*[5, 6]. It states that the Gibbs energy of activation raises through a well-defined transition state or activated complex to form the products. Assuming the rate constants k_{red} and k_{ox} meet the *Arrhenius Equation* relating them to the Gibbs energy of activation as:

$$k_{red} = A_{red} \exp\left(-\frac{\Delta G^{\dagger}_{red}}{RT}\right) \tag{1.18}$$

$$k_{ox} = A_{ox} \exp\left(-\frac{\Delta G^{\dagger}_{ox}}{RT}\right) \tag{1.19}$$

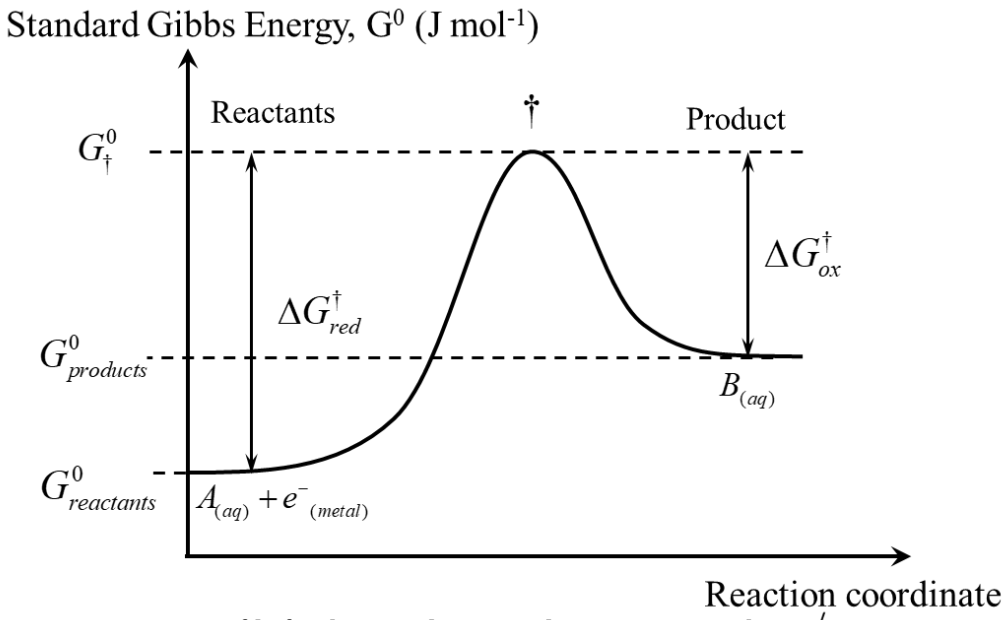


Figure 1.2 A reaction profile for the one-electron reduction process where ϕ_M is more positive relative to ϕ_S

where A_{red} and A_{ox} are the pre-exponential factors which are believed to depend on the reaction frequency of electroactive species with the electrode surface. $\Delta G^{\dagger}_{red}$ and $\Delta G^{\dagger}_{ox}$ are the Gibbs energies of activation of the reduction and oxidation (J mol^{-1}), respectively. *R* is the universal gas constant (8.314 J K^{-1} mol^{-1}) and *T* is the absolute temperature (K).

The reaction profile illustrating the positions of reactants, transition state (†) and products is shown in Figure 1.2, where $\Delta G^0_{reactants}$, $\Delta G^0_{products}$ and $\Delta G^0_{\dagger}$ are the standard molar Gibbs energies of the reactants, products and transition state (J mol^{-1}), accordingly. It can be seen from Figure 1.2 that:

$$\Delta G^{\dagger}_{red} = G^0_{\dagger} - G^0_{reactants} \tag{1.20}$$

$$\Delta G^{\dagger}_{ox} = G^0_{\dagger} - G^0_{products} \tag{1.21}$$

According to section 1.1, for the reaction shown in Eqn. (1.15):

$$
\begin{aligned}
G^0_{reactants} &= G^0_A + G^0_{e^-} \\
&= (\mu^0_A + z_A F\phi_S) + (\mu^0_{e^-} - F\phi_M) \\
&= C_1 + (z_A - 1)F\phi_S - F(\phi_M - \phi_S)
\end{aligned} \tag{1.22}
$$

$$
\begin{aligned}
G^0_{products} &= G^0_B \\
&= \mu^0_B + z_B F\phi_S \\
&= C_2 + (z_A - 1)F\phi_S
\end{aligned} \tag{1.23}
$$

where C_1 and C_2 are constants. The standard Gibbs energy of transition state, $G^0_{\dagger}$ can be described based on Eqn. (1.22) and (1.23) using the following equation:

$$
G^0_{\dagger} = C_3 + (z_A - 1)F\phi_S - \beta F(\phi_M - \phi_S) \tag{1.24}
$$

where C_3 is another constant. β is known as transfer coefficient ($0 < \beta < 1$), the magnitude of which indicates the resemblance of the transition state to reactants or products in terms of potential dependence of its standard Gibbs energy. If β is close to 1, the transition state is considered to be reactant (A) like. If β is close to 0, the transition state is considered to be product (B) like[7, 8]. Accordingly, the other transfer coefficient α is defined for convenience:

$$
\alpha = 1 - \beta \tag{1.25}
$$

The value of β (and hence α) is often found to be 0.5 indicating the transition state lies at the midpoint between the reactants and products[9].

Substituting Eqn. (1.20)−(1.24) into Eqn. (1.18) and (1.19), electrochemical rate constants can be related to ϕ_M and ϕ_S as:

$$
k_{red} \propto \exp\left[-\frac{\alpha F}{RT}(\phi_M - \phi_S)\right] \tag{1.26}
$$

$$k_{ox} \propto \exp\left[\frac{\beta F}{RT}(\phi_M - \phi_S)\right] \tag{1.27}$$

In section 1.1 we know that the quantity ($\phi_M - \phi_S$) for a single electrode-solution interface cannot be measured experimentally. Therefore we introduce the reference electrode and impose a potential *E*, at the test electrode such that ($\phi_M - \phi_S$)can be expressed as:

$$E - E_f^0 = (\phi_M - \phi_S)_{test} + C_4 \tag{1.28}$$

where $E - E_f^0$ represents the potential applied to the test electrode relative to the formal potentials of redox couple A/B which are both measured against the reference electrode SHE. C_4 is a constant. Based on Eqn. (1.28) the expressions for the electrochemical rate constants can be modified as:

$$k_{red} = k_{red}^0 \exp\left[-\frac{\alpha F(E - E_f^0)}{RT}\right] \tag{1.29}$$

$$k_{ox} = k_{ox}^0 \exp\left[\frac{\beta F(E - E_f^0)}{RT}\right] \tag{1.30}$$

where k_{red}^0 and k_{ox}^0 standard reduction and oxidation rate constants (m s^{-1}), respectively, incorporating the constant terms including C_4. Eqn. (1.17) can be expanded using Eqn. (1.29) and (1.39) to describe the flux for the electrode-solution interfacial reaction:

$$j = k_{red}^0 \exp\left[-\frac{\alpha F(E - E_f^0)}{RT}\right] c_{A,0} - k_{ox}^0 \exp\left[\frac{\beta F(E - E_f^0)}{RT}\right] c_{B,0} \tag{1.31}$$

which is known as the *Butler-Volmer* equation[10-12]. In the case of dynamic equilibrium, no net current flows and *j* is zero. Since $\alpha + \beta = 1$, the *Butler-Volmer* equation becomes:

$$E = E_f^0 + \frac{RT}{F}\ln\left(\frac{c_A}{c_B}\right) + RT\ln\left(\frac{k_{red}^0}{k_{ox}^0}\right) \tag{1.32}$$

Comparing Eqn. (1.32) with Nernst equation written in Eqn. (1.18), it can be derived that:

$$k_{red}^{0} = k_{ox}^{0} = k^{0} \tag{1.33}$$

where k^0 is defined as the standard electrochemical rate constant. k^0 provides the kinetic information of the redox couple. A high k^0 value indicates the redox reaction will achieve equilibrium over a shorter time period and *vice versa*[2]. The electrochemical rate constants under the equilibrium can be written as:

$$k_{red} = k^{0}\left[-\frac{\alpha F(E-E_f^0)}{RT}\right] \tag{1.34}$$

$$k_{ox} = k^{0}\left[\frac{\beta F(E-E_f^0)}{RT}\right] \tag{1.35}$$

For the reaction shown in Eqn. (1.15), Eqn. (1.31) suggests the net flux and current are balanced by both reduction and oxidation processes of A/B with the arbitrary potential E imposed on the test electrode. Consider the extreme circumstance, where E_f^0 is substantially larger than E, making the oxidation term negligible:

$$j = k_{red}^{0}\exp\left[-\frac{\alpha F(E-E_f^0)}{RT}\right]c_{A,0} \tag{1.36}$$

Or E is substantially larger than E_f^0 and the oxidation term is predominant:

$$j = k_{ox}^{0}\exp\left[\frac{\beta F(E-E_f^0)}{RT}\right]c_{B,0} \tag{1.37}$$

Provided that the bulk concentrations remain constant over the studied potential range, *Tafel law* can be derived:

$$\ln|I_{red}| = -\frac{\alpha FE}{RT} + C_5 \tag{1.38}$$

$$\ln|I_{ox}| = \frac{\beta FE}{RT} + C_6 \tag{1.39}$$

where I_{red} and I_{ox} are the reduction and oxidation currents, respectively. C_5 and C_6 are constants. Figure 1.3 shows the plots of ln |*I*| against *E*, known as *Tafel plot* for the one-electron transfer reduction and oxidation reactions. Transfer coefficients α and β can be determined from analysing the slopes of the present *Tafel plots*.

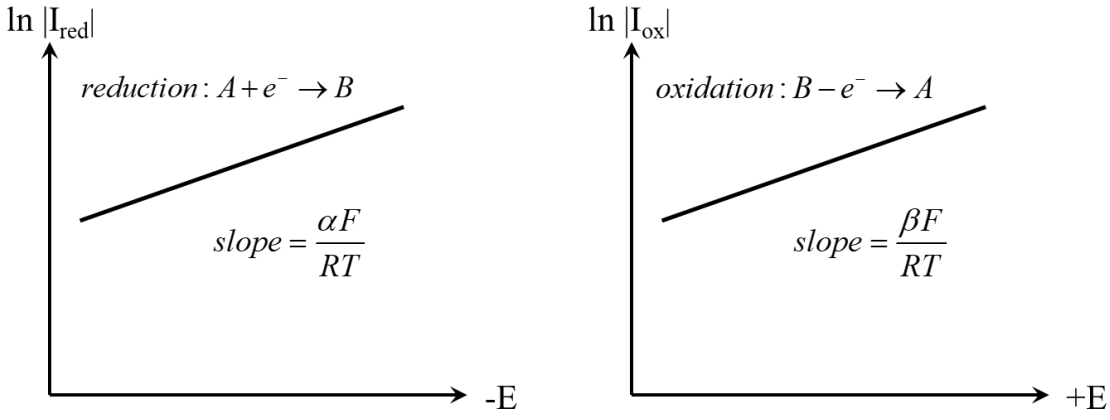


Figure 1.3 Tafel plot for the one-electron transfer reactions.

1.3 Faradaic and Non-Faradaic Processes

Two types of processes, namely Faradaic and non-Faradaic processes can occur at electrode surfaces and give rise to a current flow when a suitable potential is applied. In a Faradaic process, electrons are transferred across the electrode-solution interface which leads to redox reactions of electroactive species. This is described by Faraday's law of electrolysis[13]:

$$m = \frac{QM}{nF} \tag{1.40}$$

where *m* is the mass (g) of the electroactive species which reacts, *Q* is the total electric charge (C) passed, *F* is the Faraday constant (96485 C mol^{-1}), *n* is the number of electrons

transferred per species oxidised or reduced and M is the molar mass (g mol^{-1}) of the species.

However, currents can still flow even under the conditions where such electrochemical reactions are thermodynamically or kinetically unfavourable, as non-Faradaic processes can occur. In non-Faradaic processes, no electron passes through the electrode-solution interface, instead, the charge is built up locally by processes such as adsorption and desorption at the electrode surface, where the structure of electrode-solution interface is altered due to the change in potential or solution composition. The charging process of the electrode-solution interface is analogous to that of a capacitor since no charge is transferred through the interface regardless of the potentials imposed. Specifically, the accumulation of charge at the electrode surface caused by the imposed potential induces the redistribution of electrolyte ions and/or dipolar solvent molecules in the solution adjacent to the electrode surface via electrostatic interaction. As the result, a current, known as *capacitative current* flows through the external circuit. The capacitative current is defined by the equation:

$$I = \frac{dQ}{dt} = C_d A_{elec} \frac{dE}{dt} = C_d A_{elec} v \tag{1.41}$$

where Q is the charge (C), t is the time (s), C_d is the capacitance of the double layer per unit area (F m^{-2}), E is the applied potential (V) across the electrode/solution interface, A_{elec} is the electroactive layer area (m^2) and v is the scan rate (V s^{-1}). The whole array of charged species and oriented dipoles present at the electrode-solution interface is named the *electrical double layer*[2] which is depicted in the model shown in Figure 1.4.

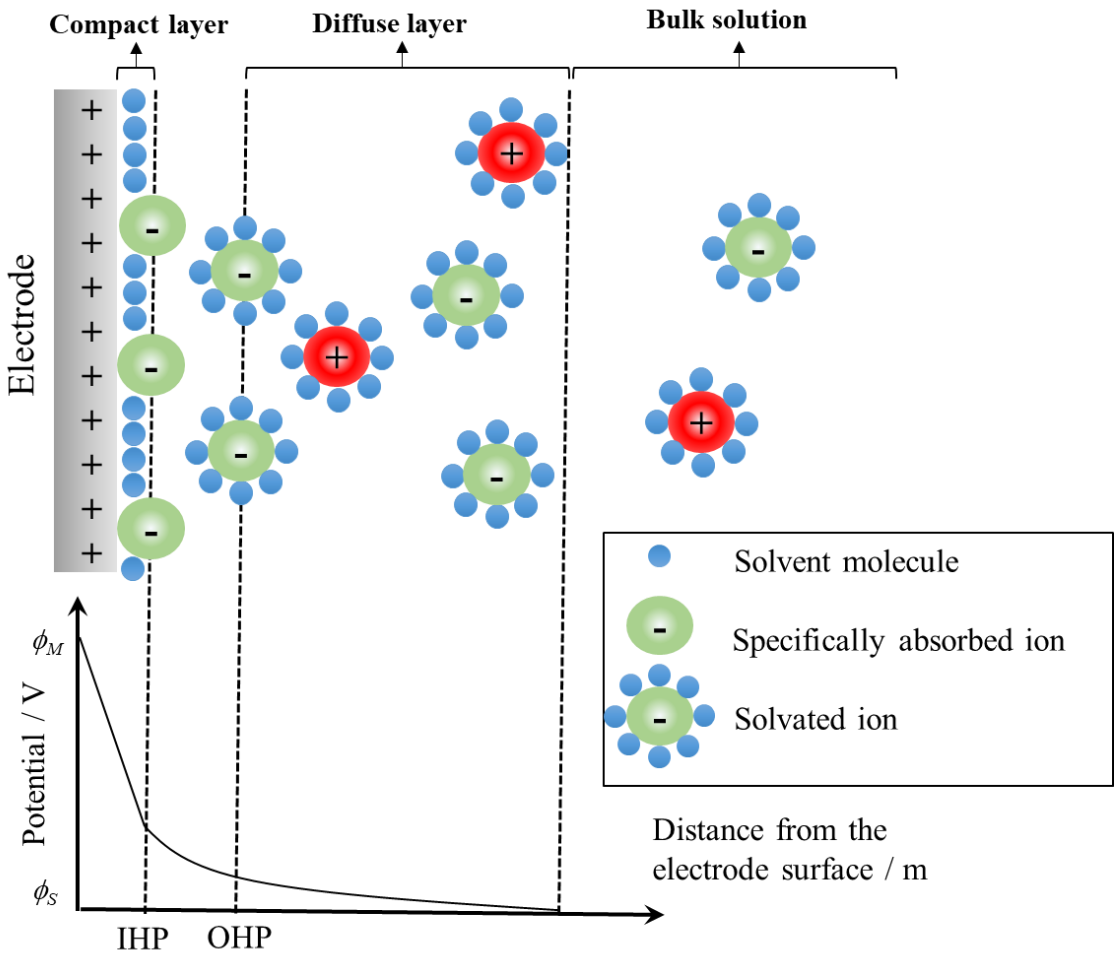


Figure 1.4. Model of the electrical double layer (top) and the potential drop $\phi_M - \phi_S$ across the double layer (bottom), where anions are specifically adsorbed at a positive electrode. The green, red and blue spheres represent the anions, cations and solvent molecules, respectively, in the solution phase.

As suggested in Figure 1.4, the *electrical double layer* is comprised of several parts. The *inner layer* which is the closest to the electrode, also called as *compact*, *Helmholtz*, or *Stern layer* contains the solvent molecules and sometimes other molecules or ions that are specifically absorbed on the electrode surface. The distance between the electrode surface and the electrical centre of these molecules (or ions which are often desolvated) is referred to as the *Inner Helmholtz Plane* (IHP). The solvated ions, however, can only interact with the electrode surface via the long-range electrostatic force, which are considered to be non-specifically absorbed. The distance from the electrical centre of the closest solvated ions to the electrode surface is known as the *Outer Helmholtz Plane*

(OHP). Due to the agitation of solution, an excess of the non-specifically absorbed ions are distributed in the region in between the OHP and the bulk solution, named the *diffuse layer*.

The thickness of the diffuse 1ayer is associated with the total ionic concentration in the solution. The Debye length κ^{-1} (Å), defined as the distance over which the induced potential decays to (1/e) of its initial value for a 1:1 electrolyte, $M^{z+}X^{z-}$ is expressed as:

$$\kappa^{-1} = \frac{1}{zF}\left(\frac{\varepsilon_0 \varepsilon_r RT}{2c}\right)^{1/2} \tag{1.42}$$

where zF (coulombs per mole) represents the charge on the species M or X of concentration c, ε_0 is the permittivity of vacuum (8.854×10^{-12} C^2 J^{-1} m^{-1}), ε_r is the dielectric constant. Theoretically, with the increase of supporting electrolyte concentration from 1 mM to 0.1 M, the Debye length falls from 100 Å to 10 Å. Thus in experimental practice, electrolytes with high ionic concentrations are added to compress the electrical double layer to ensure that the drop in electrical potential between an electrode and bulk solution occurs over a distance of ca 10 – 20 Å. The potential profile that is also shown in Figure 1.4 reveals the rapid, almost-linear drop of potential within the compact layer and the slow, gradual drop of potential from the diffuse layer to the bulk solution. This drop in potential drives the electron transfer discussed in Section 1.2 which implicitly assumed the presence of a high level of electrolyte so as to compress the diffuse layer to within a length scale compatible with electron tunnelling. More generally however the presence of double-layer capacitance and the resulting capacitative currents needs to be considered alongside the analytically useful Faradaic currents when performing electroanalysis. This is discussed in greater detail in Chapter 8.

1.4 Mass Transport

Mass transport refers to the movement of material from one location to another, originating from differences in electrical or chemical potentials at the two locations or from mechanical disturbances. Mass transport, in addition to the charge transfer discussed in previous sections, governs the kinetics of electrode reactions, and is described by the *Nernst-Plank equation* which for one-dimensional Cartesian coordinates[2] is as follows:

$$j_i(x) = -D_i \frac{\partial c_i(x)}{\partial x} - \frac{z_i F}{RT} D_i c_i \frac{\partial \phi(x)}{\partial x} + c_i v(x) \qquad (1.43)$$

where j_i (x) is the total flux (mol m^2 s^{-1}) of a species j at distance x from the electrode surface, D_i is the diffusion coefficient (m^2 s^{-1}), $c_i(x)$ is the concentration (mol m^{-3}), z_j is the ionic charge, $\phi(x)$ is the electric potential (V), and $v(x)$ is the local fluid velocity (m s^{-1}). The three terms at the right-hand side of the equation represent three forms of mass transfer, which are (from left to right) diffusion, migration and convection, respectively.

Experimental electrochemical systems are usually designed to facilitate the simple interpretation of electrochemical reactions, where the contributions of convection and migration are negligible. Each form of mass transfer and the methods to eliminate some of them are discussed below.

1.4.1 Diffusion

Diffusion is the spontaneous movement of a species from its high concentration zone towards its low concentration zone. It allows the species in the bulk solution to renew those which are depleted in the vicinity of electrode surface due to the electrochemical reaction triggered by applying a suitable potential. Diffusion is modelled by *Fick's First*

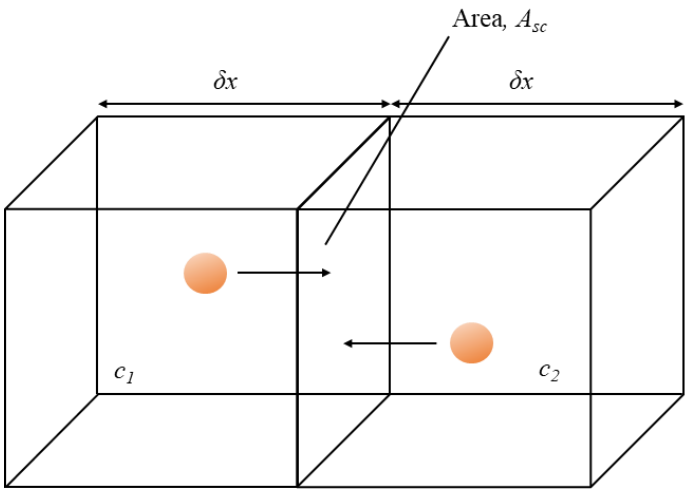


Figure 1.5. Schematic representation of the molecular basis of Fick's First Law

Law, which associates the change in concentration with space, and *Fick's Second Law* which describes the relation between the change in concentration and time[14, 15].

Fick's First Law, proposed by Fick on the basis of experiment, quantifies a diffusional flux, *J*, observed down the concentration gradient at point *x* by:

$$J = -D\frac{\partial c}{\partial x} \tag{1.44}$$

where the flux J refers to the number of moles passing through a unit area in a unit time (mol cm^{-2} s^{-1}), $\frac{\partial c}{\partial x}$ is the concentration gradient at point *x* and *D* is the diffusion coefficient (cm^2 s^{-1}). The negative sign shown in Eqn. (1.44) indicates the movement of the species is down the concentration gradient. To understand *Fick's First Law*, its molecular basis is considered using a one-dimensional cuboid model. As illustrated in Figure 1.5, a box with a width of 2δ*x is* evenly divided at point *x* into two compartments, each of which has a width of δ*x*. The cross-sectional area, A_{cs} at point *x* separates the solutions of two concentrations c_1, c_2 dividing the left and right side compartment.

Assuming that the particles (molecules, ions) in either compartment of the solutions move randomly and cross the divide into the other compartment across A_{cs} with equal possibility, for per defined time period of δt, the number of particles moving through A_{cs} from left to right side and from right to left side can be written as $\frac{1}{2}c_1 A_{cs}\delta x$ and $\frac{1}{2}c_2 A_{cs}\delta x$, respectively.

The net rate of particles transported through the plane A_{cs} within the box can thus be expressed as:

$$Rate_{net} = \frac{(c_1 - c_2)A_{cs}\delta x}{2\delta t} \tag{1.45}$$

As the local concentration gradient $\frac{\delta c}{\delta x}$ can be approximated to $-\frac{(c_1 - c_2)}{\delta x}$, Eqn. (1.45) can be rearranged as:

$$Rate_{net} \approx -\frac{A_{cs}(\delta x)^2}{2\delta t}(\frac{\partial c}{\partial x}) \tag{1.46}$$

Thus the diffusional flux J can be obtained by dividing Eqn. (1.46) with the area:

$$J = -\frac{(\delta x)^2}{2\delta t}(\frac{\partial c}{\partial x}) \tag{1.47}$$

which is equivalent to *Fick's First Law* shown in Eqn. (1.44) when

$$D = \frac{(\delta x)^2}{2\delta t} \tag{1.48}$$

It can be seen from Eqn. (1.48) that the diffusion coefficient provides a measure of the distance a particle travels in a given time. This leads to the *Einstein-Smoluchowski equation*[16, 17]*:*

$$\sqrt{\langle x^2 \rangle} = \sqrt{2Dt} \tag{1.49}$$

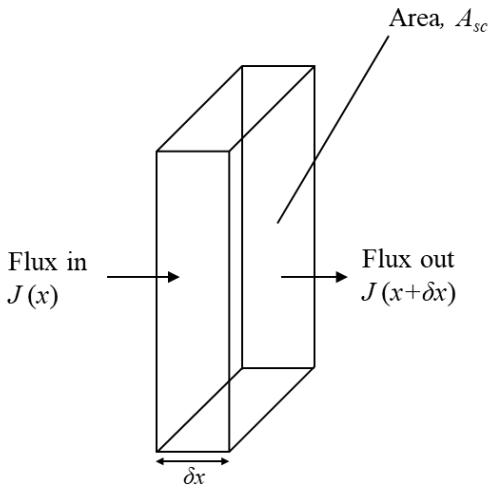


Figure 1.6. Schematic representation of the flux in and out a 'slab'.

where the $\sqrt{\langle x^2 \rangle}$ is the root mean square displacement (m). Eqn. (1.49) can be used to approximate the thickness of the diffusion layer corresponding to the electrolysis of an active species at an electrode surface where the diffusion layer relates to the zone of local depletion.

For three-dimensional diffusion, the root mean square displacements are expanded to:

$$\sqrt{\langle x^2 \rangle + \langle y^2 \rangle + \langle z^2 \rangle} = \sqrt{6Dt} \tag{1.50}$$

Fick's Second Law considers the rate of concentration variation with respect to the time at point *x* and is derived as a direct consequence of *Fick's First Law*. It is assumed that a flux enters through and leaves the slab with the thickness of δ*x* and the area of A_{sc}, as shown in the one-dimensional model in Figure 1.6. The difference between the number of molecules leaving and entering the slab over a time period of δt is:

$$\delta n = \left[j(x) - j(x+\delta x) \right] A_{cs} \delta t \tag{1.51}$$

which can be rearranged with the term of change in concentration as:

$$\left[c(t+\delta t) - c(t) \right] A_{cs} \delta x = \left[j(x) - j(x+\delta x) \right] A_{cs} \delta t \tag{1.52}$$

$$\frac{\partial c}{\partial t} = -\frac{\partial j}{\partial x} \tag{1.53}$$

Substituting *Fick's First Law* into Eqn. (1.53) gives *Fick's Second Law*:

$$\frac{\partial c}{\partial t} = D\frac{\partial^2 c}{\partial x^2} \tag{1.54}$$

1.4.2 Convection

Convection refers to the transport of species in the solution caused by external mechanical forces. There are two forms of convection: natural and forced. *Natural convection* describes species flowing from the denser to less dense region. The dense gradients present in the solution arise either from the chemical transformations at the working/counter electrode when electrolysis occurs or from localised thermal changes. The causes of the latter can be intrinsic to the electrolytic reactions where strongly exothermic or endothermic processes occur, or alternatively, imperfect theromostatting[18]. This form of convection is generally irreproducible and undesirable for electrochemical experiments. Often the experimental time for an electrochemical measurement is constrained to a short duration to minimise the effect of natural convection. Careful thermostatting is required and was performed in the experiments involved in this thesis as reported below.

Forced convection results from the mechanical stirring or agitation of the solution. It is usually deliberately introduced to dominate the mass transport in the system and give it a well-defined and easily analysed character. Controlled convection mass transport can be achieved by the stirring of the solution, by rotation or vibration of the electrode, or by the flow of solution over stationary electrodes[1, 2, 19].

1.4.3 Migration

Migration is the movement of charged species in the solution as the result of interacting with the electrical field generated from the potential drop at the electrode/solution interface[1, 2]. For any species *j*, the migratory flux, $J_{m,j}$ at point *x* is given by:

$$J_{m,j}(x) = -\frac{z_j F}{RT} D_j c_j \frac{\partial \phi(x)}{\partial x} \tag{1.55}$$

where z_j is the charge of the ion *j* and $\frac{\partial \phi(x)}{\partial x}$ is the potential gradient or electric field (V m^{-1}).

For an electroactive species, both diffusion and migration can occur at the vicinity of the electrode. The total flux J_j (mol m^{-2} s^{-1}) resulted from the mixed forms of mass transport is expressed as:

$$J_j = J_{d,j} + J_{m,j} \tag{1.56}$$

where $J_{d,j}(x)$ and $J_{m,j}(x)$ is the diffusional and migratory flux, respectively. Note that $J_{d,j}$ and $J_{m,j}$ can be in the same or opposite direction depending on the direction of the electric field and the charge on the electroactive species[20]. The detailed illustration of this is shown schematically in Figure 1.7 for the cases of positive, negative and neutral charged electroactive species during their reduction processes. The migratory flux is

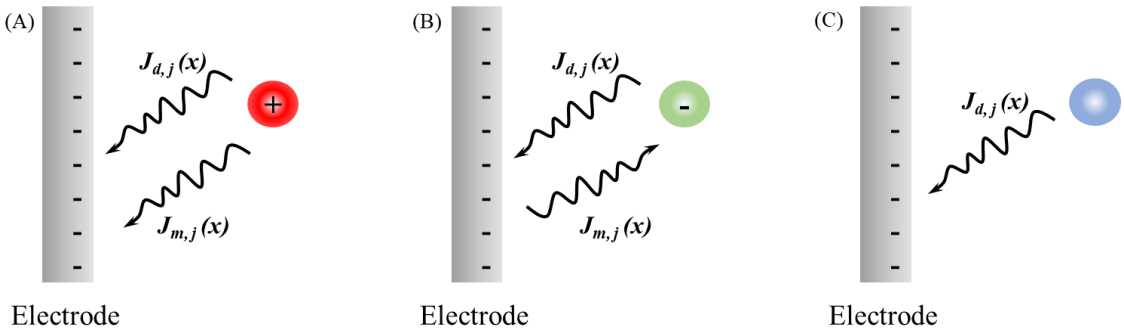


Figure 1.7. Reduction processes with different contributions of migratory flux: (a) positively charged species, (b) negatively charged species, (c) uncharged species[2].

always in the same direction with the diffusional flux when cationic species is reduced at cathodes or anionic species oxidised at anodes, while in the opposite direction to diffusional flux when anions are reduced at cathodes or cations oxidised at anodes.

Migration can strongly affect currents in electrochemical systems, imposing challenges for the mathematical interpretation of electrochemical processes. Thus, in order to minimise the contribution from migration, a sufficiently high concentration of *supporting electrolyte* is added into the system. The supporting electrolyte consists of electrochemically inert ions, typically with a high concentration of 10^{-1} M or above. These inert ions carry the vast majority of the charges of the solution such that the effect of migration can be reduced to a negligible level. There are several more advantages of using a high concentration of supporting electrolyte. First, as mentioned in Section 1.3, the supporting electrolyte compresses the electrical double layer to within 10–20 Å, which is also the distance required for electron transfer between electrode and solution via mechanical quantum tunnelling. This ensures the potential drop ($\phi_M - \phi_S$) between electrode surface and bulk solution can fully drive the Faradaic electron transfer process. Second, the Ohmic drop between the working and reference electrodes is reduced since the solution conductivity is much enhanced (see Section 1.5). Finally, the ionic strength of solution is maintained at a uniform and almost constant level which fixes the activity coefficients and hence the formal potentials of the redox couples (see Section 1.1).

1.5 Electrochemical Cells

To study electrode kinetics and perform electroanalysis, a three-electrode configuration is commonly used in electrochemical experiments. Figure 1.8

schematically shows the setup which contains a working electrode (WE), a reference electrode (RE) and a counter electrode (CE). The working electrode provides the electrochemical interface for the reactions of interest to occur. The reference electrode is required for facilitating the application of a controlled potential difference at the working electrode/solution interface, as discussed in Section 1.1. The counter electrode passes the same current as flows through the WE.

As illustrated in Figure 1.8, all three electrodes are controlled by a potentiostat, which first imposes a fixed potential, *E*, between the working electrode (WE) and the reference electrode (RE). The imposed potential can be written as:

$$E = (\phi_M - \phi_S)_{working} + IR - (\phi_M - \phi_S)_{reference} \tag{1.57}$$

The *IR* term, known as Ohmic drop, represents the product of the electrical resistance, *R*, of the bulk solution between the working and reference electrode and the current, *I*. Since the current passing at the reference electrode is negligible, the *IR* term can be neglected[1]. As detailed in section 1.1, the reference electrode serves to provide a constant value of $(\phi_M - \phi_S)_{reference}$ throughout the measurement. Thus any variation in the potential between

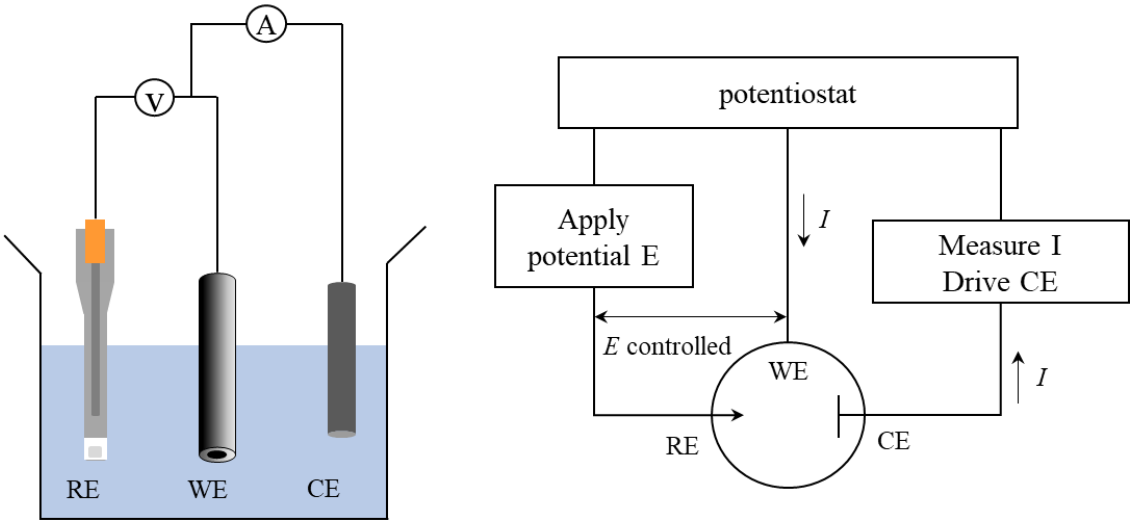


Figure 1.8. Schematic diagram of a three-electrode cell (WE: working electrode; RE reference electrode; CE: counter electrode). The voltammeter and the amperometer measure the applied voltage and the current passing WE, respectively.

the WE and the RE is directly reflected as the change in $(\phi_M - \phi_S)_{working}$. The latter controls the rate of electron transfer at the working electrode.

The potential drop $(\phi_M - \phi_S)_{working}$ on the working electrode/solution interface usually results in the flow of current in the external circuit. To measure this current as a function of the applied potential *E*, the counter electrode (CE) is introduced in the system. A CE is considered essential for the following purposes. One is that it ensures the potential of RE $(\phi_M - \phi_S)_{reference}$ remains stable. In the three-electrode setup, the CE is driven by the potentiostat to whatever potential is required to pass the same current as passing through the WE. For a hypothetical two-electrode system where only a WE and a RE are present, appreciable currents inevitably pass through the RE to complete the electric circuit. Such currents can cause chemical changes within the reference electrode and shift the potential of the reference electrode according to the Nernst equation. If this is not constant then from Eqn. (1.57) any changes in E are no longer reflected in the term $(\phi_M - \phi_S)_{working}$ so that the driving force for the electron transfer is no longer controlled. The second purpose of using CE is to reduce Ohmic drop by avoiding current flow through the RE which is unavoidable in a two-electrode system. If large currents were to pass through the RE, the *IR* term in Eqn. (1.57) will no longer be negligible and $(\phi_M - \phi_S)_{working}$ cannot be precisely controlled via the applied potential *E* as the value of *IR* becomes unknown. Note that the counter electrode is in general highly conductive with a sufficiently large surface area and inert in the studied electrolyte solution to avoid interference with the reaction of interest. The commonly chosen material is a graphite rod or a platinum wire/mesh.

The two-electrode system of a working electrode and a counter electrode may be applicable when the working electrode is a microelectrode with a dimension at the micron scale (see section 1.6). This is because the current passing through a microelectrode is so

low (~ 10^{-9} A)[21, 22] that first, the electrolytic change in the reference electrode becomes negligible and second, the *IR* term in Eqn. (1.57) is much reduced and can be ignored.

1.6 Macroelectrodes and Microelectrodes

The electrodes used as working electrodes in this thesis are categorised into two types according to their sizes: macroelectrodes and microelectrodes. The former usually has a dimension on a scale of millimetres and that of the latter is only of microns. Distinct diffusion patterns are observed at these two types of electrode surfaces due to the size difference, as shown in Figure 1.9.

For macroelectrodes, as their sizes are much larger than the thickness of diffusion layer, the one-dimension, *linear diffusion* dominates during the electrolysis where the flux of materials approaches the entire electrode surface in the perpendicular direction. Macroelectrodes are thus described to possess "uniform accessibility".

For microelectrodes, however, their sizes are smaller or comparable to the thickness of diffusion layer. The diffusion at the electrode surface is not uniform. Instead, the diffusion of the electroactive species towards a microdisc electrode as depicted in Figure

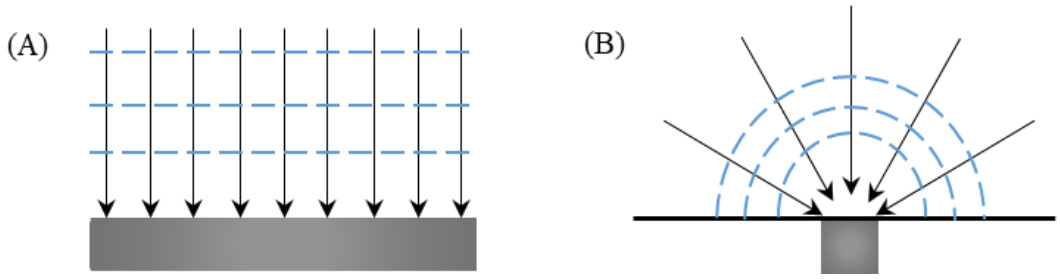


Figure 1.9. Schematic representation of diffusion at (A) macroelectrode and (B) microelectrode. The arrows represent the diffusion of electroactive species. The dashed lines represent the diffusion layers.

1.9 (B) is convergent and from all directions, forming a near hemispherical diffusion layer assuming sufficient time is given for attaining the steady state. The establishment and the features of the current (flux) at steady state are discussed in detail in section 1.7. The *convergent diffusion* is the much more efficient form of mass transport in comparison to linear diffusion, rendering microelectrodes suitable for achieving measurement of fast electrode kinetics. Owing to their small dimensions, microelectrodes are also advantageous in minimising Ohmic drop (Section 1.5), reducing capacitative currents (Section 1.3), and enhancing the Faradaic current density.

Electrochemical reactions are studied at both macro- and microelectrodes in this thesis using two popular techniques: voltammetry and chronoamperometry. These techniques will be introduced in the next section. In chapter 4, the electrochemical behaviours of piperine reduction observed at microelectrode and microelectrode are compared and the discrepancies of which between macro- and micro-electrodes are further demonstrated.

1.7 Some Electrochemical Techniques

This section introduces several conventional voltammetric methods, notably cyclic voltammetry (CV), linear sweep voltammetry (LSV), stripping voltammetry (SV), differential pulse voltammetry (DPV) and square wave voltammetry (SWV) as well as chronoamperometry and nano-impact experiments. In addition to the above techniques, a novel, semi-circular sweep voltammetry (SCV) is also used in this thesis and will be introduced in the next chapter.

1.7.1 Cyclic and Linear Sweep Voltammetry

Cyclic voltammetry (CV) and linear-sweep voltammetry (LSV) are the most frequently used electroanalytical methods. They apply linear potential sweeps at the working electrode, typically as depicted in Figure 1.10. In cyclic voltammetry, the potential wave is triangular, starting from an initial potential, E_1 to a reversal potential, E_2, and finally sweeping back to E_1[23, 24]. It can be described mathematically by:

$$E(t) = \begin{cases} E_1 \pm vt & \text{for } 0 < t < t_{switch} \\ E_2 \mp v(t - t_{switch}) & \text{for } t \geq t_{switch} \end{cases} \quad (1.58)$$

where the positive or negative sign indicates ether anodic or cathodic sweeps, t_{switch} is the time of the sweep before switching direction and v (V s^{-1}) is the scan rate defined by:

$$v = \frac{\partial E(t)}{\partial t} \quad (1.59)$$

It is given by the slope of the wave. In LSV, only the forward potential sweep is considered. Note that for both CV and LSV, the scan rate is constant throughout the entire sweep, which is a feature fundamentally different from that in the novel voltammetric techniques discussed in the next chapter.

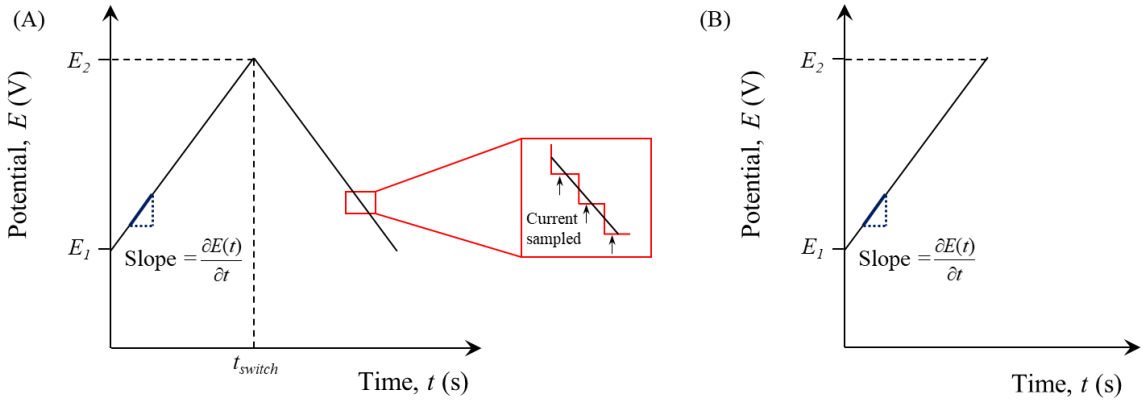


Figure 1.10. The potential-time profile of a (A) cyclic and (B) linear sweep voltammogram. The zoom-in graph in (A) shows a representation of digitally generated sequential steps.

The potential wave is usually chosen to start at an initial potential E_1 where no *Faradaic* process occurs in the solution phase for the electroactive species and to reverse or end at a high potential E_2 that fully drives the electron transfer during the oxidation/reduction of the species. In practice, a large number of small, 'staircase' like potential steps (usually less than 1 mV) are digitally generated to approximate the ramp, as shown in Figure 1.10[25]. The current is sampled at a fixed position within each potential step and plotted as a function of potential to produce a voltammogram.

Interpretations of shapes and magnitudes of voltammograms can provide abundant information of the studied redox system such as analyte concentrations, rate constants and diffusion coefficients[1, 2]. In the following sections, these cyclic voltammetric features for a one-electron transfer reduction process observed at both macroelectrodes and microelectrodes are considered.

1.7.1.1 Voltammetry at Macroelectrodes

At macroelectrodes, peak-shaped voltammograms are typically observed as the result of the influence from both electrode kinetics and from linear diffusion. The voltammogram starts from a potential corresponding to zero Faradaic current. When the potential sweep approached the formal potential, the electrochemical reaction may begin as the reaction rate is increasingly elevated with the increase of potential. Meanwhile, the depletion of reactant becomes faster leading to the rise of current until the surface concentration of reactant drops almost to zero close to where the current reaches a maximum. At this point, the electron transfer rate is balanced by the rate of diffusion of the reactant. As the sweep continues, the current starts to drop as the diffusion is no longer sufficient to replenish the consumption of reactants at the electrode surface. The forward scan results in the formation of a forward peak and a build-up of the product near the

electrode. Likewise, for the following reverse sweep, a similar pattern is observed for the reverse reaction process and a backward peak is observed.

In general, three types of voltammetric profiles with distinct characteristics in terms of electrode kinetics can be observed at macroelectrodes, namely reversible, quasi-reversible and irreversible. The reversibility reflects the rate of electrochemical reaction relative to the rate of mass transport. The former is measured by the standard electrochemical rate constant, k^0, and the latter is measured by the mass transport coefficient, m_T (m s^{-1}) defined as:

$$m_T = \frac{D}{\delta} \tag{1.60}$$

where D is the diffusion coefficient (m^2 s^{-1}) and δ is the diffusion layer thickness (m). The sweep time t (s) for conducting a voltammetric experiment can be roughly expressed as:

$$t \propto \frac{RT}{Fv} \tag{1.61}$$

where v is the voltage scan rate (V s^{-1}). Thus m_T is dependent on the following terms:

$$m_T \propto \sqrt{\frac{FDv}{RT}} \tag{1.62}$$

When $k^0 >> m_T$, the process is reversible, corresponding to *fast* electrode kinetics; when $k^0 << m_T$, the process is irreversible, corresponding to *slow* electrode kinetics. The quantitative criteria for electrochemical reversibility introduced by Matsuda and Ayabe define the parameter Λ[26]:

$$\Lambda = \frac{k^0}{\sqrt{\frac{FDv}{RT}}} \tag{1.63}$$

and suggests three ranges for the classifications of reversible, quasi-reversible and irreversible processes:

$$\text{Reversible, } \Lambda \geq 15,\ k^0 \geq 0.3\sqrt{v}\ \text{cm s}^{-1} \tag{1.64}$$

$$\text{Quasi-reversible, } 15 > \Lambda > 10^{-3},\ 2\times10^{-5}\sqrt{v} < k^0 < 0.3\sqrt{v}\ \text{cm s}^{-1} \tag{1.65}$$

$$\text{Irreversible, } \Lambda \leq 10^{-3},\ k^0 \leq 2\times10^{-5}\sqrt{v}\ \text{cm s}^{-1} \tag{1.66}$$

at the system of 298 K where the transfer coefficient α is assumed to be 0.5.

Peak potentials, peak currents and their dependences on scan rates are the important voltammetric features for studying electrode reaction kinetics. As suggested in Figure 1.11, notable differences are observed for the peak-to-peak separations (ΔE_{pp}, defined as the difference between the anodic and cathodic peak potentials) between reversible and irreversible voltammetry. For an electrochemically reversible system, the relation between surface concentration of reactive species and peak potential is described by

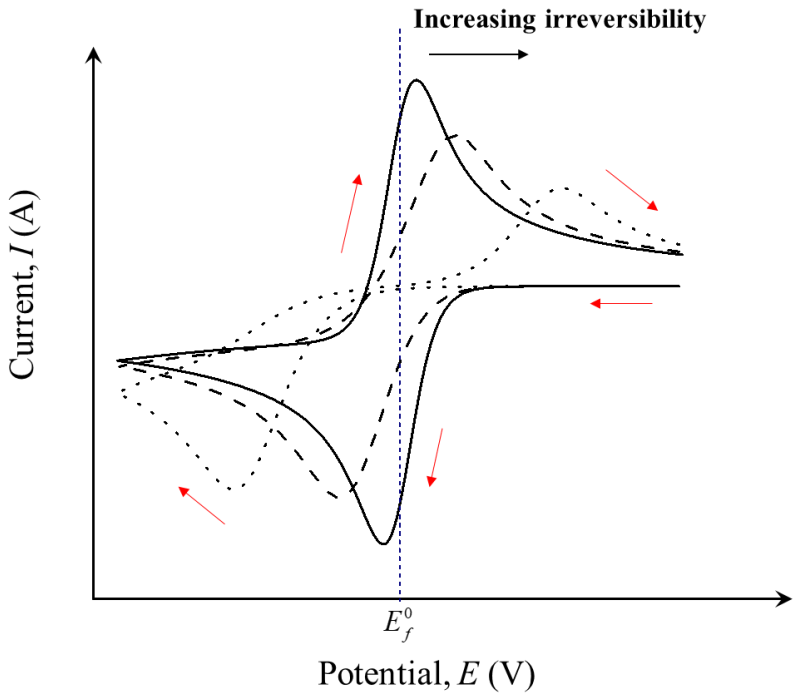


Figure 1.11. Cyclic voltammograms for a one-electron transfer reduction process at a macrodisc electrode corresponding to reversible (solid line), quasi-reversible (dash line), and irreversible systems (dot line). Red arrows show the starting point and scan direction.

Nernst Equation (Eqn.1.14) and thus the ΔE_{pp} is determined to be ca. 57 mV at 298 K for the one-electron transfer redox peaks regardless of the scan rate applied. In an irreversible system, slow electrode kinetics leads to a larger ΔE_{pp} as higher overpotentials are required for driving the redox reactions. The Nernst Equation does not apply to the voltammograms associated with an irreversible process and ΔE_{pp} grows broader with the increase of scan rate due to the enhanced mass transport rate. The mid-point potentials of the forward and backward peaks ($E_{1/2}$) in reversible and irreversible voltammetry (α =0.5) can be written as:

$$\text{Reversible: } E_{1/2} = E_f^0 + \frac{RT}{2F}\ln\left(\frac{D_{product}}{D_{reactant}}\right) \tag{1.67}$$

$$\text{Ireversible: } E_{1/2} = E_f^0 + \frac{RT}{F}\ln\left(\frac{D_{product}}{D_{reactant}}\right) \tag{1.68}$$

which are independent on scan rate and are both identical to E_f^0 when the diffusion coefficients of reactant $D_{reactant}$ and product $D_{product}$ are identical. The peak currents I_p for a diffusion-controlled, one-electron transfer reduction process of species A are related to the square root of scan rate by *Randles-Ševčík* equations for reversible and irreversible limits respectively (298 K):

$$\text{Reversible: } I_p = 0.446FA_{elec}[A]\sqrt{\frac{FDv}{RT}} \tag{1.69}$$

$$\text{Irreversible: } I_p = 0.496\sqrt{\alpha}FA_{elec}[A]\sqrt{\frac{FDv}{RT}} \tag{1.70}$$

where *[A]* is the bulk concentration of species A and A_{elec} is the electrode surface area. The other terms have been defined previously. The general forms of Eqn. (1.69) and (1.70) for multi-electron transferred process are:

$$\text{Reversible: } I_p = 0.446nFA_{elec}[A]\sqrt{\frac{nFDv}{RT}} \tag{1.71}$$

$$\text{Irreversible: } I_p = 0.496\sqrt{n' + \alpha_{n'+1}}nFA_{elec}[A]\sqrt{\frac{FDv}{RT}} \tag{1.72}$$

where *n'* is the total number of electrons transferred before the rate-determining step, $\alpha_{n'+1}$ is the transfer coefficient of the rate-determining step.

1.7.1.2 Voltammetry at Microelectrodes

Cyclic voltammetric responses obtained at microelectrodes are vastly different from those discussed above at macroelectrodes. The more efficient, convergent diffusion taking place at microelectrodes allows for the constant replenishment of electroactive species from bulk solution to electrode surface. This results in the generation of sigmoidal response reaching a steady-state current I_{ss} (A) provided that the scan rate is slow enough for such a diffusion pattern to be attained[27-29]. For a one-electron transfer process:

$$I_{ss} = 4FD[A]r_e \tag{1.73}$$

where r_e is the radius of the microdisc electrode (m). Note that as shown in Figure 1.12, the backward oxidation current is lost due to the rapid diffusion of the electro-generated species away from the electrode. The peak shape and the backward current appear only when an extremely fast scan rate is applied.

Electrochemical reversibility for voltammetry in the case of microelectrodes is characterised by the electrochemical reaction rate constant and the steady-state mass transport coefficient m_T which is dependent on the size of electrode by:

$$m_T \propto \frac{D}{r_e} \tag{1.74}$$

Analogous to the case of macroelectrodes a parameter κ is introduced[2]:

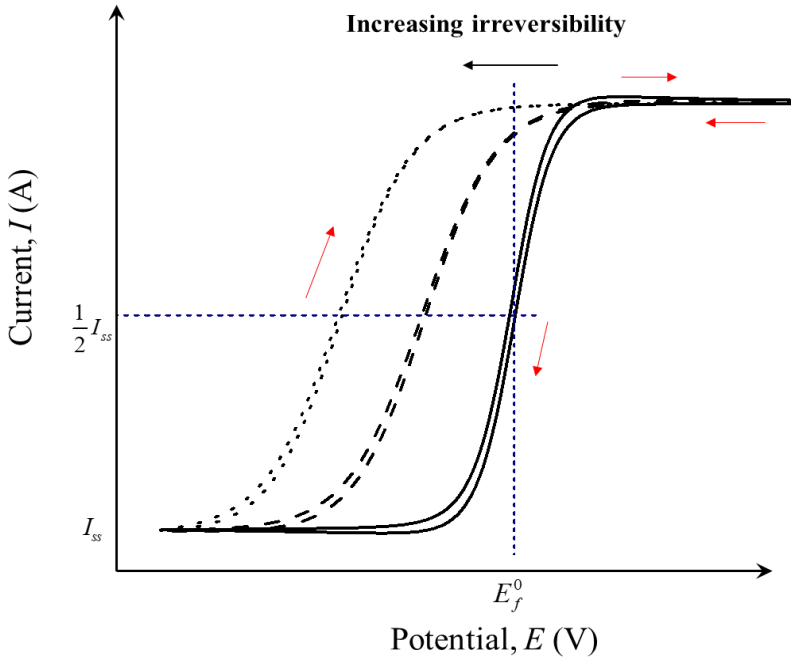


Figure 1.12. Sigmoidal cyclic voltammetric responses for a one-electron transfer reduction process at a microdisc electrode corresponding to reversible (solid line), quasi-reversible (dash line), and irreversible systems (dot line). Red arrows show the starting point and scan direction.

$$\kappa = \frac{r_e k^0}{D} \tag{1.75}$$

and used as a diagnostic parameter for three kinetic regimes:

$$\text{Revesible: } \kappa > 10 \tag{1.76}$$

$$\text{Quasi-reversible: } 10 \geq \kappa \geq 10^{-2\alpha} \tag{1.77}$$

$$\text{Irreversible: } \kappa < 10^{-2\alpha} \tag{1.78}$$

The reversibility of voltammetry is also reflected in the half-wave potential, $E_{1/2}$ where half of the steady-state current ($I = \frac{1}{2} I_{ss}$) is observed. It can be associated with E_f^0 for reversible and irreversible limits as:

$$\text{Reversible: } E_{1/2} = E_f^0 + \frac{RT}{F} \ln\left(\frac{D_{product}}{D_{reactant}}\right) \tag{1.79}$$

$$\text{Ireversible: } E_{1/2} = E_f^0 + \frac{RT}{\alpha F} \ln\left(\frac{r_e k^0}{D_{reactant}}\right) \tag{1.80}$$

Assuming $D_{reactant} = D_{product}$, for a reversible process, $E_{1/2} = E_f^0$ whereas for irreversible process $E_{1/2}$ is dependent on electrochemical rate constant. Again, $E_{1/2}$ for the latter is larger than the formal potential as higher overpotential is required for the establishment of steady state due to the sluggish kinetics, as shown in Figure 1.12.

1.7.2 Stripping Voltammetry

Stripping voltammetry is a widely employed technique in electroanalysis designed for the quantification of metals, metal complexes and organic substances that are adsorbed on electrode surfaces[30-32]. Unlike linear sweep or cyclic voltammetry where the sensitivity of detection is inevitably limited by the rate of diffusion to the electrode, stripping voltammetry usually offers lower detection limits for the analytes as it involves a 'pre-concentration step' which allows for the accumulation of the analyte on the electrode surface prior to the 'stripping step', where the electrochemical measurement is recorded in the form of a linear or a pulsed (see section 1.7.3) sweep. Four forms of stripping voltammetry are developed for various analytical systems including the long-established anodic stripping voltammetry (ASV) and cathodic stripping voltammetry (CSV). In ASV and CSV, the pre-concentration step is realised by Faradaic reaction(s). Adsorptive stripping voltammetry (AdsSV) and insertive stripping voltammetry (ISV) are the other type of stripping voltammetry where the pre-concentration step occurs via the adsorption of analyte onto the electrode surface without involving an electrolytic process. Generic preconcentration reactions in each case are shown as follows[1]:

$$\text{ASV: } M^{n+}(aq) + ne^- \rightarrow M(electrode) \tag{1.81}$$

$$\text{CSV: } 2M^{2+}(aq) + mH_2O \rightarrow M_2O_m(electrode) + 2mH^+ + 2(m-n)e^- \tag{1.82}$$

$$\text{AdsSV or ISV}: A(aq) \rightarrow A(ads) \tag{1.83}$$

In comparison to AdsSV, the recently introduced ISV includes ion insertion into a crystalline material during the pre-concentration step, ideally providing selectivity for the subsequent voltammetric detection[33, 34].

In the 'stripping' process, the potential that Faradaically oxidises or reduces the accumulated material is applied to the working electrode resulting in the voltammogram showing a characteristic peak related to the analyte of interest. According to Faraday's law of electrolysis, integrating the peak gives the stripping charge Q (C) passed during the corresponding time t_0 that is directly proportional to the amount of analyte accumulated on the electrode surface, the latter can be quantified by surface coverage Γ (mol cm^{-2})[1, 2]:

$$\Gamma = \frac{Q}{nFA_{elec}} = \frac{\int_0^{t_0} Idt}{nFA_{elec}} \tag{1.84}$$

where n is the number of electrons transferred in the stripping step.

1.7.2.1 Effect of Adsorption

Electroactive species can absorb on conductive substrates (electrodes), forming monolayers or thicker films in several different ways. Monolayers, which are the most commonly observed on the electrode surface are formed via *irreversible adsorption* or *covalent attachment*, or, in the form of *organized assemblies*, by *Langmuir-Blodgett transfer* and *self-assembly* techniques. The thicker films include polymers and inorganic films. The former can be categorised into several types including *electronically conductive polymers* and *blocking polymers* that passivate the electrode surface, formed by the process such as oxidation of phenol, as discussed in Chapter 6 of this thesis.

The strong interaction between adsorbate and electrode surface will often change the electrochemical behaviour and structure of an electrode, as well as promote/inhabit the rate of electron transfer at an electrode surface, particularly in the case of noble metal substrate[3]. Earlier studies demonstrated numerous such effects, for example, the layer of hydrous tin oxide absorbed on Pt electrode increased the hydrogen overpotential and thus allowed the electrode Pt to be used for the coulometric generation of Sn(II) from Sn(IV)[35]. The adsorption of sulphur on metals strengthened the metal-hydrogen bond which changed the activation energy of hydrogen evolution reaction and hence affected the exchange current[36].

In this thesis, the adsorptions of chlorophylls and fipronil at carbon surfaces are investigated in Chapter 5 and Chapter 8. In the particular case of chlorophylls, the irreversible, monolayer adsorption[37,38] of the monomeric form in flat orientation was reported at the metallic electrode surface in the aqueous solution[37]. The adsorptions of porphyrins were shown to have profound impacts on the adsorbate molecular properties and reactivity[39-42]. The electrochemical redox properties were thus associated with the adsorptions and self-assembly processes of the molecule on the single crystal surface[41,42]. The additional effect of aggregation in the studied media on the electrochemical behaviours of chlorophylls were also suggested[43,44]. The different aggregated states and solvated species of chlorophylls were distinguished by their redox potentials in the mixtures of organic solvent and water or ionic liquid at a hanging mercury drop[43] or gold electrode[44], respectively.

Modifications of electrodes using such monolayers or thicker films to suit particular functions are frequently called *chemically modified electrodes.* The chemically modified electrodes are employed in Chapter 6, 7 and 8 of this thesis.

1.7.2.2 Voltammetry of Surface-Adsorbed Species

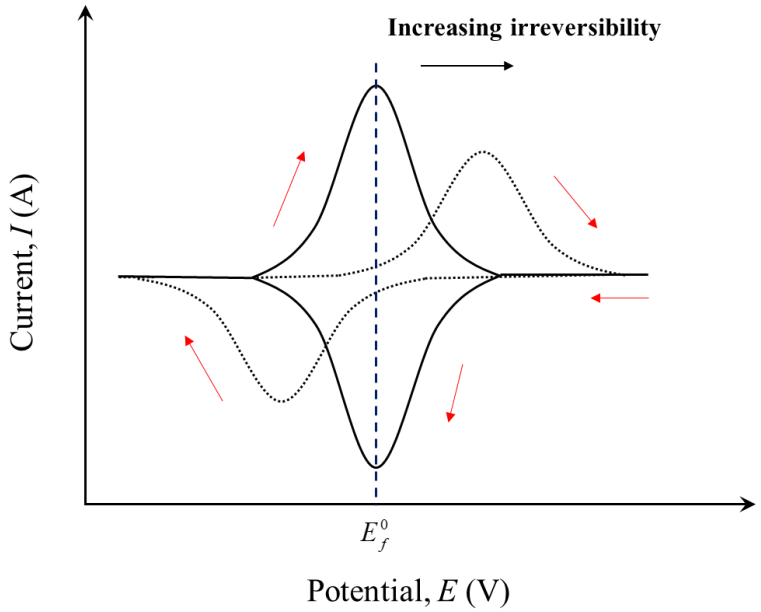


Figure 1.13. Cyclic voltammetric profiles of a surface bound species for a reversible (solid line), and irreversible limit (dot line). Red arrows show the starting point and scan direction.

The voltammetric profiles for the aforementioned surface-bound species differ significantly from those discussed in section 1.7.1 for diffusional reactions. As shown in Figure 1.13 for the species exhibiting ideal behaviour of adsorption, the current responses drop to zero at the end of the peaks and the diffusion tail is absent in both electrochemically reversible and irreversible processes. This is due to the consumption of the finite amount of electroactive species absorbed on the electrode surface so that that the peak shape is dependent solely on the rate of electron transfer. For a reversible stripping process (rapid electron transfer kinetics), the forward and backward peaks are symmetrical; the peak potential is the same as the formal potential and the peak-to-peak separation (ΔE_{pp}) is zero. In the case of irreversible process, the peak potentials shift away from the formal potential and ΔE_{pp} grows larger with slower electron transfer kinetics following the same principle discussed for the diffusional systems. The peak current for each case is given by[1]:

$$\text{Reversible: } I_p = \frac{F^2}{4RT} A_{elec} \Gamma_A \nu \tag{1.85}$$

$$\text{Ireversible: } I_p = \frac{\alpha F^2}{2.718RT} A_{elec} \Gamma_A \nu \tag{1.86}$$

assuming a reduction reaction where Γ_A is the surface coverage of the reactant. The peak currents are proportional to scan rates rather than to the square root of scan rates found for diffusion-controlled processes. This relation is often used as a critical indicator for identifying the surface-limited nature of the process.

1.7.3 Pulse Voltammetry

Pulse voltammetric techniques are widely used for electroanalytical quantifications of trace level analytes (often down to 10^{-8} M) in solutions[32,45]. In pulse voltammetric methods, a sequence of potential steps (typically with a duration of ca. 50 ms) are applied to the working electrode, triggering pulse Faradaic current responses (I_f), as depicted in Figure 1.14[1, 32]. Meanwhile, the capacitative current (I_c) arising from the double layer charging also contributes to the overall current and it drops approximately exponentially

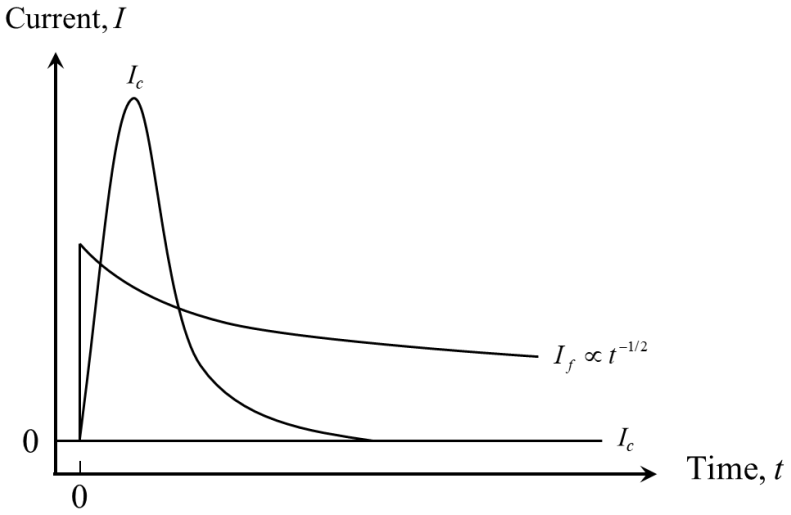


Figure 1.14. Schematic representation of the evolution of capacitative and Faradaic current resulted from the application of a potential step.

within each potential step. The decay of the Faradaic current, I_f, however, follows the Cottrell equation so that $I_f \propto t^{-1/2}$, which decays more slowly than the capacitative current. Therefore, by sampling the current late in the lifetime of each pulse, a high ratio of Faradaic to capacitative current can be realised[36]. This is the basis of enhancing sensitivity using pulse voltammetry.

In this section, two techniques are introduced, namely square wave voltammetry (SWV) and differential pulse voltammetry (DPV). In chapters 5, 7 and 8, these techniques are employed for the detection of a range of analytes and their performances are compared with other techniques.

1.7.3.2 Differential Pulse Voltammetry

Differential pulse voltammetry (DPV) is a sensitive and useful technique in which the waveform consists of fixed magnitude pulses superimposed on a linear potential ramp, as shown in Figure 1.15[2,46]. The current is measured twice, once just before the application of each pulse (at t_1) to give I_1 and once near the end of the pulse (at t_2) to give I_2. The current difference ($\Delta I = I_2 - I_1$) is plotted against the applied potential. As schematically depicted in Figure 1.15, the resulting differential pulse voltammogram contains a current peak with the height directly proportional to the concentration of analyte, c[32]:

$$I_p = \frac{nFA_{elec}D^{1/2}c}{\sqrt{\pi(t_2 - t_1)}}\left(\frac{1-\sigma}{1+\sigma}\right) \tag{1.87}$$

where σ is related to the pulse height ΔE_p by:

$$\sigma = \exp[(nF / RT)(\Delta E_p / 2)] \tag{1.88}$$

DPV very effectively corrects the capacitative background current that is assumed to

differ relatively little from sampling point 1 to 2, by subtracting I_1 from I_2. The contribution from non-Faradaic processes to the measured signal is thus minimised leading to a high signal-to-background ratio and hence high sensitivity of detection. DPV is also particularly useful for detections in mixtures by virtue of its peak-shaped response and flat background current. The resolution of voltammogram can be reasonably improved after careful selection of the analytical parameters, such as ΔE_p and scan rate, as discussed in Chapter 7.

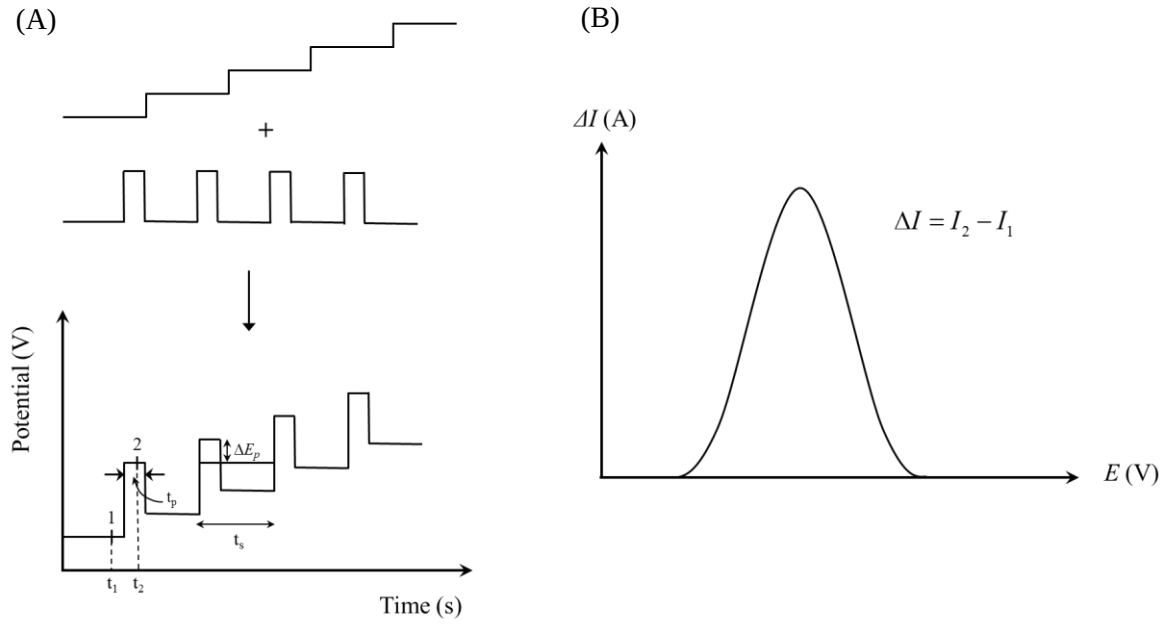


Figure 1.15. Schematic illustration of (a) DPV waveform where the pulse duration, t_p and the period of the staircase waveform, t_s are typically set as 5–100 ms and 0.5–5 s, respectively; (b)voltammetric profiles obtained from a DPV scan

1.7.3.3 Square Wave Voltammetry

Square wave voltammetry (SWV) is a large amplitude differential technique widely recognised for its high detection sensitivity[32]. In SWV, the waveform applied to the working electrode is a symmetric square wave superimposed on a base staircase potential, as shown in Figure 1.16[1, 32]. Similar to DPV, the currents are measured twice during each

square wave cycle, as I_1 and I_2 at the end of forward pulse and the end of reverse pulse, respectively. The peak-shaped square wave voltammogram is again plotted using the difference between the two measurements namely ($\Delta I = I_2 - I_1$) versus the staircase base potential, where the peak current is proportional to the concentration of analyte. In practice, the voltammogram plot of I_1 and I_2 against the applied potential are also generated, as shown in Figure 1.16.

The waveform is characterised by the pulse height, ΔE_p, the staircase height, ΔE_s, the pulse time, t_p and the cycle period, t_s. t_p is usually related to the square wave frequency f by $f = \frac{1}{2}t_p$. The scan rate can be expressed as[1]:

$$\frac{\Delta E_s}{2t_p} = f\Delta E_s \tag{1.89}$$

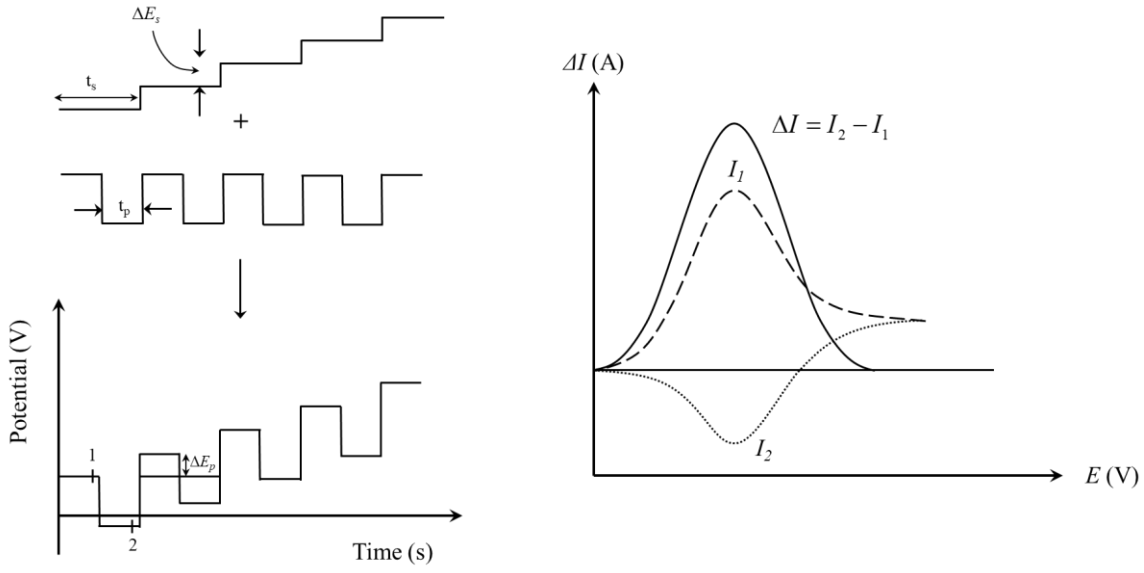


Figure 1.16. Schematic illustration of (a) SWV waveform and (b)voltammetric profiles obtained from a SWV scan

Like DPV, the major advantage of SWV is it greatly reduces the contribution of capacitative currents to the recorded current. Examples and further comparisons between

SWV and DPV are reported in Chapter 7.

1.7.4 Chronoamperometry

Chronoamperometry is a powerful electrochemical technique that measures the current with time resulting from a potential step applied to the working electrode. The potential is stepped instantaneously from E_1, where usually no Faradaic reaction takes place to an overpotential potential E_2 which is sufficiently high to consume all the electroactive species near the electrode such that diffusion control prevails. The transient current rises steeply to a large value when E_2 is initially applied. As the experiment proceeds with the potential held at E_2, the transient decreases in different ways depending on the diffusion geometry with the concentrations following *Fick's Second Law*. For a macroelectrode where the diffusion is linear and less efficient, the chronoamperometric response is characterised by the previously mentioned Cottrell equation:

$$I = \frac{nFA_{elec}c\sqrt{D}}{\sqrt{\pi t}} \tag{1.90}$$

where n is the number of electrons transferred and c is the bulk concentration of the electroactive species. According to Eqn. (1.90), as t tends to infinity, the current decays to zero since the reactants near the electrode are all depleted, as shown in Figure 1.17. In contrast for a microelectrode, the occurrence of convergent diffusion leads to a less rapid decay of current with time, which follows the *Shoup and Szabo Equation*[47]:

$$I = 4nFcDr_e f(\tau) \tag{1.91}$$

where

$$f(\tau) = 0.7854 + 0.8862\tau^{-0.5} + 0.2146\exp(-0.7823\tau^{-0.5}) \tag{1.92}$$

and the dimensionless time parameter, τ, is expressed as

$$\tau = \frac{4Dt}{r_e^{\,2}} \tag{1.93}$$

Eqn. (1.92) and (1.93) show that the current scales with D at long times but with $D^{1/2}$ at short times. Meanwhile, the current is directly proportional to nc at all times[1]. Hence it is possible to simultaneously obtain the optimum values of (D) and (nc) that best fit the measured chronoamperometric response provided the process is known to be a simple n electron reaction free of coupled chemistry on the voltammetric timescale[48]. This method is demonstrated in detail in Chapter 4 for determining D of piperine and n in its electro-reduction.

Over long times, with the expansion of the diffusion layer, the convergent diffusion becomes predominant at microelectrodes and the constant, steady state current I_{ss} is reached as described Eqn. (1.73).

Chronoamperometry is also employed in this thesis to study single entity electrochemistry, which is known as 'nano-impacts' approach and will be discussed in the next section.

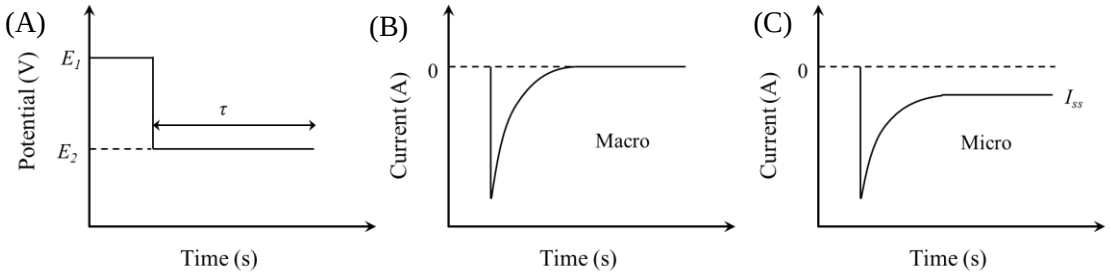


Figure 1.17. (A) The potential-time profile for a single-step chronoamperometry experiment. The resulting chronoamperometric responses at (B) macroelectrodes and (C) microelectrodes

1.7.5 The Nano-impact Method

'Nano-impacts' is a powerful electroanalytical technique that characterises individual nanoparticles in solution and provides mechanistic and kinetic insights regarding their reactivity[49-52]. This technique involves recording the chronoamperometric responses resulting from the random collisions of individual nanoparticles, by virtue of their Brownian motion, onto a potentiostated microelectrode which is immersed in their suspension. Note that microelectrodes are chosen over macroelectrodes for performing such measurements as they allow for the lower particle collision frequency leading to clear resolution of *single* impact events with much reduced background noise. Microelectrodes also provide the faster response time and lower capacitance resulting in the better time resolution.

The impact events may arise from Faradaic or non-Faradaic processes, for which the former can be categorised into direct or mediated (indirect) impacts. Direct Faradaic impacts result from direct electron transfers between the nanoparticles and the electrode surface. The redox reactions taking place involve the consumptions of nanoparticles. In

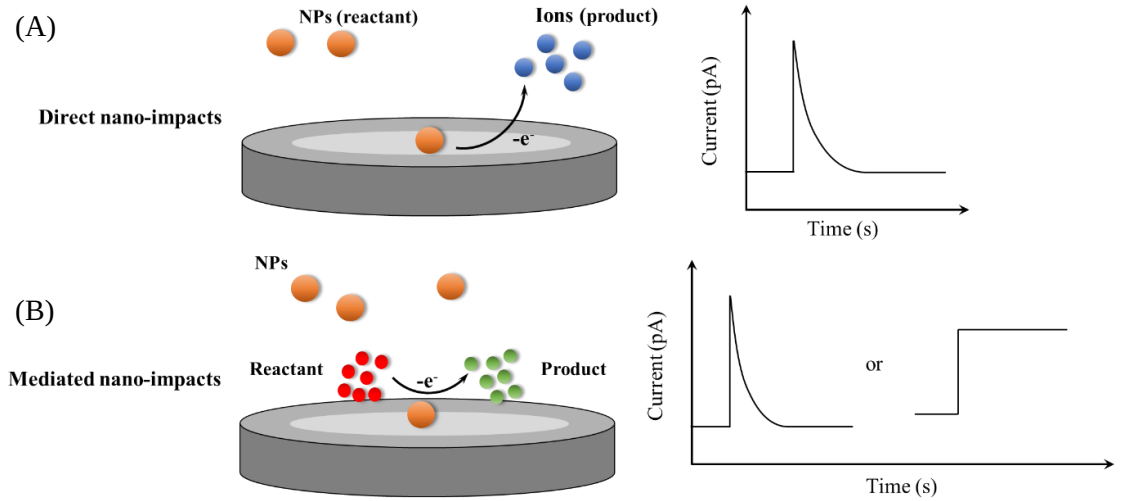


Figure 1.18. Schematic illustrations of two scenarios of nano-impact experiments: (A) direct and (B) mediated Faradaic processses. The resulted current-time transients are attached next to the corresponding diagrams.

contrast, the mediated impacts are detected for redox processes of solution-phase electroactive species mediated by the nanoparticles showing catalytic activities towards the reactions[53-55]. As illustrated in Figure 1.18, in mediated Faradaic impact events, current responses in both spiked and stepped shapes can be observed depending on the time period that the nanoparticles are in contact with the electrode surface. The current plateaus show a 'step' as the reaction continues at the surface of nanoparticles.

Capacitative (non-Faradaic) impacts originate from either displacement of charge from the electrode-electrolyte interface (double layer) or from the charging of an impacting nanoparticle the electron. In these processes where no Faradaic reaction occurs, in order to maintain charge neutrality, charge leaves or enters the electrode surface in response to the changes in ionic charge distribution at the interface caused by the collision of nanoparticles. Capacitive impacts can be seen due to such charge transfer when the applied potential at the working electrode is positive or negative to the potential of zero charge (PZC)[56, 57].

The analysis of nano-impacts is useful for characterising nanoparticles (sizing, shape and aggregation/agglomeration state) as well as understanding the mechanism and kinetics of the redox reactions of interest[49, 52]. In Chapter 8, the nano-impact method is employed in combination with the voltammetric techniques to investigate the adsorption of fipronil on carbon-nanotubes (CNTs).

Bibliography

1. R. G. Compton and C. E. Banks, *Understanding voltammetry*, World Scientific Publishing Europe, London, 3rd edn., 2018.
2. R. G. Compton and G. H. W. Sanders, *Electrode potentials*, Oxford University Press, Oxford, 1996.
3. A. J. Bard, L. R. Faulkner, C. G. Zoski and J. Leddy, *Electrochemical methods : fundamentals and applications*, Wiley, New York ; Chichester, 2nd edn., 2001.
4. W. J. Albery, *Electrode kinetics*, Clarendon Press, Oxford, 1975.
5. D. G. Truhlar, W. L. Hase and J. T. Hynes, *The Journal of Physical Chemistry*, 1983, **87**, 2664-2682.
6. D. G. Truhlar, B. C. Garrett and S. J. Klippenstein, *The Journal of Physical Chemistry*, 1996, **100**, 12771-12800.
7. R. Guidelli, R. G. Compton, J. M. Feliu, E. Gileadi, J. Lipkowski, W. Schmickler and S. Trasatti, *Pure Appl Chem*, 2014, **86**, 245-258.
8. R. Guidelli, R. G. Compton, J. M. Feliu, E. Gileadi, J. Lipkowski, W. Schmickler and S. Trasatti, *Pure Appl Chem*, 2014, **86**, 259-262.
9. A. C. Fisher, *Electrode dynamics*, Oxford University Press, Oxford, 1996.
10. J. A. V. Butler, *Transactions of the Faraday Society*, 1924, **19**, 659-665.
11. J. A. V. Butler, *Transactions of the Faraday Society*, 1924, **19**, 729-733.
12. J. A. V. Butler, *Transactions of the Faraday Society*, 1924, **19**, 734-739.
13. M. Faraday, *Philos. Trans. R. Soc. London*, 1834, **124**, 77-122.
14. A. Fick, *Annalen der Physik*, 1855, **170**, 59-86.
15. A. Fick, *The London, Edinburgh, and Dublin Philosophical Magazine and Journal of Science*, 1855, **10**, 30-39.
16. A. Einstein, *Annalen der physik*, 1905, **17**, 208.
17. M. von Smoluchowski, *Annalen der Physik*, 1906, **326**, 756-780.
18. J. K. Novev and R. G. Compton, *Current Opinion in Electrochemistry*, 2018, **7**, 118-129.
19. M. I. Montenegro, M. A. Queirós, J. L. Daschbach and North Atlantic Treaty Organization. Scientific Affairs Division., *Microelectrodes : theory and applications*, Kluwer Academic, Dordrecht ; London, 1991.
20. D. Pletcher, *A first course in electrode processes*, RSC, Cambridge, 2nd edn., 2009.
21. M. Fleischmann, F. Lasserre, J. Robinson and D. Swan, *Journal of Electroanalytical Chemistry and Interfacial Electrochemistry*, 1984, **177**, 97-114.
22. E. I. Rogers, I. Streeter, L. Aldous, C. Hardacre and R. G. Compton, *The Journal of Physical Chemistry C*, 2008, **112**, 10976-10981.
23. R. S. Nicholson and I. Shain, *Anal. Chem.*, 1965, **37**, 178-190.
24. R. S. Nicholson and I. Shain, *Anal. Chem.*, 1964, **36**, 706-723.
25. C. Batchelor-McAuley, M. Yang, E. M. Hall and R. G. Compton, *J. Electroanal. Chem.*, 2015, **758**, 1-6.
26. H. Matsuda and Y. Ayabe, *Zeitschrift für Elektrochemie, Berichte der Bunsengesellschaft für physikalische Chemie*, 1955, **59**, 494-503.
27. A. M. Bond, K. B. Oldham and C. G. Zoski, *Journal of Electroanalytical Chemistry and Interfacial Electrochemistry*, 1988, **245**, 71-104.

28. K. B. Oldham and C. G. Zoski, *Journal of Electroanalytical Chemistry and Interfacial Electrochemistry*, 1988, **256**, 11-19.
29. A. M. Bond, K. B. Oldham and C. G. Zoski, *Anal. Chim. Acta*, 1989, **216**, 177-230.
30. X. Dai, O. Nekrassova, M. E. Hyde and R. G. Compton, *Anal. Chem.*, 2004, **76**, 5924-5929.
31. M. Iwamoto and R. A. Osteryoung, *Journal of Electroanalytical Chemistry and Interfacial Electrochemistry*, 1984, **169**, 181-194.
32. J. Wang, *Analytical electrochemistry*, Wiley-VCH, Hoboken, N.J., 3rd edn., 2006.
33. A. L. Suherman, M. Lin, B. Rasche and R. G. Compton, *ACS Sensors*, 2020, **5**, 519-526.
34. A. L. Suherman, B. Rasche, B. Godlewska, P. Nicholas, S. Herlihy, N. Caiger, P. J. Cowen and R. G. Compton, *ACS Sensors*, 2019, **4**, 2497-2506.
35. A. J. Bard, *Journal of Electroanalytical Chemistry (1959)*, 1962, **3**, 117-125.
36. S. Trasatti, *Journal of Electroanalytical Chemistry and Interfacial Electrochemistry*, 1972, **39**, 163-184.
37. L. A. Khanova and M. R. Tarasevich, *Journal of Electroanalytical Chemistry and Interfacial Electrochemistry*, 1987, **227**, 99-114
38. T. Miyasaka, T. Watanabe, A. Fujishima and K. Honda, *Journal of the American Chemical Society*, 1978, **100**, 6657-6665.
39. C. L. Ni and F. C. Anson, *Inorganic Chemistry*, 1985, **24**, 4754-4756.
40. J. E. Hutchison, T. A. Postlethwaite, C. Chen, K. W. Hathcock, R. S. Ingram, W. Ou, R. W. Linton, R. W. Murray, D. A. Tyvoll, L. L. Chng and J. P. Collman, *Langmuir*, 1997, **13**, 2143-2148.
41. Y. He, T. Ye and E. Borguet, *Journal of the American Chemical Society*, 2002, **124**, 11964-11970.
42. T. Ye, Y. He and E. Borguet, *The Journal of Physical Chemistry B*, 2006, **110**, 6141-6147.
43. A. Agostiano, P. Cosma and M. Della Monica, *Journal of Electroanalytical Chemistry and Interfacial Electrochemistry*, 1990, **298**, 311-324.
44. Y. Kuroiwa, Y. Kato and T. Watanabe, *Journal of Photochemistry and Photobiology A: Chemistry*, 2009, **202**, 191-195.
45. C. M. A. Brett and A. M. O. Brett, *Electrochemistry : principles, methods, and applications*, Oxford University Press, Oxford, 1993.
46. Á. Molina and J. González, *Pulse voltammetry in physical electrochemistry and electroanalysis : theory and applications*, Springer, 1st edn., 2016
47. D. Shoup and A. Szabo, *Journal of Electroanalytical Chemistry and Interfacial Electrochemistry*, 1982, **140**, 237-245.
48. L. Xiong, L. Aldous, M. C. Henstridge and R. G. Compton, *Analytical Methods*, 2012, **4**, 371-376.
49. S. V. Sokolov, S. Eloul, E. Kätelhön, C. Batchelor-McAuley and R. G. Compton, *Physical Chemistry Chemical Physics*, 2017, **19**, 28-43.
50. M. Pumera, *ACS Nano*, 2014, **8**, 7555-7558.

51. L. K. Allerston and N. V. Rees, *Current Opinion in Electrochemistry*, 2018, **10**, 31-36.
52. N. V. Rees, *Electrochem. Commun.*, 2014, **43**, 83-86.
53. J. M. Kahk, N. V. Rees, J. Pillay, R. Tshikhudo, S. Vilakazi and R. G. Compton, *Nano Today*, 2012, **7**, 174-179.
54. X. Xiao and A. J. Bard, *Journal of the American Chemical Society*, 2007, **129**, 9610-9612.
55. X. Li, C. Batchelor-McAuley, S. A. I. Whitby, K. Tschulik, L. Shao and R. G. Compton, *Angew. Chem. Int. Ed.*, 2016, **55**, 4296-4299.
56. N. V. Rees, C. E. Banks and R. G. Compton, *The Journal of Physical Chemistry B*, 2004, **108**, 18391-18394.
57. C. E. Banks, N. V. Rees and R. G. Compton, *The Journal of Physical Chemistry B*, 2002, **106**, 5810-5813.

Chapter 2

Semi-circular Sweep Voltammetry

This chapter describes the theory of a novel voltammetric technique applying a semi-circular potential sweep instead of the usual linear sweeps in voltammetry. The first section introduces the semi-circular shape and the basic parameters of the waveform. Then the recent theoretical studies investigating the voltammetric features of semi-circular sweep voltammetry (SCV) in comparison to the conventional linear sweep voltammetry (LSV) are briefly summarised in the next section.

2.1 Semi-circular Potential Wave

As mentioned in the previous chapter, conventional cyclic voltammetry (CV) and linear sweep voltammetry (LSV) employ a linear potential wave that can be expressed as:

$$E(t) = E(t=0) \pm vt \qquad (2.1)$$

where *E(t)* is the potential applied to the working electrode with respect to the reference electrode, *E(t = 0)* is the initial potential and *v* is the scan rate which remains constant throughout the voltammetric sweep. Recently alternative, non-linear waveforms presenting with temporal and continuous gradient δ *E(t)* have been introduced by Uchida *et al.* to enhances the voltammetry in respect of electroanalysis[1-6]. One of them uses the semi-circular potential wave based on a semi-circular function that originates from the basic circle function centred at $(a, b)^2$:

$$y = \pm\sqrt{r^2 - (x-a)^2} + b \qquad (2.2)$$

where r is the radius. Applying Eqn. (2.2) to the context of voltammetry, y represents the potential, E as the function of time, t represented by x. r can be substituted by the amplitude of the sweep A_0 (V), a can be substituted with the maximum time duration for the centre of each semi-circle to be observed, t_{max}, by $a = ct_{max}$, and b can be substituted by the midpoint potential of the potential window E_{centre} (or E_{mid}, defined as $\frac{E_f - E_i}{2}$ where E_f and E_i are the final and initial potential, respectively). Eqn. (2.2) can thus be expressed as:

$$E(t) = \pm\sqrt{A_0^2 - [v(t - ct_{\max})]^2} + E_{centre} \tag{2.3}$$

and re-arranged as:

$$E(t) = \pm A_0\sqrt{\left|1 - \left[2\left(\frac{t}{t_{\max}} - c\right)\right]^2\right|} + E_{centre} \tag{2.4}$$

where $c = 0$ for $t \leq \frac{t_{max}}{2}$ and $c = 1$ for $\frac{t_{max}}{2} < t < t_{max}$.

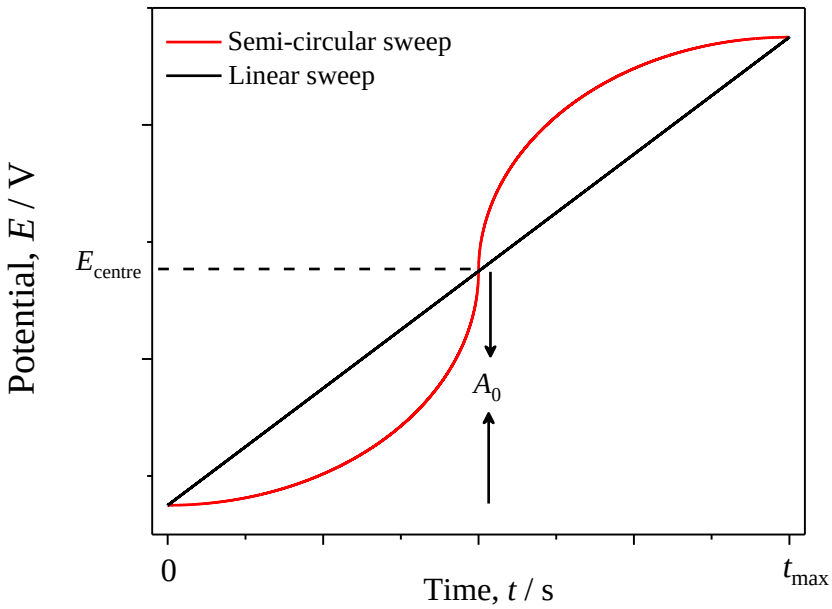


Figure 2.1 A representative diagram of linear (black) and semi-circular (red) potential sweep generated at the same average scan rate.

The waveforms of a linear sweep and a semi-circular sweep are shown in Figure 2.1. In contrast to the linear sweep, the instantaneous scan rate for semi-circular sweep varies continuously over the entire experiment duration, from near zero at t=0, to instantaneously infinite at E_{centre} and eventually returns to near zero at t=t_{max}. Note that in reality, only a large, near infinite value can be realised at E_{centre} due to instrumental limitations. The average scan rate for a semi-circular potential wave is controlled by A_0 and t_{max} which is usually kept the same as a linear potential wave for comparison in the experiments performed in this thesis.

2.2 Applications of Semi-circular Sweep Voltammetry in Electroanalysis: Theory

Several theoretical studies have been done by Uchida *et al.* utilising a simulation method to employ semi-circular sweep voltammetry (SCV) and compare its theoretical voltammetric behaviour with linear sweep voltammetry (LSV)[1-4]. The key findings in these works are reviewed in this section as they provide important implications for understanding the features in SCV which can be exploited experimentally to facilitate electroanalysis.

The semi-circular potential wave was first employed in voltammetry at a macrodisc electrode using a one-dimensional diffusion model[2]. The current responses resulting from SCV varied significantly with the shift of potential window, as opposed to those obtained using LSV showing no variance with the shift. The semi-circular sweep voltammogram, in theory, generated an infinite current when E_{centre} was adjusted to the vicinity of the

formal potential (E_f^0). An alternative approach to the usual measuring method employed in CV of finding the average potential of the oxidative and reductive peaks to estimate the formal potential of the redox couple of interest was thus proposed namely that by running multiple SCV, maximum peak current responses are predicted to be obtained at the value of E_{centre} corresponding to E_f^0 . Further, in the simulated semi-circular voltammograms where the current responses were greatly amplified at E_{centre} while suppressed in other regions, it was shown that SCV can simultaneously better detect individual species in their two-component mixtures, providing an estimation of their formal potentials. In contrast, LSV was less useful in analysing mixtures particularly when the potential difference between the two species was small.

Semi-circular sweep voltammograms at a microdisc electrode were next simulated and compared to linear sweep voltammograms[1]. The voltammograms at the microelectrode were shown to follow the similar pattern with that observed at the macroelectrode. The fast scan rate generated transiently at E_{centre} led to greatly amplified current responses when E_{centre} approaches the formal potential of the redox reaction, making SCV an advantageous technique for analysis at microelectrode particularly under non-steady state conditions.

The unique features of semi-circular voltammograms observed at a microelectrode were suggested as a new possible method for determining electrode kinetic parameters[4]. The curve shape was found to alter drastically with the change of standard electrochemical rate constant, k_0. This high sensitivity allows for the determination of values of k_0 of one order magnitude greater than using the LSV method. Specifically, the method was experimentally implemented by running multiple simulations of SCV with varying k_0 and superimposing them with the experimental data so as to find the best fit.

The semi-circular potential wave approach was also employed to stripping voltammetry as a replacement for the usual linear potential wave at a macrodisc electrode[3]. SCV was shown to produce a very large peak current and to give rise to the characteristic voltammograms with a strong dependency on the analyte formal potentials. The origins of these voltammetric features were analysed via simulation to reveal the interplay of temporal scan rate and the surface concentration. This work provided a clear theoretical demonstration of SCV facilitating electroanalysis of low concentrations of analyte by enhancing the sensitivity of detection and indicating the approximate formal potential of the redox species to confirm analyte identity.

Bibliography

1. Y. Uchida, E. Kätelhön and R. G. Compton, *Journal of Electroanalytical Chemistry*, 2018, **823**, 465-473.
2. Y. Uchida, E. Kätelhön and R. G. Compton, *Journal of Electroanalytical Chemistry*, 2018, **818**, 140-148.
3. Y. Uchida, E. Kätelhön and R. G. Compton, *Journal of Electroanalytical Chemistry*, 2019, **848**, 113290.
4. Y. Uchida, E. Kätelhön and R. G. Compton, *Journal of Electroanalytical Chemistry*, 2019, **835**, 60-66.
5. Y. Uchida, E. Kätelhön and R. G. Compton, *Journal of Electroanalytical Chemistry*, 2017, **801**, 381-387.
6. H. M. A. Amin, Y. Uchida, C. Batchelor-McAuley, E. Kätelhön and R. G. Compton, *Journal of Electroanalytical Chemistry,* 2018, **815**, 24-29.

Chapter 3

Experimental

This chapter outlines the experimental details of the chemical reagents and instrumentation used commonly in all following chapter of this thesis; specific descriptions of each experiment and/or reagents can be found in the relevant experimental sections of Chapters 4-8.

3.1 Chemicals and Reagents

All chemicals, reagents and materials described in this thesis are listed in Table 3.1. They were used as received without further purification. All solutions were prepared using deionised water (Millipore, UK) with a resistivity of 18.2 MΩ cm at 298 K.

Figure 3.1 List of chemicals, reagents and materials used in this thesis

Chemical Name	Formula	Purity	Supplier
Piperine	$C_{17}H_{19}NO_3$	≥97%	Aldrich
Sodium hydroxide	NaOH	97%	Honeywell
Ethanol	C_2H_5OH	≥99.8%	Sigma-Aldrich
Sodium chloride	NaCl	≥99.5%	Sigma-Aldrich
Potassium chloride	KCl	≥99.0%	Sigma-Aldrich
Sodium phosphate dibasic	Na_2HPO_4	≥99.0%	Sigma-Aldrich
Potassium phosphate monobasic	KH_2PO_4	≥99.0%	Sigma
Acetone	CH_3COCH_3	≥99.8%	Sigma-Aldrich
Diethyl ether	$(C_2H_5)_2O$	≥99.8%	Sigma-Aldrich
Dioxane	$C_4H_8O_2$	≥99.8%	Sigma-Aldrich

Methanol	CH_3OH	≥99.9%	Sigma-Aldrich
Petroleum ether (b.p. 40-60°C)	C_6H_{14}	≥90%	Sigma-Aldrich
Magnesium sulfate	$MgSO_4$	≥99.5%	Sigma-Aldrich
Silica gel (40-63 µm)			VWR
4-Amino-2,6-dichlorophenol	$C_6H_5Cl_2NO$	97%	Alfa Aesar
Phenol	C_6H_5OH	99.0-100.5%	Sigma-Aldrich
Sodium tetraborate	$Na_2[B_4O_5(OH)_4]\cdot 8H_2O$	97%	Sigma-Aldrich
Ascorbic acid	$C_6H_8O_6$	99.0%	Sigma-Aldrich
Acetaminophen	$C_8H_9NO_2$	98.0-102.0%	Sigma-Aldrich
Hydroquinone	$C_6H_6O_2$	99%	Sigma-Aldrich
Catechol	$C_6H_6O_2$	>99%	Sigma-Aldrich
α-D-glucose	$C_6H_{12}O_6$	96%	Sigma-Aldrich
Bamboo-like multiwalled carbon nanotubes		>95%	NanoLab
Potassium hydroxide	KOH	85.0-100.5%	WR Chemicals
Fipronil	$C_{12}H_4Cl_2F_6N_4OS$	PESTANAL®	Sigma-Aldrich
Graphene nano-platelets			Strem Chemicals
Carbon Black			Cabot Performance
Phosphoric acid	H_3PO_4	99.99%	Aldrich
Acetic acid	CH_3COOH	4,99.5%	BDH
Boric acid	H_3BO_3	99.5%	Aldrich

Real sample analysis was conducted as described in the experimental sections of Chapter 4, 5 and 7. The samples containing the target analytes were extracted from the commercial products purchased in local supermarkets, as listed in Table 3.2.

Figure 3.2 List of commercial products and the target analytes used in the real sample analysis in this thesis

Product Name	Supplier	Target analyte
Fairtrade Organic Whole Black Peppercorns	Sainsbury's	Piperine
Fresh spinach	Tesco	Chlorophyll a and b
Sainsbury's Paracetamol Capsules	Sainsbury's	Acetaminophen
Beecham's Flu Plus	Sainsbury's	Acetaminophen
Efferalgan 500mg + vitamin C 200mg Effervescent Tablets	euro-pharmas.com	Acetaminophen

3.2 Electrochemical Instrumentation

All electrochemical experiments were performed inside a Faraday cage thermostated at 298K. The conventional voltammetry including cyclic voltammetry, linear sweep voltammetry, differential pulse voltammetry and square wave voltammetry was conducted using a μAutolab II potentiostat (Metrohm-Autolab BV, Netherlands). Semi-circular potential sweep voltammetry was performed using an in-lab built potentiostat controlled by software *Python* 3.5 which allows for the generation of the required potential waveform[1, 2]. The in-lab potentiostat ensures the low-noise measurements with signal sampled at a stream rate of 100 kHz[1].

A standard three-electrode configuration was used throughout this thesis. It consists of a saturated calomel electrode (SCE +0.244 V vs. SHE, BASi Inc., Japan) as a reference electrode, a platinum wire or a graphite pod as a counter electrode and a working electrode. The details of working electrodes used vary from chapter to chapter and will be discussed in the relevant chapters.

Bibliography

1. C. Batchelor-McAuley, J. Ellison, K. Tschulik, P. L. Hurst, R. Boldt and R. G. Compton, *Analyst*, 2015, **140**, 5048-5054.
2. H. M. A. Amin, Y. Uchida, E. Kätelhön and R. G. Compton, *Journal of Electroanalytical Chemistry*, 2019, **836**, 62-67.

Chapter 4

Electrochemical Quantification of Piperine in Black Pepper

Chapters 4-5 demonstrates new electroanalytical methods using semi-circular sweep voltammetry (SCV) for the quantification of components in food products. Chapter 4 firstly employs SCV for electroanalysis of a single analyte, piperine, following which Chapter 5 focuses on the selective detections of one component within mixtures of chlorophyll a and b. The latter have closely similar redox properties precluding analysis via conventional voltammetry

In this chapter, a simple, rapid method of the detection of piperine in black pepper is reported using a voltammetric sensor based on a glassy carbon electrode (GC) with the electro-analysis following a short one-step extraction using ethanol. The method is based on the novel semi-circular potential sweep designed to maximise signal sizes and shown with context of the present analytical challenge to be essential for gathering data allowing the construction of a linear calibration curve for the analysis in the relevant range namely 0.25–5.0 mM.

The work presented in this Chapter has been published as a first author paper in *Food Chemistry*.

4.1 Introduction

Black pepper (*Piper nigrum*), known as the "king of spice", is one of the most widely consumed spices in the world. The two main components controlling the quality of black pepper are first piperine, a naturally occurring alkaloid which principally contributes to its distinct pungency and second the volatile oils responsible for its aroma[1]. As the most abundant pungent component constituting 98% of the total alkaloids in pepper[2] the piperine content has been previously used for a measure of total pungency in black pepper[1]. The percentage of piperine content was reported to vary from 2.0% to 9.0% (w/w) of black pepper among different cultivars, depending on climate, growing conditions harvesting process and the method of extractions[3, 4].

Piperine has been shown to possess diverse biological and therapeutic properties that are beneficial for human health. It exhibits anti-microbial[5], anti-depressant[6], anti-tumour[7] and high anti-oxidant activities[8]. It also exhibits a hepatoprotective property[9] and immuno-modulatory properties[10], and can act as an anti-inflammatory for the treatment of asthma[11]. The inhibitory effect of piperine in breast cancer[7] and its possible cytotoxic and anti-HIV activity[12] have also been reported. In addition, Piperine can enhance the bioavailability of a variety of drugs, such as antibiotics like norfloxacin[13] and rifampicin[14], as well as conventional herbal medicines like curcumin[15].

Owing to the importance of piperine in culinary use and biomedical applications, a simple and accurate determination of piperine is required for both the food industry and pharmaceutical use. Several analytical techniques for quantifying the amount of piperine extracted from black pepper have been reported. The colourimetric method and the Kjeldahl method rely on chemical reactions of piperine but are thought to overestimate the piperine contents due to the presence of other compounds in black pepper with similar

functional groups[4]. Gas chromatography-mass spectrometry (GC-MS), ultra-visible spectrophotometry (UV-Vis), and high-performance liquid chromatography (HPLC) offer good specificity and sensitivity[16]. In particular HPLC, provides better accuracy and hence becomes the most commonly used technique in the detection of piperine[2]. However, these methods require the use of expensive instruments and elaborate laboratory conditions to perform the analysis. Also, the complicated sample preparation steps can only be conducted by well-trained personnel and consume relatively long time rendering it difficult for frequent commercial use.

Electrochemistry as a qualitative and quantitative analytical technique can overcome the above-mentioned problems due to the simplicity of experimental set-ups, high sensitivity and cost-effectiveness. There are several reports of piperine detection using electrochemistry. Electrochemical detection (ECD) for HPLC was used with a detection limit obtained of the same order as that in UV detection[17]. Electrochemical Impedance Spectroscopy (EIS) using a surface-polarity controlled sensor with chemometric treatment was also proposed to discriminate piperine from other pungent substances[18]. These methods again involve relatively complicated treatments or analysis and no detection range was reported for applied use. A voltammetric study on a glassy carbon employing cyclic voltammetry and square wave voltammetry was reported[19], following an elaborate extraction process. Among the electrochemical techniques, cyclic voltammetry is the most frequently used, which conventionally employs triangular potential waveform where the scan rate is constant throughout the entire voltammetric sweep[20, 21].

However, recently, a method performing the voltammetry using a semi-circular potential wave has been proposed for electroanalysis[22, 23], where an infinite scan rate is

generated at the midpoint of the applied potential window and relatively low scan rates at other parts. As a result, the current response is significantly amplified at the midpoint and suppressed at other regions. The semi-circular potential sweep voltammetry offers significant improvements of the sensitivity of voltammetric measurement especially for electroanalytical purposes[22]; this is investigated in the present paper, building on the work of Jain and Verma[19], re-examining and correcting the mechanism and proposing a much simplified extraction procedure. In particular, the use of the more sensitive semi-circular potential sweep voltammetry and baseline correction facilitated the latter by allowing an optimal extraction solvent system to be employed.

In this chapter, we investigate the voltammetric and chronoamperometric behaviour of piperine and propose a reduction mechanism at both macro-and micro-electrodes. We also report an electrochemical method for the detection of piperine employing the voltammetry in combination with a semi-circular potential sweep at a glassy carbon (GC) electrode. In addition, we study real samples and suggest a simple one-step sample preparation, noting that the reductive aqueous voltammetry of piperine is not interfered by any of the inorganic ions Na^+, K^+, SO_4^{2-}, Ca^{2+}, NH_4^+, CO_3^{2-}, or the molecules glucose, fructose, vanillin, capsaicin cinnemaldehyde[19]. Finally, we demonstrate the applicability of the developed methods for the detection and quantification of piperine in black peppercorn samples.

4.2 Experimental

4.2.1 Chemicals and Reagents

All chemicals were of analytical grade and were used as received without any further purification. Piperine (≥97%) was purchased from Aldrich and sodium hydroxide (97%) was purchased from Honeywell. All solutions were prepared with ethanol (Sigma-Aldrich, ≥99.8%) or deionised water at a resistivity of 18.2 MΩ cm at 298K (Millipore, MA, USA). Sainsbury's "Fairtrade Organic Whole Black Peppercorns" were purchased from Sainsbury's (Oxford, UK). The phosphate-buffered saline (PBS, 0.1M pH = 7.4) was prepared using sodium chloride (137 mM, Sigma-Aldrich, ≥99.5%), potassium chloride (2.7 mM, Sigma-Aldrich, ≥99.0%), Sodium phosphate dibasic (10 mM, Sigma-Aldrich, ≥99.0%), and potassium phosphate monobasic (1.8 mM, Sigma, ≥99.0%).

4.2.2 Electrochemical Instrumentation and Methods

All electrochemical experiments were conducted in a Faraday cage at 298 K using a standard three-electrode system. The cyclic voltammetric measurements and chronoamperometry were performed using a μAutolab II potentiostat (Metrohm-Autolab BV, Netherlands).

For cyclic voltammetry, a glassy carbon (GC) macroelectrode (calibrated as 2.99 mm diameter) or a carbon fibre microdisc electrode (ALS Co. Ltd., Japan) was used as the working electrode, a saturated calomel electrode (SCE, ALS distributed by BASi Inc., Japan.) as the reference electrode and a graphite rod as the counter electrode. The radius of carbon fibre microdisc was calibrated electrochemically as 21.3 μm by analysing the steady state voltammetry of 1.0 mM hexaaminеruthenium(III) chloride in 0.1 M KCl

aqueous solution, using a diffusion coefficient for $[Ru(NH_3)_6]^{3+}$ of 8.43×10^{-6} cm^2s^{-1} at 298 K[24]. The resulting voltammogram is depicted in Figure 4.1. The GC macroelectrode and carbon fibre microdisc electrode were polished onto the soft lapping pads (Buehler, UK) before each voltammetric experiment, using alumina with the particle size of 1.0, 0.3 and 0.05 μm, (Buehler, IL, UK), in descending order of size, followed by polishing on a blank pad, rinsing with deionised water and drying with nitrogen. For chronoamperometry, the same carbon fibre microdisc was used as the working electrode, and the same reference and counter electrodes were used as above.

Semi-circular potential wave sweep voltammetry was carried out with a computer-controlled in-lab built potentiostat, the configuration and merits of which were described previously[22, 25]. The in-lab potentiostat ensures the low-noise measurements with signal sampled at a stream rate of 100 kHz. It was controlled by the script written in Python 3.5 to generate the required potential waveform. Modification of commercial potentiostat would likely require the addition of a suitable waveform generator. The GC electrode as above was used as the working electrode, which was held at the start potential of the

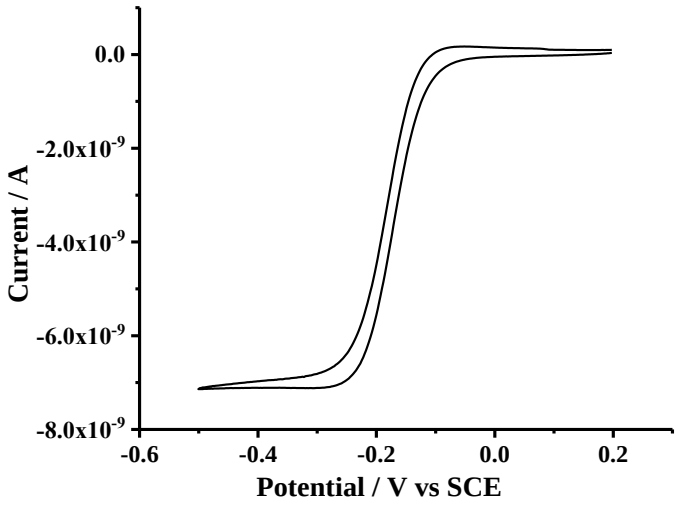


Figure 4.1. Cyclic voltammetric response of 1 mM RuHex in 0.1M KCl at a carbon fibre microdisc electrode at a scan rate of 10 mV/s.

chosen potential window for 3 s prior to applying the potential wave, with the same reference electrode and counter electrode also used as above.

4.2.3 Sample Preparation

To conduct the analysis of real samples, piperine was first extracted from black peppercorns. The black peppercorns were ground finely by the grinder provided as part of the jar containing the sample. 0.5 g of the ground sample was placed into a sampling vial, and 5 mL ethanol was added into the vial, followed by vigorously shaking for 1 minute. The vial was then sealed and placed in an ultrasonic bath (FB15050, Fisher Scientific, 50/60 Hz, 80 W, Germany) for 5–15 minutes of sonication or left to settle for 1–120 minutes. The supernatant was collected for further analysis.

4.2.4 Analytical Procedures

A piperine stock solution of 15.0 mM was prepared before being diluted with a mixture of 60% ethanol + 40% PBS at pH = 7.4 to concentration 10.0, 5.0, 4.0, 3.0, 2.5, 2.0, 1.5, 1.0, 0.75, 0.5, 0.25 mM as working solutions. This solvent was chosen due to the low solubility of piperine in aqueous solution.

For the cyclic voltammetric experiments on the study of piperine reduction, the glassy GC electrode was first placed in a solution containing 1mM piperine dissolved in a mixture of 60% ethanol + 40% PBS at pH = 7.4. Prior to the measurements, the solutions were bubbled with N_2 for 10 minutes to remove the dissolved oxygen. The potential window was chosen to be 0 to -2.5V and the voltammograms were recorded at different scan rates (25, 50, 100, 150, 200, 400 mVs^{-1}). Analogous experiments were then

conducted under air-saturated conditions. To investigate the electrochemical process under basic conditions, 1mM piperine solution containing 60% ethanol + 40% NaOH (0.1 M, 1.0 M and 2.0 M) was used with N_2 bubbling as above. The potential window was chosen as -1.2 to -1.8 V. The voltammograms were recorded at a scan rate of 1.0 Vs^{-1}.

For the chronoamperometric experiments using a carbon fibre microdisc as the working electrode, the electrode was placed in a solution containing 5, 10, 15 mM piperine in 60% ethanol + 40% PBS or 60% ethanol + 40% NaOH (0.1 M, 1.0 M and 2.0 M) mixture under degassed conditions as above. Chronoamperometric transients were recorded with a sample time of 0.002 s. The potential was stepped from 0 V to the reductive potential after the pre-equilibration for 3 s. The current was measured for 5 s, and data points before 20 ms related to non-Cottrellian behaviour as a result of considerable double-layer charging were removed[26].

For real sample analysis using GC electrodes, the extracts were obtained as above but with PBS added and were diluted with 60% ethanol + 40% PBS (dilution factor was 2) such that the voltammetric responses fell within the linear detection range. The cyclic voltammetric and semi-circular potential wave sweep voltammetric responses were recorded under air-saturated conditions at a scan rate or average scan rate of 100 (cyclic voltammetry) or 50 mVs^{-1} (semi-circular potential wave sweep voltammetry).

4.3 Results and Discussion

In the following sections, first, the electrochemical behaviour of piperine (structure shown in Figure 4.2 (A) inset) on glassy carbon (GC) macroelectrodes and carbon fibre microdisc electrodes are studied to investigate the possible mechanism of piperine

reduction. Second, the analytical responses using cyclic voltammetry and semi-circular sweep voltammetry for the detection of piperine at GC macroelectrode are studied. Finally, an optimised extraction procedure of black pepper is developed and both methods are used to quantify piperine contents in real samples.

4.3.1 Electrochemical Study of Piperine

4.3.1.1 Effect of Voltage Scan Rate

We first investigated the cyclic voltammetric signal of piperine at a glassy carbon (GC) macroelectrode. Figure 4.2 (A) depicts the voltammetric responses of piperine at GC electrode in degassed 60% ethanol + 40% PBS solution in presence and absence of 1mM piperine, at a scan rate of 100 mVs^{-1}. An electrochemically irreversible reduction peak of piperine can be observed at -1.7 V vs. SCE. The effect of scan rates on the reduction peak currents of 1.0 mM piperine at GC macroelectrode was then studied.

Cyclic voltammograms were recorded in 60% ethanol + 40% PBS at the scan rates in the range of 25 to 400 mVs^{-1} (Figure 4.2 (B)). As shown in Figure 4.2 (B) inset, the peak

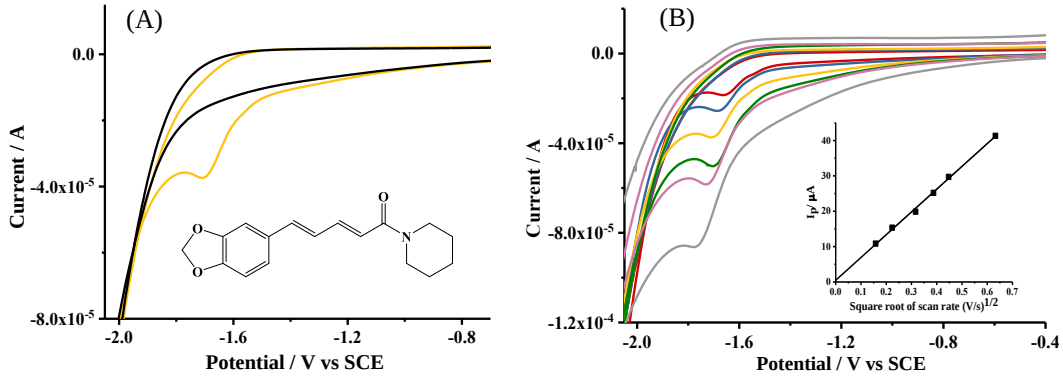


Figure 4.2. Cyclic voltammetric responses at glassy carbon (GC) macroelectrode of (A) background (black line) and 1 mM piperine (yellow line) at a scan rate of 100 mVs^{-1} (B) 1 mM piperine reduction at varying scan rates of 25 mVs^{-1}, 50 mVs^{-1}, 100 mVs^{-1}, 150 mVs^{-1}, 200 mVs^{-1}, 400 mVs^{-1}. Inset of (A) chemical structure of piperine (B) plot of peak current versus square root of scan rate.

current (I_p) was found to exhibit a linear relationship with the square root of scan rates from 25 to 400 mVs^{-1}, suggesting the reduction of piperine is a diffusion-controlled electrochemical process.

4.3.1.2 Measurement of Number of Electrons Transferred and the Diffusion Coefficient

In order to further investigate this diffusion-controlled reduction process and, in particular, to determine the diffusion coefficient of piperine in the studied system, the chronoamperometric responses of varying concentrations of piperine were recorded at a carbon fibre microdisc electrode. In the potential step chronoamperometric experiment, the potential applied to the microdisc electrode was stepped from 0 V, where no current flows, to an overpotential which ensures the reduction occurs at a rate controlled by mass transport. The overpotential we used for the chronoamperometry was determined from the cyclic voltammogram shown in Figure 4.3 as -1.8 V vs. SCE to ensure diffusion control.

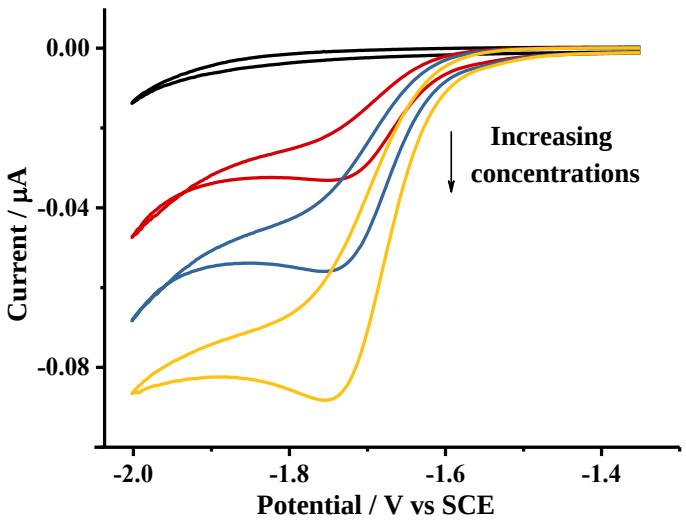


Figure 4.3. Cyclic voltammetric responses at a carbon fibre microdisc electrode of 0 mM and 5 mM, 10 mM, 15 mM of piperine solution at a scan rate of 100 mV/s.

The approximation given by the Shoup and Szabo equation to within a maximum error of not more than 0.6%[27] describes the current responses over the time scale of the chronoamperometric measurement, which is mentioned in Chapter 1:

$$I = 4nFcDrf(\tau) \tag{4.1}$$

where

$$f(\tau)=0.7854+0.8862\tau^{-0.5}+0.2146\exp(-0.7823\tau^{-0.5}) \tag{4.2}$$

and

$$\tau=\frac{4Dt}{r^2} \tag{4.3}$$

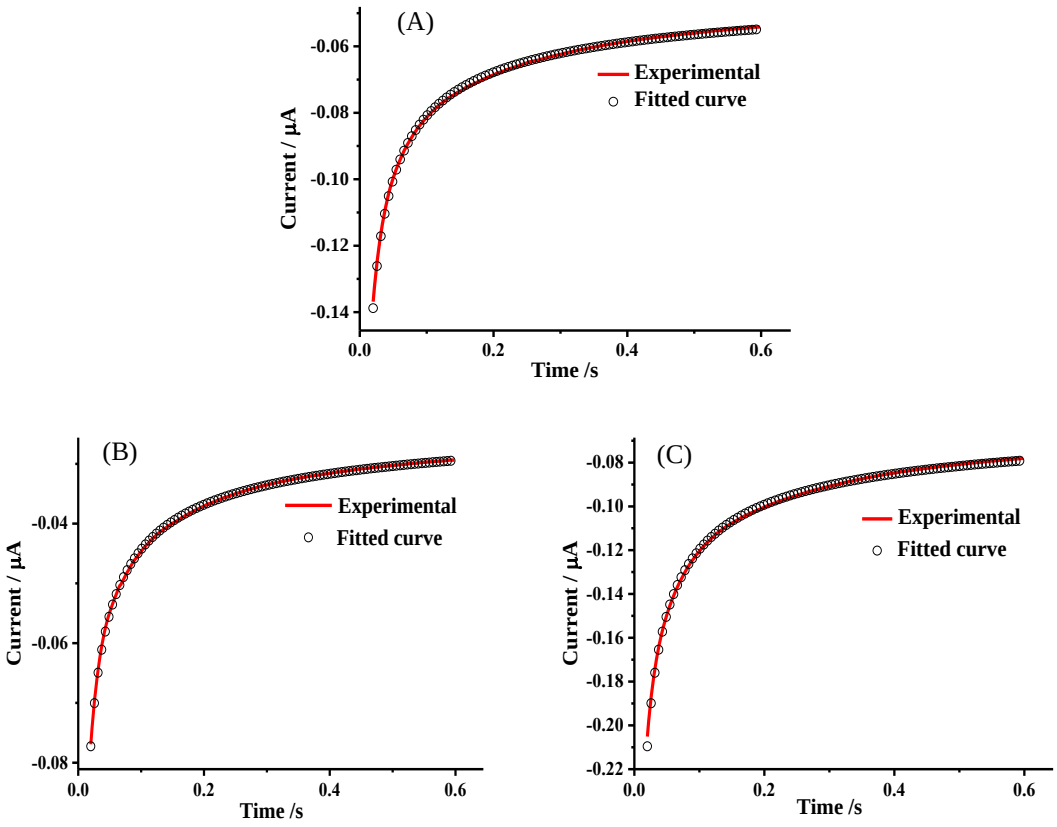


Figure 4.4. Chronoamperometric responses of (A) 10 mM (B) 5 mM (C) 15 mM piperine subtracted of solvent (red solid line) at carbon fibre microdisc, and the corresponding lines of best fits (black circles) derived from Shoup and Szabo equations at the transient time of 0.6 s.

where *I* is current, *F* is the Faraday constant, *n* is the number of electrons transferred, *D* and *c* are respectively the diffusion coefficient and the concentration of the electroactive species, *r* is the radius of the microdisc, and *t* is the time. The current dependency on diffusion coefficient changes from $I \propto \sqrt{D}$ at short time to $I \propto D$ at long time, whilst the current is proportional *(nc)* to at all times. Thus for a given known concentration, *n* and *D* can both be deduced by fitting experimental transient with the Shoup–Szabo equation as used effectively in several previous studies[28-30]. The time interval of 0.02–0.6 s of the chronoamperometric transient was analysed to obtain an accurate fit characterising the diffusional process, without including the data points describing the non-Cottrellian behaviour controlled by double-layer charging before 20 ms or an excessive contribution from the steady state current at long time[26]. The fitting was achieved via *Origin 2017*, where by inputting the known values of *r* and *c*, the software iterated through the values of *n* and *D* until an optimised fit was obtained. It is noted that since the chronoamperometric experiments were performed at the high negative potential at -1.8 V vs. SCE, the solvent transient originating from the redox reaction of solvent and the double layer charging can 'obscure' the chronoamperometric responses of interest[21]. Consequently, the transient of solvent without the addition of

piperine was subtracted from measured chronoamperometric transient before fitting with the theoretical curve for a more accurate evaluation of *n* and *D*.

Table 4.1. The values of number of electrons transferred and diffusion coefficient determined from the fitted curves of experimental data of varying concentrations of piperine.

Piperine Concentration/mM	5	10	15
No. of electrons transfer	1.03	0.84	0.96
Diffusion coefficient/ cm^2s^{-1}	4.68×10^{-6}	5.50×10^{-6}	4.47×10^{-6}

Figure 4.4 (A) shows the experimental potential step chronoamperometric curve of 10 mM piperine at carbon fibre microdisc electrode and the corresponding fit. The chronoamperometric signal again indicates the process is typically diffusion-controlled. Chronoamperometric measurements of varying concentrations of 5, 15 mM piperine were also conducted using the same analytical method, as shown in Figure 4.4 (B) and (C). The averages of results given by the fitting curves are listed in Table 4.1, which gave the diffusion coefficient of (4.9 ± 0.5) $\times 10^{-6}$ cm^2 s^{-1} (at 298 K) with the number of electrons transferred found to correspond to 1.

4.3.1.3 Possible Reaction Mechanism

Having identified the electrochemical process occurring at the microelectrode, we next compared it with the results obtained from the glassy carbon (GC) macroelectrode (Figure 4.2 (B) in Section 4.3.1.1). The peak current, I_{Irrev}, was calculated for an irreversible, one-electron electrochemical reduction using the parameters (n and D) deduced from the chronoamperometry via the *Randles-Sevcik* equation:

$$I_p = 0.496\sqrt{n' + \alpha_{n'+1}}nFA[A]\sqrt{\frac{FDv}{RT}} \qquad (4.4)$$

where n' is the number of electrons transferred before the rate-determining electron transfer, n is the total number of electrons transferred, α is the electron transfer coefficient, taken as 0.5, F is the Faraday constant, A is the electrode area, $[A]_{bulk}$ is the bulk concentration, D is the diffusion coefficient equal to 4.9×10^{-6} cm^2 s^{-1} measured in section 3.2.2, v is the scan rate, R is the gas constant and T is the temperature of 298K. Assuming $n' = 0$, n for the electron transfer at macroelectrode can also be determined using the peak currents (I_{Expt}) measured at varying scan rates using cyclic voltammetry as described in section 4.3.1.1. The obtained I_{Irrev} and I_{Expt} values are listed in Table 4.2. Comparing the

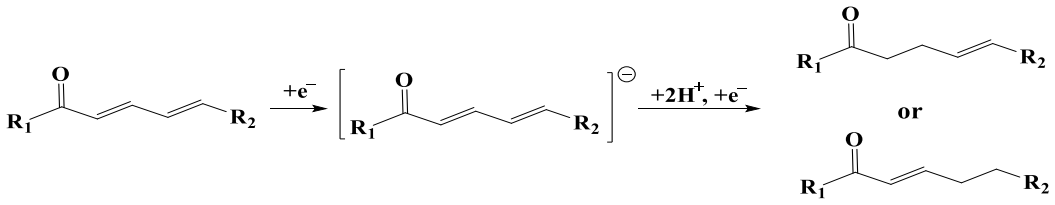
I_{Irrev} values calculated assuming a one-electron process with I_{Expt}, which characterises the electrochemical process on macroelectrode, the I_{Expt} values are ca. twice as large as the values of I_{Irrev}.

The chemical reduction of piperine under various conditions has been reported[31-33]. Either of the two carbon-carbon double bonds has been generally suggested to undergo hydrogenation in methanol (or ethanol) with a catalyst or mediator[32], although reduction leading to a α, β-unsaturated amide was also claimed[31, 33]. For the electrochemical reduction as discussed above, a possible mechanism explaining the difference between the micro- and macro-electrode voltammetry is shown in Scheme 4.1. The one-electron transfer electrochemical reduction generates the carbanion species in the first step, followed by protonation and further one-electron transfer, resulting in the formation of an unsaturated ketone. From this mechanism, the discrepancy between the electrochemical processes at macroelectrode and microelectrode can be rationalised since at carbon fibre microdisc electrode, "divergent/convergent diffusion" occurs, reflecting the significantly more efficient mass transport[21]. The intermediate, carbanion, thus may diffuse away from the electrode surface before the chemical step needed for the second electron transfer can occur. In contrast at a glassy carbon (GC) macroelectrode, the diffusion is linear, so that the loss of the carbanion intermediate is much reduced,

Table 4.2. The calculated peak currents from irreversible *Randles-Sevcik* equation, the obtained experimental peak currents and number of electrons transferred at glassy carbon electrode.

Scan rate/ mVs^{-1}	α	$D/10^{-6}$ cm^2s^{-1}	$I_{Irrev}/\mu A$	$I_{Expt}/\mu A$	n
25	0.5	4.9	5.17	10.86	2.10
50	0.5	4.9	7.31	15.36	2.10
100	0.5	4.9	10.34	19.89	1.93
150	0.5	4.9	12.66	25.21	1.99
200	0.5	4.9	14.62	29.71	2.03
400	0.5	4.9	20.67	41.33	2.00

allowing both steps to occur and an overall transfer of two electrons to take place.



Scheme 4.1. Possible two-step reaction mechanism of piperine reduction.

In order to attempt possibly slow the proton transfer step, further experiments were made at high pH. However, cyclic voltammetric measurements at GC macroelectrode and chronoamperometric measurements at carbon fibre microdisc conducted under high pH conditions in 60% ethanol + 40% aqueous solution of [NaOH] = 0.1, 1.0, 2.0 mM of varying concentrations again suggested one-electron transfer at microelectrode and a two-electron transfer process at macroelectrode (see Appendix A), consistent with the proposed mechanism.

4.3.2 Electrochemical Detection of Piperine

In this section, first, we report the analytical responses of piperine at a glassy carbon (GC) macroelectrode using conventional linear sweep cyclic voltammetry and suggest a data analysis method. Second, we carried out an analogous study using semi-circular potential sweep voltammetry with an optimised potential window to obtain amplified peaks and a simplified, improved procedure of background correction. Finally, we report a one-step extraction method of black pepper and the electrochemical detection method of the piperine content in real samples using both cyclic voltammetry and semi-circular potential sweep voltammetry.

4.3.2.1 Using Cyclic Voltammetry for the Detection of Piperine

Having investigated the electrochemical behaviour of piperine in the aqueous solution, we next turn to the detection of piperine in standard solutions and study the analytical responses of piperine at the GC macroelectrode. First, the cyclic voltammetric studies as described in section 4.3.1.1 were carried out under air-saturated conditions. Compared with the cyclic voltammetry measurements performed under degassed conditions, as expected, an additional, independent peak corresponding to oxygen reduction can be observed, as shown in Figure 4.5. Likewise, the number of electrons transferred was calculated using the measured peak currents I_{Expt} and the calculated peak currents I_{Irrev}. The number of electrons transferred at piperine reduction was found to be 2 and the diffusion coefficient determined from the slope of peak current vs. square root of scan rate plot via the multiple electron-transfer, irreversible *Randles-Sevcik* equation was 5.0×10^{-6} cm^2 s^{-1}, close to the values estimated under degassed condition (4.8×10^{-6} cm^2s^{-1}) and measured in chronoamperometry (4.9×10^{-6} cm^2s^{-1}). The obtained results indicate the oxygen shows no interference with the peak current of the piperine reduction and the

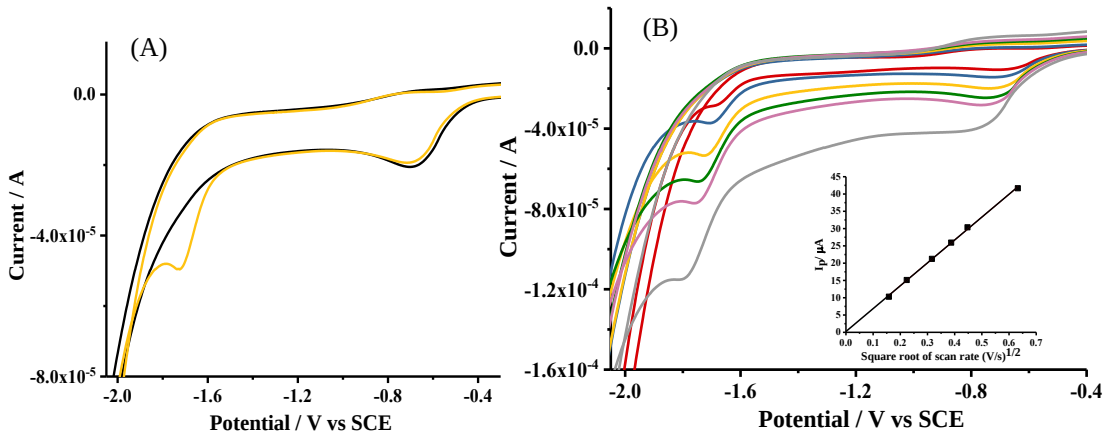


Figure 4.5. Cyclic voltammetric responses of background and 1 mM piperine reduction at glassy carbon electrode in 60 EtOH: 40 PBS under air-saturated conditions at (A) scan rate of 100 mV/s and (B) varying scan rates of 25 mV/s, 50 mV/s 100 mV/s, 150 mV/s, 200 mV/s, 400 mV/s, under air-saturated conditions. Inset of (B): plot of peak current versus square root of scan rate.

same electrochemical behaviour of piperine can be seen on GC macroelectrode regardless of the 60% ethanol + 40% PBS solution having degassed or not. Hence we conducted further measurements without degassing to allow a simpler and rapid detection of piperine.

Cyclic voltammetry was then conducted of piperine with the concentration in the range of 0.25–5.0 mM in air-saturated 60% ethanol + 40% PBS. Three scans at each concentration were conducted and the electrode was polished before each measurement. Figure 4.6 (A) depicts the cyclic voltammetric response as a function of the increasing concentration of piperine. The plot of peak height *versus* piperine concentration (Figure

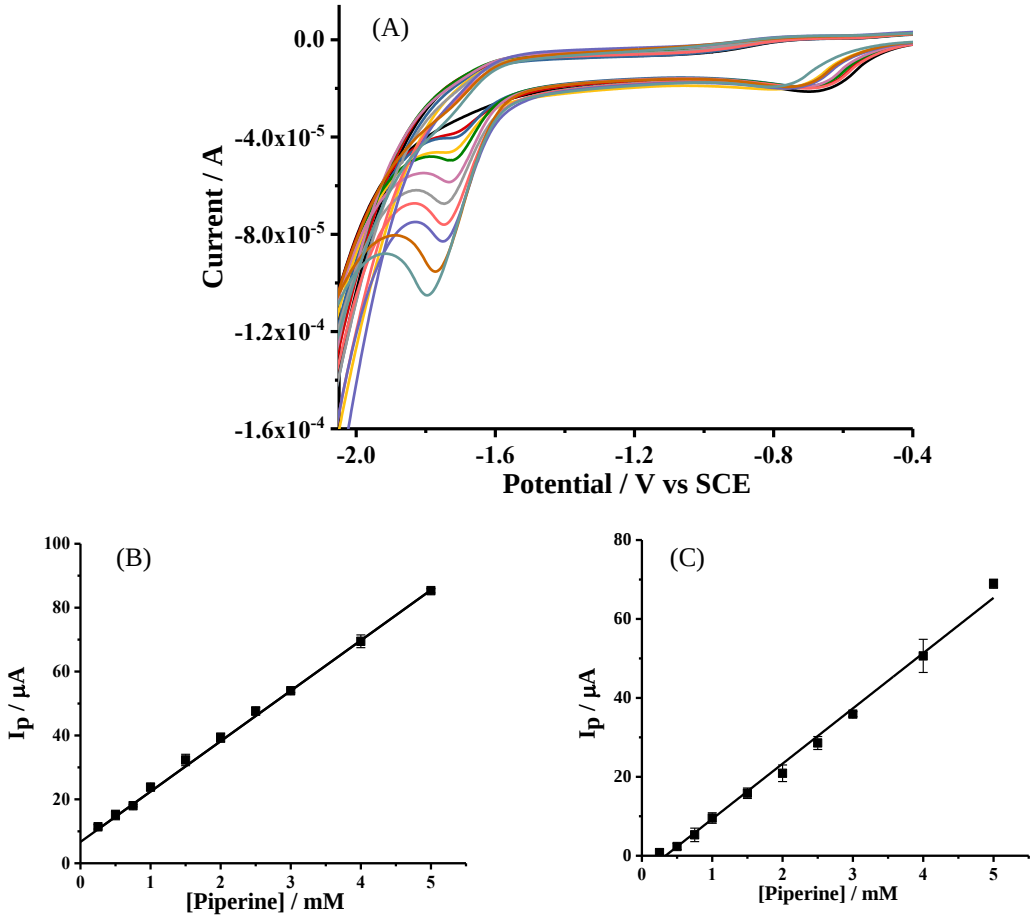


Figure 4.6. (A) Cyclic voltammetric responses of background and increasing concentrations from 0.25–5.0 mM at air-saturated condition. The scan rate was 100 mV/s. (B) Calibration curve plot using the peak heights analysed by extrapolating the baseline. (C) Calibration curve plot using the current values read from the fixed potential of -1.8 V after subtraction of background.

4.6 (B)) shows a linear relationship in the concentration range of 0.25–5.0 mM. The calibration curve is $I_p/\mu A$ = (15.76±0.15) [piperine] (mM) + (6.69±0.35) (μA), N=10, R^2 = 0.999. The peak height was analysed by the extrapolation of the baseline chosen in the vicinity of the reductive peak. Note that the calibration curve plot in Figure 4.6 (B) shows a not insignificant intercept in the y-axis making analysis unreliable.

A significant component to the background current is that resulting from the Faradaic reduction of the oxygen dissolved in the solution since as discussed above, it was chosen not to outgas this so as to give an overall simpler analytical procedure suitable to use by non-experts. Accordingly, we attempted to make a different and simpler background correction by purely measuring currents at a fixed potential on the voltammogram for all concentrations regardless of the potential of the peak current. Figure 4.6 (C) shows that if the current measured from a voltammogram recorded at 100 mVs^{-1} and at a potential of -1.80 V vs. SCE in absence of piperine is subtracted from the currents recorded under corresponding conditions in the presence of different concentrations of the analyte. Then a non-linear calibration curve results, this time with a positive x-axis intercept. The limitations of the background corrections thus far attempted lie in the relatively low signal to noise ratio of the measurement. Accordingly, we turned to the use of semi-circular voltammetry.

4.3.2.2 Using Semi-circular Potential Sweep Voltammetry for Detection of Piperine

The recently proposed method to conduct potential sweep voltammetry using a semi-circular potential waveform for electroanalysis was found to show a good agreement between theoretical predictions and experiments in the study of $[Ru(NH_3)_6]^{3+/2+}$ redox

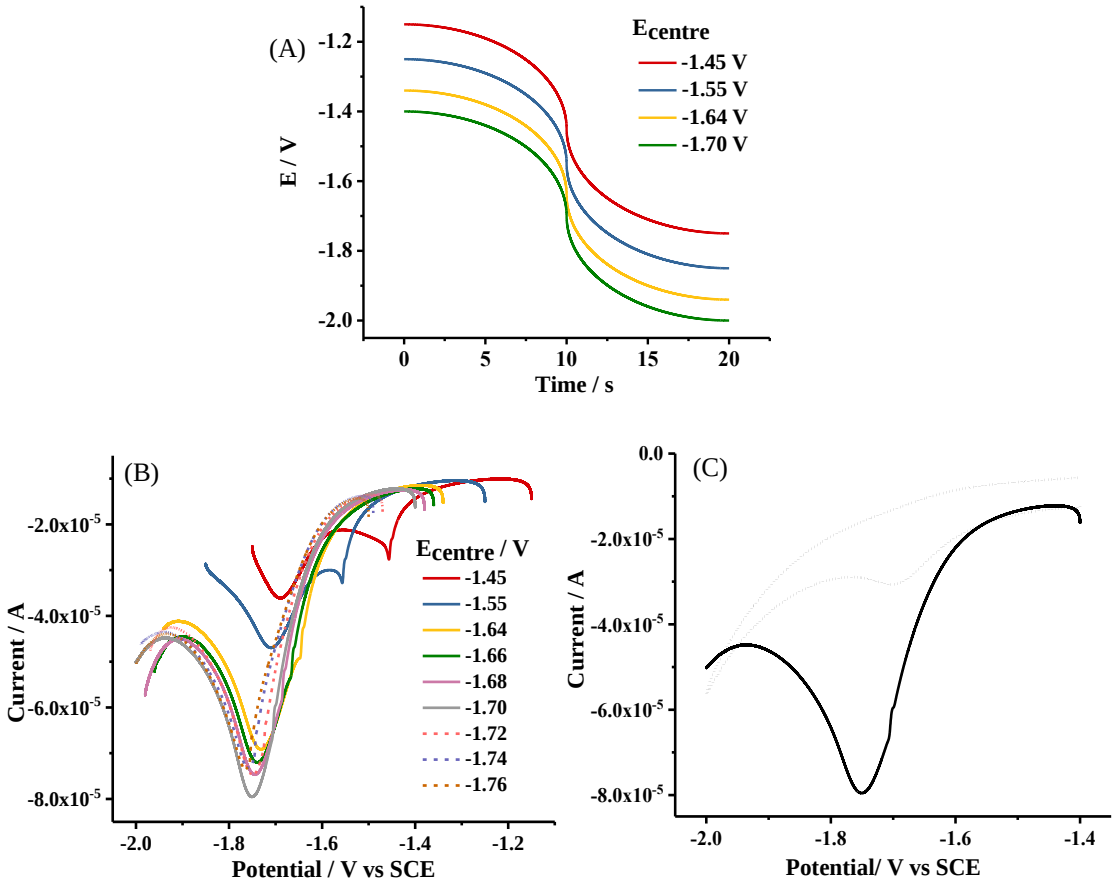


Figure 4.7 (A) Semi-circular waveforms recorded for varying E_{centre}. (B) Semi-circular potential sweep voltammetric responses of 1.5 mM of piperine at varying potential windows at scan amplitude of 0.3 V (solid lines) and 0.25 V (dash lines). (C) Semi-circular potential sweep voltammogram (solid line) at an average of scan rate of 30 mV s^{-1} vs. cyclic voltammogram (dot line) of 1.5 mM piperine at 50 mV s^{-1} over a potential window of -1.4 to -2.0 V. Scan amplitude was 0.3 V.

couple at macroelectrode[22, 23]. In particular, a notably higher current response can be achieved using this technique compared to that obtained from the conventional linear-sweep potential wave[22]. In order to improve our analytical method of the detection of piperine and illustrate this recently reported method for the first time in an analytical application, we explored the semi-circular potential sweep voltammetry of the piperine standard samples with the same concentrations at a GC electrode under air-saturated conditions.

As discussed in Chapter 2, in semi-circular potential sweep voltammetry, the potential of working electrode *E (t)* follows a semi-circular potential wave (Figure 4.7 (A)):

$$E(t) = \pm A_0 \sqrt{\left|1 - \left[2\left(\frac{t}{t_{\max}} - c\right)\right]^2\right|} + E_{centre} \qquad (4.5)$$

where A_0 is the amplitude of the potential wave, t is the time and $t_{\max}$ is the duration of a single scan between the two potential limits. $c = 0$ for $t \leqslant t_{\max}/2$, $c = 1$ for $t_{\max}/2 < t < t_{\max}$ and E_{centre} is the midpoint of the applied potential window, which is experimentally defined relative to the reference electrode with the start potential E_i and the vertex potential E_f. In contrast to the constant scan rate over the entire scan in linear sweep voltammetry, the scan rate resulting from the semi-circular wave shows significant variations with the sweep. As can be seen in Figure 4.7 (A), the scan rate is close to zero at $t = 0$ and $t = t_{\max}$ and increases transiently to infinite at E_{centre}.

As discussed in Chapter 2 and in previous work, by adjusting the position of E_{centre} to the close vicinity of the reduction potential of the studied target, the peak current reached

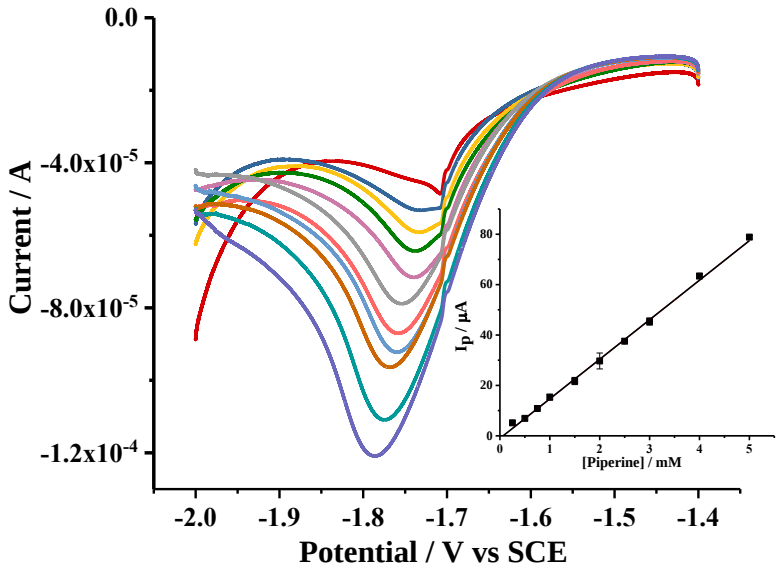


Figure 4.8. Semi-circular potential sweep voltammetric responses of the background and varying concentrations of piperine at glassy carbon (GC) electrode in 60 EtOH: 40 PBS at air-saturated conditions. Scan rate: 50 mV / s. Potential window: -1.40 to -2.0 V. Inset: Calibration curve plot using the current value at -1.80 V after the subtraction of background.

a maximum value[22, 23] . To determine the E_{centre} leading to the maximum peak current in our system, voltammetric measurements of 1.5 mM piperine in 60% ethanol + 40% PBS using scan amplitudes of 0.3 and 0.25 V were carried out. It can be seen in Figure 4.7 (B) when E_{centre} = -1.70 V with scan amplitude as 0.3 V, the peak current reached the maximum. Thus in further semi-circular potential sweep voltammetric experiments, the potential window of -1.40 to -1.70 V was employed. Comparing with cyclic voltammetry, we can see two main differences in semi-circular voltammetry. First, with the potential window thus optimised, the obtained piperine reduction peak using semi-circular potential sweep voltammetry was significantly larger compared to the peak shown in the cyclic voltammetry at the similar average scan rate (Figure 4.7 (C)). Second, in the semi-circular potential sweep voltammetry(Figure 4.7 (B) and 4.7 (C)), kinks at the midpoint can be seen, arising from reaching the nominally infinite scan rate.

Figure 4.8 depicts semi-circular potential sweep voltammetric responses for 0.25–5 mM piperine in 60% ethanol + 40% PBS as a function of increasing concentrations of piperine. The sizes of the peaks in Figure 4.8 compare favourably with the signals shown in Figure 4.6 (A). As discussed above, the obtained peak currents were substantially affected by the potential windows and values of E_{centre}. Consequently, current values at a fixed potential rather than the peak currents read at shifted potentials for varying concentrations were taken for calibration curve analysis. Several potentials near the peak potential were examined. Current values read from varying potentials near the peak potentials were plotted against the concentration of piperine in Figure 4.9. It can be seen that at -1.80 V, the best linearity (R^2 = 0.998) was found, with an intercept closest in value with the background current read from the blank scan in Figure 4.8. Therefore -1.80 V was chosen as the suitable potential in this study and the background current of 40.60 μA was subtracted from the experimental voltammograms.

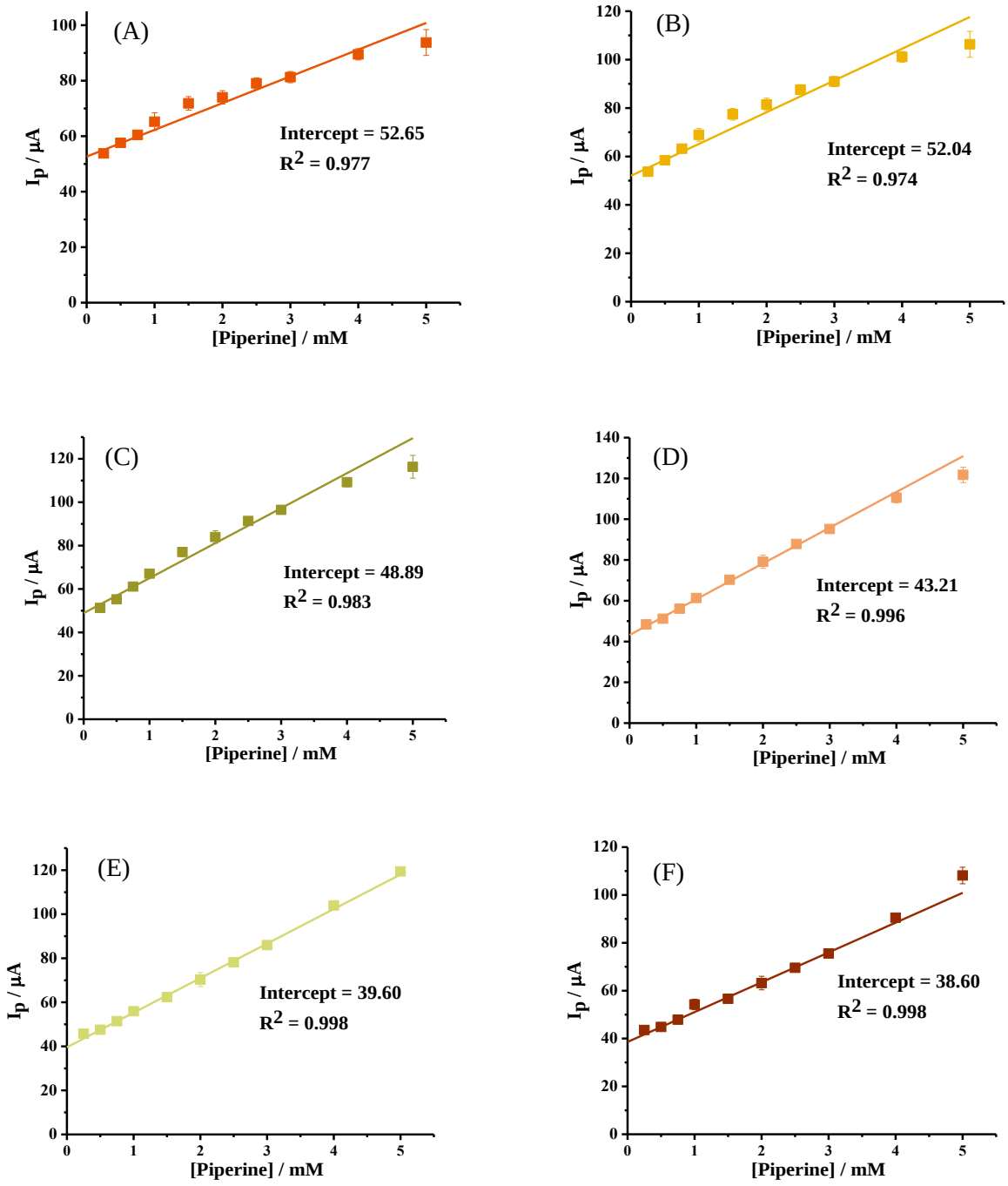


Figure 4.9. Plot of current values read from fixed potentials of (A) -1.72 V (B) -1.74 V (C) -1.76 V (D) -1.78 V (E) -1.80 V (F) -1.82 V versus concentration of piperine.

For the current values at -1.8 V, a linear behaviour was found in the plot of these current values *versus* piperine concentration, in the concentration range of 0.25–5.0 mM. After subtracting the current from a single background scan at -1.8 V vs. SCE, the

resulting calibration curve is $I_p/\mu A$ = (15.69±0.23) [piperine] (mM)-(1.00±0.54) (μA), N = 10, R^2 = 0.999 (Figure 4.8 inset).

The results provided the experimental validation for using semi-circular potential sweep voltammetry to study the analyte giving greatly amplified peaks. In the semi-circular potential sweep voltammogram, currents are read at a fixed potential and a simple background correction can be achieved via subtracting the background at the chosen potential, making the semi-circular potential sweep voltammetry a more advantageous method in data analysis than the conventional cyclic voltammetry.

4.3.3 Analysis of a Real Sample

In order to assess the feasibility and accuracy of electrochemistry for piperine analysis, we next looked at the detection of piperine in real samples. We first developed a procedure for the extraction of piperine from a black pepper sample purchased from a local supermarket**.** Among various methods of piperine isolation reported in the literature, ultrasound-assisted extraction was found to be a rapid, simple, cheap method leading to a high yield of piperine[4]. Ethanol as a cheap, easy-handling solvent was suggested to give high extraction yields along with insonation[34]. Therefore, we chose ethanol as the extraction solvent and carried out the extractions with different sonication time periods. The preparation of samples was fully described in section 4.2.3. Ethanol was added to the vials with ground samples in a fixed ratio (5 mL ethanol to 0.5 g black pepper), which was then placed in an ultrasonic bath for the sonication times of 5, 10, 15 minutes. Experiments maximising the piperine content by using a long time sonication of 1 hour sonication followed by 1 day extraction were also carried out to obtain the maximised piperine contents. After sonication/extraction, the supernatant was mixed with PBS in the

ratio of 60:40 and diluted with 60% ethanol + 40% PBS. Cyclic voltammetric measurements at a GC electrode were then conducted. The results of extracts from three separate black pepper samples were recorded for each sonication time, as shown in Figure 4.10 (A), where the results have been expressed in piperine content (%w/w) of the original sample. The resulted maximum piperine contents obtained at 1 hour sonication followed by 1 day extraction were found to be (3.66 ± 0.02) % w/w, in accordance with the values reported by literatures where the piperine content in fruit of *P. nigrum* quantified by HPLC technique was found to lie in the range of 3%–6% (w/w)[35]. For the short time extractions, the results lie in the range of (2.03 ± 0.19) % w/w to (2.27 ± 0.17) % w/w, which is approaching the maximum value at long time extractions. The short time

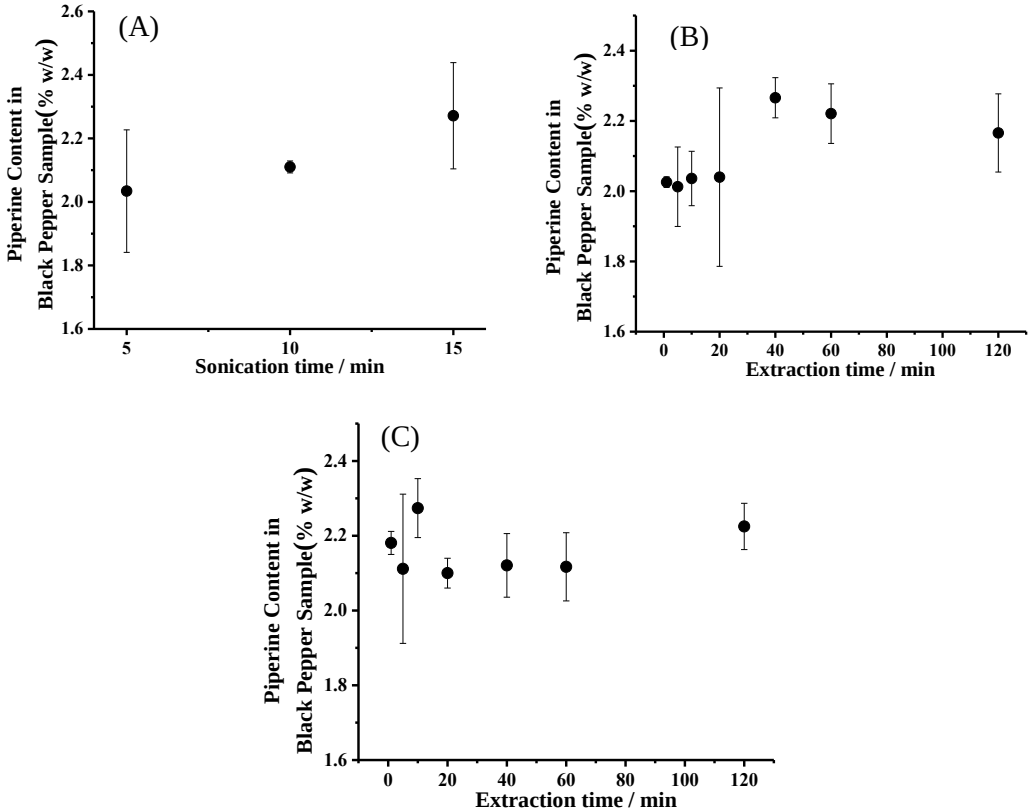


Figure 4.10. Piperine content detected in black pepper extracts at different extraction times by cyclic voltammetry using Figure 4.6(B) calibration curve: (A) With sonication from 5 to 15 minutes (B) Without sonication from 0 to 120 minutes; and by semi-circular voltammetry using Figure 4.8 calibration curve : (C) Without sonication from 0 to 120 minutes.

extraction results show no evident growth in extraction efficiency with the increasing sonication time. It can be inferred the maximum extraction for a short time period had been achieved at some point before 5 minutes of sonication or without the assistance of sonication. In order to simplify the procedure and cut down the waiting time, we carried out the extraction by simply shaking the extract for 1 minute prior to leaving the extract to settle for 1–120 minutes. The rest of the procedure was used just as the procedure above with sonication. The results (Figure 4.10 (B)) from the simplified procedure showed the piperine contents were found to be (2.01 ± 0.11) % w/w to (2.27 ± 0.06) % w/w, which were approximately in the same range as the sonication method, suggesting the extraction for a short time period was essentially completed in one minute without sonication. The extracted sample was also measured after the addition of ethanol without shaking or settling, the piperine content was found to be ca. (1.79 ± 0.06) % w/w, just slightly below the range. From the results, it can be seen the extraction of piperine in black pepper is a rather fast process given that the black pepper had been ground into small particles, and our simplified procedure with any settling time from 1 to 120 minutes

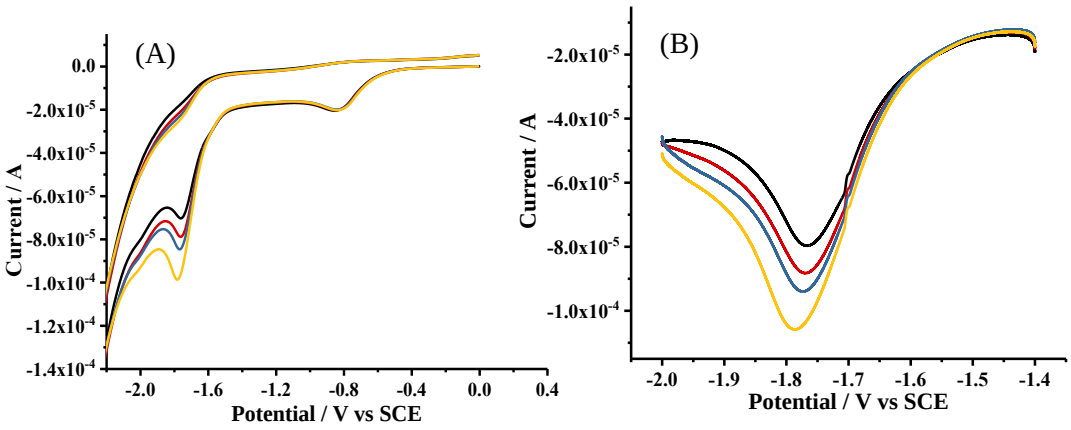


Figure 4.11. (A) cyclic voltammograms of real sample extract (black line) extracts added with 0.5 mM (red line), 1mM (blue line), 2 mM (yellow line) standard piperine solutions. The scan rate was 100mV s^{-1} (B) semi-circular potential sweep voltammograms of real sample extract (black line) extracts added with 0.5 mM (red line), 1 mM (blue line), 2 mM (yellow line) standard piperine solutions. The average of scan rate was 30mV s^{-1}

can be used for further quantification. For practical analysis, our approach offers a good compromise with rapid analysis plus a reasonable accuracy.

Having developed the extraction procedure, we next employed the semi-circular potential sweep voltammetry for the quantification of piperine in real samples. The same simplified extraction procedure as above was carried out with a settling time of 1–120 minutes using the semi-circular potential sweep voltammetric method. The piperine contents depicted in Figure 4.10 (C) lie in the range of (2.10 ± 0.03) % w/w – (2.27 ± 0.08) % w/w, which was in accordance with the result obtained from using cyclic voltammetry.

Table 4.3. Concentrations analysed by calibration curves in insets of Figure 4.4 (B) and Figure 4.7 of detected piperine in extract and extracts with standard solutions and the corresponding recoveries.

Solution	Measured Concentration Using Cyclic Voltammetry/mM	Recovery/%	Measured Concentration Using Semi-circular Potential Sweep Voltammetry /mM	Recovery/%
Extracted sample	2.2 ± 0.10		2.1 ± 0.02	
Sample+0.5mM Piperine	2.8 ± 0.04	104	2.6 ± 0.07	104
Sample+1.0mM Piperine	3.2 ± 0.03	95	3.1± 0.07	98
Sample+2.0mM Piperine	4.1 ± 0.04	94	4.1 ± 0.01	102

The accuracy of the extraction procedure was validated by a "recovery" test[36], where known concentration standard solutions were used to "spike" diluted extracts prior to voltammetric measurements. The percentage recoveries were evaluated by both cyclic voltammetric and the semi-circular potential sweep voltammetric methods and the resulted voltammograms are shown in Figure 4.11 (A) and (B). The peak heights measured in cyclic voltammograms and semi-circular potential sweep voltammograms

are converted to the concentrations of piperine using the calibration curves in Figure 4.6 (B) and Figure 4.8. Values close to 100% were attained in both methods, as suggested by Table 4.3.

4.4 Conclusions

Cyclic voltammetry and semi-circular potential sweep voltammetry have both been successfully applied to the detection and quantification of piperine in standard solutions and real samples using a glassy carbon (GC) macroelectrode. In particular, the employment of semi-circular potential sweep voltammetry provides the advantage of amplifying peaks to facilitate the electrochemical determination of species otherwise showing low sensitivity. To the best of our knowledge, this the first time semi-circular potential sweep voltammetry has been applied for electroanalytical detection. The electrochemical reduction mechanism of piperine was investigated utilizing a combination of cyclic voltammetry and potential step chronoamperometry and a possible mechanism was inferred. This proposed method of detection may become useful for application in pharmaceutical production and the food industry, serving as a facile and inexpensive substitute for HPLC and GC-MS, etc.. In the next chapter, the use of semi-circular voltammetry for the voltammetric study of mixtures with closely similar redox responses is proposed.

Bibliography

1. V. A. Parthasarathy, B. Chempakam and T. J. Zachariah, *Chemistry of spices*, CABI, London, 2008.
2. K. Hirasa and M. Takemasa, *Spice science and technology*, CRC Press, 1998.
3. K. V. Peter, *Handbook of herbs and spices*, Elsevier, 2012.
4. L. Gorgani, M. Mohammadi, G. D. Najafpour and M. Nikzad, *Comprehensive Reviews in Food Science and Food Safety*, 2017, **16**, 124-140.
5. Z. Zarai, E. Boujelbene, N. Ben Salem, Y. Gargouri and A. Sayari, *LWT - Food Science and Technology*, 2013, **50**, 634-641.
6. Q. Mao, Z. Huang, X. Zhong, Y. Xian and S. Ip, *Neurochemistry International*, 2014, **74**, 36-41.
7. C. D. Doucette, A. L. Hilchie, R. Liwski and D. W. Hoskin, *The Journal of Nutritional Biochemistry*, 2013, **24**, 231-239.
8. R. S. Vijayakumar, D. Surya and N. Nalini, *Redox Report*, 2004, **9**, 105-110.
9. E. P. Sabina, A. D. H. Souriyan, D. Jackline and M. K. Rasool, *Asian Pacific Journal of Tropical Medicine*, 2010, **3**, 971-976.
10. E. S. Sunila and G. Kuttan, *Journal of Ethnopharmacology*, 2004, **90**, 339-346.
11. S.-H. Kim and Y.-C. Lee, *Journal of Pharmacy and Pharmacology*, 2009, **61**, 353-359.
12. C. Shimada, Y. Uesawa, M. Ishihara, H. Kagaya, T. Kanamoto, S. Terakubo, H. Nakashima, K. Takao, T. Miyashiro, Y. Sugita and H. Sakagami, *Anticancer Research*, 2014, **34**, 4877.
13. K. Janakiraman and R. Manavalan, *African Journal of Traditional Complementary and Alternative Medicines*, 2008, **5**, 257-262.
14. V. Balakrishnan, S. Varma and D. Chatterji, *Current Science*, 2001, **80**, 1302-1305.
15. K. Mueller and J. Hingst, *The athlete's guide to sports supplements*, Human Kinetics, 2013.
16. I. Noyer, B. Fayet, I. Pouliquen-Sonaglia, M. Guerere and J. Lesgard, *Analusis*, 1999, **27**, 69-74.
17. W. Ternes and E. L. Krause, *Analytical and Bioanalytical Chemistry*, 2002, **374**, 155-160.
18. M.-J. Ju, K. Hayama, K. Hayashi and K. Toko, *Sensors and Actuators B: Chemical*, 2003, **89**, 150-157.
19. R. Jain and A. Verma, *International Journal of Electrochemical Science*, 2017, **12**, 3459-3471.
20. A. J. Bard, L. R. Faulkner, C. G. Zoski and J. Leddy, *Electrochemical methods : fundamentals and applications*, Wiley, New York ; Chichester, 2nd edn., 2001.
21. R. G. Compton and C. E. Banks, *Understanding voltammetry*, World Scientific Publishing Europe, London, 3rd edn., 2018.
22. H. M. A. Amin, Y. Uchida, E. Kätelhön and R. G. Compton, *Journal of Electroanalytical Chemistry*, 2019, **836**, 62-67.
23. Y. Uchida, E. Kätelhön and R. G. Compton, *Journal of Electroanalytical Chemistry*, 2018, **818**, 140-148.
24. Y. Wang, J. G. Limon-Petersen and R. G. Compton, *Journal of Electroanalytical Chemistry*, 2011, **652**, 13-17.

25. C. Batchelor-McAuley, J. Ellison, K. Tschulik, P. L. Hurst, R. Boldt and R. G. Compton, *Analyst*, 2015, **140**, 5048-5054.
26. L. Xiong, L. Aldous, M. C. Henstridge and R. G. Compton, *Analytical Methods*, 2012, **4**, 371-376.
27. D. Shoup and A. Szabo, *Journal of Electroanalytical Chemistry and Interfacial Electrochemistry*, 1982, **140**, 237-245.
28. C. E. Banks, R. G. Evans, J. Rodrigues, P. G. Turner, T. J. Donohoe and R. G. Compton, *Tetrahedron*, 2005, **61**, 2365-2372.
29. D. S. Silvester, A. J. Wain, L. Aldous, C. Hardacre and R. G. Compton, *Journal of Electroanalytical Chemistry*, 2006, **596**, 131-140.
30. C. A. Paddon, D. S. Silvester, F. L. Bhatti, T. J. Donohoe and R. G. Compton, *Electroanalysis*, 2007, **19**, 11-22.
31. A. P. da Silva, S. D. C. Mota, L. W. Bieber and M. Navarro, *Tetrahedron*, 2006, **62**, 5435-5440.
32. R. Gallagher, R. Shimmon and A. M. McDonagh, *Forensic Science International*, 2012, **223**, 306-313.
33. M. E. Pedersen, B. Metzler, G. I. Stafford, J. Van Staden, A. K. Jäger and H. B. Rasmussen, *Molecules*, 2009, **14**, 3833-3843.
34. S. S. Rathod and V. K. Rathod, *Industrial Crops and Products*, 2014, **58**, 259-264.
35. P. K. Mukherjee, *Quality control and evaluation of herbal drugs: Evaluating natural products and traditional medicine*, Elsevier, 2019.
36. G. P. Carr and J. C. Wahlich, *Journal of Pharmaceutical and Biomedical Analysis*, 1990, **8**, 613-618.

Chapter 5

Selective Voltammetric Detection of Chlorophylls Using a Semi-circular Potential Wave

In this chapter, a simple electrochemical method employing a novel semi-circular potential sweep voltammetry on a glassy carbon (GC) electrode is developed to distinguish and quantify the two main components of chlorophyll (chlorophyll a and b) present in their mixtures. The semi-circular potential sweep generates large, transient scan rates, enabling the selective detection of species with closely similar oxidation (or reduction) potentials. The proposed method shows good applicability in mixtures of chlorophyll a (Chl a) and chlorophyll b (Chl b) with concentrations ranging from 46.2 to 110.8 μM and 46.2 to 92.4 μM respectively, which were prepared to mimic varying compositions of chlorophyll a and b in nature for the application in food quality control. The method is successfully applied to real samples of spinach.

The work presented in this Chapter has been published as a first author paper in *Food Chemistry*.

5.1 Introduction

As discussed in previous chapters, cyclic voltammetry (CV) is a widely used technique, in particular, for initial analysis of new redox systems, providing abundant information such as rate constants, formal potentials, electron transfer coefficients to study the kinetics and thermodynamics of electrochemical reactions[1]. It employs a linear potential waveform[2]:

$$E(t) = E(t=0) \pm vt \tag{5.1}$$

where the ± sign indicates the oxidation or reduction of the studied reaction and *v* is the scan rate that remains constant. However, an alternative method has been proposed recently, employing a semi-circular potential wave as follows[3, 4]:

$$E(t) = \pm A_0 \sqrt{\left|1 - \left[2\left(\frac{t}{t_{\max}} - c\right)\right]^2\right|} + E_{centre} \tag{5.2}$$

where A_0 is the amplitude of the potential wave, *t* is the time and $t_{\max}$ is the duration of a single scan between the two potential limits. *c* = 0 for $t \leqslant t_{\max}/2$, *c* = 1 for $t_{\max}/2 < t < t_{\max}$. E_{centre} is the midpoint of the applied potential window, which is experimentally defined relative to the reference electrode with the start potential E_i and the vertex potential E_f. The main features of semi-circular potential wave in contrast to conventional linear wave are that it generates an instantaneous infinite scan rate at the midpoint of the potential window and relatively slower scan rates in other regions. The current response, which is dependent on the scan rate, can thus be selectively amplified at a desired potential while compressed at others. This novel method giving significant current amplification was validated by Uchida *et al.* via simulation[5], where its use for determining standard electrochemical rate constants, k_0, with one magnitude greater

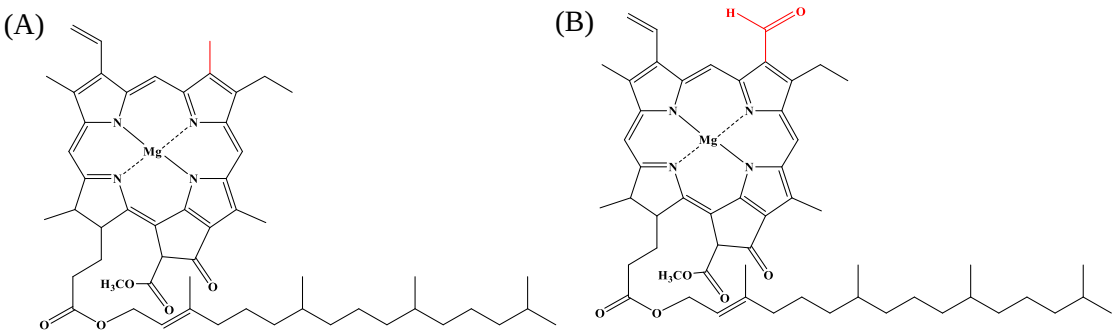
accuracy than via conventional CV was also suggested[5]. The experimental verification of semi-circular potential sweep voltammetry was performed on the well-known redox couple $Ru(NH_3)_6^{3+/2+}$, showing good agreement with theory and a potential application in determining formal potentials[6].

The use of semi-circular potential sweep voltammetry for electro*analytical* applications is just beginning to be investigated computationally and experimentally. The main advantage of applying a semi-circular potential wave is its ability to generate the markedly increased current response and thus improve the detection sensitivity. This was demonstrated by Uchida *et al.* in a theoretical study employing semi-circular potential sweep in stripping voltammetry designed for the adsorbed species[7]. Further, the use of semi-circular potential sweep voltammetry in experiments for a diffusion-controlled electrochemical process to obtain amplified signals facilitating simple data analysis was demonstrated in the last chapter on the quantification of piperine in black pepper[8].

In order to further appreciate semi-circular potential sweep voltammetry and in particular, develop it into a powerful tool for electroanalytical applications, we herein apply the semi-circular potential sweep voltammetry to the analysis of a mixture of two species. As predicted by Uchida *et al* on the basis of computational simulation[4], semi-circular voltammetry is advantageous over conventional CV in distinguishing two individual species from a mixture, in particular, when they have closely similar peak potentials in classical CV. To demonstrate this, chlorophyll a (Chl a) and chlorophyll b (Chl b), with closely similar redox potentials are studied experimentally[9-11].

The chlorophylls are a group of tetrapyrrolic pigments involved in photosynthesis in higher plants, algae, and some species of bacteria. Chl a and Chl b are two major light-absorbing pigments[12], playing pivotal roles in the electron transfer that occurs at the

reaction centres of both photosystem I and photosystem II . They are very similar in structure and found to coexist in many oxygenic photosynthetic organisms[12]. Both of them possess the porphyrin ring coordinating to a central magnesium ion while Chl a distinguishes from Chl b by its 7-methyl-substituent rather than 7-formyl functional group (Scheme 5.1 (A)(B)). The chlorophylls were reported to show prooxidant activities under light, transferring the energy absorbed from light to the present triplet oxygen to form highly reactive singlet oxygen but act as antioxidants at dark conditions owing to the structure of their porphyrin rings. Chl a was found to possess a higher prooxidant activity than Chl b whereas Chl b is a stronger antioxidant[13].



Scheme 5.1. Chemical structures of (A) chlorophyll a and (B) chlorophyll b.

Due to their important roles in the photosynthetic process and abundant presences in nature, determinations of chlorophylls are required for both mechanism investigations and industrial/agricultural analysis including quality control of crops[14] and food products[15], as well as measurements of phytoplankton[16] biomasses for applications in water quality monitoring and environmental pollution assessment. In particular, for many types of edible oil products, for example and notably, extra virgin olive oil, chlorophylls and their degradation products such as pheophytins and pyropheophytins can serve as indicators of the product storage stability due to their prooxidant or antioxidant behaviours, which have clear effects on the photosensitized oxidation or autoxidation of

the product[13]. Extra virgin olive oil has generally been suggested as needing to be stored in the dark to maintain its overall oxidative stability and nutritional value, preventing the degradation of some minority compounds including chlorophyll (present mainly as pheophytin a in this product) which reduces the autoxidation of the oil in the dark[17, 18]. Light accelerates the oil oxidation by triggering the reaction of singlet oxygen via photosensitized oxidation. Packaging technologies such as applying oxygen scavengers[17] and light filtering packaging materials[19] can help better maintain the quality of oil under light, although they may become less effective when high concentrations of chlorophyll as prooxidant are present[19]. Moreover, pyropheophytins have been reported to be very sensitive to temperature, another factor affecting the shelf-life of extra virgin olive oil, therefore these molecules can be used as a freshness parameter indicating exposure to temperatures above 25 ° C[20].

5.2 Experimental

5.2.1 Chemicals and Reagents

Chlorophyll a and b were extracted and partially purified from fresh spinach leaves based on a previously published method[31], followed by subsequent purification performed on a silica gel column chromatography using 60 Å silica gel 40-63 μm purchased from VWR. The detailed procedure was as follows: Spinach leaves (100g fresh weight) were blended with a hand blender in 500 mL acetone for 3 min. The obtained green extract was filtered through the 185mm diameter Whatman No.1 filter paper to remove the plant materials. The acetone extract was first mixed with ca. 70 mL dioxane (≥99.8%, Sigma-Aldrich) and 80-100 mL de-ionised water, followed by another addition

of 150 mL of acetone: dioxane (7:1, v/v) and ca. 25 mL of water. The precipitate yielded from each dioxane addition was collected. The final precipitate was then dissolved in 500 mL methanol (≥99.9%, Sigma-Aldrich) containing 125 mL of petroleum ether (b.p. 40-60°C, ≥90%, Sigma-Aldrich). Next ca. 250 mL of deionised water was added into the solution with gentle stirring to create a transfer of chlorophylls from the methanol to the petroleum ether phase. The upper petroleum ether layer was then washed several times with 80% (v/v) aqueous methanol and the bottom aqueous layer was discarded. The aforementioned steps eliminate the yellow pigments (carotenoids and xanthophylls) from the chlorophyll solution to facilitate an easier separation in column chromatography. The petroleum ether solution of chlorophylls was dried with anhydrous $MgSO_4$ (≥99.5%, Sigma-Aldrich), which was then filtered off from the solution. The crude chlorophyll solution was evaporated and resolubilised in the minimum volume of diethyl ether for column chromatography.

For column chromatography, a silica gel column was used in a solvent system of pentane (≥99.0%, Sigma-Aldrich), diethyl ether and acetone. The 80 % pentane: 20% diethyl ether was added to the column first, followed by 80 % pentane: 10% diethyl ether: 10% acetone and finally 70 % pentane: 10% diethyl ether: 20% acetone. The pigments were eluted and collected in the order of carotenes, pheophytin a, chlorophyll a, pheophytin b, chlorophyll b, xanthophylls. Analytical thin-layer chromatography (TLC) was then performed on Merck silica gel 60 F254 plates and visualised with UV light (254 or 365 nm).

The spinach was purchased fresh from a local supermarket (Tesco, Oxford, UK). The products of Chl a and Chl b obtained from 100 g spinach were weighed as 22.3 mg and 6.2 mg and dissolved in acetone or diethyl ether for further measurements. Stock

solutions in acetone were stored in the dark at -19 °C. The purity and concentration of samples were routinely checked by UV-vis spectroscopy in ether solutions. All other chemicals were of analytical grade and were used received without any further purification. The chlorophyll solutions were prepared with acetone (≥99.8%) and diethyl ether (≥99.8%) purchased from Sigma-Aldrich. All solutions for electrochemical measurements were prepared with deionised water at a resistivity of 18.2 MΩ cm at 298K (Millipore, MA, USA). The phosphate-buffered saline (PBS, 0.1 M, pH=7.4) was prepared using sodium chloride (137 mM, ≥99.5%), potassium chloride (2.7 mM, ≥99.0%), sodium phosphate dibasic (10 mM, ≥99.0%), and potassium phosphate monobasic (1.8 mM, ≥99.0%), purchased from Sigma-Aldrich.

5.2.2 Apparatus

UV-vis spectroscopy was conducted using a Shimadzu spectrometer UV-1800 and quartz cells with a 10 mm optical path. The absorbance was recorded from 800– 300 nm and a baseline correction was conducted prior to all measurements.

All electrochemical experiments were conducted with a standard three-electrode system in a Faraday cage at 298K. The cyclic voltammetric measurements were performed using a μAutolab II potentiostat (Metrohm-Autolab BV, Netherlands). Semi-circular potential wave sweep voltammetry was carried out with a computer-controlled in-lab built potentiostat ensuring the low-noise measurements with signal sampled at a stream rate of 100 kHz[6, 32]. The potentiostat was controlled by the script written in Python 3.5 to generate the required potential waveform. For the voltammetric measurements, a glassy carbon (GC) macroelectrode (diameter calibrated as 2.99 mm) was used as the

working electrode, a saturated calomel electrode (SCE, ALS distributed by BASi Inc., Japan.) as the reference electrode and a graphite rod as the counter electrode. The GC electrode was polished onto the soft lapping pads (Buehler, UK) with alumina (particles size of 1.0 and 0.3 μm, Buehler, IL, UK) before each voltammetric experiment, followed by sonication in water and drying with nitrogen.

5.2.3 Analytical Procedures

The purities of the Chl a and Chl b fractions obtained from column chromatography were first examined in ether solutions using UV-vis spectroscopy. The spectral absorption properties (adsorption peak shapes, adsorption maxima and band ratios) shown on the UV-vis spectra of Chl a and Chl b were compared with the values reported in the literature. Chl a and Chl b were next resolubilised in acetone and prepared as stocking solutions (370 μM). The concentrations of Chl a and Chl b solutions in acetone were determined using UV-vis spectroscopy. The stock solutions were then diluted to the concentrations of 1.45–111 μM as standard working solutions.

All experiments were conducted under dim light and the solutions were bubbled with N_2 for 10 minutes to remove dissolved oxygen before each measurement. The chlorophyll standard mixture solutions are prepared by adding increasing concentrations of Chl a or Chl b from 9.24–64.6 μM to a 1:1 mixture containing 46.2 μM Chl a and Chl b. For cyclic voltammetric and semi-circular potential sweep voltammetric experiments using the standard solutions, the GC electrode was immersed in the Chl a and/or Chl b acetone solutions for one minute to allow the adsorption of chlorophyll onto the electrode surface.

The electrode was then gently rinsed with deionised water and transferred to the blank degassed PBS solution at pH 7.4 for voltammetric measurements.

For real sample analysis, the yielded crude product from the extraction of spinach without column chromatographic purification was diluted with acetone until the voltammetric responses fell within the linear detection range (dilution factor =50) and used for the initial cyclic voltammetric and semi-circular voltammetric tests. The same electrode preparation procedure was used as above. The Chl a standard solutions in the concentration range of 23.1–80.9 μM were then added to the crude for quantification in real samples using semi-circular potential sweep voltammetry.

5.3 Results and Discussion

In the following sections, first, the purities and the concentrations of chlorophyll a (Chl a) and chlorophyll b (Chl b) samples are examined using UV-vis spectroscopy. Next, the electrochemical behaviour of Chl a and Chl b separately adsorbed on a GC electrode are studied and compared using CV. Further, semi-circular potential sweep voltammetry is employed for selective detection of Chl a and Chl b in a 1:1 mixture of them, as well as compared to the conventional CV method. The potential window is optimised to give the best resolution of chlorophyll peaks in mixture detection and used for the standard additions analysis of Chl a and Chl b. Finally, standard additions of Chl a to a real sample of spinach is conducted to validate the method for possible application in food quality control.

5.3.1 UV-vis Spectroscopic Examinations of Chlorophylls

The UV-vis spectra of Chl a and Chl b obtained from column chromatography in ether solution are shown in Figure 5.1. The determined spectral properties including absorption maxima λ_{max} red, λ_{max} blue, and the measured absorbance (abs.) ratio of blue/red are listed in Table 5.1 and were found in good agreement with the values reported by Strain *et al.*[33] and Zscheile *et al.*[34]. The concentrations of tested Chl a and Chl b solutions were calculated using the measured absorbance and the reported molar coefficients at λ_{max} red[33] according to the Beer-Lambert law:

$$A = \varepsilon cL \tag{5.3}$$

where A is the measured absorbance (in Absorbance Units (AU)), L the path length (1 cm), ε is the molar extinction coefficient of Chl a or Chl b and c the concentration of Chl a or Chl b.

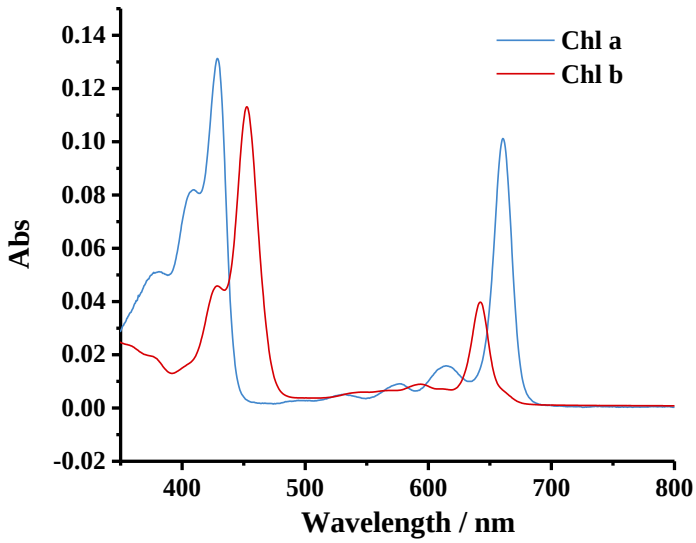


Figure 5.1. UV-vis spectra of Chl a and Chl b recorded in diethyl ether.

Table 5.1. Spectral properties of Chl a and Chl b obtained from Figure 5.1, recorded in diethyl ether at 25 °C

Properties	Chl a	Chl b
λ_{max} , red / nm	660.5	642.5
λ_{max}, blue / nm	428.5	452.5
Ratio abs., blue / red	1.30	2.84

5.3.2 Electrochemical Behaviours of the Two Chlorophylls

5.3.2.1 Effect of Voltage Scan Rate

The voltammetric behaviour of Chl a and Chl b separately on a GC electrode were first investigated using conventional cyclic voltammetry. The GC electrode was immersed in 23.1 μM of Chl a or 11.6 μM of Chl b solutions for one minute before being transferred to a degassed PBS solution. Cyclic voltammetric responses of Chl a and Chl b were recorded at a scan rate of 100 mV s^{-1}, showing an irreversible oxidation peak at +0.54V

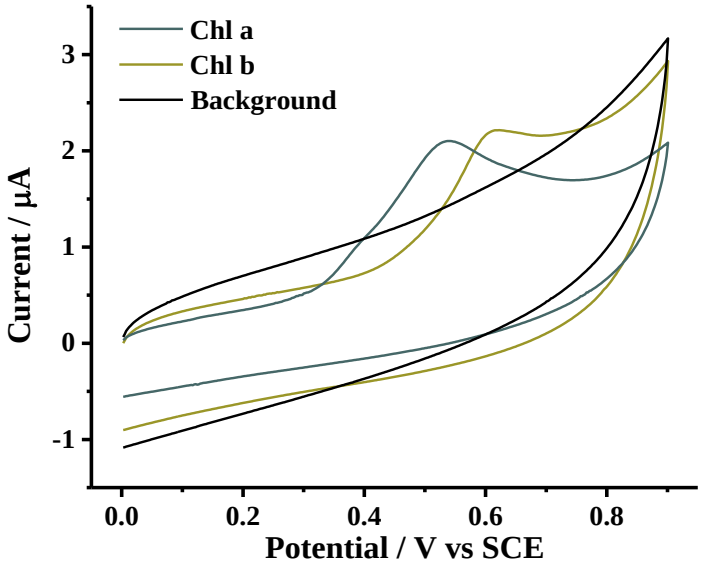


Figure 5.2. Cyclic voltammetric responses of background, 23.1 μM Chl a and Chl b at GC electrode measured in PBS under degassed condition. Scan rate was 100 mVs^{-1}.

vs. SCE for Chl a and another irreversible oxidation peak at +0.62 V vs. SCE for Chl b in the chosen potential window. As can be seen in Figure 5.2, the voltammograms of the two chlorophylls appeared to be closely similar at GC electrode, except that the oxidation of Chl b is shifted to a slightly more positive potential, which reflects the change of a – CH_3 substituent group (Chl a) to an electron-withdrawing group –CHO (Chl b) reducing the electron density of chlorophyll π-conjugated system[12, 35].

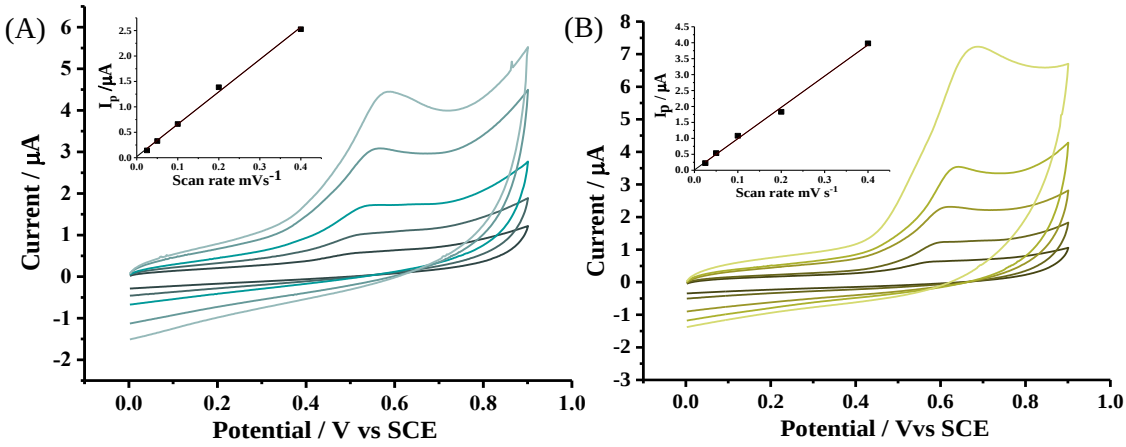


Figure 5.3. Cyclic voltammetric responses of (A) 11.6 µM Chl a oxidation and (B) 23.1 µM Chl b at GC electrode in PBS at varying scan rates of 25 mvs^{-1}, 50 mvs^{-1}, 100 mvs^{-1}, 150 mvs^{-1}, 200 mvs^{-1}, 400 mvs^{-1}, under degassed condition. Inset: plot of peak current versus scan rate.

To confirm the adsorption of Chl a and Chl b onto GC electrode surface, the effects of scan rate on the oxidation peak currents were studied. Figure 5.3 (A) and (B) depicts the cyclic voltammograms of Chl a and Chl b recorded at the scan rates in the range of 25 to 400 mVs^{-1}. Linear relationships between peak currents and scan rates were found for both compounds from 25 to 400 mVs^{-1} (Insets of Figure 5.3 (A) and 2(B)), suggesting the observed oxidations of Chl a and Chl b are both surface bound processes.

5.3.2.2 Adsorption on GC Electrode

Having identified the chlorophyll electrochemistry as from surface-confined species, the adsorption of the chlorophylls on GC electrode surface was next investigated. First,

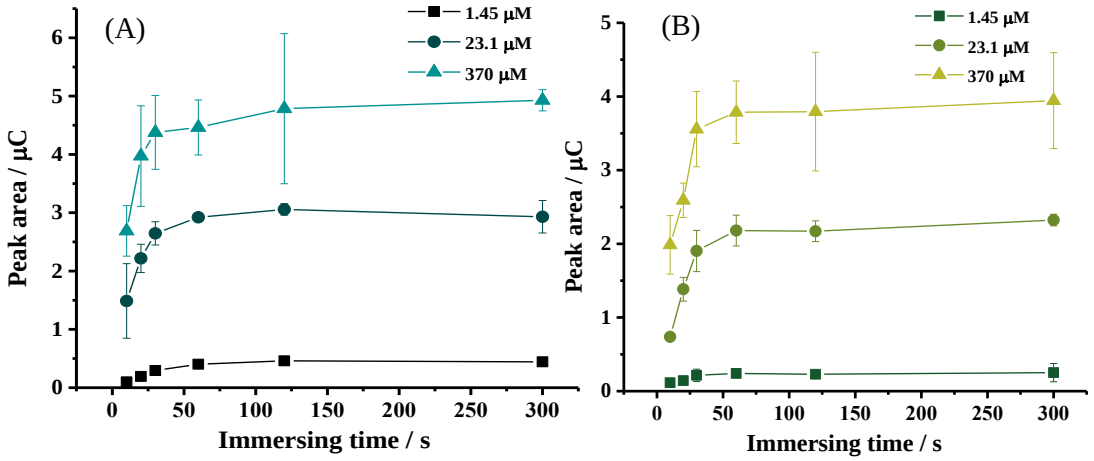


Figure 5.4. The plots of peak areas vs. immersing times of 1.45, 23.1, 370 µM (A) Chl a and (B) Chl b obtained from cyclic voltammetric responses at GC electrode in PBS at a scan rates of 100 mvs^{-1}.

three concentrations (1.45, 23.1, and 370 µM) of Chl a and Chl b solutions were chosen to study the effect of immersing time on chlorophyll adsorption on GC electrode using cyclic voltammetry. The oxidative peak areas were depicted as the function of immersing times in Figure 5.4 (A) and (B). It can be seen for both species, the peak areas increased slowly after 30 s and started reaching a plateau after ca. 1 min at all of the three concentrations. Therefore, an accumulation time of 1 min was used in further voltammetric tests in the concentration range of 1.45–370 µM for sensitive and reproducible detection of the chlorophylls.

The cyclic voltammetric responses of Chl a in the concentration range of 1.45–370 µM, at a scan rate of 100 mVs^{-1} were recorded in Figure 5.5 (A), which was analysed with Langmuir isotherm according to the following equation:

$$\theta = \frac{K[C]}{1 + K[C]} \tag{5.4}$$

where θ is the fractional occupancy of the adsorption sites, K is the equilibrium constant for adsorption and *[C]* is the concentration of Chl a. Eq. (4) can be rewritten as:

$$\frac{1}{Q}=\left(\frac{1}{KQ_{\max}}\right)\left(\frac{1}{[C]}\right)+\frac{1}{Q_{\max}} \tag{5.5}$$

where Q is the voltammetrically measured charge transferred during oxidation of the species at the studied concentrations and Q_{max} is maximum charge transfer at saturation of the surface with Chl a. The Langmuir plot shown in Figure 5.5 (B) exhibits a linearity ($1/Q$ (μC^{-1}) = (3.290±0.119) $1/C$ (μM^{-1}) + (0.237 ± 0.0378), R^2=0.996), suggesting the Chl a adsorption is well-described by the Langmuir isotherm. The equilibrium constant K and maximum charge transfer Q_{max} were calculated to be 0.072 $\mu M^{-1}$and 4.2 μC, respectively.

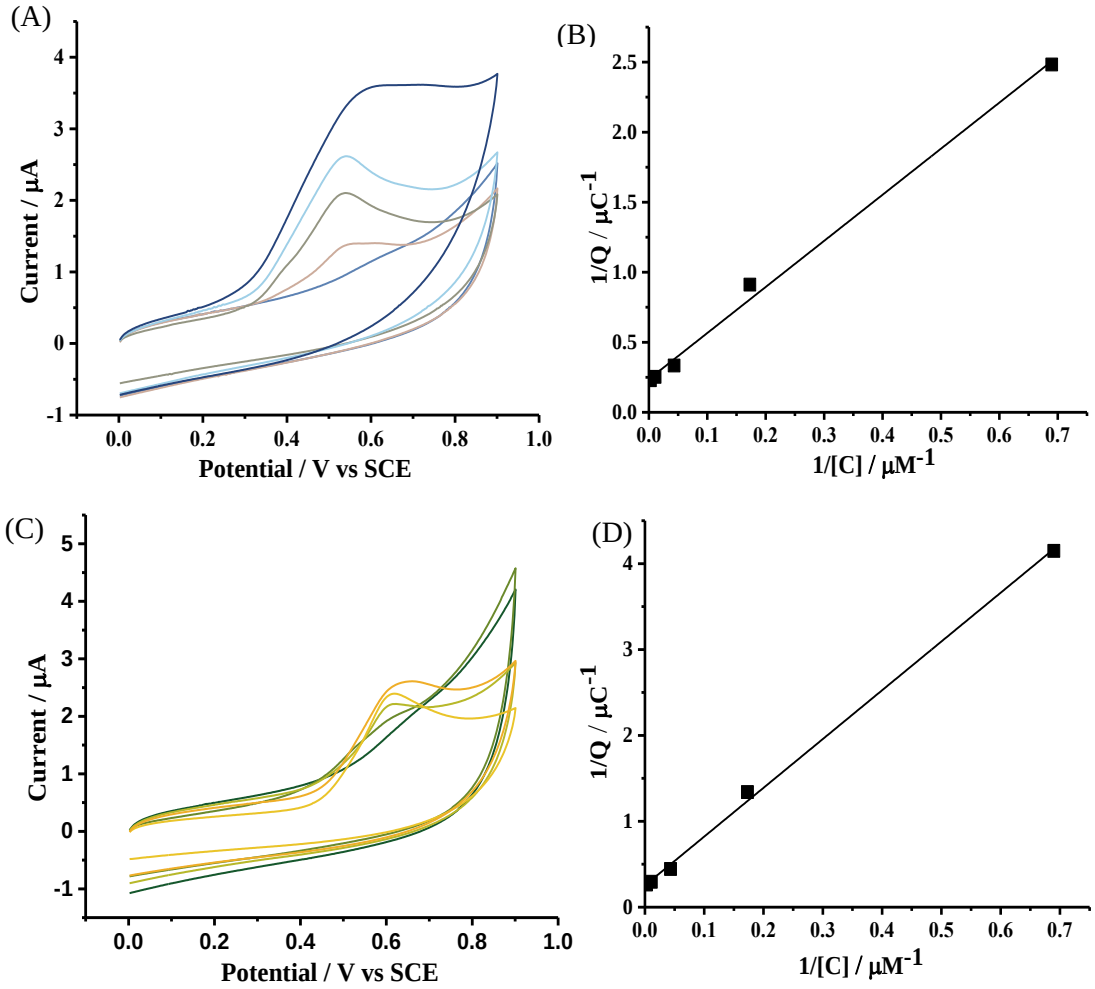
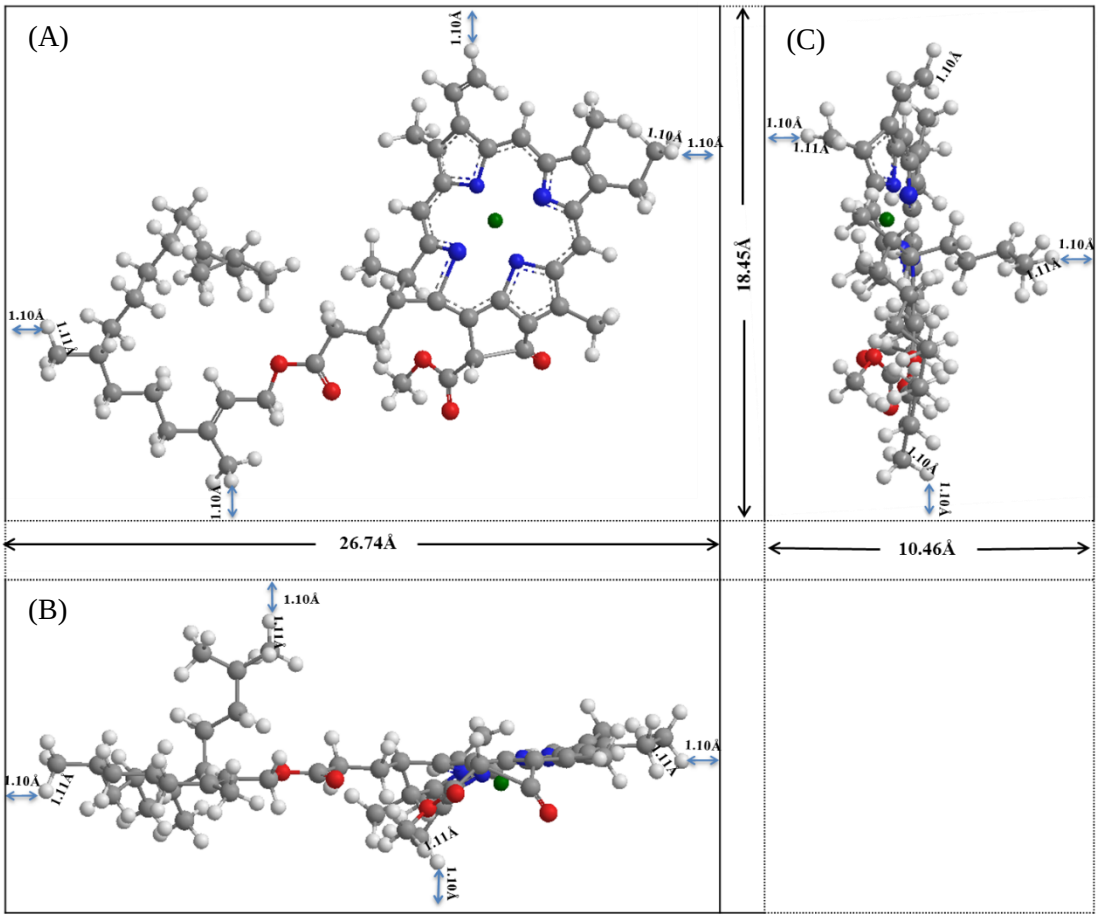


Figure 5.5. Cyclic voltammetric responses of increasing concentrations from 1.45-370 μM of (A) Chl a and (C) Chl b at GC electrode in PBS. Langmuir plot of (B)1.45-370 μM Chl a using peak area obtained from (A) and (D) 1.45-370 μM Chl b using peak area obtained from (B).

In order to estimate the approximate area of a Chl a molecule adsorbed on GC, the theoretical areas of the molecule in all three possible flat molecular orientations were calculated using the rectangular box model presented in Scheme 5.2. All side lengths were estimated by trigonometry for bond lengths, bond angles and van der Waals radii of the terminating atoms. The bond length, bond angles data were obtained from ChemDraw 16.0 software and the van der Waals radii of the terminating atoms values are those tabulated by Rowland [36]. This method has been reported in several previous studies for other organic molecules [37]; [38]. Scheme 1 shows the flat view (A), edgewise view (B) and endwise view (C) of Chl a adsorption on GC electrode and the corresponding areas A_{fl}, A_{ed}, A_{en} can be estimated as 4.93, 2.80, 1.93 × 10^{-14} cm^2. The number of molecules adsorbed on the electrode surface (N_{ads}) can be calculated using $N_{ads} = A_{electrode} / A_{chl\text{-}a}$,



Scheme 5.2. Rectangular box model of Chl a molecule for (A) flat view, (B) edgewise view and (C) endwise view

where $A_{electrode}$ is the electroactive surface area and $A_{chl\text{-}a}$ corresponds to A_{fl}, A_{ed} or A_{en}. However, the electroactive surface area can deviate substantially from the geometric area of electrode and greatly depends on the surface roughness factor, which is reported as ranging from 1.7 to 4.1 for the GC electrode[39]. Thus $A_{eletrode}$ can be estimated as 0.12–0.29 cm^2 and the maximum charge transfer Q_{max} for three possible molecular orientations can be calculated using N_{ads} and electron fundamental charge e (1.602×10^{-19} C) by $Q_{max} = N_{ads} \times e$. Assuming close-packed, monolayer adsorption and a two electron transfer process, the maximum charge transfer for three molecular orientations Q_{fl}, Q_{ed} and Q_{en} were calculated to lay in the ranges of 0.78–1.9 μC, 1.4–3.3 μC, 2.0–4.8 μC, respectively. Since the experimental Q_{max} values obtained from Figure 2(D) fall into the range of Q_{en}, it can be inferred that the Chl a adsorption follows the orientation of the endwise views (Scheme 5.2 (C)).

Following the same procedure, voltammetric responses of Chl b at the same concentration range of 1.45–370 μM were shown in Figure 5.5 (C). The double reciprocal plot in Figure 5.5 (D) again shows linearity ($1/Q$ (μC^{-1}) = (5.679±0.120) $1/C$ (μM^{-1}) + (0.254 ± 0.0383), R^2=0.998), as predicted by the Langmuir isotherm, giving the equilibrium constant as 0.045 μM^{-1} and the maximum charge transfer as 3.9 μC. The maximum charge transfers of Chl b and Chl a were found to be very close in values. Since they possess closely similar molecular structures and thus similar surface areas, it can be inferred that the adsorption of Chl b on a GC electrode is similar to that suggested above for Chl a.

5.3.3 Detection of Chlorophyll a and b in Mixtures

5.3.3.1 Selective Detection in Standard Mixture Solutions

Voltammetry with a semi-circular potential wave with an average scan rate of 100 mVs^{-1} (Figure 5.6) was employed for the electrochemical identification and quantification of Chl a and Chl b in the two-component mixture owing to its capacity for distinguishing two species with similar redox potentials[4]. The GC electrode was prepared with the same procedure as above for CV and measured in PBS solution (pH =7.4). The semi-circular potential sweep voltammograms of backgrounds and a 1:1 mixture solution containing 46.2 μM Chl a and Chl b at varying potential windows are shown in Figure 5.7. The influence of the adjustment of potential windows by moving the centre of the sweep relative to the potential of maximum current was discussed in previous work [6, 8]. By approximating the midpoint of potential window E_{centre} (E_{mid}) to the oxidative potential of the studied compounds, maximum peak currents can be obtained. As depicted in Figure 5.7, a set of broad peaks can be observed in the presence of a Chl (a + b) mixture, as well as an additional very sharp peak near E_{centre}, where the infinite temporary scan rate is

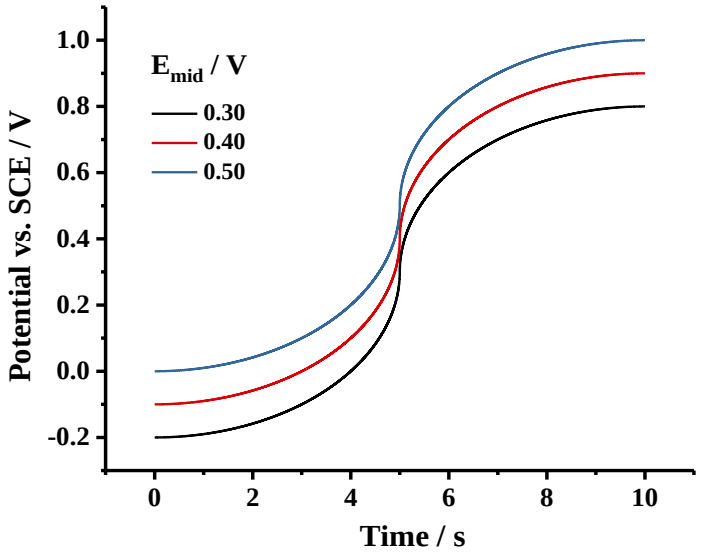


Figure 5.6. Semi-circular potential waveforms applied for varying E_{centre}.

generated. With the shift of potential windows towards the more positive E_{centre}, both of

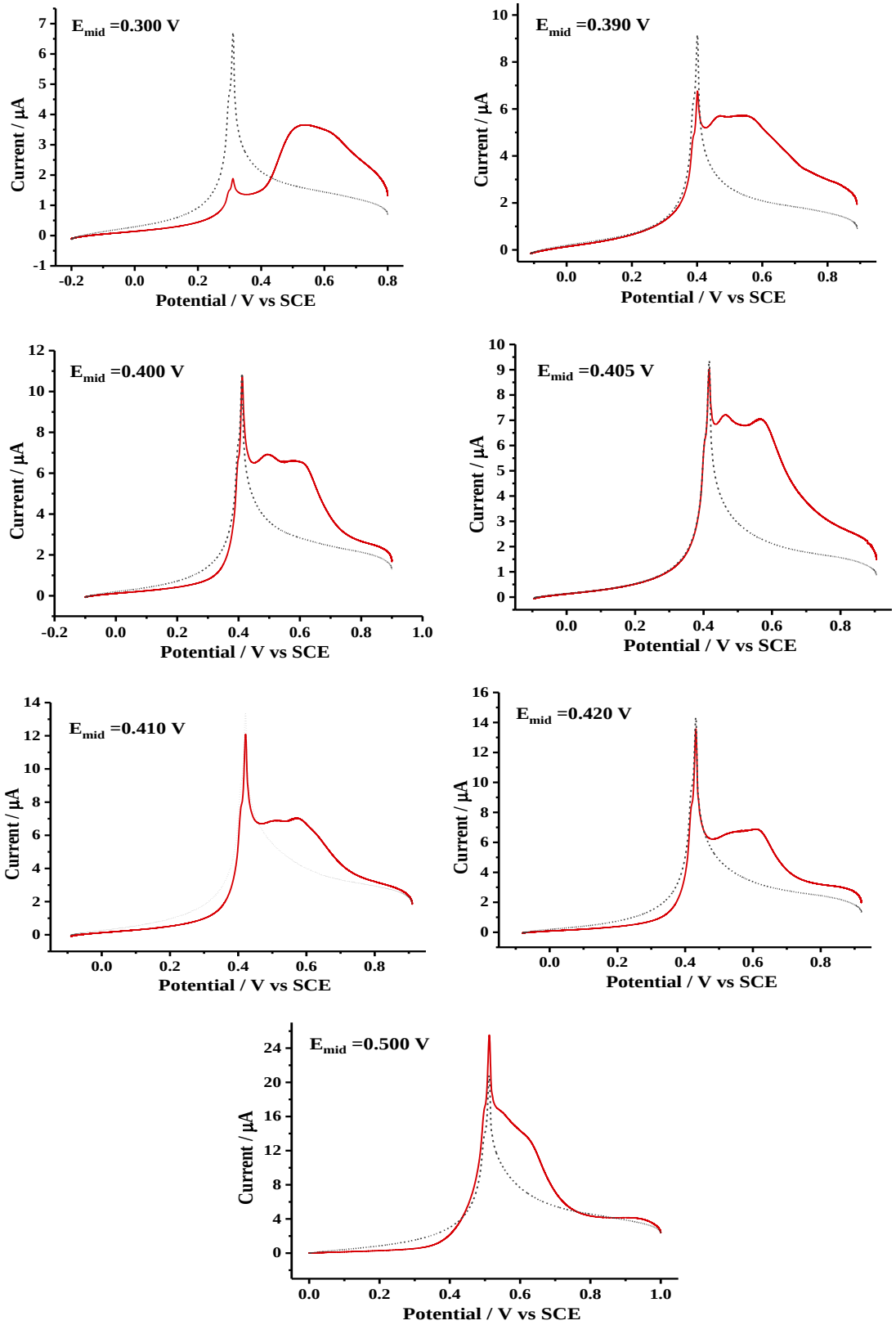


Figure 5.7. Voltammetric responses of 0 and 46.2 µM of 1:1 Chl a: Chl b mixture solutions at varying potential windows. The average of scan rate was 100 mVs^{-1}. The scan amplitude was 0.5 V.

the broad peaks increase in amplitude, while the second peak grows more rapidly and the resolution of two broad peaks in voltammograms improves with increasing peak separations until E_{centre} reached +0.405 V, two distinct peaks can be seen at +0.46 V and +0.57 V. From E_{centre} = 0.410V, two peaks began to decrease in resolution and finally merged with the sharp peak at E_{centre} = +0.500 V. As for the sharp peak, it continually grew with the increase of positive potentials, suggesting the possible contributions from the capacitive current.

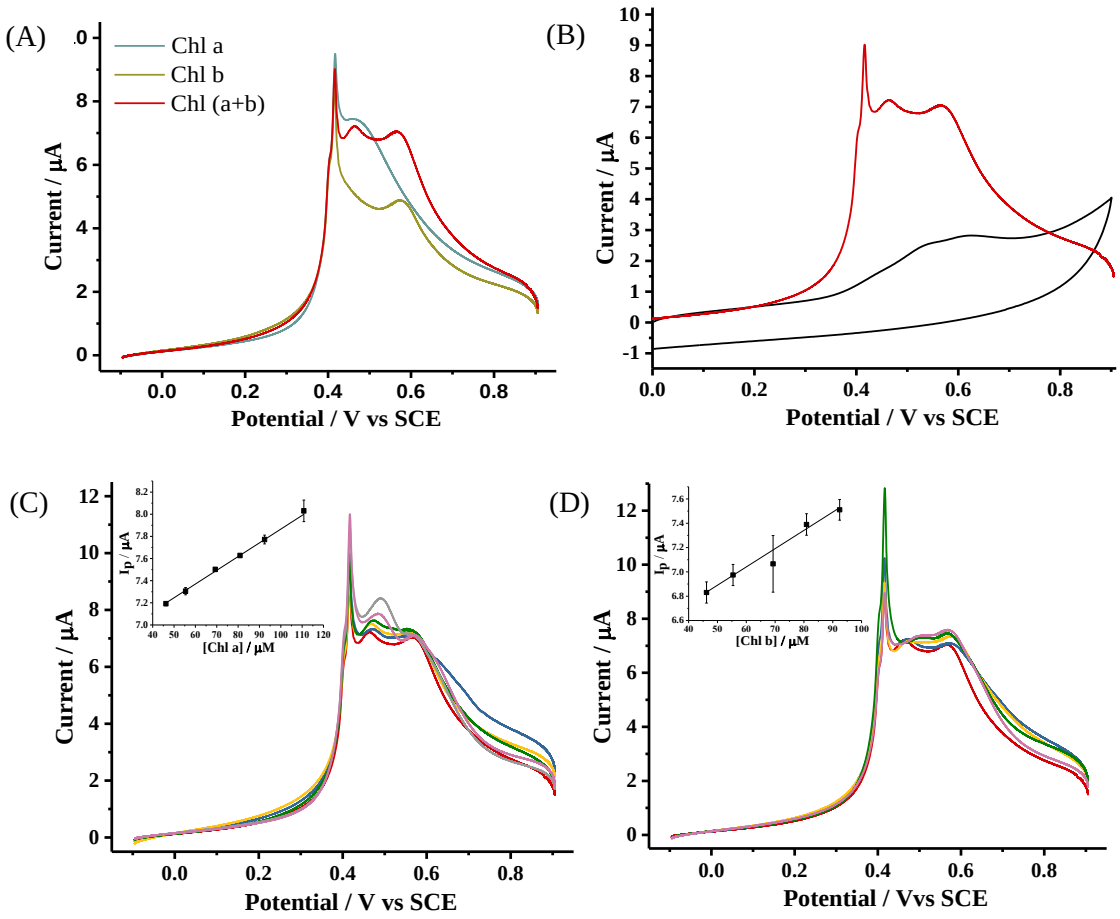


Figure 5.8. Semi-circular potential sweep voltammetric responses recorded at the potential window with E_{centre} = +0.405 V of (A) 46.2 µM of Chl a, Chl b and their 1:1 mixture; (B) 46.2 µM 1:1 Chl a: Chl b mixture (red line) in comparison to cyclic voltammogram (black line); standard additions of (C) 0-64.6 µM of Chl a and (D) 0-46.2 µM of Chl b to a 46.2 µM 1:1 Chl a: Chl b mixture solution. The insets of (C): Plot of currents read at +0.47 V increase with Chl a concentration in the range of 46.2-110.8 µM; (D): Plot of currents read at +0.57 V increase with Chl b concentration in the range of 46.2-92.4 µM. The average scan rate was 100 mVs^{-1}.

The semi-circular potential sweep voltammetric responses of both Chl a and Chl b were recorded separately in the potential window of E_{centre} = +0.405 V and compared with the mixture voltammogram (Figure 5.8 (A)). The two peaks present in the mixture voltammogram were found at similar peak positions in the case of the isolate components, thus they can be identified as successfully recorded Chl a and Chl b peaks. The recorded semi-circular voltammograms with a potential window applied at E_{centre} = +0.405 V showed excellent repeatability in the detection of mixtures, giving stable oxidation signals of Chl a and Chl b that can be measured for both singular components and mixtures with peak potential within a few millivolts.

Figure 5.8 (B) compares the conventional cyclic voltammetric responses with the semi-circular voltammetric responses at the same average scan rate (100 mVs^{-1}) under the optimised potential window. It can be seen that using the semi-circular potential wave, the peak currents gained significant amplification in the region near E_{centre} with the large, transient scan rates changing within the sweep, making the Chl a and Chl b peaks clearly distinguishable within the 1:1 mixture. In stark contrast, the cyclic voltammogram shows no clear separation of the peaks due to the closeness of the oxidation potentials of two species. Thus the semi-circular voltammetry was seen to be more advantageous for the selective detection in mixtures. It was used for further quantifications of chlorophyll mixtures at the optimised potential window with E_{centre} = +0.405 V, as next discussed.

The validated method was applied first for the detection of standard mixture solutions containing varying concentrations of Chl a and Chl b. The solutions were prepared by standard addition of Chl a or Chl b solutions to an initial 1:1 mixture containing a total of 46.2 μM Chl (a + b) and adsorbed on the GC electrode using the procedure reported above, the voltammetry was then measured in PBS solution (pH =7.4). Three scans were

conducted for each Chl a or Chl b concentration and the electrode was polished prior to each scan. The semi-circular potential sweep voltammetric responses were recorded as a function of the concentrations of Chl a (Figure 5.8 (C)) and Chl b (Figure 5.8 (D)). The currents resulting from Chl a standard addition were measured at a fixed potential of +0.47 V and found to exhibit a linear relationship in the concentration range of 46.2–111μM (Figure 5.8 (C) inset, $I_p/\mu A = (1.24 \times 10^{-2} \pm 3.12 \times 10^{-4})$ [Chl a] (μM) + $(6.63 \pm 2.43 \times 10^{-2})$ (μA), N=6, R^2=0.997)). Linear behaviour was also obtained for currents recorded at the fixed potential of +0.57 V for the analysis of Chl b standard addition. In the range of 46.2–92.4μM, $I_p/\mu A = (1.50 \times 10^{-2} \pm 8.88 \times 10^{-4})$ [Chl b] (μM) + $(6.14 \pm 6.33 \times 10^{-2})$ (μA), N=5, R^2=0.990 (Figure 5.8 (D) inset). It can be seen that the currents read at the chosen potentials near Chl a and Chl b peaks increase linearly with the standard additions of each component. Good reproducibility was obtained between separate experiments and sequential voltammetric measurements (see error bars in Figures 5.8 and 5.9), allowing analysis of the mixture and suggesting semi-circular potential sweep voltammetry is a useful analytical technique in selective detection and quantification of individual species within a mixture of them.

5.3.3.2 Detection in Real Samples

In order to access the full applicability of the developed method for mixture detection, chlorophyll determination in a real sample was next investigated. As is general for common green plants, the spinach crude product obtained from the mentioned extraction procedure (Section 5.2.1) without purifying by column chromatography contains several pigment components including carotenoids (carotenes and xanthophylls), chlorophylls (Chl a and Chl b) and pheophytins (pheophytin a and b). Nonetheless, Chl a is the most abundant pigment consisting of ca. 58%–75% of the total pigments in spinach[40, 41].

Therefore, we sought to detect the Chl a content selectively in the mixture of crude extract as a measure for spinach quality control. Cyclic voltammetry and semi-circular voltammetry were first performed for the diluted spinach extract at the average scan rate of 100 mVs^{-1} using the potential window with the optimised E_{centre} value of +0.405 V. From Figure 5.9 (A), two main peaks arising from the analyte can be observed in semi-circular voltammogram, which merged as one broad peak in cyclic voltammogram, again suggesting that the semi-circular voltammetry can provide improved resolution and accuracy in mixture detection.

To identify the Chl a peak in extract voltammogram and quantify the Chl a contents in spinach, the extract sample was next 'spiked' with Chl a standard solutions. The semi-circular potential sweep voltammetric responses of the spiked solutions with the addition of Chl a in the concentration range of 23.1–80.9 µM was depicted in Figure 5.9 (B). A linear relationship was established between currents read at +0.49 V and the concentration of Chl a: $I_p/\mu A = (2.24 \times 10^{-2} \pm 1.30 \times 10^{-3})$ [Chl a] (µM) + (7.93±7.12× 10^{-2}) (µA), N=6, R^2=0.987) (Figure 5.9 (B) Inset). The Chl a concentration in the spinach

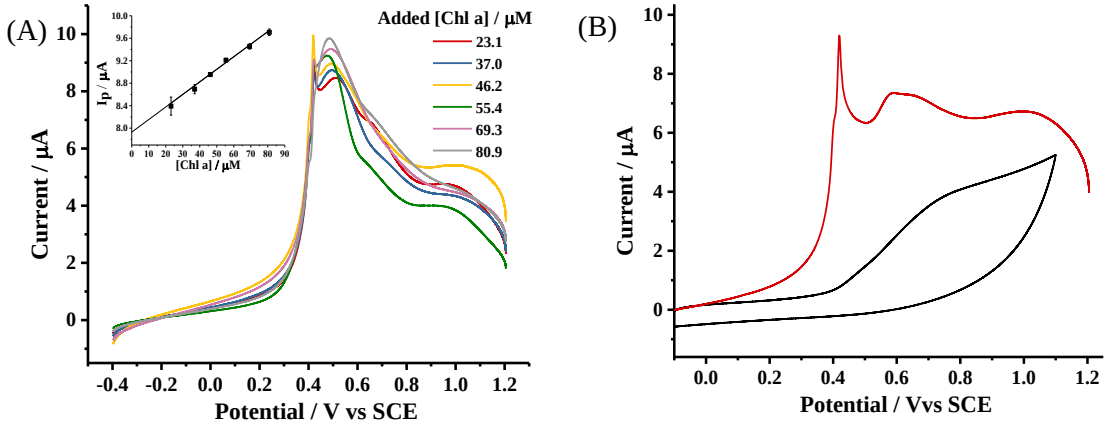


Figure 5.9. Semi-circular potential sweep voltammetry for the real sample: Semi-circular potential sweep voltammetric responses at the potential window with E_{centre} = +0.405 V of (A) the real sample extracted from spinach in comparison to cyclic voltammogram (black line). (B) standard additions of 23.1-80.9 µM of Chl a solutions to the real sample extracted from spinach at the potential window with E_{centre} = +0.405 V. Inset of (B): Plot of currents read at +0.49 V increase with Chl a concentration in the range of 23.1-80.9 µM The average scan rate was 100 mVs^{-1}.

extract can be determined as ca. 105 μM from the intercept of Figure 5.9 (B) inset combined with the linear expression in Inset of Figure 5.8 (C). This can be converted into the Chl a content in fresh, raw spinach as ca. 235 mg / kg and can be estimated as ca. 188–259 mg / kg dry matter using the spinach moisture content of 89%–92% [42, 43], consistent with the Chl a fraction weighed after column chromatography and the Chl a contents reported in the literature using HPLC method [44].

5.4 Conclusions

We have studied the electrochemical process of two chlorophyll species, Chl a and Chl b on a GC electrode based on their cyclic voltammograms and introduced a novel method for the selective detection of the individual species in the mixtures of them, using the semi-circular potential sweep voltammetry. The conventional cyclic voltammetric study revealed the close similarity between the voltammograms of Chl a and Chl b, in particular, the similar peak potentials, yet failed to distinguish them with good resolution when they were

present in a mixture. The semi-circular potential wave employing the potential window with the optimised E_{centre} can selectively detect the mixtures of Chl a and Chl b in the concentration range of 46.2–111 μM and 46.2–92.4 μM, respectively, complementing the conventional method in electroanalysis. The developed method was also successfully applied for analysing the real sample ‘spiked’ with Chl a, suggesting the potential use of semi-circular potential sweep voltammetry for the electroanalytical detection of mixtures consisting of more than one electrochemically active species with closely similar peak

potentials, as the results of a simpler extraction / purification process suitable for practical use.

Bibliography

1. A. J. Bard, L. R. Faulkner, C. G. Zoski and J. Leddy, *Electrochemical methods : fundamentals and applications*, Wiley, New York ; Chichester, 2nd edn., 2001.
2. R. G. Compton and C. E. Banks, *Understanding voltammetry*, World Scientific Publishing Europe, London, 3rd edn., 2018.
3. Y. Uchida, E. Katelhon and R. G. Compton, *Journal of Electroanalytical Chemistry*, 2018, **823**, 465-473.
4. Y. Uchida, E. Katelhon and R. G. Compton, *Journal of Electroanalytical Chemistry*, 2018, **818**, 140-148.
5. Y. Uchida, E. Katelhon and R. G. Compton, *Journal of Electroanalytical Chemistry*, 2019, **835**, 60-66.
6. H. M. A. Amin, Y. Uchida, E. Katelhon and R. G. Compton, *Journal of Electroanalytical Chemistry*, 2019, **836**, 62-67.
7. Y. Uchida, E. Kätelhön and R. Compton, *Journal of Electroanalytical Chemistry*, 2019, **848**, 113290.
8. Y. Wang, L. Chen, K. Chaisiwamongkhol and R. G. Compton, *Food Chemistry*, 2019, **309**, 125606.
9. M. Kobayashi, S. Ohashi, K. Iwamoto, Y. Shiraiwa, Y. Kato and T. Watanabe, *Biochimica et Biophysica Acta-Bioenergetics*, 2007, **1767**, 596-602.
10. Y. Nonomura, S. Igarashi, N. Yoshioka and H. Inoue, *Chemical Physics*, 1997, **220**, 155-166.
11. J. C. Goedheer, G. H. H. Dehaas and P. Schuller, *Biochimica et Biophysica Acta*, 1958, **28**, 278-283.
12. H. Scheer, *Chlorophylls*, CRC Press, Boca Raton, Florida, 1991.
13. E. Choe and D. B. Min, *Comprehensive Reviews in Food Science and Food Safety*, 2006, **5**, 169-186.
14. J. Zhang, W. Han, L. Huang, Z. Zhang, Y. Ma and Y. Hu, *Sensors (Basel)*, 2016, **16**, 437.
15. B. Schoefs, *TrAC Trends in Analytical Chemistry*, 2003, **22**, 335-339.
16. J. N. Boyer, C. R. Kelble, P. B. Ortner and D. T. Rudnick, *Ecological Indicators*, 2009, **9**, S56-S67.
17. T. Cecchi, P. Passamonti and P. Cecchi, *Food Chemistry*, 2010, **120**, 730-735.
18. S. F. Silva, C. A. R. Anjos, R. N. Cavalcanti and R. M. D. Celeghini, *Food Chemistry*, 2015, **179**, 35-43.
19. D. Trypidis, D. L. Garcia-Gonzalez, A. Lobo-Prieto, N. Nenadis, M. Z. Tsimidou and N. Tena, *Food Chemistry*, 2019, **295**, 94-100.
20. L. Conte, A. Milani, S. Calligaris, P. Rovellini, P. Lucci and M. C. Nicoli, *Foods*, 2020, **9**.

21. E. Ergun, B. Demirata, G. Gumus and R. Apak, *Analytical and Bioanalytical Chemistry*, 2004, **379**, 803-811.
22. L. P. Vernon and G. R. Seely, *The chlorophylls*, Academic Press, New York, 1966.
23. K. Maxwell and G. N. Johnson, *Journal of Experimental Botany*, 2000, **51**, 659-668.
24. L. A. Khanova and M. R. Tarasevich, *Journal of Electroanalytical Chemistry*, 1987, **227**, 99-114.
25. A. Agostiano, P. Cosma and M. Dellamonica, *Bioelectrochemistry and Bioenergetics*, 1990, **23**, 311-324.
26. E. P. Suponeva, A. A. Kazakova and B. A. Kisselev, *Bioelectrochemistry and Bioenergetics*, 1989, **22**, 75-81.
27. Y. G. Yang, R. L. Zhou, Y. Y. Han and Y. S. Jiang, *Journal of Electroanalytical Chemistry*, 1994, **370**, 269-271.
28. R. M. Pemberton, A. Amine and J. P. Hart, *Analytical Letters*, 2004, **37**, 1625-1643.
29. I. Novak and S. Komorsky-Lovric, *Electroanalysis*, 2012, **24**, 1957-1965.
30. E. P. Suponeva, S. Hotchandani, C. Arbour and B. A. Kisselev, *Biologicheskie Membrany*, 1996, **13**, 229-235.
31. K. Iriyama and M. Shiraki, *Journal of Liquid Chromatography*, 1979, **2**, 255-276.
32. C. Batchelor-McAuley, J. Ellison, K. Tschulik, P. L. Hurst, R. Boldt and R. G. Compton, *Analyst*, 2015, **140**, 5048-5054.
33. H. H. Strain, M. R. Thomas and J. J. Katz, *Biochimica Et Biophysica Acta*, 1963, **75**, 306-311.
34. F. P. Zscheile and C. L. Comar, *Bot. Gaz.*, 1941 **102**, 463-481.
35. J. E. Falk and K. M. Smith, *Porphyrins and metalloporphyrins*, Elsevier, Amsterdam, 1975.
36. S. S. Batsanov, *Inorganic Materials*, 2001, **37**, 871-885.
37. L. F. Chen, E. E. L. Tanner, C. H. Lin and R. G. Compton, *Chemical Science*, 2018, **9**, 152-159.
38. L. F. Chen, X. T. Li, E. E. L. Tanner and R. G. Compton, *Chemical Science*, 2017, **8**, 4771-4778.
39. R. W. Murray, *Molecular design of electrode surfaces*, Wiley, New York, 1992.
40. F. Khachik, G. R. Beecher and N. F. Whittaker, *Journal of Agricultural and Food Chemistry*, 1986, **34**, 603-616.
41. U. Kidmose, M. Edelenbos, L. P. Christensen and E. Hegelund, *Journal of Chromatographic Science*, 2005, **43**, 466-472.
42. H. Isleroglu, M. Sakin-Yilmazer, T. Kemerli-Kalbaran, A. Uren and F. Kaymak-Ertekin, *International Journal of Food Properties*, 2017, **20**, 2456-2465.
43. Engineering ToolBox, Water Content in Food and other Products, https://www.engineeringtoolbox.com/water-content-d_131.html, (accessed December 2019)
44. B. Lopez-Ayerra, M. A. Murcia and F. Garcia-Carmona, *Food Chemistry*, 1998, **61**, 113-118.

Chapter 6

An Approach to the Electroanalysis of Electrode Passivating Analytes: The Determination of Phenol

This chapter focuses on demonstrating the use of semi-circular sweep voltammetry (SCV) in the selective detection of a target analyte facilitating by the presence of a second species. In this chapter, an electrode-passivating species – phenol - is electrochemically determined using semi-circular sweep voltammetry (SCV) on a basal plane pyrolytic graphite (BPPG) electrode. The electrode fouling caused by the polymerisation of phenol is prevented at low concentrations by introducing the second species, 4-Amino-2,6-dichlorophenol (PAP) to reduce the polymerisation of phenol in the vicinity of the electrode surface. Semi-circular sweep voltammetry (SCSV) is employed to amplify the analytical signal realising the detection of phenol in the concentration range of 25–800 μM without the problems of electrode fouling see in the absence of PAP.

The work presented in this Chapter 6 has been published as a first author paper in *ChemElectroChem*.

6.1 Introduction

The many attractions of amperometric electro-analysis – sensitivity, low cost, ease of use and sometimes selectivity – are well-rehearsed and in favourable situations, conventional voltammetry[1,2], often enhanced by pulse voltammetry[3] where necessary, can allow the practical measurement of many and diverse analytes ranging from gas sensors for oxygen[4], hydrogen sulphide[5], anaesthetic gases[6], and of carbon monoxide in smoke detectors, to enzyme electrodes most notably for blood glucose[7], to bacteria[8] and to specialist pH measurements[9,10] as is evident from the ever-increasing variety of such electrochemical sensors sold commercially[11-13].

The generic feature of amperometric sensors, namely the creation of a concentration-related Faradaic current, requires sustained oxidation or reduction of the analyte of interest, at least for a sufficient time for a meaningful measurement to be made. Whilst this is clearly possible in the many cases alluded to above given the correct choices of electrode materials, electrode geometries, solvents, and in aqueous systems pH, as well as the potentials applied to the electrode, in other cases the electrolysis induces the passivation of the electrode surface precluding useful analytical measurement. An example of this occurs in the electro-oxidation of phenols where the generated phenoxy radical polymerise onto the electrode surface leading to the rapid passivation of the electrode[14]:

$$PhOH \xrightarrow{-e^-,\ -H^+} PhO^{\cdot} \longrightarrow Polymers$$

The passivation is sufficiently strong and rapid to prevent the electro-analysis of concentrations of phenol above a critical threshold above which meaningful analysis is impossible on the timescale of the sought voltammetric measurement.

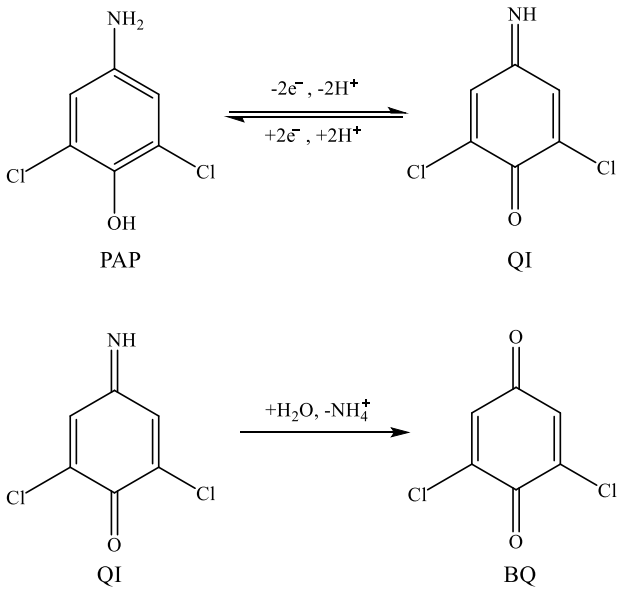
To overcome the electrode fouling problem with phenol, various electrode materials and modifications were suggested in the literature[14-18]. However, the electrode modifications require elaborate and complicated procedures and produce surfaces which often have only a short lifetime sometimes being limited to a single analytical measurement. Use of an unmodified electrode is much more convenient and often gives more repeatable results comparing to using a modified electrode.

In the present paper we develop a likely generic approach to the solution of the electrode passivation problem in the specific context of phenol oxidation at an unmodified carbon electrode in which a second species (Y) is generated electrochemically from an introduced additive, X, and used to diminish the concentration of phenol undergoing direct oxidation at the electrode by virtue of the reaction:

$$X - ne^- \longrightarrow Y$$

$$Y + PhOH \longrightarrow \text{Products}$$

where the products are soluble. In the approach taken this process occurs in parallel with the oxidation of phenol to the extent that the magnitude of the phenol concentration is the



Scheme 6.1. Structures of PAP (X) and its oxidised products, quinone imine (QI) and benzoquinone (BQ).

vicinity of the electrode is reduced below the threshold value required for polymerisation and hence for electrode passivation. In the following we use the two-electron oxidation of 4-Amino-2,6-dichlorophenol (PAP) acting as species X to generate the quinonimine species Y as shown in Scheme 6.1[19-23], noting that the quinonimine undergoes slow hydrolysis on the voltammetric timescale as also shown in Scheme 6.1. The oxidation of PAP occurs at less positive potentials than those required for the oxidation of phenol. Thus, if a voltammetric scan is made two features are apparent; first the oxidation of PAP to Y at low positive potentials and second the analytically useful oxidation of phenol at more positive values. Of course, the 'dilution' of the phenol concentration in the vicinity of the electrode leads to a decrease in the analytical signal in comparison to what might be observed if, hypothetically, the phenol could be directly oxidised without electrode passivation. Hence in order to boost the sensitivity in the experiments reported below, we replace the conventional linear sweep voltammetry (LSV) with the recently advocated 'semi-circular' voltammetry (SCV)[24-26] so as to apply a voltage scan rate which is relatively slow at the potentials required for PAP oxidation but significantly faster in the

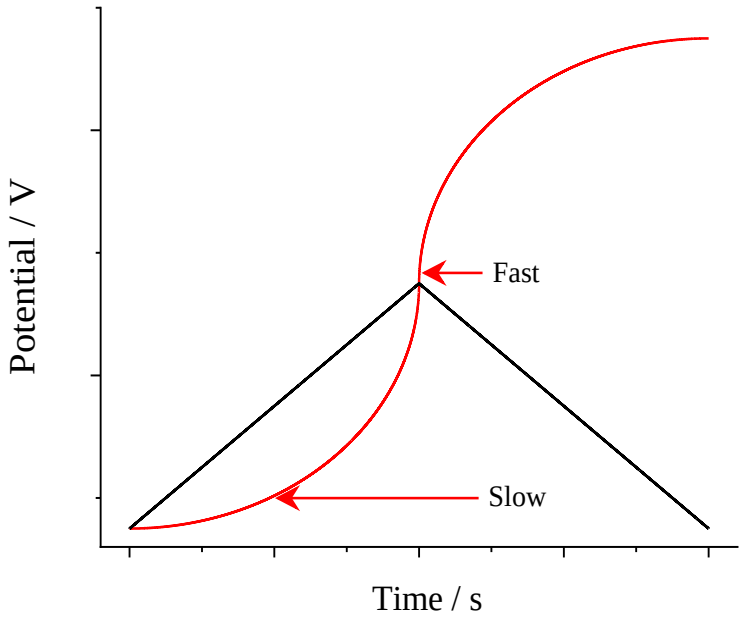


Figure 6.1. Waveforms of cyclic voltammetry (black line) and semi-circular sweep voltammetry (red line) at the same average scan rate.

region of the phenol oxidation (Figure 6.1). As depicted in Figure 6.1, the terms ‘slow’ and ‘fast’ are relative to the average scan rate throughout the semi-circular scan. This has the effect of, first, generating a relatively thicker reaction layer of Y near the electrode for homogeneous chemical reaction with phenol as a result of the initially slower scan. Second, it has the effect of enhancing the size of the peak current for the phenol oxidation and hence also the analytical signal because of the transiently faster scan rate at the potential of analysis. In this way higher concentrations of phenol of up to ca. 800 micro-molar can be analysed quantitatively.

6.2 Experimental

6.2.1 Chemicals and Reagents

All chemicals were of analytical grade and were used received without any further purification. PAP (97%) was purchased from Alfa Aesar and phenol (99.0–100.5%) was purchased from Sigma-Aldrich. All aqueous solutions were prepared with deionised water at a resistivity of 18.2 MΩ cm at 298K (Millipore, MA, USA). The borate buffer solution (0.1M) was used as supporting electrolyte and was prepared using sodium tetraborate (Sigma-Aldrich, 97%) and sodium hydroxide (Sigma-Aldrich, 97%). The borate buffer solution was made at pH = 10.0 and checked with a Hach Lange Sension+ PH31 pH meter. Stock solutions of phenol (10 mM) was prepared by dissolving phenol in ethanol (Sigma-Aldrich, $\geqslant$ 99.8%). The stocked solution was then diluted with aqueous solutions to the required concentrations.

6.2.2 Apparatus

All electrochemical experiments were performed in a Faraday cage at 295K using a three-electrode configuration. Cyclic voltammetric measurements were carried out using a μAutolab II potentiostat (Metrohm-Autolab BV, Netherlands). Semi-circular sweep voltammetric measurements were performed using an in-lab built potentiostat giving low-noise measurements and a high sampling rate of 100 kHz[27]. The in-lab built potentiostat was controlled by software *Python* 3.5 to generate the required potential waveforms. For all experiments, a basal plane pyrolytic graphite (BPPG) with a 4.9 mm diameter was used as the working electrode, a saturated calomel electrode (SCE, ALS distributed by BASi Inc., Japan.) was used as the reference electrode and a platinum wire was used as the counter electrode. The working electrode was polished using soft lapping pads with alumina of decreasing particle sizes (1.0, 0.3 and 0.05 μm) (Buehler, IL, UK), followed by sonication in water. Solutions were bubbled with nitrogen for 10 minutes before each measurement.

6.3 Results and Discussion

In the following sections, first, the voltammetric response of phenol in a pH 10 borate buffer solution at a BPPG electrode is examined and the electrode fouling problem was identified. Next, the electrochemical behaviour of PAP is reported followed by that of phenol in the presence of PAP and a possible mechanism is inferred with respect to the crucial role of PAP in protecting the electrode surface which facilitates phenol electro-analysis. Further, in the system with PAP present, semi-circular sweep voltammetry

(SCV) is employed to realise a sensitive electroanalytical detection of phenol under an optimised potential window. Finally, the analytical method was optimised.

6.3.1 Electrochemistry of Phenol

We first examined the initial voltammetric response of phenol in a pH 10 borate buffer solution at a BPPG electrode. Figure 6.2 depicts the cyclic voltammograms of 1mM phenol in the pH 10 borate buffer solution recorded at a scan rate of 50 mVs^{-1}. An electrochemical oxidation peak is seen at ca. +0.50 V vs. SCE and was found to decrease significantly over multiple scans. The apparent oxidative transfer coefficient (β)[28] was determined to be 0.85 using Tafel analysis of the first scan (Figure 6.3), which suggests the near reversible behaviour was observed for phenol at the applied scan rate. Hence, the total number of electrons transferred corresponding to phenol oxidation was estimated in two different ways using a diffusion coefficient in aqueous solution, reported as 9.2×10^{-10} m^2 s^{-1} at 295K in literature[29], namely *via* both the irreversible and reversible, multiple electron-transfer *Randles-Sevcik* equations[2] as 2.3 or 2.2, respectively. The observed features can be interpreted as a multi-step process, including the de-protonation,

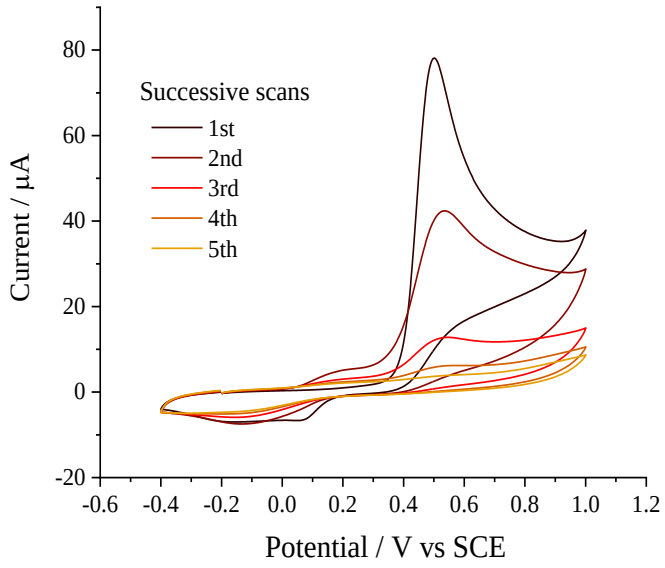


Figure 6.2. Cyclic voltammograms of successive scans of 1mM phenol in a pH 10 borate buffer solution at a BPPG electrode. The scan rate was 50 mVs^{-1}.

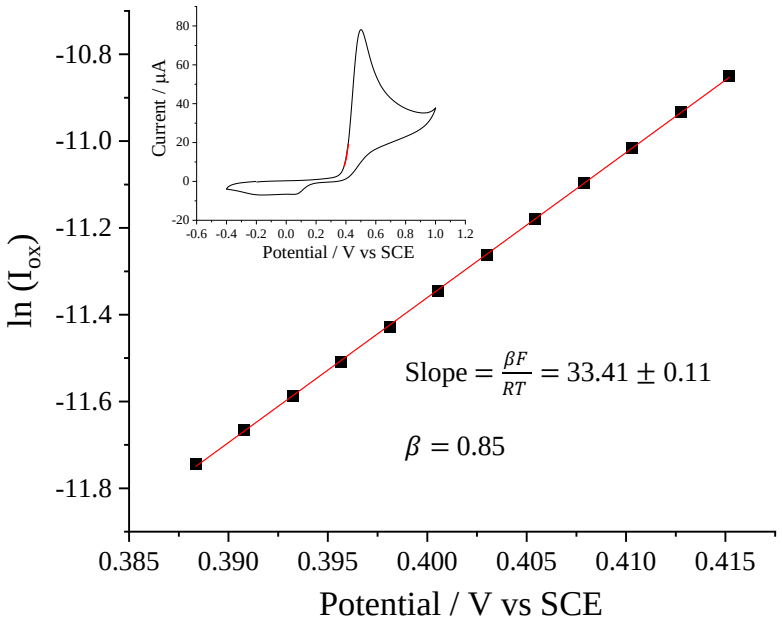
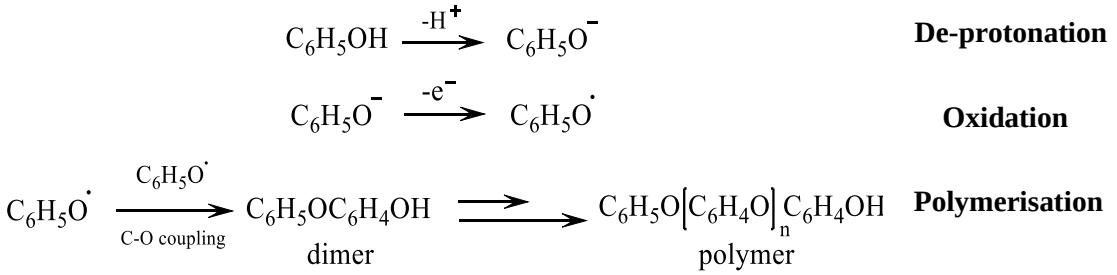


Figure 6.3. Tafel analysis for voltammogram of 1st scan of 1 mM phenol electro-oxidation. The scan rate was 50 mVs^{-1}. Inset shows the 1st scan voltammogram (black line) and the Tafel analysis region (highlighted in red region), where diffusion has almost negligible effect on.

oxidation, and polymerisation of phenol[15, 30] (Scheme 6.2). At the pH values near to, or higher than the pK_a of phenol (9.98, 25 °C)[31], phenol is deprotonated and oxidised to phenoxy radical in the first step, with fast (near reversible) electrode-kinetics[2] in a one-electron-transfer process, as indicated by the large β value close to 1. The phenoxy radical is then thought to react with other phenoxy radicals and/or phenol and undergo polymerisation, which is responsible for the observed large total number of electrons transferred. It has been reported that the polymeric and oligomeric products form strongly adsorbed, insulating layers on the electrode surface[17, 30]. As shown in Figure 6.2, the



Scheme 6.2. Electro-polymerisation of phenol at the BPPG electrode in the pH 10 borate buffer solution.

layers clearly have a pronounced, accumulating effect on the analytical responses of phenol oxidation on the BPPG electrode over a short time period, diminishing the signal rapidly from over 80 μA to near 0 μA and precluding direct analysis.

6.3.2 Phenol Detection in the Presence of PAP

6.3.2.1 Electrochemistry of PAP

The electrochemical behaviour of PAP in pH 10 borate buffer solution on BPPG was studied first and the results compared with previous studies[24,32]. The cyclic voltammetric response of 1 mM PAP recorded at 100 mVs^{-1} in Figure 6.4 shows an oxidation peak at ca. +0.04 V vs SCE and a corresponding backward reduction peak at ca. -0.05 V vs SCE. The effect of variable scan rates on the oxidation peak currents of PAP was studied in the range of 5–400 mVs^{-1}. Figure 6.5 shows the cyclic voltammograms recorded at the varying scan rates in the studied range. The peak heights were found to exhibit a linear dependence of the square root of scan rate, indicating a diffusion-controlled process (Inset

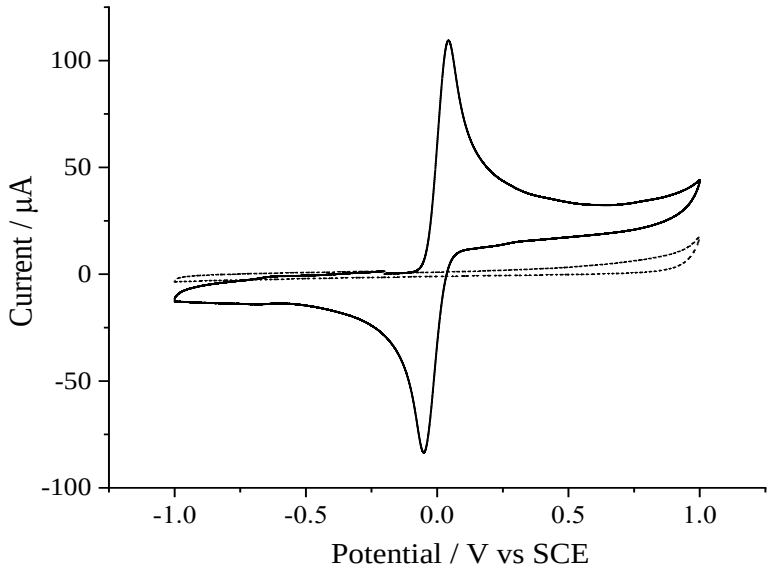


Figure 6.4. Cyclic voltammetric responses of 1mM PAP (solid line) and background (dash line) in the pH 10 borate buffer solution at the BPPG electrode. The scan rate was 100 mVs^{-1}.

of Figure 6.5). Tafel analysis was performed on several cyclic voltammograms, revealing the transfer coefficient value (β) to be ca 1.5. It can be confirmed from the β values that the oxidation of PAP corresponds to a two-electron transfer process, where the second electron transfer is rate-determining step[2]. Using a β value of 1.5 obtained from the voltammograms recorded at a moderate scan rate of 25 mVs^{-1} (Figure 6.6), the diffusion coefficient at 295 K for a two electron-transfer process can be estimated to be 4.5×10^{-6} $cm^2\ s^{-1}$, in agreement with the diffusion coefficient values of PAP reported in literature[33-37]. It can be seen in Figure 6.4 and Figure 6.5 that the reduction peaks are smaller than the corresponding oxidation peak, suggesting a loss of the oxidised product from a possible further reaction. The instability the oxidised product generated in the forward scan can be identified by comparing the ratios of oxidation peak currents to reduction peak currents at the varying scan rates in the range of 5-400 mVs^{-1} (Table 6.1). With the

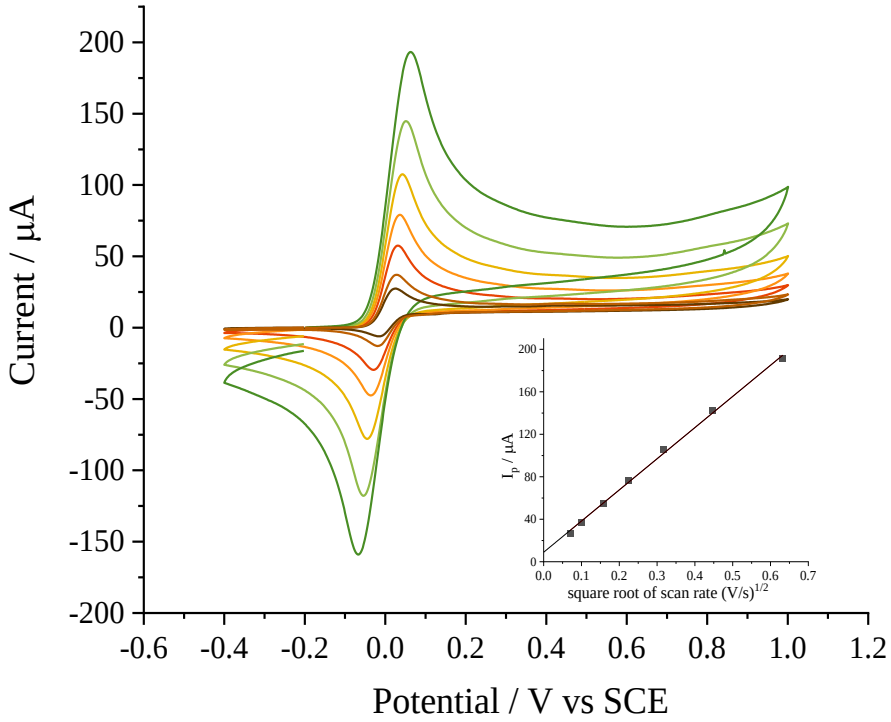


Figure 6.5. Cyclic voltammograms of 1mM PAP in the pH 10 borate buffer solution at the BPPG electrode recorded at scan rates of 5 mVs^{-1}, 10 mVs^{-1}, 25 mVs^{-1}, 50 mVs^{-1}, 100 mVs^{-1}, 200 mVs^{-1}, 400 mVs^{-1}. Inset: plot of peak current (background corrected) versus square root of scan rate.

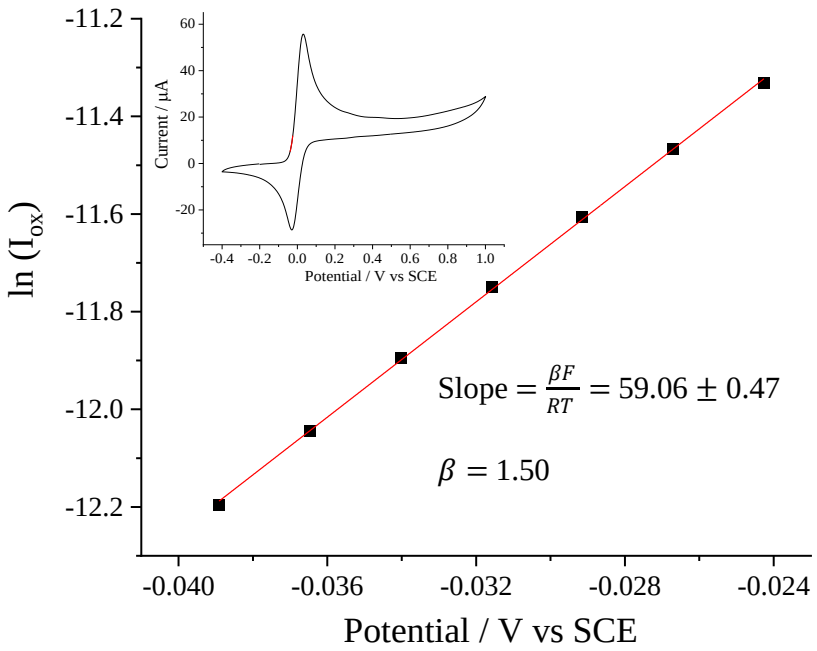


Figure 6.6 Tafel analysis for voltammogram of 1 mM PAP recorded at the scan rate of 25 mVs^{-1}. Inset shows the voltammogram recorded at 25 mVs^{-1} (black line) and the selected Tafel analysis region (highlighted in red region) where the diffusion effect is almost negligible.

increase of scan rate, the loss of reduction peak on the reverse scan becomes less significant since less time is given to the oxidised product for the next-step reaction during the voltammetric measurement[2]. The observed features are consistent with the literature, where the reactions have been reported as two-electron, two-proton transfer processes occurring between PAP-QI redox couple, followed by a slow hydrolysis step of QI to form BQ via an EC mechanism (Scheme 6.1)[32,34,35]. In the above,the PAP electro-oxidation mechanism and the electron transfer steps have been examined and the diffusion of PAP characterised. We next turn to the oxidation of PAP in the presence of phenol.

Table 6.1. Ratios of the oxidation peak currents to the reduction peak currents (both background-corrected) at varying scan rates from 5 to 400 mVs^{-1}.

Scan rate / mVs^{-1}	5	10	25	50	100	200	400
$I_{p\,ox}/I_{p\,red}$ ratios	1.66	1.59	1.43	1.32	1.20	1.09	1.08

6.3.2.2 Phenol Detection in the Presence of PAP Using CV

We next explored the role PAP can play in the electrochemical process of phenol oxidation and the possible electroanalytical detection of phenol in the presence of PAP using CV. Phenol was added to a pH 10 borate buffer solution containing 1mM PAP to give concentrations in the range of 25–800 μM. The cyclic voltammetric responses of the solutions with additions of 0–800 μM phenol on the BPPG electrode were recorded at 50mVs^{-1} and shown in Figure 6.7 (A). Two major changes of voltammograms with the increasing concentrations of phenol additions can be observed. First, for the peaks

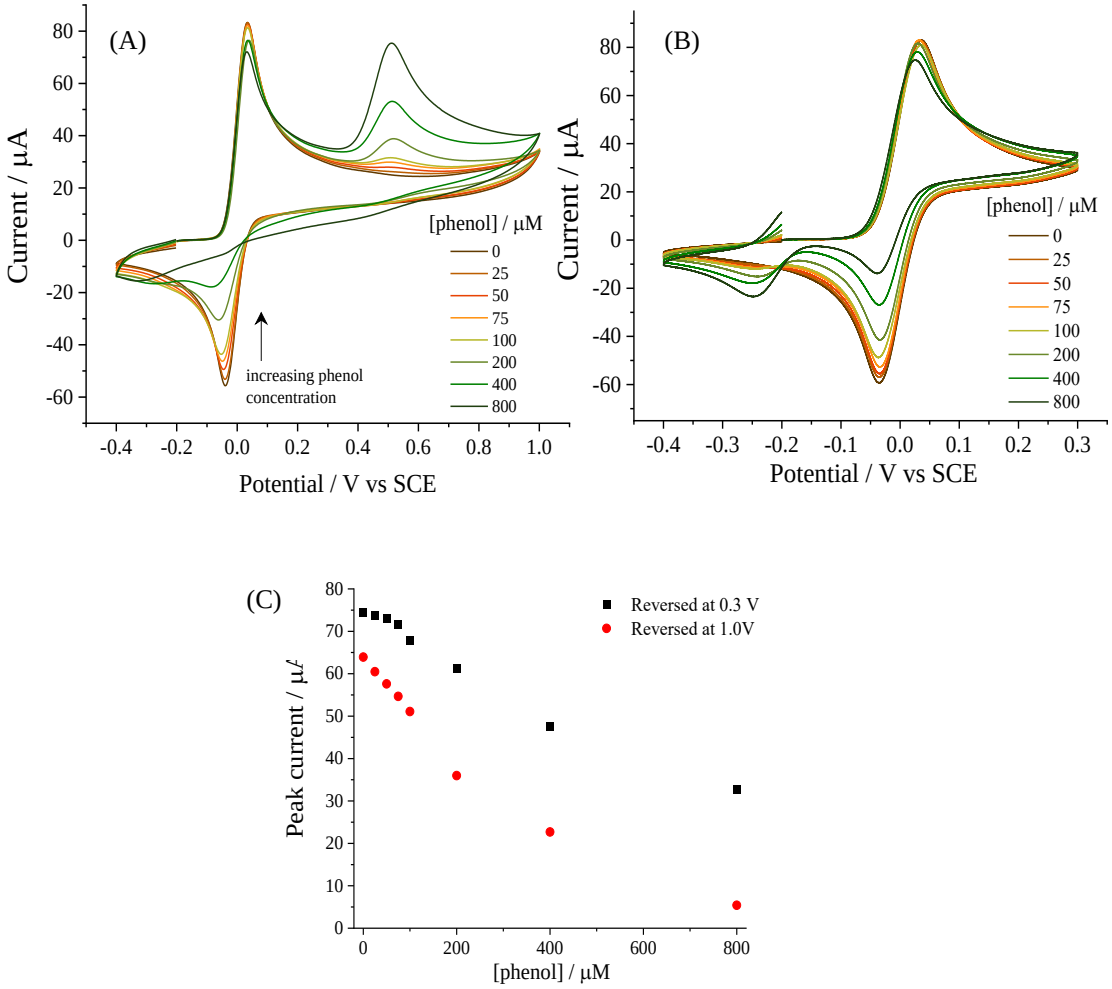


Figure 6.7. Cyclic voltammetric responses of phenol addition to the pH 10 borate buffer solution containing 1mM PAP, swept from -0.2 V to +1.0 V (A), and +0.3V (B) vs. SCE. The scan rate was 50 mVs^{-1}. (C) Comparison of the reduction peaks currents (background-corrected) obtained from (A) and (B).

expected for the PAP-QI redox reactions, a noticeable decrease was seen for the reduction peaks at ca. -0.04 V vs. SCE with increasing concentrations of phenol from 25 μM to the maximum concentration of 800 μM, where the peak height was reduced to near zero. The change in the oxidation peaks at +0.04 V vs. SCE were negligible. Previous studies[38-41] suggest under conditions of pH = 9–10, phenol or some substituted phenols can react with dichloro-benzoquinone monoamine, in what is known as the 'Gibbs reaction'. The latter is often used in *homogeneous* solutions for phenol detection via the chemical oxidation of a dichloro-aminophenol, such as PAP. In Figure 6.7 (A) the decreasing backward reduction peak heights can be inferred as a result of losing oxidised PAP owing to the Gibbs reaction with increasing amounts of phenol, and possibly, further reaction with phenoxy radicals. The second feature shown to change with the additions of phenol is that a new peak at ca. +0.51 V vs. SCE has emerged and grown with the increasing phenol concentration. This is most likely due to the direct oxidation of phenol, which switches on at a very similar potential of +0.50 V vs. SCE to that seen in Figure 6.2 for the oxidation of phenol in the absence of PAP. The second peak will be further investigated using semi-circular voltammetric signals below. Prior to that the interaction of phenol with oxidised PAP was clarified.

Figure 6.7 (B) depicts the cyclic voltammogram swept from the same starting potential of -0.2 V vs. SCE but reversed at 0.3 V vs. SCE, before the onset of the second oxidation, leaving only the unreacted phenol with the oxidised PAP in the reaction system. A similar trend of a decrease in the peak height of reduction peak with the increase of phenol concentration can be seen in Figure 6.7 (B) as compared to Figure 6.7 (A) but with significantly less sensitivity to the amount of phenol present, as seen in Figure 6.7 (C). It can be inferred that phenol and the product of the second oxidation, which are likely to

be phenoxy radicals from the direct oxidation of phenol are both involved in the reaction with the oxidised PAP. In Figure 6.7 (B), additional reduction peaks were observed for the higher phenol concentrations as a result of the greater participation of phenol in the reaction with oxidised PAP without the presence of phenoxy radicals.

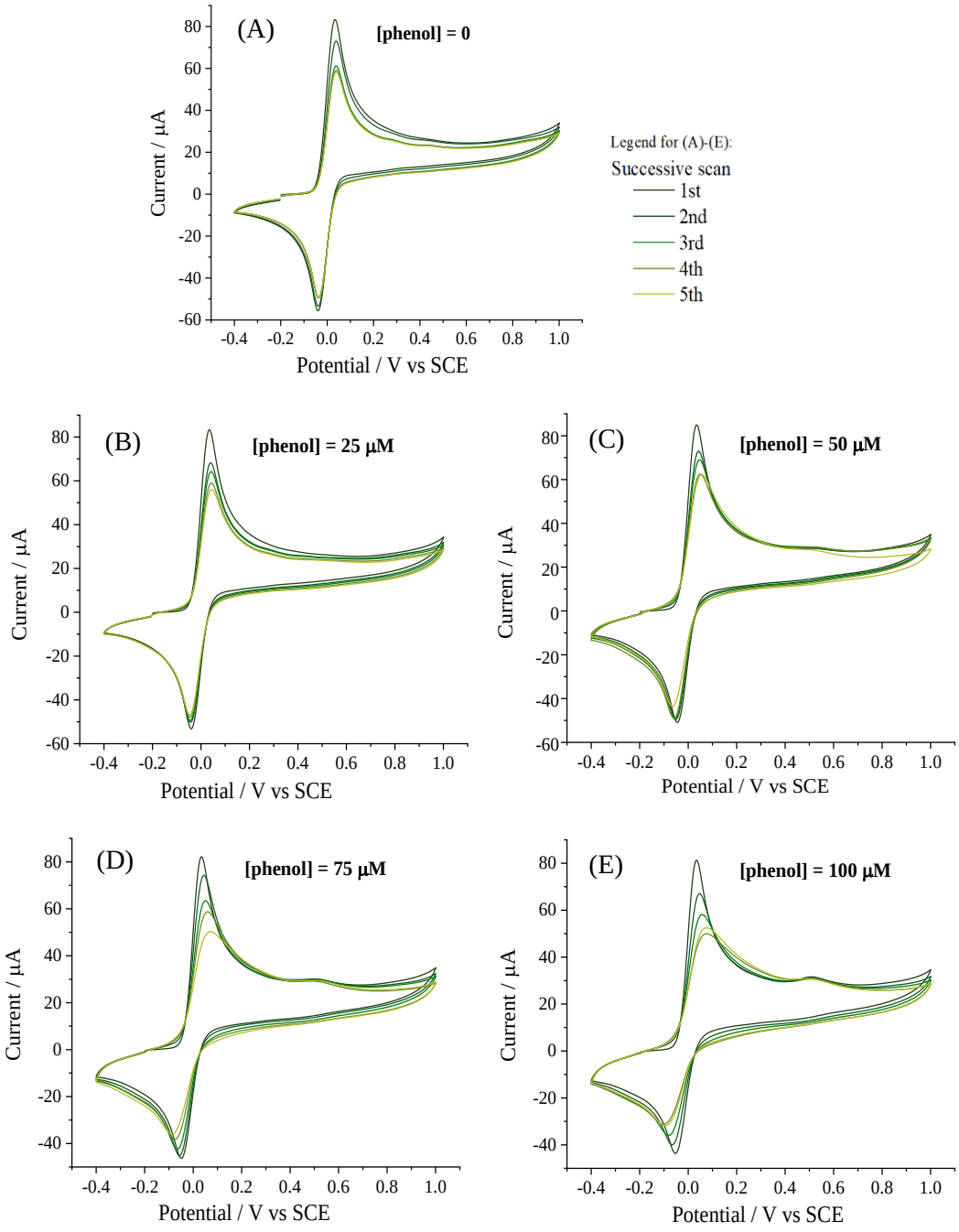
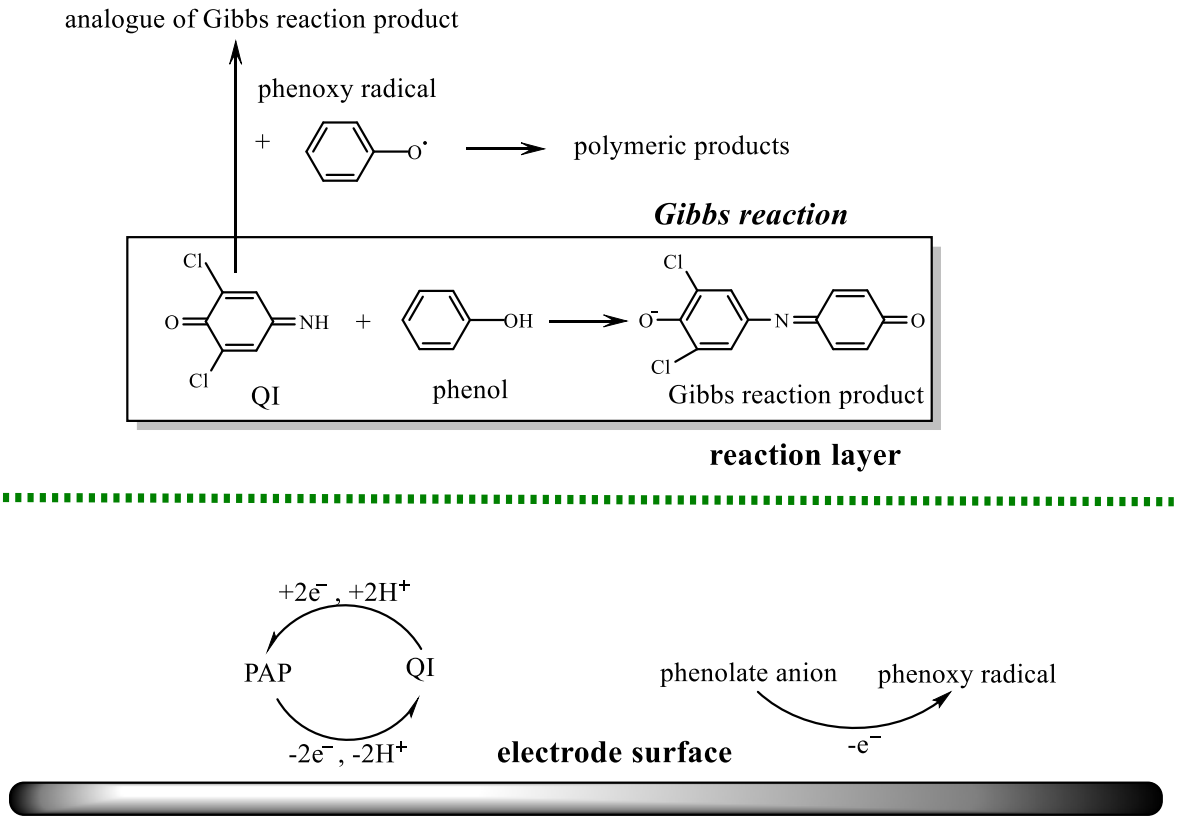


Figure 6.8. Cyclic voltammetric responses of (A)0 (B) 25 µM (C) 50 µM (D) 75 µM (E) 100 µM phenol addition to 1mM PAP in the pH 10 borate buffer solution at the BPPG electrode recorded for multiple scans at a scan rate of 50 mVs^{-1}.

In order to investigate the mechanism in the light of the known Gibbs reaction and, in particular, to understand the participation of phenol and the electro-oxidised phenol in the reaction with oxidised PAP, successive cyclic voltammetric measurements were conducted for varying concentrations of phenol. The effect of PAP on the electrode fouling caused by phenol, as discussed in Section 6.3.1 was investigated. As can be seen in Figure 6.8, in the phenol concentration range of 25–100 μM, the PAP oxidation peaks show a ca. 30% decrease in peak currents over five cycles regardless of the presence of phenol. However, the peak currents of the second oxidation peak corresponding to the direct oxidation of phenol remained unchanged over five scans. It can be inferred the electrode surface was protected from the formation of the previously discussed polymeric film, which results from the oxidation of phenol and precludes useful analysis of high phenol concentrations. Combining the above observations, a possible mechanism where PAP acting as a mediator preventing the electrode passivation during phenol electro-oxidation can be suggested (Scheme 6.3). Firstly, phenol was deprotonated and the oxidation occurred. Next, QI generated from the oxidation of PAP becomes involved and reduces the amount of phenol in the locality of the electrode via either direct reaction with phenol and oxidised phenol, avoiding the products that may 'block' the electrode, including problematic polymers at the remote reaction layer. In other words, the oxidised PAP allows the possible electro-analysis of phenol at the corresponding potential by preventing electrode fouling by reducing the critical threshold concentration of oxidised phenol needed to form the blocking polymeric layer. It is possibly achieved by also shifting some of the overall phenol oxidation reaction physically away from electrode surface into an adjacent reaction layer. This provides a basis for establishing the method of phenol quantification by adding 1mM PAP in the pH 10 system to detect phenol in the concentration range of 25–100 μM, where a protected, clean electrode surface at the

required potential for phenol oxidation is ensured. However, although, as shown by the stability of the phenol oxidation peak in Figure 6.8, the approach allows for reproducible oxidative voltammetry of phenol it necessarily reduces the size of the phenol oxidation peak over what, hypothetically, would be seen if the direct oxidation could proceed without electrode fouling. In the following section we suggest how this drawback can be overcome and remedied.



Scheme 6.3. Mechanism of phenol oxidation in the presence of PAP and 'electrode protection' in the pH 10 borate buffer solution at the BPPG electrode.

6.3.2.3 Phenol Detection in the Presence of PAP Using SCV

Having investigated the electrochemical process of phenol with the presence of PAP in the studied system, we now turn to developing the method to enhance the

electroanalytical performance of phenol using SCV. As discussed in the previous studies[25-27,42,43], applying a semi-circular potential wave over a chosen potential window can selectively amplify the current responses in the vicinity of the midpoint of the potential window (defined as E_{mid}), where scan rate reaches a near infinite value (reflecting experimentally, ultimately the limitations of the potentiostat employed). The approach correspondingly suppresses the current responses at the other regions, where the scan rate is relatively slow. The semi-circular sweep voltammetric responses of 100 μM phenol with the presence of 1 mM PAP in the pH 10 borate buffer solution at the BPPG electrode were recorded at varying potential windows. The potential window was adjusted by shifting E_{mid} from -0.15 to +0.75 V vs. SCE whilst held at the same scan amplitude of 0.8 V and the same average scan rate of 50 mVs^{-1}. Three peaks can be seen in Figure 6.9 changing with the potential windows. Two of them are the oxidation peaks (seen at ca. +0.04 V and ca. +0.50 V vs. SCE respectively for a potential window with

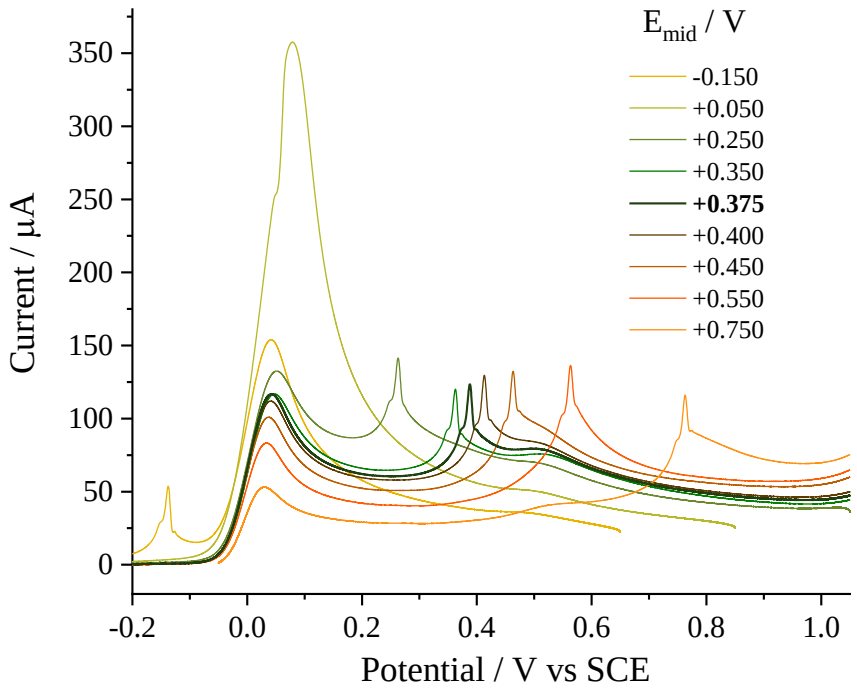


Figure 6.9. Semi-circular sweep voltammetric responses of 100 μM phenol in the pH 10 borate buffer solution containing 1mM PAP at the BPPG electrode recorded at potential windows with varying E_{mid}. The average of scan rate was 50 mVs^{-1}. The scan amplitude was 0.8 V.

E_{mid} of +0.375 V) due to the PAP and phenol oxidation reactions. The third sharp peak (at +0.375 V vs. SCE, the midpoint of the potential window) arises from the transiently nominally infinite scan rate (within limitations of the potentiostat electronics), which, as previously noted[42,43] is attributed to strong capacitive charging currents. With the adjustment of potential windows, the two oxidation peak currents increased significantly when E_{mid} approached their oxidation potentials and decreased when E_{mid} moved away from the oxidation potentials. The sharp peak was shown to affect the sizes and shapes of two oxidation peaks as E_{mid} was close to the oxidation potentials of two peaks and even merged with the bigger PAP peak when E_{mid} moved to +0.05 V vs SCE. Thus, as suggested by Figure 6.9, with a fixed scan amplitude of 0.8 V, the E_{mid} of potential window was optimised as +0.375 V vs SCE to give the largest possible size as well as a clearly distinguishable shape of the phenol related peak.

Table 6.2. Slope values of the plots of phenol peak currents against phenol concentration obtained from the voltammograms of 0-100 μM of phenol in the pH 10 borate buffer solution present with 1mM PAP recorded at varying scan amplitudes. The average scan rate was 50mVs^{-1}.

	LSV	**Semi-circular sweep voltammetry**						
Scan amplitude / V		0.20	0.30	0.35	0.425	0.80	0.90	1.0
E_{mid} / V vs SCE		0.375	0.325	0.350	0.325	0.375	0.375	0.375
Slope of I_p /μA vs.[phenol]/μM plot	0.07	0.10	0.10	0.11	0.14	0.20	0.21	0.22

Three repeating sets of phenol solutions within the chosen concentration range of 0–100 μM (Section 6.3.2.2) were prepared and the signals of each solution were measured in the developed system present with 1 mM PAP using semi-circular sweep voltammetry. All peak currents were obtained by subtracting the zero concentration current values, which was read at a fixed potential near the peak potential in the voltammogram in

absence of phenol, from the current values read at the same, fixed potential in the voltammograms of 25–100 μM phenol. The peak currents were plotted against phenol concentrations for the evaluation of detection sensitivities. Table 6.2 records the slopes values peak current-concentration plots at a range of scan amplitudes from 0.2 V to a maximum of 1.0 V, constrained by the need for the phenol oxidation peak to remain distinguishable from the sharp peak at E_{mid}, which grew with the increasing scan amplitudes. As suggested by Table 6.2, the potential window with a large scan amplitude of 1.0 V and the E_{mid} of +0.375 vs SCE leads to the largest slope values, thus can be used as an optimal for a fast and sensitive detection of phenol.

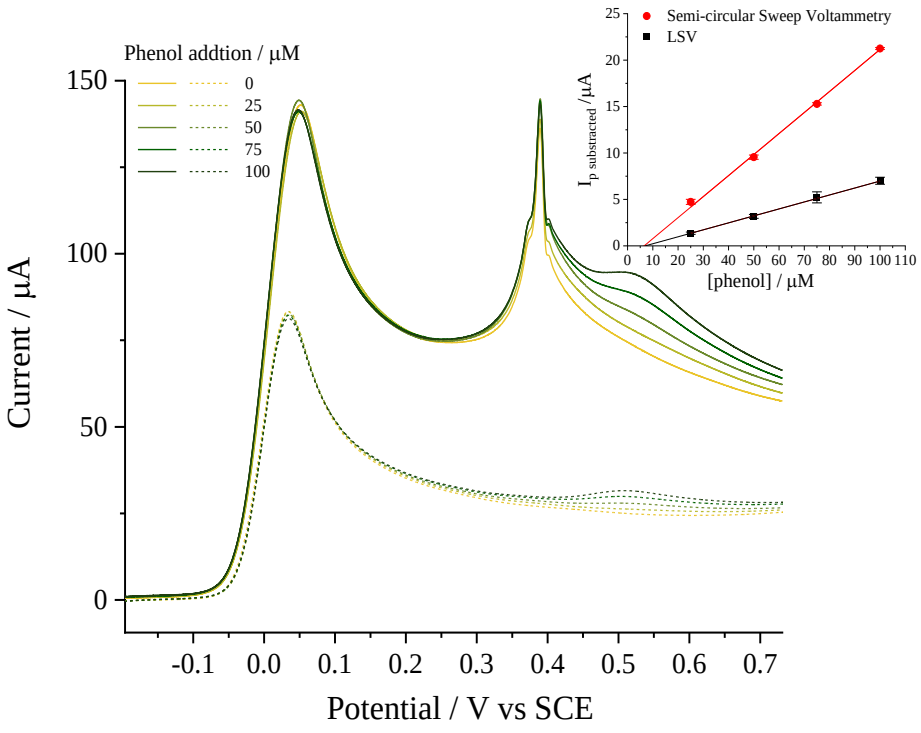


Figure 6.10. Semi-circular sweep (solid lines) vs linear sweep (dash lines) voltammetric responses of 0-100 μM phenol in the pH 10 borate buffer solution containing 1mM PAP recorded at the potential windows with E_{mid} of +0.375 V vs. SCE and scan amplitude of 1.0 V.

In Figure 6.10, the semi-circular sweep voltammetric responses recorded using the potential window thus optimised are compared with the linear sweep voltammetric responses of the studied concentration range of phenol in the system present with PAP recorded at the same average scan rate (50 mVs^{-1}). It is evident the phenol oxidation peak was largely amplified when the semi-circular potential sweep was applied. The peak currents analysed from semi-circular sweep voltammogram show a linear dependence on phenol concentration in the range of 25–100 μM, which can be described as: $I_p/\mu A$= (0.22 ± 6.9× 10^{-3}) [phenol] (μM) + (1.49 ± 0.59) (μA), N=4, R^2=0.998 (Inset of Figure 6.10). The sensitivity of detection was improved ca. 3 times compared to that seen when employing conventional LSV (Table 6.2). In both cases, strong dependences on the phenol concentration were found for the second oxidation peak current, revealing marked contributions from the direct oxidation of phenol. This has now been demonstrated from the analytical perspective.

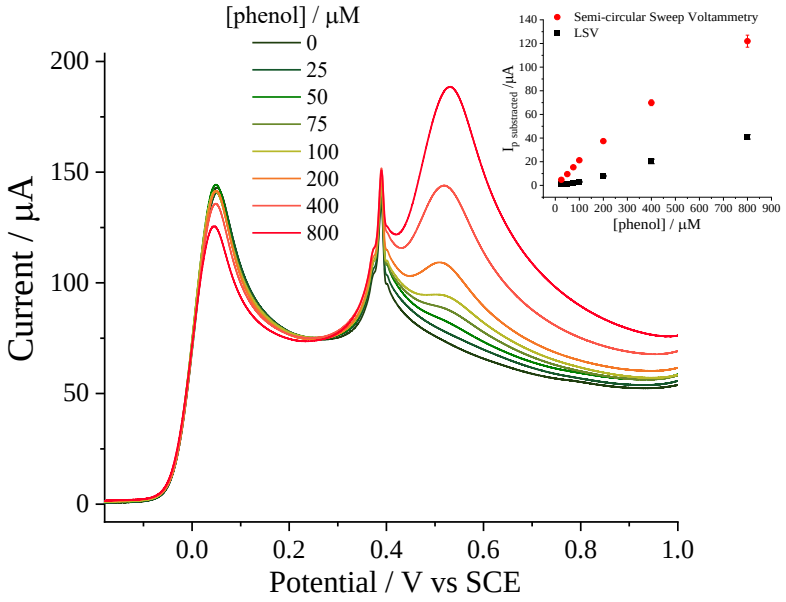


Figure 6.11. Semi-circular sweep voltammetric responses of 0-800 μM phenol in the pH 10 borate buffer solution containing 1mM PAP recorded at the optimised potential window. The average of scan rate was 50 mVs^{-1}. Inset: Plot of subtracted peak currents obtained from linear and semi-circular voltammograms versus phenol concentration.

Next semi-circular sweep voltammetry of higher concentrations of 200-800 μM of phenol in the presence of 1 mM PAP was performed using the optimised potential window. Figure 6.11 records the semi-circular voltammograms of phenol in the range of 0–800 μM and the inset graph compares the peak currents obtained from semi-circular and linear voltammograms graph. It can be seen that the greatly amplified current responses of the second peak offer the better sensitivity of signals to phenol concentrations over the whole concentration range, suggesting the advantage of semi-circular sweep voltammetry to linear sweep voltammetry in the electro-analysis of interest due to its selective amplification facilitated by the adjustment of potential windows and high sensitivity.

Finally, we investigated the possibility of further improving the sensitivity by raising the average scan rate to 200 mVs^{-1}. Table 6.3 summarises the detection sensitivity of phenol in the concentration range of 25–100 μM in the presence of 1mM PAP using LSV and semi-circular sweep voltammetry. It is evident that over a fixed potential window, applying higher average scan rates facilitates a more sensitive phenol detection over the studied concentration range, although semi-circular sweep voltammetry offers a relatively greater advantage over the conventional LSV at the lower average scan rate.

Table 6.3. Slope values of the plots of phenol peak currents against phenol concentration which obtained from the voltammograms of 0-100 μM of phenol in the pH 10 borate buffer solution present with1 mM PAP recorded at varying scan rates using LSV and semi-circular voltammetry.

	Slopes of I_p /μA vs.[phenol]/μM plots at varying scan rates / mV s^{-1}			
	25	50	100	200
LSV	0.053	0.072	0.13	0.17
Semi-circular sweep voltammetry	0.19	0.22	0.31	0.36

6.4 Conclusions

We have developed an electroanalytical method for the detection of high concentrations of phenol without the problem of electrode fouling by introducing a second species, PAP, into the solution to be studied, facilitating phenol detection via a possible 'electrode protection' mechanism. Semi-circular potential sweep voltammetry was applied to amplify the analytical signal. Under an optimised potential window with the scan amplitude of 1.0 V centred on a potential of +0.375 vs SCE, phenol concentrations in the range 25–800 μM were measured without problems of electrode fouling.

Bibliography

1. J. Wang, *Analytical electrochemistry*, Wiley-VCH, Hoboken, N.J., 3rd edn., 2006.
2. R. G. Compton and C. E. Banks, *Understanding voltammetry*, World Scientific Publishing Europe, London, 3rd edn., 2018.
3. Á. Molina, J. González, *Pulse Voltammetry in Physical Electrochemistry and Electroanalysis. Theory and Applications*, Springer, Berlin, 2016..
4. L. C. Clark, R. Wolf, D. Granger and Z. Taylor, *Journal of Applied Physiology*, 1953, **6**, 189-193.
5. P. Jeroschewski, K. Haase, A. Trommer and P. Grundler, *Electroanalysis*, 1994, **6**, 769-772.
6. W. J. Albery, W. N. Brooks, S. P. Gibson, M. W. Heslop and C. E. W. Hahn, *Electrochimica Acta*, 1979, **24**, 107-108.
7. A. E. G. Cass, G. Davis, G. D. Francis, H. A. O. Hill, W. J. Aston, I. J. Higgins, E. V. Plotkin, L. D. L. Scott and A. P. F. Turner, *Analytical Chemistry*, 1984, **56**, 667-671.
8. S. Kuss, R. A. S. Couto, R. M. Evans, H. Lavender, C. C. Tang and R. G. Compton, *Analytical Chemistry*, 2019, **91**, 4317-4322.
9. K. Chaisiwamongkhol, C. Batchelor-McAuley and R. G. Compton, *Analyst*, 2019, **144**, 1386-1393.

10. ANB Sensors, http://www.anbsensors.com, (accessed April 2020).

11. Zimmer Peacock, https://www.zimmerpeacock.com, (accessed April 2020).

12. Sensirion, https://www.sensirion.com/en, (accessed April 2020).

13. Metrohm DropSens, http://www.dropsens.com, (accessed April 2020).

14. J. Wang, M. Jiang, F. Lu, *Journal of Electroanalytical Chemistry*, 1998, **444**, 127-132.

15. M. Gattrell, D. W. Kirk, *Journal of the Electrochemical Society*, 1993, **140**, 1534-1540.

16. J. Iniesta, P. A. Michaud, M. Panizza, G. Cerisola, A. Aldaz, C. Comninellis, *Electrochimica Acta*, 2001, **46**, 3573-3578.

17. N. B. Tahar, A. Savall, *Electrochimica Acta*, 2009, **55**, 465-469.

18. J. M. Skowronski, P. Krawczyk, *Journal of Solid State Electrochemistry*, 2004, **8**, 442-447.

19. K. Chen, Z. L. Zhang, Y. M. Liang, W. Liu, *Sensors-Basel*, 2013, **13**, 6204-6216.

20. M. Del Pilar Taboada Sotomayor, A. A. Tanaka, L. T. Kubota, *Journal of Electroanalytical Chemistry*, 2002, **536**, 71-81.

21. B. Rezaei, M. K. Boroujeni, A. A. Ensafi, *Electrochimica Acta*, 2014, **123**, 332-339.

22. R. Sha, S. K. Puttapati, V. V. S. S. Srikanth, S. Badhulika, *Journal of Electroanalytical Chemistry*, 2017, **785**, 26-32.

23. L. Fernández, C. Borrás, H. Carrero, *Electrochimica Acta*, 2006, **52**, 872-884.

24. D. Hawley and R. N. Adams, *Journal of Electroanalytical Chemistry*, 1965, **10**, 376-386.

25. Y. Uchida, E. Katelhon, R. G. Compton, *Journal of Electroanalytical Chemistry*, 2018, **818**, 140-148.

26. Y. Uchida, E. Katelhon, R. G. Compton, *Journal of Electroanalytical Chemistry*, 2019, **835**, 60-66.

27. Y. Wang, L. Chen, K. Chaisiwamongkhol, R. G. Compton, *Food chemistry*, 2019, **309**, 125606.

28. C. Batchelor-McAuley, J. Ellison, K. Tschulik, P. L. Hurst, R. Boldt and R. G. Compton, *Analyst*, 2015, **140**, 5048-5054.

29. R. Guidelli, R. G. Compton, J. M. Feliu, E. Gileadi, J. Lipkowski, W. Schmickler and S. Trasatti, *Pure and Applied Chemistry*, 2014, **86**, 245-258.

30. R. Niesner and A. Heintz, *Journal of Chemical and Engineering Data*, 2000, **45**, 1121-1124.

31. F. Bruno, M. C. Pham and J. E. Dubois, *Electrochimica Acta*, 1977, **22**, 451-457

32. M. D. Liptak, K. C. Gross, P. G. Seybold, S. Feldgus and G. C. Shields, *Journal of the American Chemical Society*, 2002, **124**, 6421-6427.

33. H. Bramwell, A. E. G. Cass, P. N. B. Gibbs and M. J. Green, *Analyst*, 1990, **115**, 185-188.

34. E. R. Lowe, C. E. Banks and R. G. Compton, *Analytical and Bioanalytical Chemistry*, 2005, **383**, 523-531

35. H. J. Salavagione, J. Arias, P. Garces, E. Morallon, C. Barbero and J. L. Vazquez, *Journal of Electroanalytical Chemistry*, 2004, **565**, 375-383.

36. C. Hoffman, M. de la Rosa, M. R. Anderson, C. Rhodine and W. G. Kuhr, *ECS Transactions* 2017, **80**, 1319-1332.

37. R. N. Adams, *Electrochemistry at solid electrodes*, Dekker, New York, 1969**.**

38. H. D. Gibbs, *Journal of Biological Chemistry*, 1927, **72**, 649-664

39. J. R. Baylis, *Journal of the American Water Works Association*, 1928, **19**, 597-604.

40. J. C. Dacre, *Analytical Chemistry*, 1971, **43**, 589-591.

41. M. B. Ettinger and C. C. Ruchhoft, *Analytical Chemistry*, 1948, **20**, 1191-1196.

42. Y. Uchida, E. Katelhon and R. G. Compton, *Journal of Electroanalytical Chemistry*, 2018, **823**, 465-473.

43. H. M. A. Amin, Y. Uchida, E. Katelhon and R. G. Compton, *Journal of Electroanalytical Chemistry*, 2019, **836**, 62-67.

Chapter 7

Semi-circular Sweep Voltammetry. Bio-analytical Applications

This chapter develops further the applications of semi-circular voltammetry in the analysis of mixtures of analytes. Specifically, semi-circular sweep voltammetry (SCV) is applied to the simultaneous electroanalytical determination of solutions containing two components with similar oxidation potentials which precludes their resolution using conventional voltammetric methods including linear sweep, square wave and pulse voltammetries. Three such biologically important mixtures, ascorbic acid / acetaminophen, glucose / ethanol and hydroquinone / catechol were studied, analytical methods developed and the method of semi-circular sweep voltammetry shown to give notable advantages over the other conventional analytical voltammetries in terms of signal resolution and the sensitivity of the detection. Favourable accuracy was obtained using electrodes with either simple or no modification required in the established linear detection ranges.

The work presented in this Chapter 7 has been published as a first author paper in *Biosensors and Bioelectronics*.

7.1 Introduction

Analytical voltammetry is usually performed using a linear potential sweep and measuring the resulting currents. Often pulses or oscillations are imposed on the sweep in the form of square wave or differential pulse voltammetry with a significant increase in sensitivity and, with careful analysis, provide increased information about the electrode process of interest[1-3]. Such approaches to analysis offer speed of measurement, require low-cost equipment and often generate attractively low limits of detection coupled with good sensitivity. As a result, amperometric chemical sensors dominate the market for blood glucose sensors[4,5] and are strong competitors in the gas sensing area[6] building on the original Clark cell for oxygen detection with many companies now offering electrochemical sensors for carbon monoxide (smoke detectors), ammonia, hydrogen sulphide, carbon dioxide and nitrogen oxides[7-10]. That said one generic weakness of amperometric detection concerns the selectivity of measurement which is overcome, for example, in the case of glucose detection by employing enzymes to impose the selectivity and making the measurement indirectly, often via the detection of hydrogen peroxide. However, this weakness, in the opinion of the author of this thesis, may account for the rather niche status of amperometric electrochemical bio-sensors within the entire field of bio-analytical measurements viewed holistically.

Earlier chapters have described the introduction of the innovative approach to voltammetry which is not based on a linear potential sweep but rather on an increasing potential where the instantaneous potential scan rate varies with potential[11-16]. Most notably, but not exclusively[15-16], this work has utilised a semi-circular potential sweep in which the instantaneous scan rate varies from zero to near infinite (within the limitations of the controlling electronics) at the mid-point of the scan, as shown in Figure 7.1. This

has been used for fundamental studies of some redox couples. This thesis is concerned with the possible application of such variable scan rate potential sweep methods in electro-analysis. In particular it is interesting to explore whether semi-circular voltammetry (SCV) can be usefully applied to enhance the selectivity of electroanalytical detection noting that the magnitude of the current response in linear sweep voltammetry increases markedly with scan rate both for diffusional and thin-layer/adsorptive systems[17]. As a consequence, one peak in a voltammogram might be enhanced in comparison with another peak if the former experiences a greater instantaneous voltage scan rate than the latter. Proof of concept of this idea was presented in Chapter 5 via the successful voltammetric resolution of chlorophyll a and b in their mixtures despite them having closely similar oxidation potentials[18].

In this chapter, we apply the SCV technique to 3 different bio-analytical challenges in each of which a mixture of two components with near identical redox potentials is interrogated to explore and validate the generality of the approach especially in the context of biosensors. These mixtures are the detections of ascorbic acid (AA)

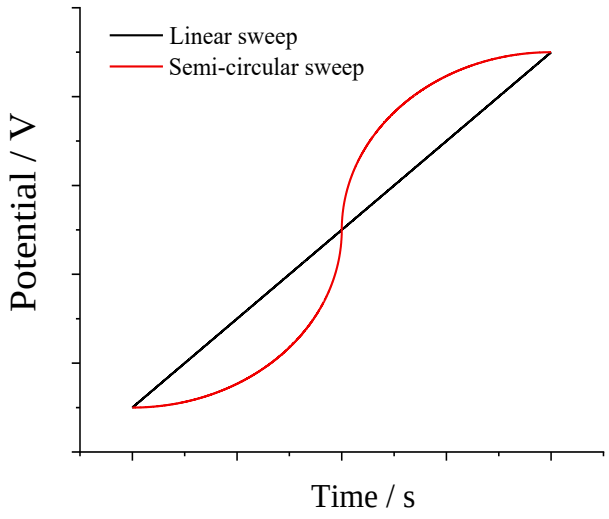


Figure 7.1. Waveforms of cyclic voltammetry (black line) and semi-circular sweep voltammetry (red line) at the same average scan rate.

/ acetaminophen (AC), glucose (Glu) / ethanol mixtures and hydroquinone (HQ) / catechol (CC). AC is a widely used analgesic and antipyretic drug which co-exists with AA, an essential water-soluble vitamin in various biological matrices[19-20]. The mixtures of AA and AC were also seen in some pharmaceutical formulations as the presence of AA was shown to intensify the therapeutic effect of AC whilst compensating for its hepatotoxicity[21]. Ethanol is one of the major interferences for blood glucose detection[4]. The concentrations of ethanol and Glu are also used as quality indicators for alcoholic beverages during fermentation[22, 23]. HQ and CC are two isomers of dihydroxybenzene that coexist as pollutants in environmental samples due to their high toxicity and low degradability[24]. The selective determinations of the individual analytes in the above mixtures are of great importance in the corresponding areas of medical monitoring in biological fluids, food and pharmaceutical quality control and environmental pollution assessment. Through the investigations of these systems, the applicability of SCV technique and its advantages over conventional voltammetric techniques are demonstrated.

7.2 Experimental

7.2.1 Chemicals and Reagents

All chemicals were of analytical grade and were used as received without any further purification. Ascorbic acid (AA, 99.0%), acetaminophen (AC, 98.0–102.0%), hydroquinone (HQ, 99%), catechol (CC, >99%), α-D-glucose (96%), ethanol (≥99.8%) were purchased from Sigma-Aldrich. The bamboo-like multi-walled carbon nanotubes, b-MWCNTs (30 ± 10 nm diameter, 5–20 μm length, >95% purity) were purchased from

NanoLab (Brighton, MA, USA). Sainsbury's Own Brand paracetamol capsules and Beecham's Flu Plus were purchased from a local supermarket (Sainsbury's Oxford, UK). Efferalgan 500mg + vitamin C 200mg effervescent tablets were purchased online from euro-pharmas.com. All aqueous solutions were prepared with deionised water at a resistivity not less than 18.2 MΩ cm at 298K (Millipore, MA, USA). Phosphate-buffered saline (PBS, 0.1 M, pH = 7.4) or 1.0 M potassium hydroxide solution was used as supporting electrolytes. PBS was prepared using sodium chloride (137 mM, Sigma-Aldrich, ⩾99.5%), potassium chloride (2.7 mM, Sigma-Aldrich, ⩾99.0%), sodium phosphate dibasic (10 mM, Sigma-Aldrich, ⩾ 99.0%) and potassium phosphate monobasic (1.8 mM, Sigma, ⩾99.0%). 1.0 M KOH was prepared using potassium hydroxide pellets (85.0-100.5%) purchased from WR Chemicals. All prepared solutions were degassed for 10 minutes prior to each measurement.

7.2.2 Apparatus

All electrochemical experiments were performed with a three-electrode system inside a Faraday cage thermostated at 298K. Cyclic voltammetry (CV), differential pulse voltammetry (DPV) and square wave voltammetry (SWV) were conducted using a μAutolab II potentiostat (Metrohm-Autolab BV, Netherlands). Semi-circular potential sweep voltammetry (SCV) was performed using an in-lab built potentiostat controlled by software *Python* 3.5 for the generations of required potential waveforms[25]. The working electrodes used were variously a glassy carbon (GC) macroelectrode (diameter of 3 mm), an MWCNTs-modified glassy carbon (MWCNTs/GC) macroelectrode, a commercially available screen-printed electrode modified with multiwalled-carbon nanotubes by the

manufacturer (CNT-SPEs, diameter of 4 mm, DropSens, Asturias, Spain), or a nickel micro-wire electrode (diameter of 50 μm, length of 1mm). A saturated calomel electrode (SCE, ALS distributed by BASi Inc., Japan) was employed as the reference electrode and a graphite rod was employed as the counter electrode.

The GC electrode was polished on the soft lapping pads with alumina of decreasing particle sizes (1.0, 0.3 and 0.05 μm) (Buehler, IL, UK), and subsequently sonicated in water. The MWCNT/GC was prepared by a drop-casting method. The MWCNTs were partially dispersed in acetone (1 mg/1 mL) to form a 'suspension', which was then sonicated in an ultrasonic bath for 10 minutes without further functionalisation[26]. 5-60 μL of the suspension was drop-casted (in 5 μL aliquots) to the clean GC electrode surface, followed by the evaporation of the solvent at room temperature[26, 27]. The electrode was rinsed with acetone and polished following the above procedure after each voltammetric scan, then replaced with a new drop cast for the next scan. This is to ensure a clean modified electrode surface and stable capacitive currents facilitating simple data analysis whilst testifying to the reproducibility of the electrode modification.

7.2.3 Sample Preparation

For the analysis of real samples, AA and/or AC we used the contents of either a Paracetamol Capsule, the powder in a Beechams Sachet or an "Efferalgan + Vitamin C" Effervescent Tablet. In the first case, the capsule was first opened. Then the outside shell was discarded and the active component was dissolved in 1000 mL water. The sachet and tablet were directly dissolved in 1000 mL water. In all three cases, 10 mL of solutions with real samples dissolved in were placed into the centrifuge tube and centrifuged at 4000 rpm for 10 minutes to remove the insoluble solids. 0.1 mL of the supernatant was

collected and diluted with PBS until the voltammetric responses fell within the linear detection range (dilution factors were 100 for Paracetamol Capsules, 125 for Beechams Sachet and 100 for Efferalgan + Vitamin C Effervescent Tablets).

7.3 Results and Discussion

In the following sections, three different model analytical systems each consisting of two components are examined voltammetrically so as to identify the merits of semi-circular voltammetry (SCV). In each case under conventional cyclic voltammetry (CV), the voltammetric signals from the two components overlap to a significant extent so as to make the analytical determination of the mixture difficult or impossible using linear sweep voltammetry at a planar electrode. Specifically mixtures of ascorbic acid (AA) / acetaminophen (AC), glucose (Glu) / ethanol and hydroquinone (HQ) /catechol (CC) are used as model systems to explore the value and possible superiority of SCV in the simultaneous determination of individual species in each mixture. In each example system, first, the electrochemistry of the studied species on the working electrode of interest was examined using CV. Next, the performance of SCV was compared with the other commonly used voltammetric methods, including linear sweep voltammetry (LSV), square wave voltammetry (SWV) and differential pulse voltammetry (DPV). Meanwhile, in combination with the use of SCV, the development of specific electrochemical detection and quantification methods were demonstrated for each system. In section 7.3.1, a method of quantifying the AC contents of real pharmaceutical samples is developed. In section 7.3.2, the use of a Ni electrode to develop non-enzymatic sensors for systems containing both glucose and ethanol is advocated. In section 7.3.3, a GC electrode is

modified with MWCNTs by a dropcasting method to better resolve the isomers of HQ and CC and the effects of SCV on the sensitivity are explored.

7.3.1 Ascorbic Acid and Acetaminophen

7.3.1.1 Electrochemical behaviours of ascorbic acid and acetaminophen

The separate electrochemical behaviours of ascorbic acid (AA) and acetaminophen (AC) at a GC electrode were first investigated using CV. The individual cyclic voltammetric responses of 1mM AA (red line) and AC (blue line) in pH 7.4 PBS were recorded at 50 mVs^{-1} as shown in Figure 7.2. The oxidation peak occurred at 0.32 V vs SCE for AA and 0.44 V vs SCE for AC. The effects of variable scan rates on the peak currents of AA and AC were studied (Figure 7.3 (A) and (B)). The peak currents of both AA and AC exhibited linear dependences on the square roots of scan rates in the range of 25–500 mVs^{-1} (Inset of Figure 7.3 (A) and (B)), suggesting the electro-oxidation of AA and AC are both diffusion-controlled processes. The electro-oxidations of AA and AC at the studied pH have been reported in the literature both as two-electron, two-proton processes (Inset of Figure 7.2)[28-30]. The transfer coefficient (β) values for the two-electron

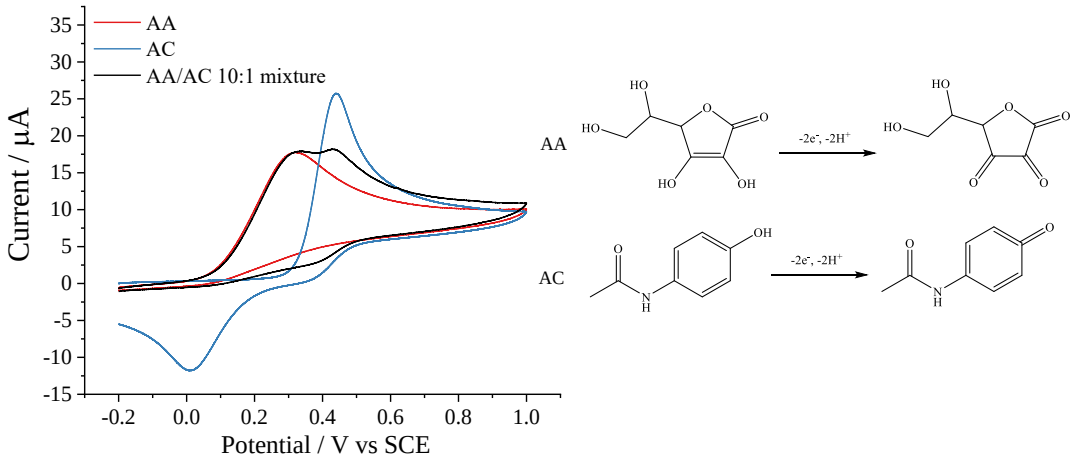


Figure 7.2. Triangular sweep cyclic voltammetric responses of 1 mM AA, 1 mM AC and of a mixture containing 1mM AA and 0.1 mM AC at a scan rate of 50 mVs^{-1}. Inset: The two-electron, two-proton oxidation of AA (upper) and AC (lower)[28-30].

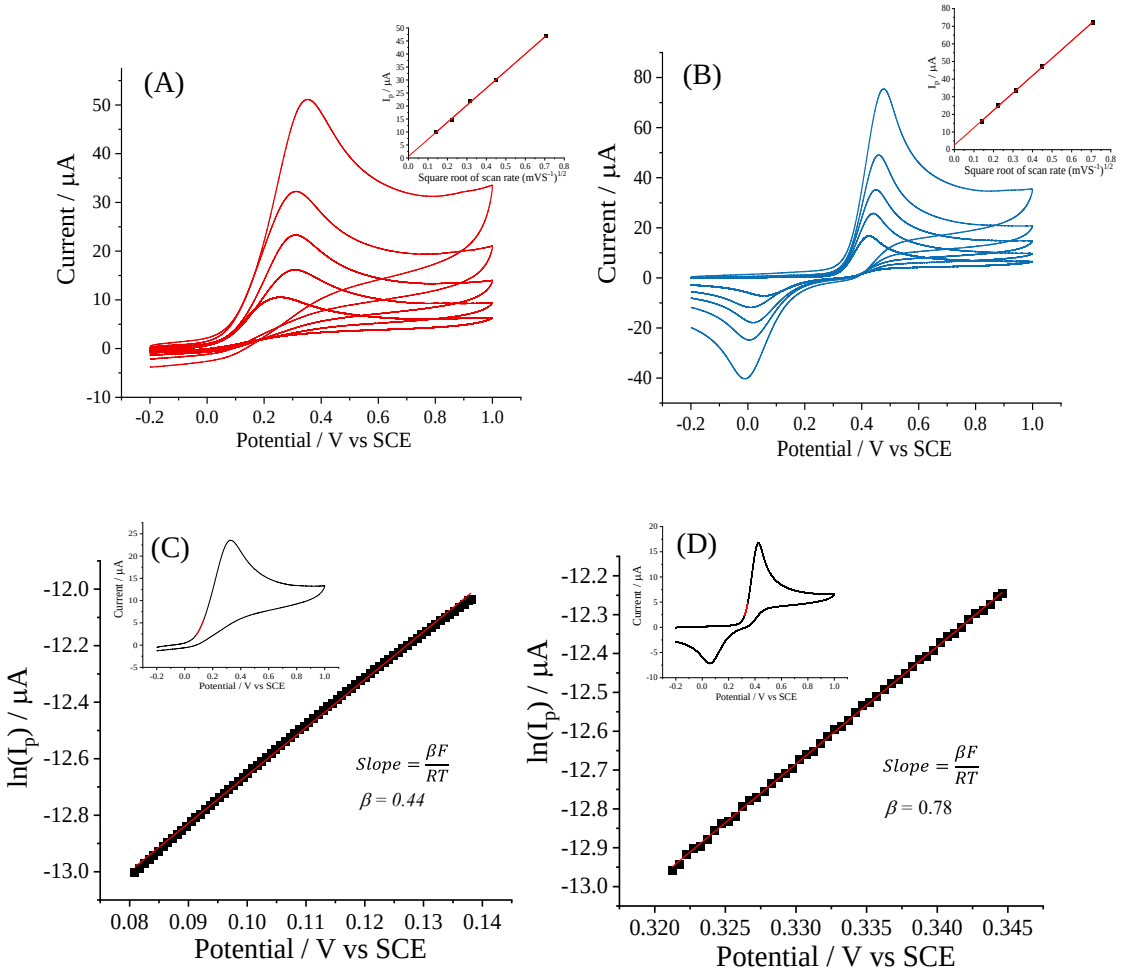


Figure 7.3. Triangular sweep cyclic voltammetric responses (A) 1 mM AA and (B) 1 mM AC at varying scan rates of 25 mVs^{-1}, 50 mVs^{-1}, 100 mVs^{-1}, 200 mVs^{-1}, 500 mVs^{-1} at GC electrode in PBS and the corresponding Tafel analysis of the voltammograms of 1 mM (C) AA and (D) AC, both recorded at 100 mVs^{-1}. Insets of (A) and (B): plots of peak currents versus square roots of scan rates of (A) 1 mM AA and (B) 1 mM. Insets of (C) and (D): the voltammograms (black line) and the Tafel analysis regions (highlighted in red regions) where diffusion plays an almost negligible role.

transferred oxidation process of AA and AC were determined from the Tafel slopes in the corresponding Tafel analysis, as shown in Figure 7.3 (C) and Figure 7.3 (D) to be 0.44 for AA and 0.78 for AC, confirming that the oxidations of both AA and AC correspond to processes where the first-electron transfer is the rate-determining step[17]. The diffusion coefficient of AA and AC at 298 K were calculated as 5.9×10^{-6} cm^2 s^{-1} for AA and 7.0×10^{-6} cm^2 s^{-1} for AC, using the irreversible multiple electron-transfer

Randles-Sevcik equations[17], assuming overall two-electron oxidations and the measured transfer coefficients. The values are in good agreement with literature values[31-34].

A cyclic voltammogram of the mixture containing 1 mM AA and 0.1 mM AC is shown in Figure 7.2 (black line). Two broad, merged, strongly overlapping peaks can be seen near 0.33 V and 0.44 V vs SCE, belonging to AA and AC, respectively. The high level of overlap indicates that a more sensitive and selective voltammetric method offering better resolution was required for the analysis of such mixtures.

7.3.1.2 The Determination of Acetaminophen in the Presence of Ascorbic Acid

Next, the electroanalytical responses of AC in the presence of high levels of AA were explored on a GC electrode. In order to evaluate the applicability of different voltammetric techniques for the detection of AC in AA/AC mixture system such that the optimal resolution of the voltammograms and sensitivity of detection can be obtained, the commonly used LSV, SWV, DPV techniques and the recently developed SCV method were employed and compared. As discussed above and previously[12, 14, 18, 35], SCV applies a semi-circular wave over a chosen potential window, which generates a near infinite scan rate at the mid-point of potential windows (defined as E_{mid}) and relatively low scan rates elsewhere. Thus it can selectively determine individual species in the mixtures by amplifying the signal closer to E_{mid} and relatively suppressing the signal further from E_{mid}. Voltammograms of 100 μM AC in the presence of 1 mM AA and with varying potential windows were recorded as shown in Figure 7.4 (A), suggesting an optimised E_{mid} as 0.6 V vs SCE for the detection of AC where a scan amplitude of 0.7 V is used to further optimise the resolution of the voltammogram (Figure 7.4 (B)). A similar

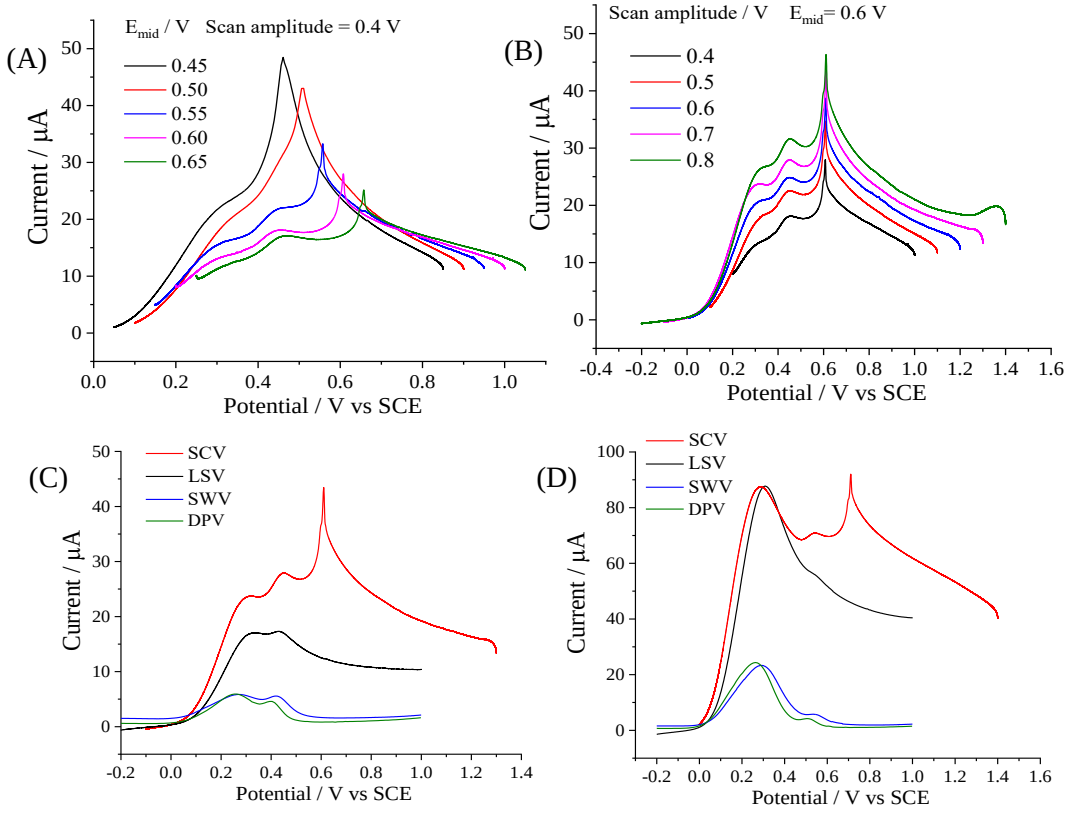


Figure 7.4. Semi-circular sweep voltammetric responses of 100 µM AC in the presence of 1mM AA at the GC electrode recorded at potential windows with (A) varying E_{mid} (B) varying scan amplitudes. Semi-circular sweep, linear sweep, square wave and differential pulse voltammetric responses of 100 µM AC in the presence of (C) 1 mM and (D) 5 mM AA. The E_{mid} of the potential windows used in SCV at the potential was 0.6 V vs. SCE in (C) and 0.7 V vs. SCE in (D). The scan amplitude and the average of scan rate used in (C)-(D) were 0.7 V and 50 mVs^{-1}, respectively.

procedure was performed and the potential window for the voltammograms of 100 µM AC in the presence of an even higher concentration of 5 mM AA was centred at 0.7 V vs SCE with a scan amplitude of 0.7 V applied. Figure 7.4 (C) and 7.4 (D) compare semi-circular voltammetric responses under the optimised potential windows with the linear, square wave and differential pulse voltammetric responses of 100 µM AC in the presence of 1 mM and 5 mM AA, at the same average scan rate of 50 mVs^{-1}. It can be seen that LSV resulted in the poorest resolution, whereas SWV, DPV and SCV were shown to separate the peaks of AA and AC to different extents. The peak separations in square

wave, differential pulse, semi-circular voltammograms were 147 mV, 146 mV and 137 mV, all representing an analytically useful improvement over the value of 99 mV in the linear sweep voltammogram. In particular, SCV provides the best-resolved peaks at 0.32 V, 0.45 V vs SCE in the 1 mM AA system and 0.29 V, 0.55 V vs SCE in the 5 mM AA system since the current responses generated at the potential of AC were closer to E_{mid} and largely amplified relative to the competing signal. The additional peak near E_{mid} arises from the nominally infinite transient scan rate (within limitations the of the potentiostat electronics) leading to strong capacitive currents[12, 18]. SCV is thus shown to be advantageous in the way that it can selectively amplify the current responses of species present in low concentrations despite the presence of another species of similar oxidation potential with 10- or 50-fold of the concentrations.

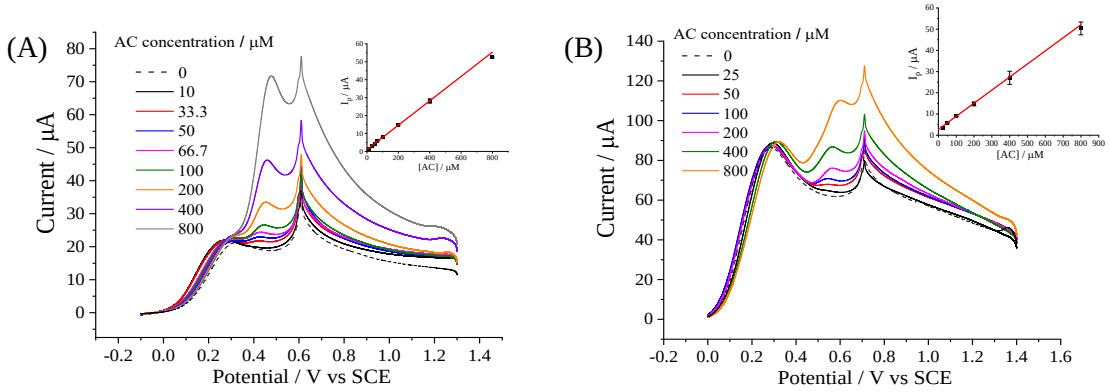


Figure 7.5. Semi-circular voltammetric responses of (A) 10-800µM AC in the presence of 1 mM AA and (B) 25-800µM AC in the presence of 5 mM AA. The E_{mid} of the potential windows was 0.6 V vs. SCE in (G) and 0.7 V vs. SCE in (H). The scan amplitude was 0.7 V. The average scan rate was 50 mVs^{-1}. Insets: Plots of subtracted peak currents obtained from linear sweep voltammograms versus AC concentration.

Having compared the resolutions of the voltammograms, we next explored the sensitivity of detection under different types of analytical voltammetry. Additions of 10–800 µM AC to 1 mM and 5 mM AA were conducted. The mixtures were prepared as three repeated sets and determined using SCV, LSV, SWV, DPV. Table 7.1 lists the linear detection ranges of AC and the peak current (I_p) – concentration ([AC]) relationships

obtained from the voltammograms in Figure 7.5 and Appendix B1. Similar linear ranges of 10–800 μM and 25–800 μM were found for the detection of AC in the 1 mM and 5 mM AA systems using the four studied voltammetric techniques. However, SCV showed the highest sensitivity of detection, showing a significant improvement of 2–3 times in comparison to the other techniques while retaining favourable linearity, even in the 5 mM AA system. It is concluded that SCV facilitates high-sensitivity detection of species in the presence of high interferent levels due to the amplified current responses and enhanced resolutions of the voltammograms.

Table 7.1. Comparison of linear ranges and sensitivities of detections of AC in the presence of 1 mM and 5 mM AA using LSV, SWV, DPV, SCV.

AA presence in the mixture systems	Techniques	Linear concentration range of AC	I_p / [AC]
1 mM	LSV	10–800 μM	I_p/ μA = 2.89 ×10^{-2}([AC] / μM) + 14.7, N=8, R^2=0.999
	SWV		I_p/ μA = 1.96 ×10^{-2} ([AC] / μM) + 3.37, N=8, R^2=0.999
	DPV		I_p/ μA = 2.22 ×10^{-2} ([AC] / μM) + 2.29, N=7, R^2=0.989
	SCV		I_p/ μA = 6.80 ×10^{-2} ([AC] / μM) + 1.08, N=8, R^2=0.998
5 mM	LSV	25–800 μM	I_p/ μA = 1.69 ×10^{-2} ([AC] / μM) + 53.0, N=6, R^2=0.964
	SWV		I_p/ μA = 1.88 ×10^{-2} ([AC] / μM) + 3.47, N=6, R^2=0.993
	DPV		I_p/ μA = 2.26 ×10^{-2} ([AC] / μM) + 1.79, N=6, R^2=0.994
	SCV		I_p/ μA = 6.17 ×10^{-2} ([AC] / μM) + 2.76, N=8, R^2=0.994

7.3.1.3 Real Sample Analysis

As discussed in Section 7.3.1.2, SCV shows a significant advantage in determining the AC content in the mixtures of AA and AC over other techniques displaying high sensitivity and favourable resolution. To assess the reliability and feasibility of SCV for the electroanalysis of real samples, analysis of three separate real samples was performed.

These were (A) commercial paracetamol capsules from the Sainsbury's, (B) the product Beechams Flu Plus from the Beechams and (C) the product EfferalganVitamineC from the UPSA. AC is the major component of the three studied medicinal samples and AA is present at a high level in the latter two cases. Three independent analyses were performed for each sample as described in section 7.2.3 and measured using SCV. As is apparent in Figure 7.6, the oxidation peak of AC was identified in the semi-circular voltammograms for all three medicines at 0.44 V vs SCE. A minor peak at ca. 0.2 V can be seen in Figure 7.6 (C), which is likely due to the contribution from a small amount of AA present in EfferalganVitamineC. The content of AC in the studied sample was determined using the calibration curve shown in Figure 7.5 (A), exhibiting results within a 6% deviation from the amount declared by the manufacturer (Appendix C). Subsequently, known concentrations of standard solutions were added to 'spike' to each sample. Figure 7.6 also

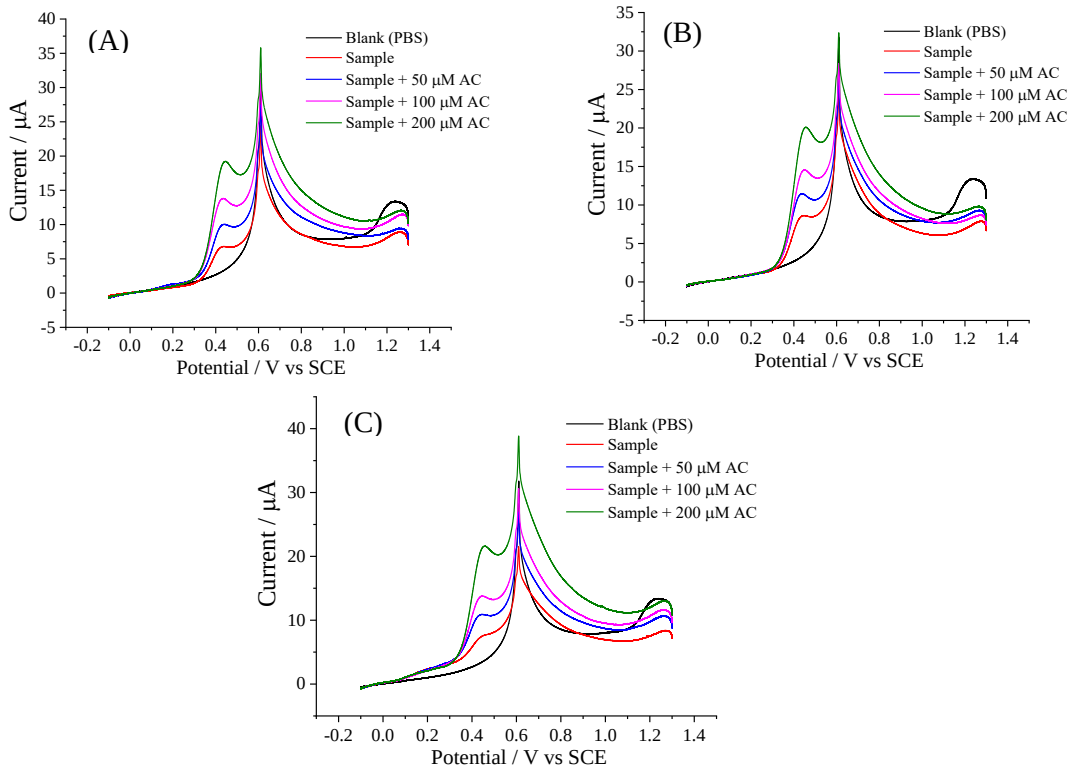


Figure 7.6. Standard additions of 50-200 µM of AC solutions to the real samples of (A) Paracetamol (B) Beechams (C) Efferalgan at the potential window with E_{mid}=0.6 V and the scan amplitudes was 0.7 V and the average scan rate was 50 $mVs^{-1.}$

depicts the resulting semi-circular voltammograms of samples with 50–200 μM AC standard solutions added. The recovery was calculated as 93–110% for the three medicines (Appendix C). Note that the recovery is close to 100%, indicating that AC is the only substance contributing to the measured current at the corresponding potential without interference caused by other compounds.

7.3.2 Glucose and Ethanol

7.3.2.1 Voltammetric Characterisation

The cyclic voltammetric response and electro-activity of glucose (Glu) and ethanol at a nickel micro-wire electrode in the alkaline buffer solution 1M KOH was first explored. The cyclic voltammograms of the separate components and the mixture of 1 mM glucose and 3.43 mM ethanol are displayed in Figure 7.7. As shown in Figure 7.7 (A), an electro-oxidation peak in KOH at Ni electrode was observed at 0.37 V vs SCE in the absence of either analyte, which was enhanced and shifted to a ca. 40mV more positive potential on the addition of 1 mM Glu. An extra signal at the potential of 0.45 V vs SCE was seen in Figure 7.7 (B) for a KOH solution containing 3.43 mM ethanol. The observed electrochemical signals were consistent with the reported mechanisms (Scheme 7.1)[36-38] of electro-oxidations of organic compounds including Glu and ethanol catalysed by Ni

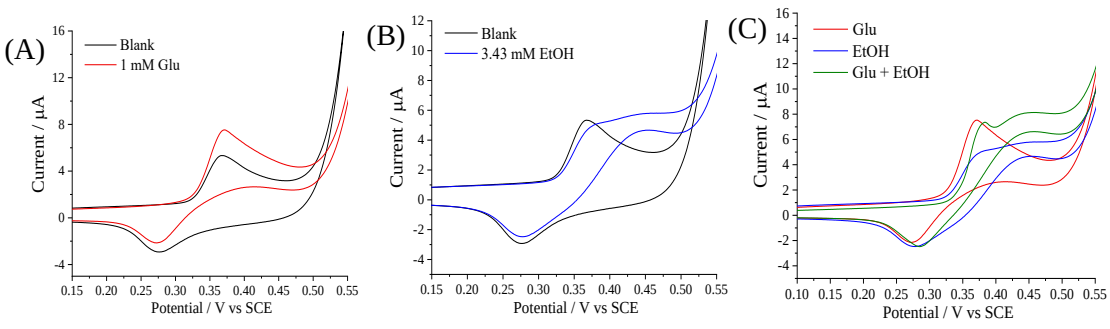
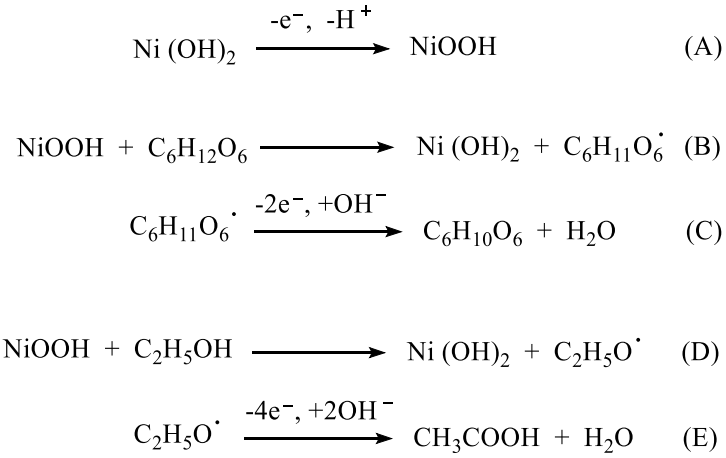


Figure 7.7. Triangular sweep cyclic voltammetric responses of (A)1 mM Glu and blank, (B)3.43 mM EtOH and blank and (C) the mixture containing 1 mM Glu and 3.43 mM EtOH comparing with the singular components at Ni micro-wire electrode measured in 1M KOH at a scan rate of 100 mVs^{-1}.

electrode in the alkaline electrolyte. As shown in scheme 7.1, the surface of Ni exists as Ni $(OH)_2$ in alkaline medium at the starting potentials used to record the voltammograms shown which undergoes electro-oxidation to form NiOOH (Scheme 7.1(A)). This process



Scheme 7.1. The catalytic mechanism of the oxidations of glucose (A)-(C) and ethanol (A), (D), (E) at Ni electrode[36-38].

is consistent with the oxidation observed at 0.37 V vs SCE depicted in Figure 7.7 (A). The NiOOH / Ni $(OH)_2$ redox couple catalyses the electrochemical oxidations of glucose and ethanol via the shown plausible intermediates in multistep reactions (Scheme 7.1(B)–(E))[4]. Note that the slight decrease of backward reduction peaks in Figure 7.7 (A) and (B) are due to the regeneration of $Ni(OH)_2$ following the catalytic oxidation of Glu or ethanol.

As depicted in Figure 7.7 (C), the signals of the mixture of Glu and ethanol appeared in the cyclic voltammogram overlap and are difficult to distinguish as the oxidations of glucose and ethanol occurs at very similar potentials, which correspond closely with the oxidation potential of the $Ni(OH)_2$ surface. The voltammetric response of ethanol at Ni micro-wire electrode resembles a ‘steady-state’ response, different from the ‘peak-shaped’ responses of Glu obtained at the same scan rate. A voltammetric method to separate the signals exhibiting different characteristics is evidently required for the simultaneous detection of glucose and ethanol in their mixtures.

7.3.2.2 Simultaneous Determinations of Glucose and Ethanol

Four analytical voltammetry, LSV, SCV, SWV and DPV were applied to compare their capabilities for resolving the glucose (Glu) / ethanol mixture. As discussed in section 7.3.1.2, the optimisation of the potential window used in SCV is crucial for separating closely overlapped signals. Figure 7.8 depicts the semi-circular voltammograms of the mixture containing 1 mM glucose and 3.43 mM ethanol measured at varying potential windows. The best-defined peaks were observed at 0.33 V and 0.44 V vs SCW when E_{mid} is positioned at 0.15 V vs SCE for a potential window of 0.8 V. Figure 7.9 compares the semi-circular voltammogram applying the optimised potential window with the linear-sweep, square wave and differential pulse voltammograms measured at the same average scan rate of 100 mVs^{-1} for the same mixture. The advantage of using SCV for the detection of Glu / ethanol mixture is evident as LSV, SWV and DPV all failed to effectively resolve the voltammetric signals from the mixture in contrast to SCV.

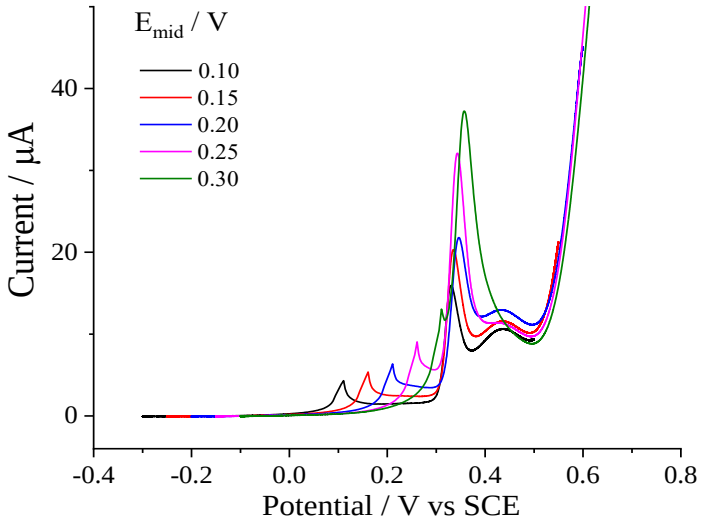


Figure 7.8. Semi-circular sweep voltammetric responses of the mixture 1 mM glucose and 3.43 mM ethanol at the Ni electrode recorded at potential windows with varying E_{mid}. The scan amplitude was 0.4 V and the average of scan rate was 100 mVs^{-1}.

The developed method was next applied for the determination of Glu or ethanol in the standard mixture solution. Figure 7.10 (A) shows the semi-circular responses of the additions of 0–13.7 mM ethanol to 1 mM Glu. The SCV data for different ethanol additions as analysed following subtraction of the curve seen in the absence of ethanol resulting in a peak current showing a linear dependence on ethanol concentration over the range of 0.274–13.7 mM (I_p/μA= 2.20 [EtOH] (μM) + 1.79 (μA), N=7, R^2=0.993, Figure 7.10 (A) Inset). It can be seen that over the studied concentration range, the voltammetric responses remained as 'peak-shaped' since a relatively low scan rate was applied to the oxidation potential of ethanol at Ni electrode, offering easily measurable peak currents having a linear relation with concentration. The semi-circular responses resulting from Glu additions made in the presence of 3.43 mM ethanol are depicted in Figure 7.10 (B). The linear range was found to be 0–1.25 mM for the observed peak currents contributed by the oxidations of both the Ni electrode and the added Glu. (I_p/μA= 9.87 [Glu] (μM) + 10.8 (μA), N=6, R^2=0.983, Figure 7.10 (B) Inset).

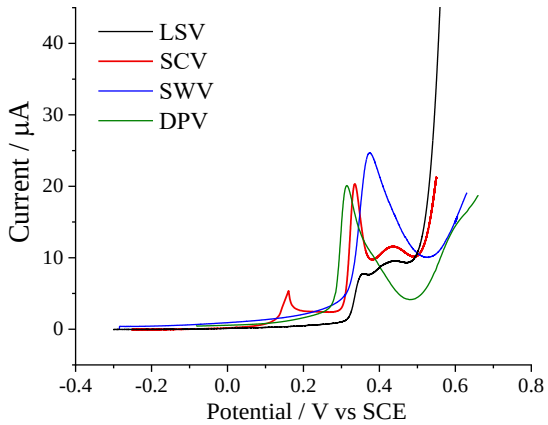


Figure 7.9. Linear sweep, semi-circular sweep, square wave,and differential pulse and voltammetric responses of the mixture 1 mM glucose and 3.43 mM ethanol. The average scan rate applied in all voltammograms were 100 mV s^{-1}. For SCV, the potential windows was centred at 0.15 V vs SCE and the scan amplitude was 0.4 V. For SWV, the frequency was 50 Hz, the step potential was 2 mV and the amplitude was 20 mV. For DPV, the step potential was 2 mV, the interval time was 20 ms, the modulation amplitude was 30 mV and the modulation time was 40 ms.

In the Glu / ethanol system, SCV has shown its advantage in resolving the mixtures over the other voltammetry at a Ni micro-wire electrode. The simultaneous electroanalysis of glucose and ethanol was achieved with good accuracy and simplicity using the suggested method without elaborate electrode modification.

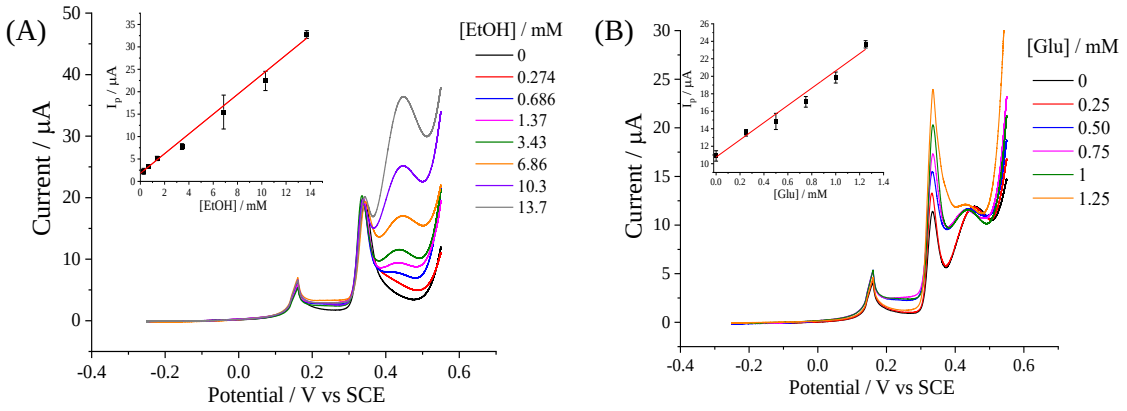


Figure 7.10. Semi-circular voltammetric responses of (A) 0-13.7 mM EtOH in the presence of 1 mM Glu (B) 0-1.25 mM Glu in the presence of 3.43 mM EtOH at Ni micro-wire electrode in 1M KOH. The E_{mid} was 0.15 V vs SCE, scan amplitude was 0.4 V and the average scan rate was 100 mVs^{-1}. Insets: Plots of peak currents obtained from semi-circular voltammograms versus (A) EtOH and (B) Glu concentration.

7.3.3 Hydroquinone and Catechol

7.3.3.1 Electrochemical Behaviours of Hydroquinone and Catechol

The cyclic voltammetric response of a 1:1 mixture of 0.5 mM hydroquinone (HQ) and catechol (CC) was first explored in pH 7.4 PBS buffer at an unmodified GC electrode, a carbon-nanotube modified screen-printed electrode (CNT-SPE) and an MWCNT modified GC (MWCNT/GC) electrode. In the light of recently-developed voltammetric sensors for the dihydroxybenzene isomers using carbon-nanotube modified carbon-based electrodes[39-43] MWCNTs/GCs were prepared using a simple dropcast method fully described in section 7.2.2 The dropcast volume of MWCNTs-acetone suspension was

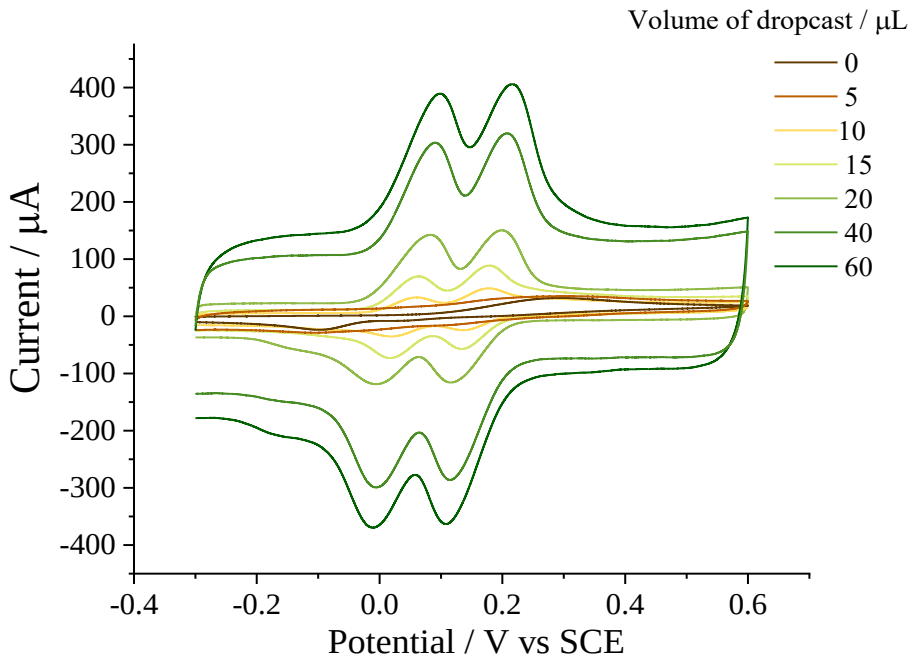


Figure 7.11. Cyclic voltammetric responses of the mixture contain 0.5 mM HQ and 0.5 mM AC at GC electrode dropcasted with 0-60 µL of MWCNTs-acetone suspension. The scan rate was 50 mVs^{-1}.

chosen as 20 µL, which was suggested by Figure 7.11 to be the minimum volume to form a sufficiently thick layer (mass of 20 µg, thickness estimated to be ca. 2 µm - see Appendix D1) covering the GC surface such that a stable and reproducible voltammetric response was observed. As depicted by the dotted line in Figure 7.12 (A), at the unmodified GC electrode, the oxidation peaks of HQ and CC are merged into one broad peak at 0.30 vs SCE. The resolution of the voltammetric responses slightly improved in the case of the commercially supplied CNT-SPE, depicted by the dashed line in Figure 7.12 (A), where two strongly overlapping peaks can be observed at 0.096 V and 0.20 V vs SCE. The solid line depicts the signals recorded at MWCNTs/GC. Two well-defined, distinguishable, sharp peaks were observed at 0.074 and 0.19 V vs SCE. The MWCNT material, particularly when used as a coating on GC electrode is thus shown to be

analytically useful in resolving the present mixture as expected from literature reports.

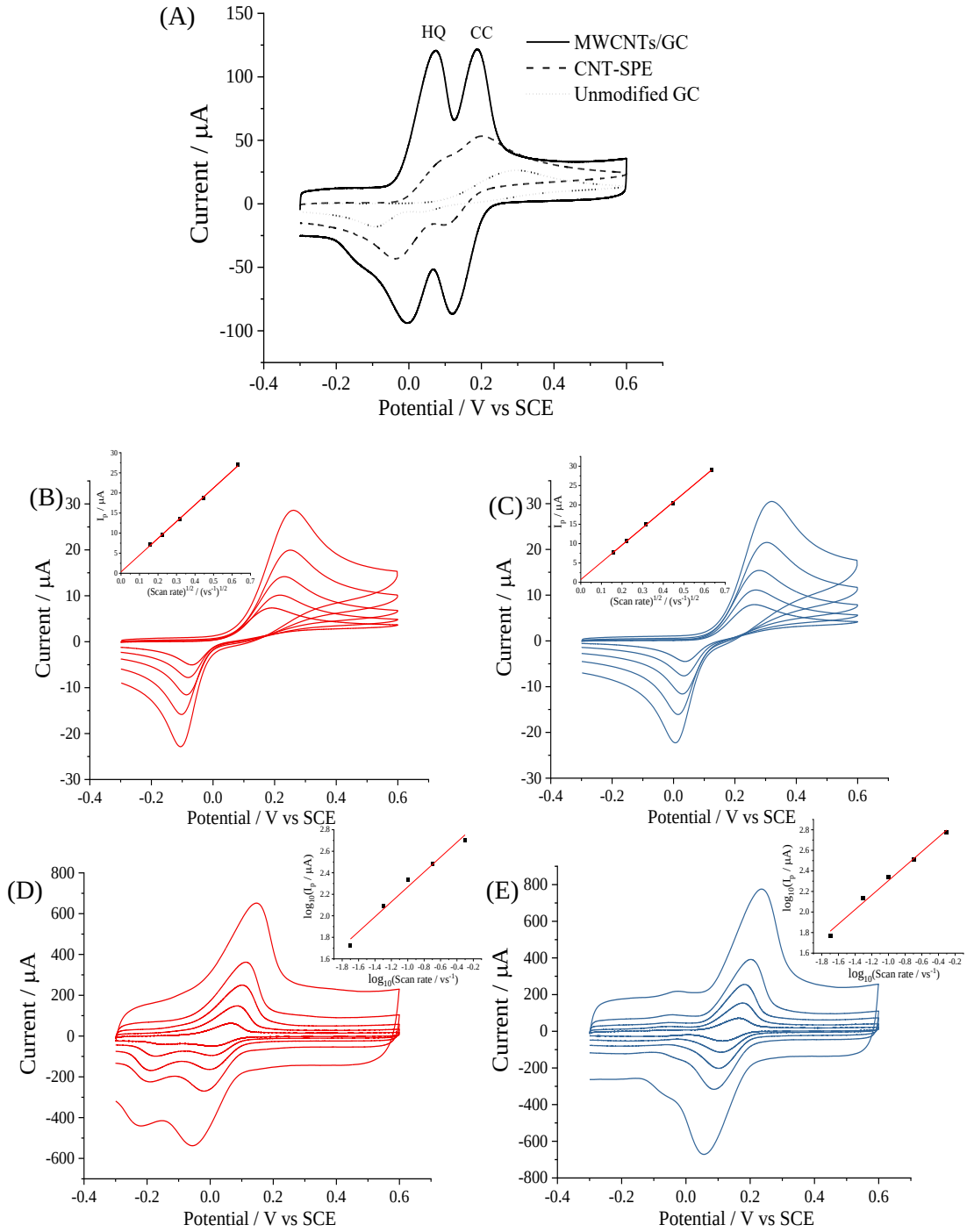


Figure 7.12. Triangular sweep cyclic voltammetric responses of (A) the mixture contain 0.5 mM HQ and 0.5 mM CC at unmodified GC electrode (dotted line), CNT-SPE (dashed line) and MWCNTs/GC electrode (solid line) at a scan rate of 50 mVs^{-1}, 0.5 mM HQ at (B) GC electrode and (D) and MWCNTs/GC electrode, 0.5 mM CC at (C) GC electrode and (E) MWCNTs/GC electrode, recorded at varying scan rates of 20 mVs^{-1}, 50 mVs^{-1}, 100 mVs^{-1}, 200 mVs^{-1}, 500 mVs^{-1}; Insets of (B) and (C): plots of peak current versus square roots of scan rates; insets of (D) and (E): the log-log plots of peak current versus scan rate. The dropcast volume at GC electrode was 20 µl.

Accordingly we employed MWCNTs/GC for further simultaneous determinations of HQ and CC and to explore the further improvements offered by SCV.

Next, the effect of scan rate on the peak currents of the separate individual species HQ and CC was studied. The cyclic responses of 0.5 mM HQ or CC at the unmodified GC and the MWCNTs/GC electrode were recorded separately at the scan rates of 20–500 mVs^{-1}, as shown in Figure 7.12 (B)–(E). Figure 7.12 (B) and 7.12 (C) depict the cyclic voltammograms and the plots of peak currents versus square root of scan rate obtained at unmodified GC electrode. Linear relations were found between the oxidation peak currents and the square root of scan rates, (Figure 7.12 (B) and 7.12 (C) Insets), suggesting the oxidation processes of HQ and CC were under diffusion-controlled at the unmodified GC electrode. The diffusion coefficients of HQ and CC were estimated using the peak currents measured at unmodified GC electrode via irreversible multiple electron-transfer *Randles-Sevcik* equation. Assuming the overall two-electron transfer[44] and the transfer coefficient was 0.5, the diffusion coefficients were found to be 7.9×10^{-6} cm^2/s for HQ and 9.0×10^{-6} cm^2/s for CC, consistent with the values reported in literature[45-46].

Figure 7.12 (D) and (E) show the cyclic voltammograms and the log-log plots of peak current versus scan rate obtained at MWCNTs/GC. It can be seen that at MWCNTs/GC electrode the oxidation potentials of HQ and CC shifted to the less positive potentials and the peak-peak separations were much reduced, indicating the oxidation processes possibly become apparently more electrochemically-reversible at the MWCNT surface. However a significant increase in the current responses is also observed. The slopes of the log-log plots were found to be 0.69 for the voltammograms of HQ and 0.70 for the voltammograms of CC. The observed slope values neither correspond to the value of 0.5, expected for the semi-infinite planar diffusion of the electroactive species, nor the value

of 1.0 reflecting the occurrence of pure 'thin-layer' diffusion[47-50] or adsorptive voltammetry. Instead the slope values are likely to suggest the electrochemical behaviour of HQ and CC is a mix of semi-infinite planar diffusion in the solution and diffusion within the layer coupled with 'thin-layer' effects and/or the adsorption within MWCNT layers. The significant contribution of the latter was also indicated by the observed large current increase. The transition from planar diffusion to 'thin-layer' diffusion can also cause the decreases in peak-peak separations and the shifts of peak oxidations seen in Figure 7.12 (D) and (E), facilitating the differentiation of the signals from each other in a mixture of HQ and CC[15,18]. In particular, the effect of thin layer diffusion is to shift the voltammetric signal to being close to the formal reversible potential of the couple under study and the voltammetric data shown in Figure 7.12 (D) and (E) suggests a difference of ca. 110 mV in the values for CC and HQ.

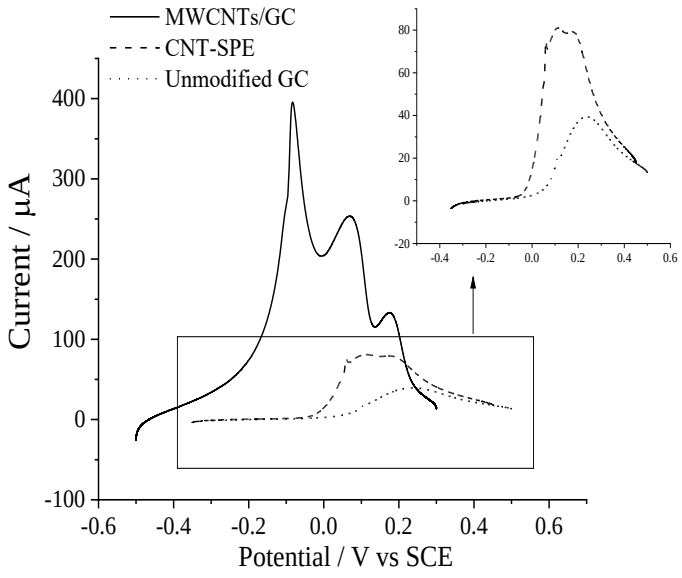


Figure 7.13. Semi-circular voltammetric responses of the mixture contain 0.5 mM HQ and 0.5 mM CC at unmodified GC electrode (dotted line), E_{mid} was 0 V vs SCE; CNT-SPE (dashed line) E_{mid} was 0.05 V vs SCE; and at MWCNTs/GC electrode (solid line), E_{mid} was -0.10 V vs SCE. The scan amplitudes were 0.4 V and the average scan rate was 50 mVs^{-1} in all cases.

Attempts to usefully resolve the voltammetric signals from mixtures of HQ and CC using SCV at a bare GC electrode or at an SPE-CNT were unsuccessful (Figure 7.13) so the SCV technique was next applied to enhance the sensitivity of detection via the use of MWCNT/GC electrodes.

7.3.3.2 Simultaneous Determinations of Hydroquinone and Catechol at an MWCNTs/GC Electrode

The analytical response of mixtures containing 5 – 500 mM concentrations of HQ or CC were investigated using LSV, DPV and SCV, similar to the work described in section 7.3.1.2. The mixed solutions were prepared by standard additions of HQ or CC to obtain the concentration range of 5-500 μM in the mixtures. The resulting voltammograms at MWCNTs/GC are shown in Figure 7.14 and Appendix B2. As discussed in 7.3.1.2, in the semi-circular voltammogram, the peaks can be selectively amplified when the E_{mid} of the applied potential window was shifted closer to the corresponding oxidation potentials. Semi-circular voltammetric measurements were made on 500 μM HQ+CC 1:1 mixture using potential windows with varying E_{mid} (Figure 7.14 (A)). As shown in Figure 7.14 (B)-(D), E_{mid} was adjusted to -0.10 V vs SCE and to 0.35 V vs SCE, for the separate selective determination of HQ and CC, respectively, where the optimal resolutions of both HQ and CC signals with selective amplifications were obtained. Under the chosen SCV potential window for HQ, the HQ oxidation peak was observed at 0.07 V vs SCE and is significantly larger in size than the CC oxidation peak observed at 0.17 V vs SCE. The additional peak at E_{mid} arises from capacitive currents which are largest when the instantaneous sweep rate is greatest. Similarly under the SCV when the potential window is suitably optimised for CC the relative sizes of HQ and CC peaks are reversed and the CC oxidation peak at 0.17 V vs SCE is enhanced. Figure 7.14 (B) compares linear sweep,

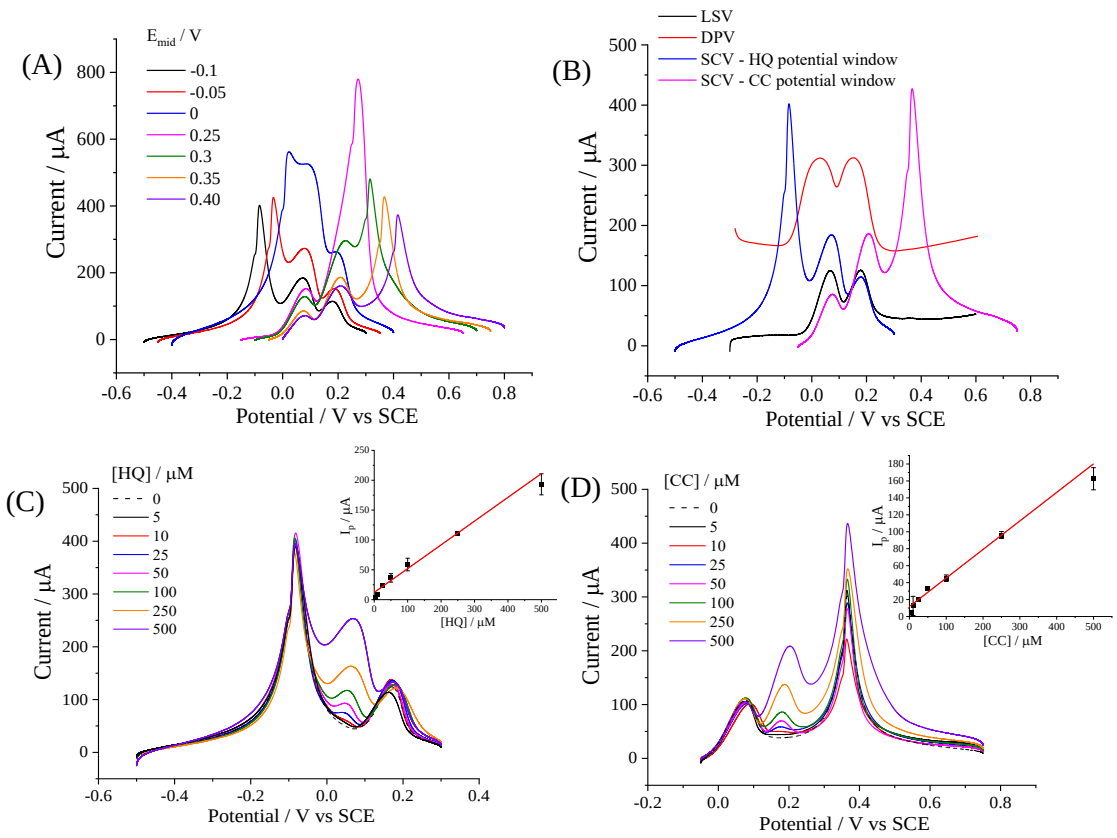


Figure 7.14. (A) Semi-circular sweep voltammetric responses of the 1:1 mixture containing 500 µM HQ and CC 1:1 at the GC electrode recorded at potential windows with varying E_{mid}. (B) Linear, differential pulse and semi-circular voltammetric responses of 500 µM HQ+CC 1:1 mixture. Semi-circular voltammetric responses of (C) 5-500µM HQ in the presence of 500 µM CC (D) 5-500 µM CC in the presence of 500 µM HQ at MWCNTs/GC electrode. The average scan rate applied in all voltammograms were 50 mV s^{-1}. For SCV, the HQ potential windows were centred at -0.10 V vs. SCE and the CC potential window was centred at 0.35 V vs. SCE. The scan amplitude applied in (A)-(D) was 0.4 V. Insets of (C) and (D): plots of subtracted peak currents obtained from semi-circular voltammograms versus (C) HQ and (D) CC concentration.

differential pulse and semi-circular voltammograms of 500 µM HQ+CC 1:1 mixture recorded at MWCNTs/GC at the same average scan rate of 50 mVs^{-1}. It can be seen from Figure 7.14 (B) that overall good resolutions were obtained via all three voltammetric techniques owing to the merit of using the MWCNTs/GC electrode, as discussed in 7.3.3.1. In comparison to LSV and SCV, DPV resulted in broader peaks but offers large peak currents due to the large extent of apparent reversibility in the present reaction system.

The linear ranges and sensitivities of the simultaneous detections of HQ and CC in their mixtures are compared as shown in Table 7.2. The calibration curve expressions of I_p-[HQ] and I_p-[CC] suggest that in the cases of both HQ and CC, a linear range of 5-500 mM were found using LSV and SCV. SCV offers the more favourable sensitivity due to the selective amplification of the oxidation peaks of HQ and CC under the different potential windows. It is evident that SCV is particularly useful in sensitivity enhancement for systems showing full or partial thin-layer voltammetry where the peak currents scale linearly with scan rate rather than the square root of scan rate as for semi-infinite diffusive voltammetry leading to a larger relative sensitivity for SCV under these conditions.

Table 7.2. Comparison of linear ranges and sensitivities of simultaneous detections of HQ and CC using LSV, SWV, DPV, SCV.

Presence of CC in mixtures	Techniques	Linear concentration range of HQ	I_p / [HQ]
500 μM	LSV	5–500 μM	I_p/ μA = 0.248 ([HQ]/ μM) + 0.588, N=7, R^2=0.994
	DPV	5–100 μM	I_p/ μA = 1.18 ([HQ]/ μM) + 21.3, N=5, R^2=0.916
	SCV	5–500 μM	I_p/ μA = 0.398 ([HQ] / μM) + 12.2, N=7, R^2=0.998
Presence of HQ in mixtures	Techniques	Linear concentration range of CC	I_p / [CC]
500 μM	LSV	5–500 μM	I_p/ μA = 0.196 ([HQ]/ μM) + 16.4, N=7, R^2=0.977
	DPV	5–100 μM	I_p/ μA = 0.960 ([HQ]/ μM) + 18.4, N=5, R^2=0.947
	SCV	5–500 μM	I_p/ μA = 0.337 ([HQ] / μM) + 11.8, N=7, R^2=0.970

In the developed method, MWCNTs/GC was used to distinguish the mixtures of HQ and CC, the isomers oxidised at very similar potentials, in combination with the employment of SCV which reinforced the resolutions of the voltammograms and improved the sensitivity of detection ca. 1.6 times from using conventional LSV in the concentration range of 5–500 μM.

7.4 Conclusions

We have shown the value of using the novel voltammetric method of SCV for use in the electroanalysis of mixtures of ascorbic acid/acetaminophen, glucose/ethanol and hydroquinone /catechol. Compared to other conventional analytical voltammetry, LSV, DPV and DPV, SCV shows a significant advantage for the selective detections of the species in the model systems in the following two aspects. First, SCV resolves signals that are strongly overlapped and are not distinguished using other voltammetry, offering the best possible voltammetric resolution amongst the methods compared. Second, SCV amplifies its peak current thus improving the sensitivity of detection. Using SCV at unmodified GC, Ni or MWCNTs drop-casted GC electrodes for the simultaneous detection of species in each of the above analytical systems improves the analytical performance over the conventional methods, serving as a simple and accurate alternative to the existing electrochemical methodology without resort to elaborate electrode modification and/or strict experimental conditions.

Bibliography

1. J. Wang, *Analytical electrochemistry*, Wiley-VCH, Hoboken, N.J., 3rd edn., 2006.
2. C. M. A. Brett and A. M. O. Brett, *Electrochemistry : principles, methods, and applications*, Oxford University Press, Oxford, 1993.
3. Á. Molina and J. González, *Pulse Voltammetry in Physical Electrochemistry and Electroanalysis Theory and Applications*, 1st edn., 2016.
4. K. E. Toghill and R. G. Compton, *International Journal of Electrochemical Science*, 2010, **5**, 1246-1301.
5. R. Wilson and A. P. F. Turner, *Biosensors and Bioelectronics*, 1992, **7**, 165-185.
6. L. Xiong and R. G. Compton, *International Journal of Electrochemical Science*, 2014, **9**, 7152-7181.
7. Honeywell, https://sensing.honeywell.com/, (accessed December 2020).
8. Alphasense, http://www.alphasense.com/, (accessed December, 2020).
9. Citytech, https://www.citytech.com/en-gb/, (accessed December, 2020).
10. Sensirion, https://www.sensirion.com/en/, (accessed December, 2020).
11. Y. Uchida, E. Katelhon and R. G. Compton, *Journal of Electroanalytical Chemistry*, 2018, **823**, 465-473.
12. Y. Uchida, E. Katelhon and R. G. Compton, *Journal of Electroanalytical Chemistry*, 2018, **818**, 140-148.
13. Y. Uchida, E. Kätelhön and R. Compton, *Journal of Electroanalytical Chemistry*, 2019, **848**, 113290.
14. Y. Uchida, E. Katelhon and R. G. Compton, *Journal of Electroanalytical Chemistry*, 2019, **835**, 60-66.
15. Y. Uchida, E. Kätelhön and R. G. Compton, *Journal of Electroanalytical Chemistry*, 2017, **801**, 381-387.
16. Y. Uchida, E. Kätelhön and R. G. Compton, *Journal of Electroanalytical Chemistry*, 2018, **810**, 135-144.
17. R. G. Compton and C. E. Banks, *Understanding voltammetry*, World Scientific Publishing Europe, London, 3rd edn., 2018.
18. Y. Wang, L. Chen and R. G. Compton, *Food Chemistry*, 2020, **323**, 126844.
19. R. Săndulescu, S. Mirel and R. Oprean, *Journal of Pharmaceutical and Biomedical Analysis*, 2000, **23**, 77-87.
20. M. E. Bosch, A. J. R. Sánchez, F. S. Rojas and C. B. Ojeda, *Journal of Pharmaceutical and Biomedical Analysis*, 2006, **42**, 291-321.
21. S. J. Padayatty, A. Katz, Y. Wang, P. Eck, O. Kwon, J.-H. Lee, S. Chen, C. Corpe, A. Dutta, S. K. Dutta and M. Levine, *Journal of the American College of Nutrition*, 2003, **22**, 18-35.
22. Y. Kitagawa, K. Kitabatake, M. Suda, H. Muramatsu, T. Ataka, A. Mori, E. Tamiya and I. Karube, *Analytical Chemistry*, 1991, **63**, 2391-2393.
23. L. V. Shkotova, N. Y. Piechniakova, O. L. Kukla and S. V. Dzyadevych, *Food Chemistry*, 2016, **197**, 972-978.
24. T. Xie, Q. Liu, Y. Shi and Q. Liu, *Journal of Chromatography A*, 2006, **1109**, 317-321.
25. C. Batchelor-McAuley, J. Ellison, K. Tschulik, P. L. Hurst, R. Boldt and R. G. Compton, *Analyst*, 2015, **140**, 5048-5054.
26. K. Chaisiwamongkhol, C. Batchelor-McAuley, S. V. Sokolov, J. Holter, N. P. Young and R. G. Compton, *Applied Materials Today*, 2017, **7**, 60-66.

27. Y. Y. Chan, A. Y. S. Eng, M. Pumera and R. D. Webster, *ChemElectroChem*, 2015, **2**, 1003-1009.
28. I. F. Hu and T. Kuwana, *Analytical Chemistry*, 1986, **58**, 3235-3239.
29. R. Rice, C. Allred and R. Mccreery, *Journal of Electroanalytical Chemistry*, 1989, **263**, 163-169.
30. D. Nematollahi, H. Shayani-Jam, M. Alimoradi and S. Niroomand, *Electrochimica Acta*, 2009, **54**, 7407-7415.
31. D. Robinson, J. E. Anderson and J. L. Lin, *Journal of Physical Chemistry*, 1990, **94**, 1003-1005.
32. A. A. Ensafi, B. Rezaei, S. Z. M. Zare and M. Taei, *Sensors and Actuators B: Chemical*, 2010, **150**, 321-329.
33. A. C. F. Ribeiro, M. C. F. Barros, L. M. P. Veríssimo, C. I. A. V. Santos, A. M. T. D. P. V. Cabral, G. D. Gaspar and M. A. Esteso, *The Journal of Chemical Thermodynamics*, 2012, **54**, 97-99.
34. R. R. Pandey, H. S. Alshahrani, S. Krylyuk, E. H. Williams, A. V. Davydov and C. C. Chusuei, *Electroanalysis*, 2018, **30**, 886-891.
35. Y. Wang and R. G. Compton, *ChemElectroChem*, 2020, **7**, 3508-3516.
36. M. Fleischmann, K. Korinek and D. Pletcher, *Journal of Electroanalytical Chemistry and Interfacial Electrochemistry*, 1971, **31**, 39-49.
37. M. Fleischmann, K. Korinek and D. Pletcher, *Journal of the Chemical Society, Perkin Transactions 2*, 1972, 1396-1403.
38. C. Zhao, C. Shao, M. Li and K. Jiao, *Talanta*, 2007, **71**, 1769-1773.
39. Z. Wang, S. Li and Q. Lv, *Sensors and Actuators B: Chemical*, 2007, **127**, 420-425.
40. D.-M. Zhao, X.-H. Zhang, L.-J. Feng, L. Jia and S.-F. Wang, *Colloids and Surfaces B: Biointerfaces*, 2009, **74**, 317-321.
41. A. J. S. Ahammad, T. Akter, A. A. Mamun, T. Islam, M. M. Hasan, M. A. Mamun, S. Faraezi, F. Z. Monira and J. K. Saha, *Journal of the Electrochemical Society*, 2018, **165**, B390-B397.
42. F. Hu, S. Chen, C. Wang, R. Yuan, D. Yuan and C. Wang, *Analytica Chimica Acta*, 2012, **724**, 40-46.
43. X. Yue, S. Pang, P. Han, C. Zhang, J. Wang and L. Zhang, *Electrochemistry Communications*, 2013, **34**, 356-359.
44. T. A. Enache and A. M. Oliveira-Brett, *Journal of Electroanalytical Chemistry*, 2011, **655**, 9-16.
45. E. Burestedt, A. Narvaez, T. Ruzgas, L. Gorton, J. Emnéus, E. Domínguez and G. Marko-Varga, *Analytical Chemistry*, 1996, **68**, 1605-1611.
46. W. M. Flarsheim, Y. M. Tsou, I. Trachtenberg, K. P. Johnston and A. J. Bard, *Journal of Physical Chemistry*, 1986, **90**, 3857-3862.
47. I. Streeter, G. G. Wildgoose, L. Shao and R. G. Compton, *Sensors and Actuators B: Chemical*, 2008, **133**, 462-466.
48. M. C. Henstridge, E. J. F. Dickinson, M. Aslanoglu, C. Batchelor-McAuley and R. G. Compton, *Sensors and Actuators B: Chemical*, 2010, **145**, 417-427.
49. G. P. Keeley and M. E. G. Lyons, *International Journal of Electrochemical Science*, 2009, **4**, 794-809.
50. M. J. Sims, N. V. Rees, E. J. F. Dickinson and R. G. Compton, *Sensors and Actuators B: Chemical*, 2010, **144**, 153-158.

Chapter 8

Optimising Adsorptive Stripping Voltammetry; Strategies and Limitations

In this chapter, the widely employed electroanalytical technique of adsorptive stripping voltammetry (AdsSV) is critically assessed and evaluated at a wide and diverse range of unmodified and nano-particle modified carbon electrodes using the analyte fipronil as a paradigmatic case. The generic electroanalytical performances of the nano-particle modified electrodes are investigated and compared with the unmodified electrodes revealing similar LOD values and pointing to intrinsic limitations of AdsSV arising from the non-independence of the Faradaic and capacitive signals during the stripping step. Methods for facilitating the adsorption or using different waveforms that may offer a more favourable limit of detection (LOD) at the nano-particle modified electrodes are suggested and assessed, specifically the use of adsorption onto particles *prior* to their use for modifying electrodes and also the recently introduced method of semi-circular voltammetry (SCV).

The work presented in this Chapter 8 has been published as a first author paper in *ChemElectroChem*.

8.1 Introduction

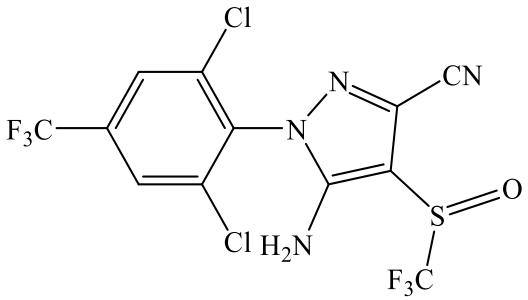
Stripping voltammetry is a widely adopted strategy in electro-analysis since it offers the opportunity to enhance the sensitivity of the electrochemical method and to reach lower limits of detection than those direct forms of voltammetry where the size of the analytical signal is inevitably limited by the rate of diffusion to the electrode[2, 3]. The constraint created by diffusional rate limitation imposes rather severe generic limitations on direct voltammetry such as linear sweep and cyclic voltammetry as well as, ultimately, the various forms involving pulses and waves[4]. This can be partly moderated by the use of microelectrodes[5] and their arrays[6-8] but invariably diffusion provides a fundamental rate-determining limitation constraining sensitivity.

The attraction of stripping voltammetry is that the analyte is pre-concentrated, including from ultra-dilute solutions below the detection range for direct voltammetry, onto the electrode surface prior to electrochemical analysis in the form of a potential sweep (linear or pulsed) in which a Faradaic current is passed as a result of the oxidation or reduction of the accumulated analyte. By prolonging the period of accumulation the limit of detection (LOD) can in favourable cases be suitably shrunk to meet the stringent demands of certain analytical challenges including the detection of manganese in tea[9], lead in petrol[10], and cadmium in blood[11].

Stripping voltammetry comes in four forms of which anodic and cathodic stripping voltammetry (ASV and CSV) are the most familiar and where a Faradaic reaction is used to realise the pre-concentration step, for example by the reduction of Pb (II) to metallic Pb in the case of ASV[10, 12] or its oxidation to PbO_2 in CSV[13]. These chemical processes are reversed during a linear potential sweep which either oxidises the Pb or reduces the PbO_2. The third type of SV is the recently introduced insertive stripping voltammetry [14,

[15], whilst the topic of this chapter is to explore the limitations of adsorptive stripping voltammetry (AdsSV).

In AdsSV, as the name suggests, pre-concentration occurs via adsorption onto the electrode surface. This may take place directly onto an electrode, for example, a mercury surface as in the AdsSV analysis of vanadium[16] or onto a modified electrode in which a convenient and attractive electrode, frequently carbon of some form, is supplemented by the addition of a surface layer designed to enhance adsorption so ideally promoting analysis via AdsSV. The surface modification may take the form of a chemisorbed monolayer, a polymeric layer, or as considered in this chapter a layer of bespoke particles. In the case of particle modified electrodes (PMEs) a huge diversity of materials has been used including carbon nanotubes[17-20], carbon black[21, 22], TiO_2 nanoparticles[23] and metal (Au, Ag, Pt *etc.*) nanoparticles[24-26]. We have shown elsewhere[27] that the requirements for the modification are rather stringent unless the particles form a conducting layer since if the binding of the analyte with the modifying particles is too weak then little signal enhancement is seen, but if the interaction is too strong then the analyte is not released sufficiently quickly to usefully benefit the analysis. Even with optimised absorption the merits of the approach can be limited to less than an order of magnitude improvement in analytical signals[26].



Fipronil

Scheme 8.1. Structure of Fipronil (5-amino-1-[2,6-dichloro-4-(trifluoromethyl)phenyl]-4-[(trifluoromethyl)sulfinyl]-1H-pyrazole-3-carbonitrile)

In this chapter, we consider the limitations of AdsSV with electrically conducting particle layers from a different perspective, namely to address the question as to what extent the *quantity* of material absorbed influences the analytical signal. This is an easily controllable variable in the design of PMEs via simply changing the number (or total mass) of particles adsorbed on the electrode surface. On first thought it is obvious that the Faradaic signal seen on the stripping potential scan will increase with the amount of material adsorbed and that the latter will enhance the voltammetric signal. However, ultimately the limit of detection is controlled by the ratio of the Faradaic analytical signal as compared to the background currents flowing during the potential scan in which the adsorbed analyte is oxidised or reduced. These Faradaic currents scale both with the voltage scan rate and with the amount adsorbed. However the amount adsorbed will reflect the surface area of the particles used for the modification. At the same time as the background currents are essentially capacitive they too will scale with both voltage scan rate and with the total particle surface area. Hence it is not obvious that increasing the number of particles modifying the surface is analytically helpful. It is the purpose of this chapter to explore if this prediction reflects analytical reality and also to compare different adsorbing surfaces to see the extent to which the inferences are general. Specifically this chapter considers surface modified with particles of carbon nanotubes (CNTs), graphene nano-platelets (GNPs) and carbon black (CB) as well as unmodified surfaces of glassy carbon (GC), basal place graphite (BPPG) and edge plane graphite (EPPG). In the case of particles such as CNTs we complement the AdsSV data with single entity electrochemical measurements[28-30] to confirm adsorption and the amount of this on the individual particles used in the PME.

As a model target analyte, we consider the molecule fipronil (Scheme 8.1), a phenyl-pyrazole insecticide used for pest control on crops, household pets and domestic

animals[31, 32]. Fipronil and its metabolites display neurotoxicity[33] and potential genotoxicity[34] towards non-target animals including humans[35, 36]. The wide use of fipronil has raised concerns because of the residual fipronil present in soil or aquatic ecosystems [33, 37] given its threat to human health[38]. The methods reported for the analysis of fipronil are mostly chromatographic[39-43], while recently some cheap and rapid techniques have emerged[44-51] including a few electrochemical methods[46-51]. The method we evaluate in the present chapter employing AdsSV on the aforementioned carbon electrodes, particularly on a CNT modified surface can be seen in principle as an electroanalytical method alternative to the existing analytical methods for fipronil determination. However the intrinsic limitations of the AdsSV method as evaluated in the following indicates a clear lower limit for electroanalytical detection via this approach; clarifying the reasons for this are the primary aims of this chapter.

8.2 Experimental

8.2.1 Chemicals and Apparatus

All chemicals were of analytical grade and were used received without any further purification. Fipronil (FIP, Pantanal®) and methanol (≥99.0% purity) were purchased from Sigma-Aldrich. The bamboo-like multi-walled carbon nanotubes (b-MWCNTs, 30 ± 10 nm diameter, 5–20 μm length, >95% purity) were purchased from NanoLab, Brighton, MA, USA. Graphene nano-platelets (GNPs, 15 μm in width, 6-8 nm in thickness) with a known average area of 297 ± 152 μm^2 (from scanning electron microscopy[1]) were purchased from Strem Chemicals, MA, USA. Carbon Black (CB, M 1100, Monarch®) was purchased from Cabot Performance, Billerica, MA, USA. All

aqueous solutions were prepared with deionised water with a resistivity of 18.2 MΩ cm at 298K (Millipore, MA, USA). The Britton–Robinson (BR) buffer (0.1 M, pH = 8.0) was prepared using sodium hydroxide (97% purity, Sigma-Aldrich), phosphoric acid (99.99% purity, Aldrich), acetic acid (99.5% purity, BDH), boric acid (99.5% purity, Aldrich) and potassium chloride (≥99.0% purity, Sigma-Aldrich). Stock solutions of FIP (5 mM) were prepared by dissolving FIP in methanol. All solutions of required concentrations were prepared freshly every day from the stock solution by dilution with the mixture of 60% B-R buffer (pH 8.0) and 40% methanol.

All electrochemical experiments were performed at 298K with a standard three-electrode configuration inside a Faraday cage by using an in-lab built potentiostat. As previously described[52], the potentiostat was software controlled by *Python* 3.5 to generate the required potential waveforms and measurements with low noise and a high sampling rate (100 kHz maximum).

8.2.2 Voltammetry on Carbon Macroelectrodes

For voltammetric experiments, several carbon-based macroelectrodes were used variously as the working electrode. A saturated calomel electrode (SCE, BASi Inc., Japan) was used as the reference electrode and a graphite rod as the counter electrode. The macroelectrodes employed as working electrodes were a glassy carbon (GC) electrode with a diameter of 3.0 mm, a basal plane pyrolytic graphite (BPPG) electrode with a diameter of 4.9 mm, an edge plane pyrolytic graphite (EPPG) with a diameter of 4.3 mm and the same glassy carbon electrode modified with carbon black (CB), multiwalled carbon nanotubes (MWCNTs) or graphene nanoplatelets (GNPs).

The GC and EPPG electrodes were polished on soft lapping pads with alumina of decreasing particle sizes (1.0, 0.3 and 0.05 μm) (Buehler, IL, UK), followed by sonication for 10 seconds in pure water. The BPPG electrode surface was prepared by polishing on the sandpaper of grade P4000 and then repeatedly for several times pressing on and then removing from the sticky tape, 'cellotape' (Henkel AG, Dusseldorf, Germany), before finally washing with acetone[53]. The CB, MWCNTs and GNPs modified GC electrodes were prepared by a dropcast method. The nanoparticle materials were first dispersed (1 mg/1 mL) in either pure methanol or methanol solutions containing varying concentrations of FIP by sonication for 30 minutes without further functionalisation. 2.5–30 μL of the obtained suspensions (with or without the modification by FIP) were then dropcasted (in 2.5 μL aliquots) onto the clean GC electrode, followed by solvent evaporation under a gentle N_2 flow[54, 55].

Cyclic voltammetric experiments were conducted at unmodified GC, BPPG, EPPG or modified GC electrodes in blank solution (the mixture of 60% B-R buffer (pH 8) and 40% methanol) or 0.1 mM FIP solution to investigate the influence of scan rate. Adsorptive stripping voltammetry (AdsSV), adsorptive square wave voltammetry (AdsSWV), adsorptive semi-circular sweep voltammetry (AdsSCV), prior-adsorptive stripping voltammetry (pAdsSV) were conducted in order to understand the adsorption process and assess the detection sensitivity at the carbon-based electrodes. AdsSV, AdsSWV and AdsSCV were conducted by immersing the electrode (unmodified GC, BPPG, EPPG or GC electrode dropcasted with unmodified MWCNTs or GNPs) in the standard solutions of varying concentrations of FIP. The accumulation of FIP onto the electrode surface was performed under open-circuit potential conditions with stirring of the solution for 0-6

minutes. The pAdsSV measurements were made in the blank solution using the GC electrode dropcasted with CB and GNPs pre-modified by FIP.

8.2.3 Nano-impact Experiments

Nano-impact experiments were conducted by measuring the chronoamperometry at a carbon fibre wire microelectrode system using the same reference and counter electrode as above. Note the potentiostat used in this work ensures an accurate conservation of the charge transferred during a particle-impact event[29]. The carbon fibre wire microelectrode was fabricated from a carbon fibre (diameter 7.0 μm, Goodfellow, Cambridge, UK) following the procedure introduced previously[56]. The length of the microelectrode was 1mm. 10 μL of MWCNT suspension prepared as described in 8.2.2 was added to 10 mL of the blank solution or the 0.1 mM FIP solution, followed immediately by a chronoamperometric measurement. The chronoamperograms were recorded for 20 s at varying potentials from 0.8–1.7 V vs SCE.

8.3 Results and Discussion

In the following sections, first, adsorptive stripping voltammetry (AdsSV) or, novelly, prior-adsorptive stripping voltammetry (pAdsSV) is applied to examine the electrochemical signals of fipronil (FIP) at six types of carbon electrode surfaces. The adsorption of FIP on glassy carbon (GC), basal plane pyrolytic graphite (BPPG), edge plane pyrolytic graphite (EPPG), multiwalled carbon nanotubes (MWCNTs) and graphene nanoplatelets (GNPs) surfaces are investigated and characterised. Next, the

adsorption of FIP on single MWCNTs is investigated via nano-impacts. Finally, in the last section, the electroanalytical performances of AdsSV on these five carbon electrode surfaces are compared. The effects of the types and the amounts of carbon materials on the detection limit are demonstrated, then, in combination with the results obtained in the previous two sections, explanations are offered for the presented merits and limitations of employing AdsSV at the unmodified and nano-particle modified surfaces. Also in this section, electroanalysis of FIP using adsorptive square wave (AdsSWV) and adsorptive semi-circular sweep voltammetry (AdsSCV) is evaluated at optimised MWCNT electrode surfaces.

8.3.1 Electrochemical Behaviour of Fipronil

The voltammetric responses of the FIP in a mixture of 60% pH 8.0 B-R buffer and 40% methanol were first explored at all carbon surfaces of interest. Figure 8.1 depicts the

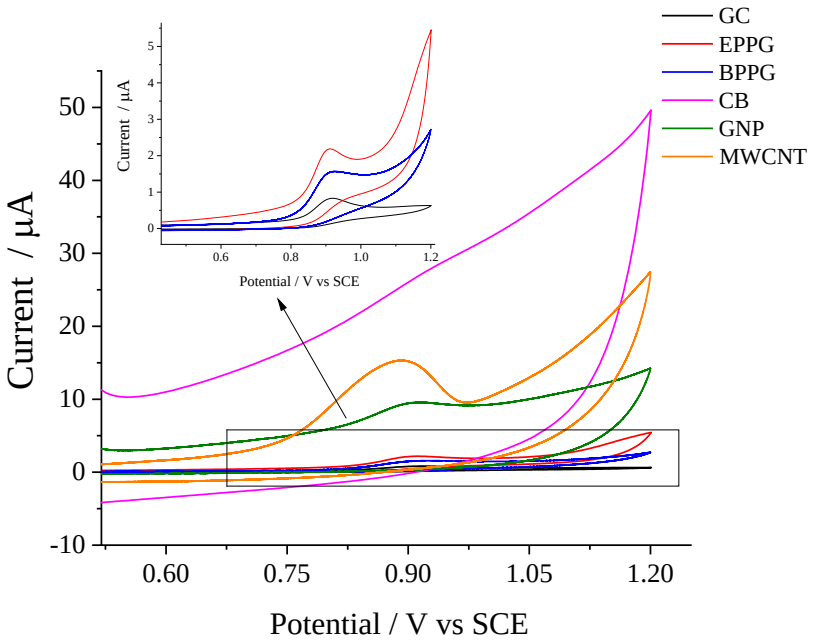


Figure 8.1. The adsorptive stripping cyclic voltammetric responses of 0.1 mM FIP on unmodified GC, BPPG, EPPG, CB modified GC, GNPs modified GC and MWCNTs modified GC electrode in a mixture of 40% methanol and 60% PH 8 B-R buffer. The voltammograms were either recorded after a 2-mintue open circuit accumulation or a dropcast of nanoparticle materials modified with FIP at the scan rate of 5 mV/s.

cyclic voltammetric responses of the 0.1 mM FIP solution obtained at the unmodified GC, EPPG and BPPG electrodes overlaid with those obtained at CB, GNP and MWCNT modified GC electrodes. The masses of MWCNTs, GNPs and CBs dropcasted on the GC electrode was 10 μg, 10 μg and 25 μg, respectively. The voltammetric responses at the electrode modified with other amounts of MWCNTs and GNPs are shown and discussed in section 8.3.3. The unmodified GC, EPPG, BPPG electrode and MWCNT modified GC electrode were immersed in the 100 μM FIP solution under open circuit conditions for an optimised accumulation time of 2 minutes (the optimisation is shown in Figure 8.2) and subsequently the voltammetric responses were recorded. The adsorption of FIP on GNPs and CB were facilitated via immersion in a 100 μM FIP methanol solution prior to dropcasting. The voltammetry at the electrode dropcasted with GNPs or CB was then recorded in a blank solution. This method used for GNPs and CB modified GC electrodes

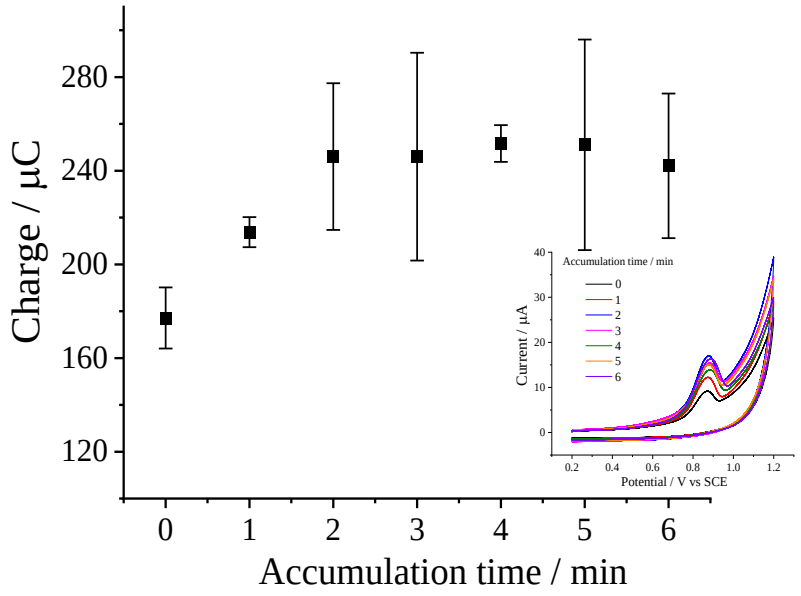
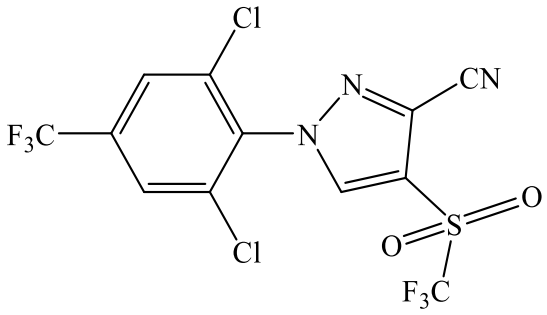


Figure 8.2. The plot of charge (error bar attained from three independent dropcasts) against accumulation time of 0-6 minutes under open circuit condition. The charges were obtained from the integration of peaks that were analysed by subtracting an 8th order polynomial fitted baseline from the voltammograms shown in the inset. Inset: The adsorptive stripping voltammetric responses recorded for MWCNT (10 μg) modified GC electrode immersing in 0.1 mM FIP solution at a scan rate of 5 mVs^{-1}

is introduced here as pAdsSV. In this method, thought to be novel, the modifying particles are saturated with the adsorbate *prior* to drop-casting in contrast to the usual method in which the sequence is reversed, namely drop-casting followed by transfer of the electrode to the analyte solution for analysis. We label this approach pAdsSV and have found it helpful in minimising the loss of particles from the electrode surface if long times are needed for accumulation. This technique was applied to enable a maximum adsorption of analyte to the electrode surface and hence boost the sensitivity of detection. This will be further demonstrated and discussed in section 8.3.3. The voltammograms were recorded using a slow scan rate of 5 mVs^{-1} to attain a favourable resolution of signals particularly for the nano-particle modified electrode surfaces. As shown in Figure 8.1, oxidation peaks were observed at similar potentials at all carbon surfaces, which are 0.92 V vs SCE for GC and BPPG, 0.91 V vs SCE for EPPG and GNP and 0.89 V vs SCE for MWCNT surface. No FIP related signal was seen on CB modified electrodes. This likely reflects structural differences between CB and the graphitic forms of carbon[57-60] leading to negligible adsorption on CB where graphitic planes are absent. CB was not investigated further.

Next, to further study the adsorption of FIP onto the various electrode surfaces, the effect of scan rate was investigated at the unmodified GC, BPPG and EPPG electrode, as



Fipronil Sulfone

Scheme 8.2. The structure of the possible product of fipronil oxidation, fipronil sulfone[46,61].

well as the MWCNTs and GNPs modified GC electrodes using the stripping voltammetry analytical procedures as described above. The results are shown in Appendix E. The peak currents are linear with scan rate and the slopes of the corresponding log-log plots were close to 1 at the five surfaces in the low scan rate ranges, suggesting the oxidation processes of FIP are surface controlled. The oxidation was suggested to correspond to a two-electron transfer process generating fipronil-sulfone[46] (structure shown in Scheme 8.2), which is a well-recognised oxidative degradation product of FIP[61].

Having identified the surface-bound nature of the FIP oxidation processes, the adsorptions of FIP on the five carbon surfaces were next characterised by considering the possible approximate applicability of the Langmuir isotherm[62]:

$$\theta = \frac{K[FIP]}{1 + K[FIP]} \tag{8.1}$$

where θ is the fractional occupancy of the adsorption sites, K is the equilibrium constant for adsorption and *[FIP]* is the concentration of FIP. Eqn. (8.1) can be re-written as:

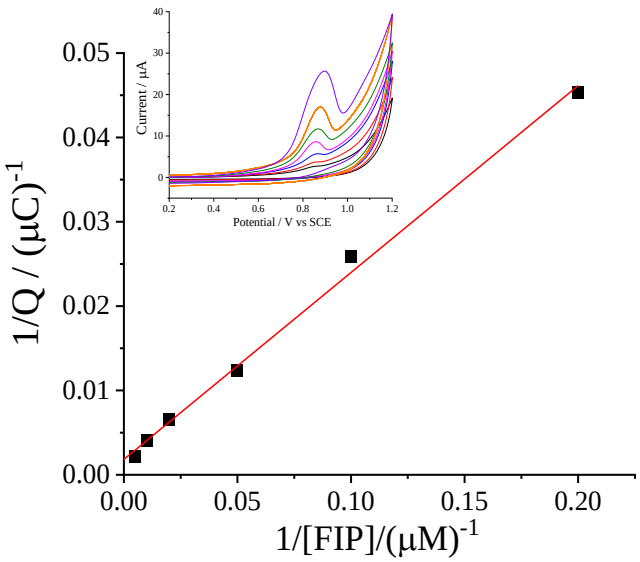
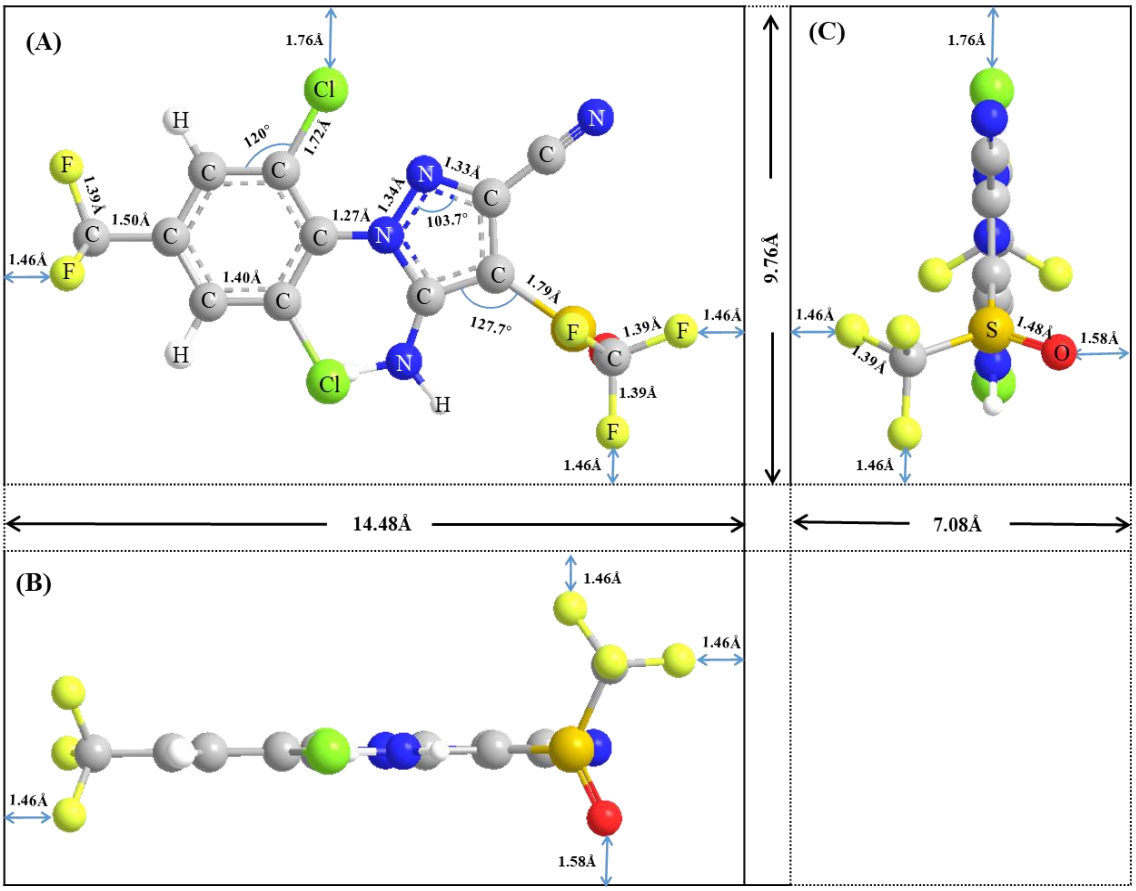


Figure 8.3. The plot of *1/Q* against *1/C* where the peak area values obtained from the adsorptive stripping voltammograms of 5-200 μM FIP at MWCNTs modified GC (inset). The peak areas were analysed by subtracting an 8th order polynomial fitted baseline from the original voltammograms.

$$\frac{1}{Q}=\left(\frac{1}{KQ}\right)\left(\frac{1}{[FIP]}\right)+\frac{1}{Q_{\max}} \qquad (8.2)$$

where Q is the voltammetrically measured charge transferred during oxidation of the species at the studied concentrations. Q_{max} is the maximum charge transfer at the surface saturated with FIP. Voltammetric responses at the GC, BPPG, EPPG, MWCNT and GNP surfaces were recorded in varying concentrations of FIP solutions using the same procedure as above. Figure 8.3 shows an example of Langmuir plot obtained from the voltammograms of 5–200 µM FIP recorded at the MWCNT modified GC electrode (shown in the inset of Figure 8.3). Linearity ((1/ Q (µC^{-1}) = (0.22±0.0070) 1/C (µM $^{-1}$) + (0.0018 ± 0.000067), R^2=0.996) was found in the double reciprocal plot, as predicted by the Langmuir isotherm. Thus K and Q_{max} were determined according to Eqn. (8.2) as (8.2



Scheme 8.3. Rectangular box model of FIP molecule: (A) flat view, (B) edgewise view and (C) endwise view.

± 0.3) $\times 10^{-3}$ $\mu m^{-1}$and (546 ± 20.3) μC, respectively. Similarly Q_{max} was determined for the other four carbon surfaces where similar linearity was observed. In comparison to the unmodified surfaces, the Q_{max} obtained at the particle modified electrode surfaces are significantly larger due to the much increased adsorption (Appendix F). In all cases the data were not inconsistent with the Langmuir isotherm.

The theoretical area per FIP molecule, A_{FIP} was estimated using a simple 'rectangular box model'[63, 64] as presented in Scheme 8.3. The dimensions of the molecule are shown in all three possible flat molecular orientations. All side lengths were estimated by trigonometry using bond lengths, bond angles and the van der Waals radii of the terminating atoms. The bond length, bond angles data were obtained from ChemDraw 16.0 software. The van der Waals radii of the terminating atoms values are those tabulated by Rowland[65]. The areas corresponding to the adsorption of FIP in flat (A), edgewise (B) and endwise (C) orientations A_{fl}, A_{ed} and A_{en} were estimated as 14×10^{-15} cm^2, 12.5×10^{-15} cm^2 and 7×10^{-15} cm^2 respectively. Assuming close-packed, monolayer adsorption of FIP and the number of electrons transferred (n) is 2, the number of molecules adsorbed on electrode surfaces (N_{ads}) can be thus determined from Q and the electron fundamental charge e (1.602×10^{-19} C) by $N_{ads} = Q/(ne)$. Accordingly the "real" surface area of the electrode, $A_{electrode}$, available for adsorption of FIP, can be estimated using N_{ads} and A_{FIP} by $A_{electrode} = N_{ads} \times A_{FIP}$. Table 8.1 lists the values of the charge transfer occurring in 0.1 mM FIP solution, Q_0 and the area, $A_{electrode}$ obtained for the five studied surfaces as well as the geometric areas of the three unmodified electrodes and the surface areas of the two modified electrodes characterised by the supplier and an independent SEM study[1]. As can be seen in Table 8.1, the electro-active surface areas of the unmodified electrodes were approximately 2.3–5.5 times of the geometric areas. Under the aforementioned

assumption of monolayer adsorption, this suggests a considerable contribution from the roughness of these surfaces. In fact the roughness factor for GC electrodes is reported as lying in the range 1.7–4.1[66]. High roughness levels of pyrolytic graphite electrode surfaces have also been noted[67-69]. However for the nano-entity modified electrode surfaces, the electro-active area values indicate likely sub-monolayer adsorption at both GNP and MWCNT surfaces. The low levels of adsorptions are possibly caused by desorption[63] of FIP and/or the aggregation/agglomeration of the dropcasted MWCNTs leading to the reduced surface accessibility. To further investigate this and to assess the potential of improving the detection sensitivity the single entity electrochemistry of MWCNT was studied as an example in the next section.

Table 8.1. The charge, geometric or characterised areas electro-active areas found in the 0.1 mM FIP solution for GC, BPPG, EPPG, MWCNT, GNP surfaces.

Surface	Q_0/ **μC**	**Geometric or characterised area /cm^2**	**Electro-active area / cm^2 assuming the molecule landed with the side of:**		
			flat view(A)	Edgewise view (B)	Endwise view (C)
GC	8.83	7.07×10^{-2}	39×10^{-2}	34×10^{-2}	19×10^{-2}
BPPG	19.9	18.9×10^{-2}	88×10^{-2}	78×10^{-2}	43×10^{-2}
EPPG	18.2	14.5×10^{-2}	80×10^{-2}	71×10^{-2}	40×10^{-2}
MWCNT	246	20–40[a]	11	10	5
GNP	42.2	6.2 ± 3.2[b]	1.9	1.6	0.9

[a] The value was calculated from the specific surface area provided by the supplier NanoLab

[b] The value was estimated using SEM[1], see Appendix D2 for the calculation.

8.3.2 Adsorption on Single Carbon Nanotubes: A Nano-impact Study

The oxidation of FIP on individual MWCNTs was investigated using the nano-impact method[28-30]. 10 μL of an MWCNT in methanol suspension was added to 10 mL of a solution of 60% pH 8.0 B-R buffer and 40% methanol containing 0.1 mM FIP and was

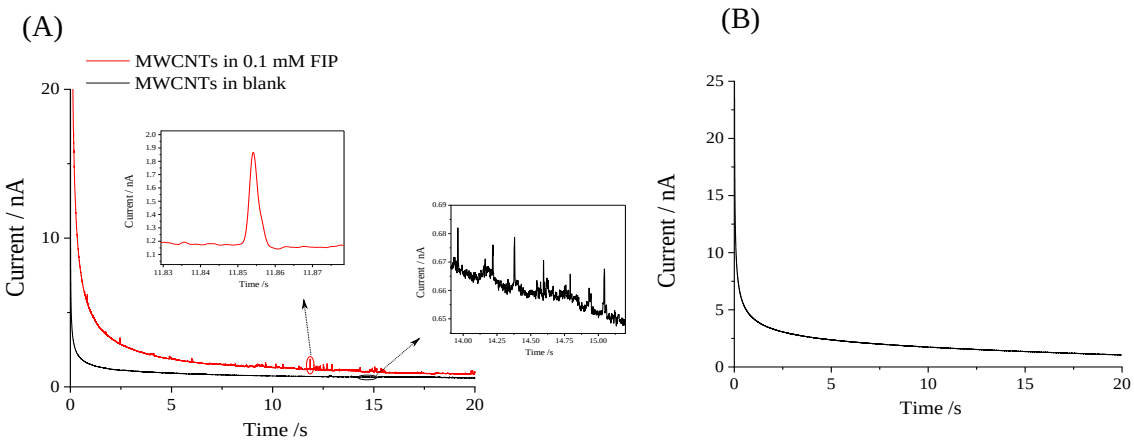


Figure 8.4. (A) Representative chronoamperogram recorded at 1.6 V vs SCE with the presence and absence of 0.1 mM FIP in a 10 µg MWCNT suspension for the duration of 20 seconds. The enlarged graphs show the oxidative spikes resulting from FIP oxidation (red) and the capacitive spikes (black). (B)Representative chronoamperometric profile of 0.1 M FIP in a mixture of 60% pH 8 B-R buffer solution and 40% methanol without the addition of MWCNT suspension at 1.6 V vs. SCE.

left for 5 minutes allowing for the adsorption of FIP. A fresh carbon fibre electrode was immersed in the new suspension and chronoamperograms were immediately recorded with the potential held at a value in the range of 0.8–1.7 V vs SCE for the duration of 20 seconds. Chronoamperograms were also recorded at the same potentials in the same FIP solution but without the presence of MWCNTs and in the suspension of the same amount of MWCNTs in the blank solution without the presence of FIP. As shown in the representative chronoamperograms in Figure 8.4 (A), large oxidative spikes (of average duration (7.6 ± 3.3) s) were observed for the suspensions of MWCNTs in the presence of FIP and inferred to be Faradaic. Much smaller spikes (of average duration (4.7 ± 2.2) s) were observed in the absence of FIP and concluded to be capacitive (see below). Each spike corresponds to a collision of an individual MWCNT with the micro-electrode as a result of the Brownian motion of the MWCNTs[29, 30]. This was confirmed by Figure 8.4 (B) showing the chronoamperogram recorded in the 0.1 mM FIP solution at the same potential of 1.6 V SCE in the absence of MWCNTs where no spikes were detected. The average charge passed per spike were obtained from averaging the integration of each

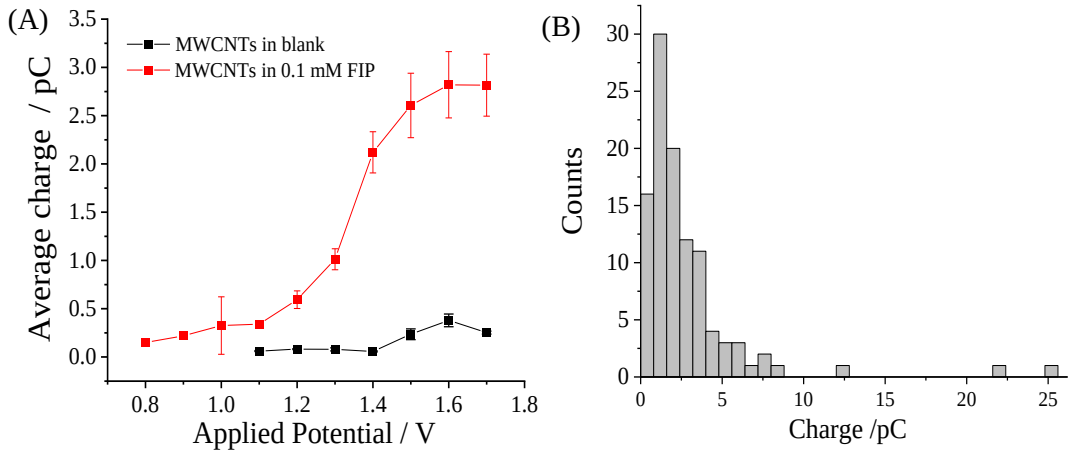


Figure 8.5. (A) The average charge transferred per spike at varying potentials of 0.8-1.7 V vs SCE. No spikes were detected in the blank MWCNT suspension at potentials lower than 1.1 V vs SCE. The error bars are the standard error bar which defined by $SD/(n)^{1/2}$, where SD is the standard deviation and n is the number of the spikes at each potential. (B) The charge distribution of the 106 spikes detected at 1.6 V SCE.

single-peaked, sharp shaped spike for each potential (Figure 8.5 (A)). The 'quasi-step' like impacts and the multi-peaked spikes were excluded since they may likely be the results of simultaneous collisions of aggregated MWCNTs or arise from the adsorption onto the electrode of the MWCNTs as has been noted in other solvents[70, 71]. As revealed by Figure 8.5 (A), the average charges measured for the spikes detected in the MWCNTs-FIP suspension are very significantly larger than those detected in the blank MWNCT suspension and increase to a limiting value with the increase of potential particularly in the range of 1.1–1.5 V SCE consistent with the Faradaic oxidation of FIP. As established previously the spikes may result from the Faradaic and/or the capacitive charge transfer process occurring during the collision between the nano-particles and microelectrode[1, 29]. The Faradaic charge transferred during the impact timescale increases substantially when an over-potential enabling the redox reaction to proceed is applied, which is consistent with the case observed for MWCNTs-FIP suspension. In contrast the small spikes detected in the blank MWCNT suspension show a small and potential insensitive

magnitude over the whole potential range, as shown in Figure 8.5 (A), indicating the sole contribution is from the capacitive charge transfer at electrode-electrolyte interface taking place when the applied potential deviates from the potential of zero charge[1, 72, 73].

Chronoamperograms at 1.6 V vs SCE were analysed where the average charge per Faradaic spike reaches a plateau (see Figure 8.5 (A)) and the Faradaic oxidation of FIP was thought complete. A total number of 106 single-peaked, sharp-shaped spikes were collected from eight independent chronoamperograms. As the capacitative charge transferred is relatively negligible, the measured charge transferred per spike can be approximated to the charge transferred in the electro-oxidation of the FIP at a single MWCNT. Figure 8.5 (B) shows the charge distribution of the collected spikes assuming a uniform adsorption reflects the surface area distribution of the individual MWCNTs present in the suspension. Using the equations described in section 8.3.1, the surface area of a single MWCNT can be estimated from the charge passed per spike and the area per FIP molecule assuming monolayer close-packed coverage.

The average charge of the collected spikes is (2.82±0.34) μA (standard error applied), from which the mean surface area of single MWCNT was calculated as (12.4±1.5), (11.0±1.3) or (6.1±0.7) μm^2 which correspond to the adsorption via flat, edgewise, endwise orientation, respectively (see Appendix D2). The electro-active surface area obtained from nano-impacts lies approximately in the same range with the specific surface area estimated from the supplier's data (4-9 μm^2), suggesting the adsorption of FIP on a single MWCNT is monolayer in extent.

In comparison to the sub-monolayer coverage estimated for the dropcasted MWCNTs immersing in the same concentration of FIP solution, the coverage on the dispersed MWCNTs is distinctly higher and limits (Figure 8.5) at the monolayer. Thus the impact

experiments confirm that FIP molecule adsorbed onto MWCNTs in a monolayer manner and hence that adsorption is partially diminished in the case of MWCNT dropcast layers where aggregation/agglomeration of the nanotubes may operate to the detriment of full adsorption.

8.3.3 Analytical Performances of Different Carbon Electrode Surfaces

First, the analytical responses of FIP at the particle modified electrodes (PME) and the unmodified GC, BPPG and EPPG electrodes were compared. Figure 8.6 (A)-(D) depict the background-subtracted adsorptive stripping voltammetric responses of varying concentrations of FIP in 60% pH 8 B-R buffer and 40% methanol at GC, BPPG, EPPG and MWCNTs modified GC electrodes. Peak area (charge) rather than peak height was chosen as it is the more robust analytical parameter in comparison to the latter for measuring the peak sizes in the baseline-subtracted voltammograms. The stripping charges were obtained from integration of the oxidation peaks shown in Figure 8.6 (A)–(D) and were linear with concentrations in the ranges of 3–20 μM at both the GC and BPPG electrode, 5–40 μM at the EPPG electrode and 2.5–20 μM at the MWCNTs modified electrode. As can be seen, the oxidation peak with the largest magnitude was found at the MWCNTs modified GC electrode, where the obtained charge is ca. 16 times larger in comparison with which found at the unmodified GC. However, the linear ranges were very similar to those found at the unmodified electrodes and the detection limit was obtained as 2.5 μM at the MWCNTs modified GC electrode, which is not significantly lower than the detection limits at the unmodified GC (3 μM), BPPG (3 μM) and EPPG (5 μM) electrodes.

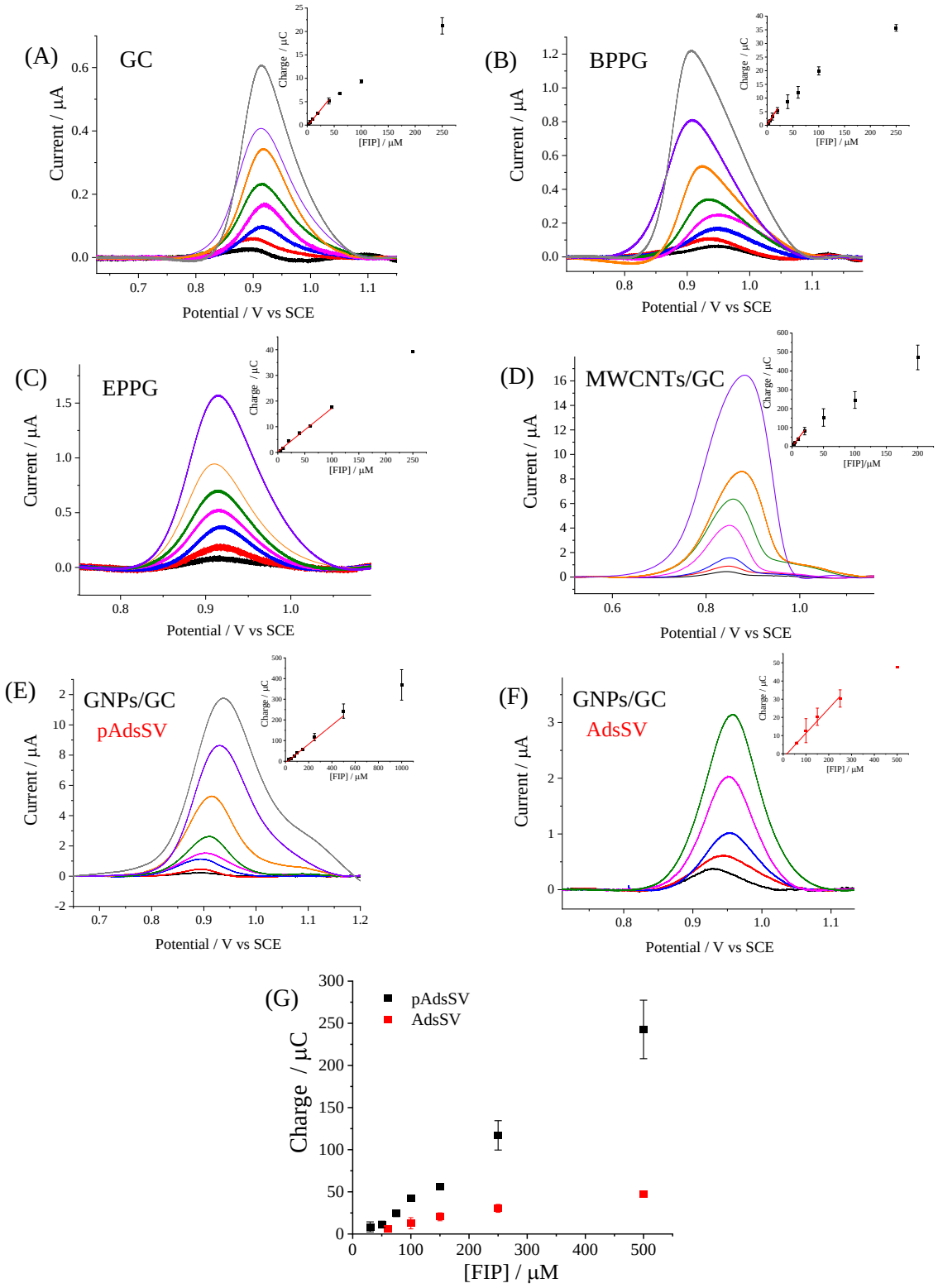


Figure 8.6. The adsorptive stripping voltammetric responses of varying concentrations of FIP recorded after a 2-mintue open circuit accumulation at (A) unmodified GC, (B) BPPG, (C) EPPG, (D) 10 µg MWCNTs modified GC (MWCNTs/GC) and (E) 10 µg GNPs modified GC electrode (GNPs/GC) or recorded at (F) the GC electrode dropcasted with 10 µg FIP-modified GNPs at the scan rate of 5 mV/s. The shown voltammograms were subtracted with an 8th order polynomial fitted baseline. The plots of charge versus concentration were shown in the insets and (G), where the charge was obtained from the three repeating voltammetric measurements.

Figure 8.6 (E)-(G) compare the voltammetric performances at the GNP modified GC electrode recorded using the suggested novel pAdsSV (Figure 8.6 (E)) to those using conventional AdsSV which involves immersing the electrode dropcasted with the unmodified GNPs in varying concentrations of FIP under open circuit condition for 2 minutes (Figure 8.6 (F)). It is shown clearly by Figure 8.6 (G) that the pAdsSV resulted in greater signals and the lower detection limit. The advantage of employing pAdsSV at GNPs modified GC electrode over AdsSV is thus demonstrated. Using the more sensitive pAdsSV, the linear detection range at the GNPs modified GC electrode was found to shift to the higher concentrations of 30–500 μM.

Next, to better understand the factors contributing to the differences and similarities in the observed signal sizes and the detection limits at different electrode surfaces, the capacitances of each electrode were considered. The capacitance describes the double-layer charging at the electrode-solution interface and, if constant, is related to the electrode surface area by[74]:

$$\Delta I = 2AC_d v \tag{8.3}$$

where ΔI is the difference between the measured forward and backward current, A is the effective surface area, C_d is the capacitance per unit area and v is the scan rate. Using Eqn. (8.3) the capacitances can be determined from the cyclic voltammograms measured in the blank solution of 60% B-R buffer and 40% methanol at GC, BPPG, EPPG, MWCNTs and GNPs modified GC electrode. For each electrode, varying scan rates were applied and linear plots of ΔI (read at the potential of 0.5 V vs SCE) versus v were obtained, from the slope of the plots the capacitances at 0.5 V vs SCE can be calculated (see Appendix G1). Table 8.2 lists the overall capacitance and the specific capacitance of each electrode estimated using the electro-active surface areas and characterised surface

areas shown in Table 8.1 for unmodified electrodes and PMEs, respectively. It can be seen in Table 8.2 that the overall capacitances which are controlled by the surface areas are much smaller for unmodified electrodes in comparison to the PMEs. The specific capacitances of all studied carbon surfaces lie in the similar ranges of 5.3–64 μF/cm^2, close to the typical double-layer capacitance values[74, 75]. Note that unlike true capacitors, the double layer capacitance is often dependent on the potentials applied[74].

Table 8.2. Summary of capacitances, specific capacitances, the lowest detectable concentrations and the signal to background ratios in the voltammograms of the lowest detectable concentration of the studied electrode surfaces. The ranges shown for the specific capacitance reflect both the ranges of the surface areas and the standard deviations of the estimated capacitances.

Electrode	**Overall capacitance / μF**	**Specific capacitance / μF cm^{-2}**	**Signal to background ratio**	**LOD / μM**
GC	7.8 ± 0.24	20–42	0.10	3
BPPG	9.6 ± 0.08	11–22	0.15	3
EPPG	25 ± 0.33	31–64	0.095	5
MWCNTs / GC	210 ± 3.4	5.3–11	0.10	2.5
GNPs / GC	210 ± 6.0	34 ± 17	0.025	60

Table 8.2 also summarises the lowest detected concentration of FIP at each electrode and the signal to background ratios of the peaks current read from the lowest concentration voltammograms shown in Figure 8.6 (A)-(E) and the capacitative currents read at the same potentials in Appendix G1. The signal to background ratio reflects the relation of the aforementioned capacitative charge and the stripping charge associated with the amounts of electro-active adsorbate present. As suggested by Table 8.2 the signal to background ratios values of three unmodified electrodes and the MWCNTs modified GC electrode are similar and are larger than the GNPs modified GC electrode. This pattern was also observed for LOD and hence it can be concluded that the LOD is

dependent on the signal-background ratio rather than solely the magnitude of signal. Thus despite the fact that larger signals were seen at the PMEs with larger surface areas, the LODs of AdsSV are also affected by proportionally larger capacitances presented and are intrinsically limited by an upper limit of monolayer adsorption, as discussed in section 8.3.2.

Having compared the different types of carbon materials, we next focus on the PMEs and investigate the effect of the amounts of nano-particles used for modifying the electrode. Figure 8.7 (A) and (B) show the background-subtracted AdsSV voltammograms of 0.1 mM FIP recorded at a GC electrode modified with either 5–30 µg of MWCNTs or 2.5–20 µg of following the procedures described in section 8.3.1. Figures

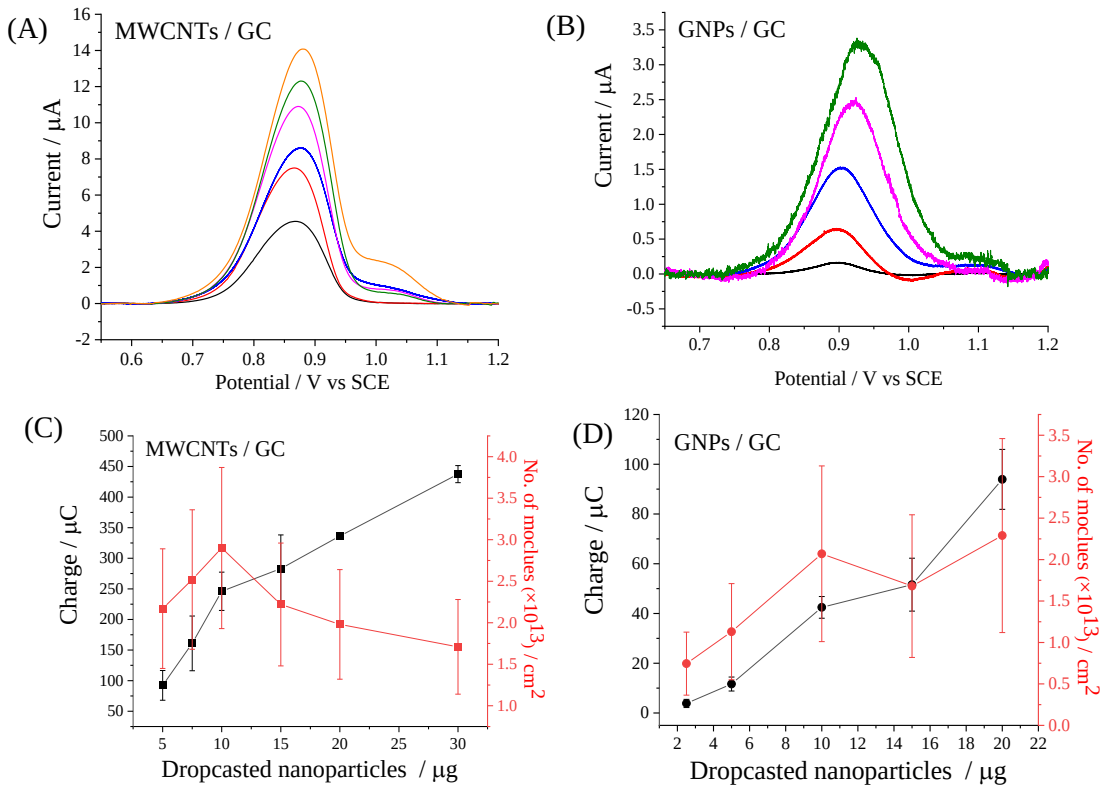


Figure 8.7. The background-subtracted adsorptive stripping voltammetric responses of 0.1 mM FIP at (A) 5, 7.5, 10, 15,20 and 30 µg MWCNTs modified GC and (B) 2.5, 5, 10, 15 and 20 µg GNPs modified GC electrode. The relations of charges and the surface coverage (in number of molecules per unit) obtained from oxidation peak in (A) and (B) were plotted in (C) and (D), respectively.

8.7 (C) and (D) plot the charges (*Q*) and the surface coverages (number of molecules absorbed per unit area) of FIP on the nanoparticle surfaces. The latter was estimated by N_{ads} / $A_{electrode}$, where N_{ads} was the total number of molecules adsorbed on electrode surfaces calculated from *Q* as described in section 8.3.1 and $A_{electrode}$ was the surface area of varying mass of MWCNTs and GNPs calculated in Appendix D2. As suggested in Figure 8.7 (C) and (D), the oxidative charge broadly increased with the amount of nano-particles dropcasted but the charge per unit area of adsorbing surface remained approximately constant. The former was again attributed to the larger surface areas of the nanoparticles used, which was evidenced by the voltammograms measured at the electrodes modified with the same amounts of MWCNTs and GNPs in the blank solution (see Appendix G2), where the capacitative currents scaled with the increasing amounts of MWCNTs and GNPs.

From the discussions earlier in this section increasing the amount of particles on the surface also increases the capacitive signals and using a larger surface area is unable to

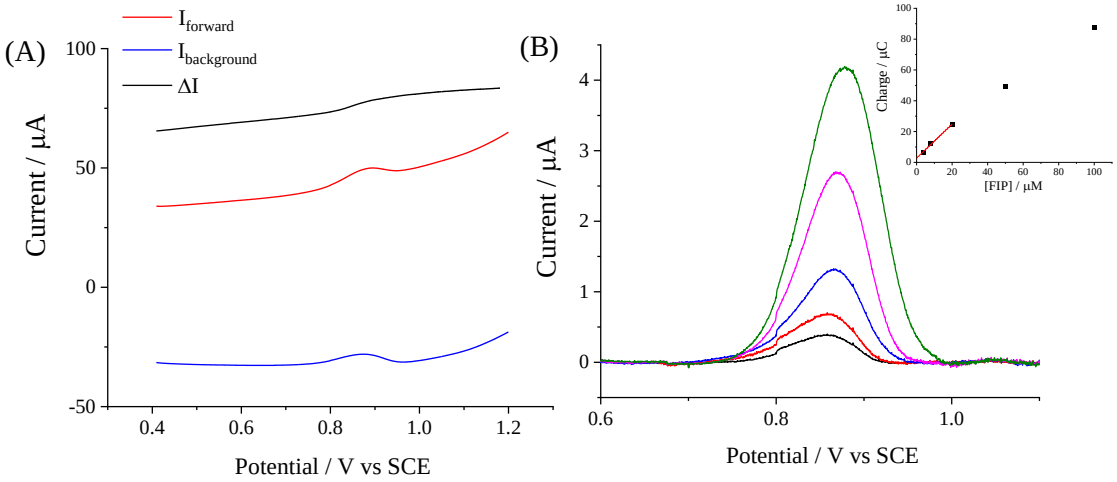


Figure 8.8 (A) The adsorptive square wave voltammetric response of 0.1 mM FIP at the MWCNTs modified GC electrode in a mixture of 40% methanol and 60% PH 8 B-R buffer. The voltammograms were recorded after a 2-mintue open circuit accumulation. The frequency was 10 Hz, the step potential was 0.5 mV, the amplitude was 50 mV and the scan rate was 5 mVs^{-1}. (B) The forward scans of adsorptive square wave voltammetric responses of varying concentrations of FIP. Inset; the plots of charge obtained from the voltammograms versus concentration.

enhance the LOD unless the adsorption per unit area is also boosted. For the subsequent analytical studies using either MWCNTs and GNPs, 10 μg was chosen as the mass for the preparation of the PMEs.

Finally, the possibility of further improving the limit and sensitivity of detection by employing the voltammetric techniques with different potential waveforms was examined at the optimised MWCNTs modified GC electrode surface where a relatively favourable analytical performance using AdsSV was observed. The commonly used adsorptive square wave voltammetry, AdsSWV, was first attempted however, the signal was lost in the voltammograms since the backward and forward signals were found to cancel out. The example voltammogram is shown in Figure 8.8 (A). Figure 8.8 (B) records the forward scans in varying concentrations of FIP solutions and the LOD was found to be 4 μM (Inset of Figure 8.8 (B)).

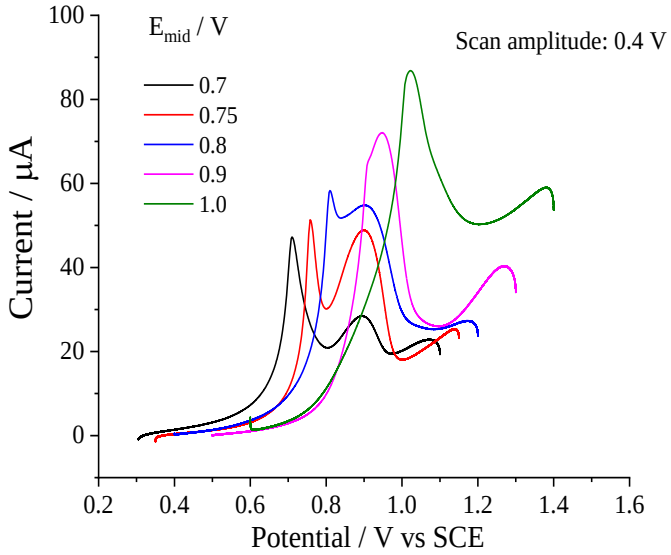


Figure 8.9. The adsorptive semi-circular sweep voltammetric responses of 0.1 mM FIP at the MWCNTs modified GC electrode using varying potential window with E_{mid} of 0.7-1.0 V vs SCE. The voltammograms were recorded after a 2-mintue open circuit accumulation. The scan amplitude was 0.4 V and the average scan rate was 5 mV/s.

Next we turned to the recently advocated semi-circular potential sweep voltammetry (SCV) but, novelly, with a pre-concentration step applied, AdsSCV. The SCV technique was reported in earlier chapters and elsewhere[76-79]. Briefly, the scan rate varies over the potential window generated by a semi-circular potential wave function. The midpoint of the potential window (E_{mid}) can be adjusted to approximate the redox potential where the scan rate reaches a near infinite value and the present signals are greatly amplified. Here the E_{mid} was optimised as 0.75 V vs SCE (see Figure 8.9) and the resulting adsorptive semi-circular voltammetric response of 0.1 mM FIP was compared with the adsorptive linear sweep voltammetric response in Figure 8.10 (A). The voltammograms of varying concentrations of FIP solutions ranging from 0 to 100 μM obtained using AdsSCV are shown in Figure 8.10 (B) and the linear detection range was found to be 1–32 μM. The LOD obtained using AdsSCV was 1 μM, which is somewhat but not substantially lower in comparison to using the other two conventional electroanalytical techniques (4 μM for the forward scan of AdsSWV and 2.5 μM for the linear sweep AdsSV).

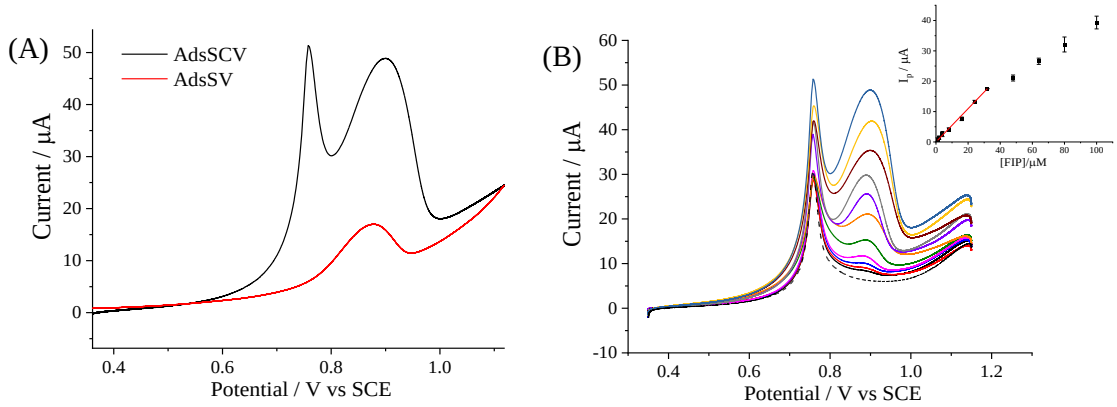


Figure 8.10. The adsorptive semi-circular sweep voltammetric responses at the MWCNTs modified GC electrode using a potential window with E_{mid} of 0.75 V vs SCE and the scan amplitude of 0.4 V of (A) 100 μM FIP solution overlaid with the adsorptive linear sweep voltammetric response at the same average scan rate of 5 mV/s and (B) 0 to 100 μM of FIP solutions. Inset of (B): The obtained peak currents with the subtraction of the value read at 0.90 V vs SCE of the blank solution voltammogram (dash line)

8.4 Conclusions

This chapter demonstrates the limitations and optimising strategies of the electroanalytical detection using adsorptive stripping voltammetry for the model molecule FIP so as to give generic insights. The adsorption of FIP at the unmodified electrodes (GC, BPPG EPPG electrode) and the PMEs (MWCNTs and GNPs modified GC electrode) was evidenced and characterised using the voltammetric studies and via nano-impact experiments at the single MWCNT surface. The adsorptions were identified to be no more than mono-layer for all the studied electrode surfaces. This intrinsically limits the LODs reflected by the signal to background ratios. The PMEs shows no obvious advantage in comparison to the unmodified electrodes in terms of improving the LOD despite larger signals are detected since an increased area for adsorption is offset by an increased capacitive charging signal. Nonetheless, two strategies were developed for PMEs to enhance the analytical performance, specifically the use of pAdsSV technique facilitating the adsorption of FIP at GNPs modified GC electrode and the use of AdsSCV technique at MWCNTs modified GC electrode which selectively amplifies the signal and results in the low LOD.

Bibliography

1. J. Poon, C. Batchelor-McAuley, K. Tschulik and R. G. Compton, *Chemical Science*, 2015, **6**, 2869-2876.
2. J. Wang, *Analytical electrochemistry*, Wiley-VCH, Hoboken, N.J., 3rd edn., 2006.
3. C. M. A. Brett and A. M. O. Brett, *Electrochemistry : principles, methods, and applications*, Oxford University Press, Oxford, 1993.
4. Á. Molina and J. González, *Pulse voltammetry in physical electrochemistry and electroanalysis : theory and applications*, Springer, 1st edn., 2016.
5. M. Fleischmann and S. Pons, *Analytical Chemistry*, 1987, **59**, 1391A-1399A.
6. H. P. Wu, *Analytical Chemistry*, 1993, **65**, 1643-1646.
7. L. J. Magee and J. Osteryoung, *Analytical Chemistry*, 1989, **61**, 2124-2126.
8. R. G. Compton, G. G. Wildgoose, N. V. Rees, I. Streeter and R. Baron, *Chemical Physics Letters*, 2008, **459**, 1-17.
9. A. J. Saterlay, J. S. Foord and R. G. Compton, *Analyst*, 1999, **124**, 1791-1796.
10. A. N. Blythe, R. P. Akkermans and R. G. Compton, *Electroanalysis*, 2000, **12**, 16-20.
11. J. Kruusma, L. Nei, J. L. Hardcastle, R. G. Compton, E. Lust and H. Keis, *Electroanalysis*, 2004, **16**, 399-403.
12. C. Prado, S. J. Wilkins, F. Marken and R. G. Compton, *Electroanalysis*, 2002, **14**, 262-272.
13. A. J. Saterlay, C. Agra-Gutiérrez, M. P. Taylor, F. Marken and R. G. Compton, *Electroanalysis*, 1999, **11**, 1083-1088.
14. A. L. Suherman, M. Lin, B. Rasche and R. G. Compton, *ACS Sensors*, 2020, **5**, 519-526.
15. A. L. Suherman, B. Rasche, B. Godlewska, P. Nicholas, S. Herlihy, N. Caiger, P. J. Cowen and R. G. Compton, *ACS Sensors*, 2019, **4**, 2497-2506.
16. C. Agra-Gutiérrez and R. G. Compton, *Electroanalysis*, 1998, **10**, 204-206.
17. M. C. Henstridge, E. J. F. Dickinson, M. Aslanoglu, C. Batchelor-McAuley and R. G. Compton, *Sensors and Actuators B: Chemical*, 2010, **145**, 417-427.
18. R. T. Kachoosangi, G. G. Wildgoose and R. G. Compton, *Analytica Chimica Acta*, 2008, **618**, 54-60.
19. R. T. Kachoosangi, M. M. Musameh, I. Abu-Yousef, J. M. Yousef, S. M. Kanan, L. Xiao, S. G. Davies, A. Russell and R. G. Compton, *Analytical Chemistry*, 2009, **81**, 435-442.
20. K. Chaisiwamongkhol, K. Ngamchuea, C. Batchelor-McAuley and R. G. Compton, *Analyst*, 2016, **141**, 6321-6328.
21. T. W. B. Lo, L. Aldous and R. G. Compton, *Sensors and Actuators B: Chemical*, 2012, **162**, 361-368.
22. W. T. P. dos Santos, H. M. A. Amin and R. G. Compton, *Sensors and Actuators B: Chemical*, 2019, **279**, 433-439.
23. P. Nayak, R.-C. Xie, R. G. Palgrave and R. G. Compton, *ChemElectroChem*, 2021, **8**, 911-917.
24. X. Dai, O. Nekrassova, M. E. Hyde and R. G. Compton, *Analytical Chemistry*, 2004, **76**, 5924-5929.
25. X. Dai and R. G. Compton, *Analyst*, 2006, **131**, 516-521.

26. A. L. Suherman, K. Ngamchuea, E. E. L. Tanner, S. V. Sokolov, J. Holter, N. P. Young and R. G. Compton, *Analytical Chemistry*, 2017, **89**, 7166-7173.
27. S. Eloul and R. G. Compton, *The Journal of Physical Chemistry C*, 2014, **118**, 24520-24532.
28. M. Pumera, *ACS Nano*, 2014, **8**, 7555-7558.
29. S. V. Sokolov, S. Eloul, E. Kätelhön, C. Batchelor-McAuley and R. G. Compton, *Physical Chemistry Chemical Physics*, 2017, **19**, 28-43.
30. W. Cheng and R. G. Compton, *TrAC Trends in Analytical Chemistry*, 2014, **58**, 79-89.
31. A. Aajoud, P. Ravanel and M. Tissut, *Journal of Agricultural and Food Chemistry*, 2003, **51**, 1347-1352.
32. N. Simon-Delso, V. Amaral-Rogers, L. P. Belzunces, J. M. Bonmatin, M. Chagnon, C. Downs, L. Furlan, D. W. Gibbons, C. Giorio, V. Girolami, D. Goulson, D. P. Kreutzweiser, C. H. Krupke, M. Liess, E. Long, M. McField, P. Mineau, E. A. D. Mitchell, C. A. Morrissey, D. A. Noome, L. Pisa, J. Settele, J. D. Stark, A. Tapparo, H. Van Dyck, J. Van Praagh, J. P. Van der Sluijs, P. R. Whitehorn and M. Wiemers, *Environmental Science and Pollution Research*, 2015, **22**, 5-34.
33. A. S. Gunasekara, T. Truong, K. S. Goh, F. Spurlock and R. S. Tjeerdema, *Journal of Pesticide Science*, 2007, **32**, 189-199.
34. N. Yildirim and G. Agar, *Toxicology and Industrial Health*, 2015, **32**, 1450-1455.
35. C. Vidau, R. A. González-Polo, M. Niso-Santano, R. Gómez-Sánchez, J. M. Bravo-San Pedro, E. Pizarro-Estrella, R. Blasco, J.-L. Brunet, L. P. Belzunces and J. M. Fuentes, *NeuroToxicology*, 2011, **32**, 935-943.
36. L. W. Pisa, V. Amaral-Rogers, L. P. Belzunces, J. M. Bonmatin, C. A. Downs, D. Goulson, D. P. Kreutzweiser, C. Krupke, M. Liess, M. McField, C. A. Morrissey, D. A. Noome, J. Settele, N. Simon-Delso, J. D. Stark, J. P. Van der Sluijs, H. Van Dyck and M. Wiemers, *Environmental Science and Pollution Research*, 2015, **22**, 68-102.
37. J. L. Miller, T. S. Schmidt, P. C. Van Metre, B. J. Mahler, M. W. Sandstrom, L. H. Nowell, D. M. Carlisle and P. W. Moran, *Science Advances*, 2020, **6**, 1299.
38. C. C. Tingle, J. A. Rother, C. F. Dewhurst, S. Lauer and W. J. King, *Reviews of environmental contamination and toxicology*, 2003, 1-66.
39. B. Morzycka, *Journal of Chromatography A*, 2002, **982**, 267-273.
40. T. Wang, J. Hu and C. Liu, *Environmental Monitoring and Assessment*, 2014, **186**, 2767-2774.
41. Y. Cheng, F. Dong, X. Liu, J. Xu, W. Meng, N. Liu, Z. Chen, Y. Tao and Y. Zheng, *Analytical Methods*, 2014, **6**, 1788-1795.
42. X. Li, H. Li, W. Ma, Z. Guo, X. Li, S. Song, H. Tang, X. Li and Q. Zhang, *Food Chemistry*, 2019, **281**, 85-90.
43. R. Tomazini, G. M. Grosseli, D. N. R. de Sousa, P. S. Fadini, F. T. Saia, A. Langenhoff, B. van der Zaan and A. A. Mozeto, *Analytical Methods*, 2020, **12**, 3242-3249.
44. N. Vasylieva, K. C. Ahn, B. Barnych, S. J. Gee and B. D. Hammock, *Environmental Science & Technology*, 2015, **49**, 10038-10047.
45. Q. Tu, M. E. Hickey, T. Yang, S. Gao, Q. Zhang, Y. Qu, X. Du, J. Wang and L. He, *Food Control*, 2019, **96**, 16-21.

46. R. H. O. Montes, R. M. Dornellas, L. A. J. Silva, A. L. Squissato, E. M. Richter and R. A. A. Munoz, *Journal of Solid State Electrochemistry*, 2016, **20**, 2453-2459.
47. F. Okumura, R. B. Amaral, E. Orestes, A. B. Silva and L. H. Mazo, *Journal of the Brazilian Chemical Society*, 2016, **27**, 925-932.
48. M. Maulidiyah, T. Azis, L. Lindayani, D. Wibowo, L. O. A. Salim, A. Aladin and M. Nurdin, *Journal of Electrochemical Science and Technology*, 2019, **10**, 394-401.
49. M. Nurdin, O. A. Prabowo, Z. Arham, D. Wibowo, M. Maulidiyah, S. K. M. Saad and A. A. Umar, *Surfaces and Interfaces*, 2019, **16**, 108-113.
50. S. Kumar, N. Vasylieva, V. Singh, B. Hammock and S. G. Singh, *Electroanalysis*, 2020, **32**, 2056-2064.
51. S. El-Akaad, M. A. Mohamed, M. M. Elmasri, N. S. Abdelwahab, E. A. Abdelaleem, S. De Saeger and N. Beloglazova, *Journal of The Electrochemical Society*, 2020, **167**, 027543.
52. C. Batchelor-McAuley, J. Ellison, K. Tschulik, P. L. Hurst, R. Boldt and R. G. Compton, *Analyst*, 2015, **140**, 5048-5054.
53. R. R. Moore, C. E. Banks and R. G. Compton, *Analytical Chemistry*, 2004, **76**, 2677-2682.
54. Y. Y. Chan, A. Y. S. Eng, M. Pumera and R. D. Webster, *ChemElectroChem*, 2015, **2**, 1003-1009.
55. K. Chaisiwamongkhol, C. Batchelor-McAuley, S. V. Sokolov, J. Holter, N. P. Young and R. G. Compton, *Applied Materials Today*, 2017, **7**, 60-66.
56. J. Ellison, C. Batchelor-McAuley, K. Tschulik and R. G. Compton, *Sensors and Actuators B: Chemical*, 2014, **200**, 47-52.
57. M. A. Fryling, J. Zhao and R. L. McCreery, *Analytical Chemistry*, 1995, **67**, 967-975.
58. C. A. Thorogood, G. G. Wildgoose, A. Crossley, R. M. J. Jacobs, J. H. Jones and R. G. Compton, *Chemistry of Materials*, 2007, **19**, 4964-4974.
59. R. Murray and i. A. Bard, *by AJ Bard, Marcel Dekker, New York*, 1984, **13**, 191.
60. C. E. Banks, T. J. Davies, G. G. Wildgoose and R. G. Compton, *Chemical Communications*, 2005, 829-841.
61. M. Li, P. Li, L. Wang, M. Feng and L. Han, *Journal of Agricultural and Food Chemistry*, 2015, **63**, 4435-4443.
62. P. W. Atkins and J. De Paula, *Atkins' Physical Chemistry*, Oxford University Press, Oxford, 9th edn., 2010.
63. L. Chen, X. Li, E. E. L. Tanner and R. G. Compton, *Chemical Science*, 2017, **8**, 4771-4778.
64. W. T. P. dos Santos and R. G. Compton, *Sensors and Actuators B: Chemical*, 2019, **285**, 137-144.
65. S. S. Batsanov, *Inorganic Materials*, 2001, **37**, 871-885.
66. R. W. Murray, *Molecular design of electrode surfaces*, Wiley, New York, 1992.
67. H. Chang and A. J. Bard, *Journal of the American Chemical Society*, 1991, **113**, 5588-5596.
68. R. T. Kachoosangi, C. E. Banks, X. Ji and R. G. Compton, *Analytical Science*, 2007, **23**, 283-289.
69. L. Xiao, E. J. F. Dickinson, G. G. Wildgoose and R. G. Compton, *Electroanalysis*, 2010, **22**, 269-276.

70. X. Li, C. Batchelor-McAuley, K. Tschulik, L. Shao and R. G. Compton, *ChemPhysChem*, 2015, **16**, 2322-2325.
71. X. Li, C. Lin, C. Batchelor-McAuley, E. Laborda, L. Shao and R. G. Compton, *The Journal of Physical Chemistry Letters*, 2016, **7**, 1554-1558.
72. N. V. Rees, C. E. Banks and R. G. Compton, *The Journal of Physical Chemistry B*, 2004, **108**, 18391-18394.
73. C. E. Banks, N. V. Rees and R. G. Compton, *The Journal of Physical Chemistry B*, 2002, **106**, 5810-5813.
74. A. J. Bard and L. R. Faulkner, *Electrochemical Methods*, 2001, **2**, 580-632.
75. R. G. Compton and C. E. Banks, *Understanding voltammetry*, World Scientific Publishing Europe, London, 3rd edn., 2018.
76. Y. Wang, L. Chen, K. Chaisiwamongkhol and R. G. Compton, *Food Chemistry*, 2020, **309**, 125606.
77. Y. Wang, L. Chen and R. G. Compton, *Food Chemistry*, 2020, **323**, 126844.
78. Y. Uchida, E. Kätelhön and R. G. Compton, *Journal of Electroanalytical Chemistry*, 2019, **848**, 113290.
79. Y. Uchida, E. Kätelhön and R. G. Compton, *Journal of Electroanalytical Chemistry*, 2019, **835**, 60-66

Chapter 9

Overall Conclusions

Improving the sensitivity and selectivity of amperometric detections have always been the essential objectives for improving electroanalysis. This thesis investigated the *generic* method of developing simple-to-use and cost-effective voltammetric sensors accomplishing such objectives by employing the novel semi-circular potential sweep to replace the conventional cyclic or linear sweep. The developed method was applied to tackle the analytical challenges that may be found in a range of food, biological and environmental samples.

First, the method for detection and quantification of piperine in black pepper was introduced. Semi-circular voltammetry (SCV) was employed as an electroanalytical detection method, which gave significantly amplified peaks over the conventional voltammetry resulting in a linear calibration curve in the required analytical range. A simple and rapid one-step extraction method in ethanol was developed. The applicability of this electrochemical analysis to determine and quantify piperine in black peppercorn samples was demonstrated.

The method for the selective electrochemical detection of mixtures with chlorophyll a and chlorophyll b was next demonstrated. The novel semi-circular potential sweep was employed in the developed method and show clear advantages over conventional voltammetry in distinguishing two species with closely similar peak potentials in the mixtures. Linear relationships in the required analytical concentration ranges were established for the quantifications of chlorophyll a and chlorophyll b in their mixtures.

The developed electroanalytical method was also applied to determine chlorophyll a content in a real sample of spinach.

Further, an electrochemical method for the determination of the electrode passivating species phenol using the semi-circular sweep voltammetry was developed. A second species was introduced into the studied solution to effectively limit the polymerisation of phenol which caused the fouling of electrode surface. SCV was employed in the developed method to amplify the analytical signals and improve the sensitivity of detection without the electrode fouling problem.

The *generic* applicability of SCV as an electroanalytical method was then demonstrated by studying three different mixtures as model systems for comparison. SCV was used to analytically resolve three different mixtures of two components of biological importance (ascorbic acid/acetaminophen, glucose/ethanol and hydroquinone/catechol mixtures) in which conventional voltammetry (linear sweep, differential pulse and square wave voltammetry) led to significantly overlapping peaks which precluded useful measurement. Using SCV the different signals were selectively amplified leading to signal resolution along with an increase in sensitivity.

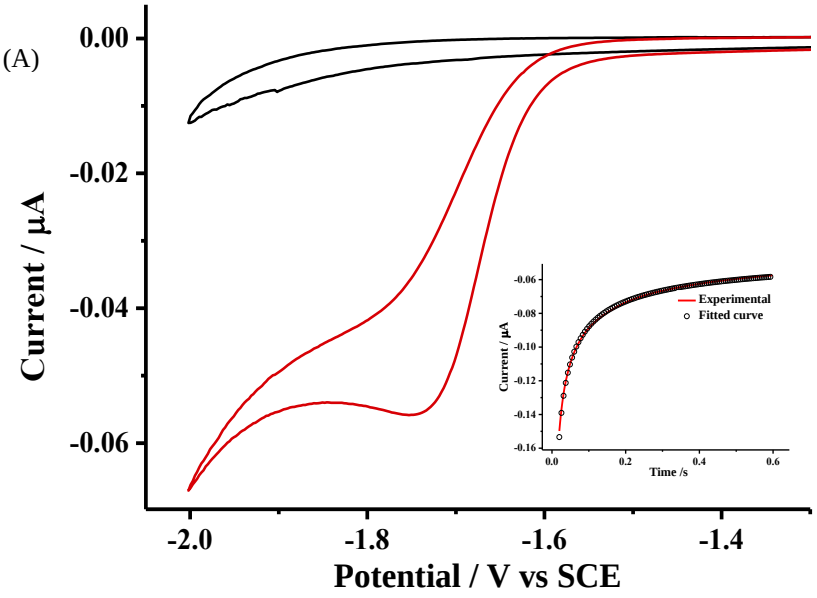
Finally, the widely used electroanalytical method, adsorptive stripping voltammetry at a range of carbon electrodes, particularly carbon nano-particle modified electrodes in respect of the analyte fipronil was evaluated. The electroanalytical performances of the studied electrode were compared and optimised. The intrinsic limitations in terms of Limits of Detection and of sensitivity of the Adsorptive Stripping Method were elucidated using a combination of voltammetry including semi-circular voltammetry method and nano-impact measurements. Chapter 8 provides an explicit direction to the design and realisation of sensors based on the adsorptive approach.

In summary, this thesis develops the novel semi-circular voltammetric protocols for electroanalysis which offers favourable sensitivity and resolution in comparison to conventional voltammetric techniques. The features of the semi-circular voltammograms obtained using the optimised potential windows facilitates detections in the studied systems while requires no elaborate electrode modification procedures. Meanwhile, this thesis provides a guide for performing electroanalysis using a range of electrochemical techniques with the critical understanding of electrochemical processes of target analytes.

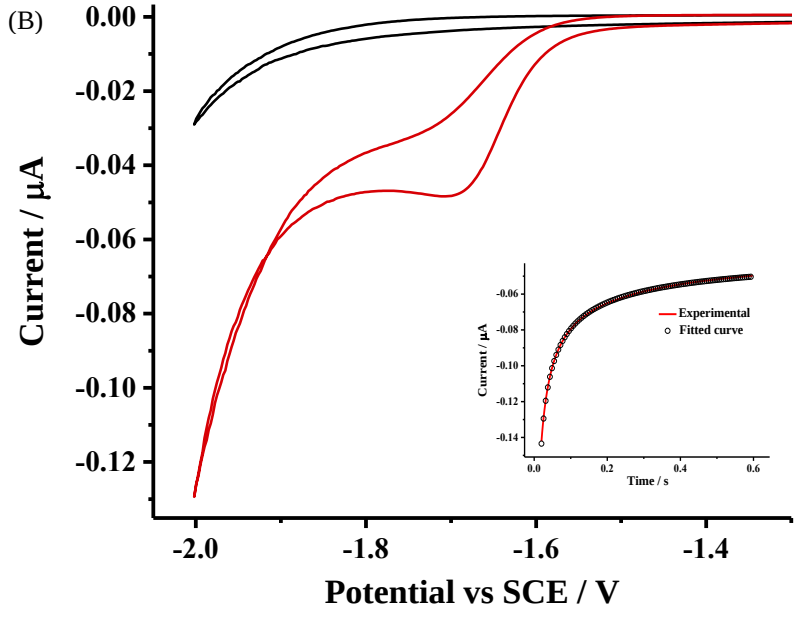
Appendix A

Study of piperine electrochemistry in 60% ethanol + 40% NaOH aqueous solutions

(A)



(B)



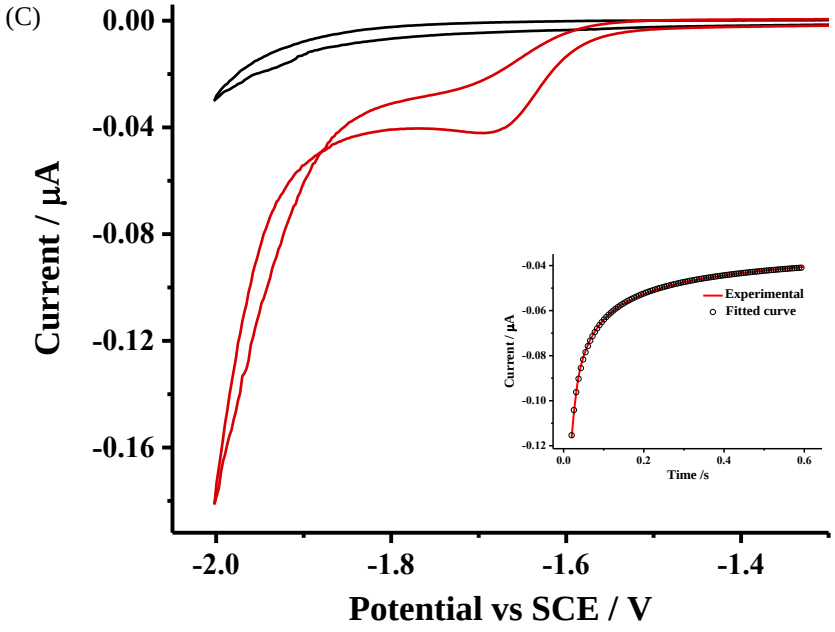


Figure A1. Cyclic voltammetric responses of 10 mM piperine in 60 EtOH: 40 NaOH ((A) 0.1 M (B) 1.0 M (C)2.0 M aqueous solution) and background. Inset: Chronoamperometric response of 10 mM piperine subtracted of solvent (red solid line) at carbon fibre microdisc, and corresponding line of best fit (black circles) derived from the Shoup and Szabo equations at the transient time of 0.6 s, at a scan rate of 100 mVs^{-1}.

Table A1. The values of number of electrons transferred and diffusion coefficient determined from the fitted curves of experimental data of 10 mM piperine in 60 EtOH: 40 NaOH varying concentrations of aqueous solutions.

NaOH concentration in solvent / M	0.1	1.0	2.0
No. of electron transfer	1.04	1.21	0.94
Diffusion coefficient/ cm^2s^{-1}	4.61×10^{-6}	3.20×10^{-6}	3.36×10^{-6}

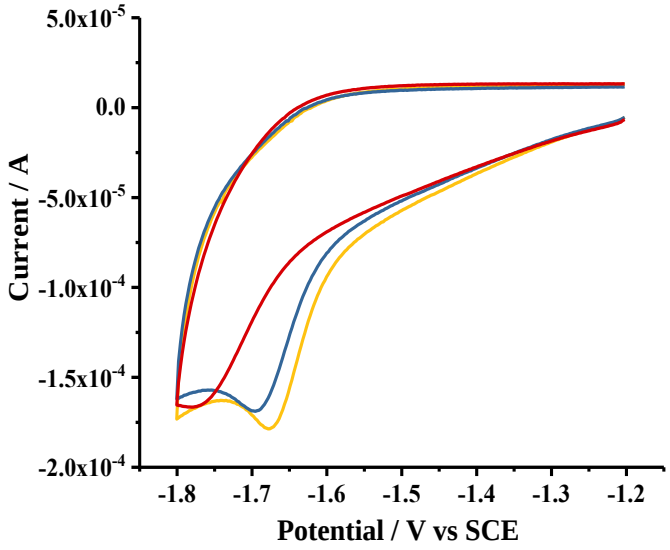


Figure A2. Cyclic voltammetric responses of 1 mM piperine at glassy carbon macroelectrode in varying NaOH aqueous concentrations of 60 EtOH: 40 NaOH. Red line: 0.1 M NaOH; Blue line: 1.0 M NaOH; Yellow line: 2.0 M NaOH. Scan rate = 1.0 V/s

Table A2. The calculated peak currents from the irreversible Randles-Sevcik equation, the obtained experimental peak current and number of electrons transferred at glassy carbon macroelectrode in NaOH aqueous solutions (0.1–2.0 M).

NaOH concentration/M	Scan rate/ mVs^{-1}	α	$D/10^{-6}$ cm^2s^{-1}	I_{Irrev}/ μA	I_{Expt}/ μA	n
0.1	1000	0.5	4.61	31.77	64.97	2.04
1.0	1000	0.5	3.20	26.47	69.90	2.64
2.0	1000	0.5	3.36	27.12	74.05	2.73

Appendix B

Analytical responses obtained using LSV, SWV, DPV

B1. Voltammograms Measured for the Ascorbic acid/Acetaminophen systems

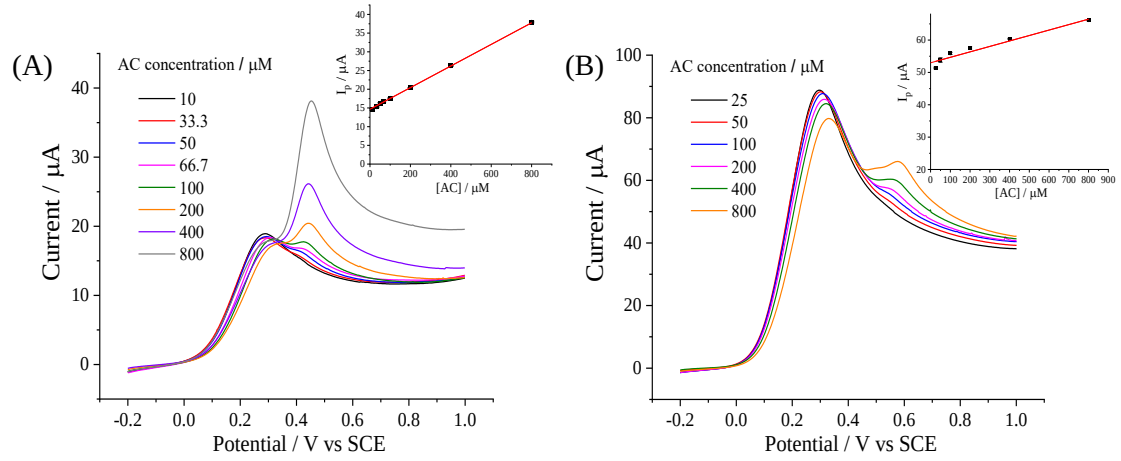


Figure B1. Linear voltammetric responses of (A) 10-800µM AC in the presence of 1 mM AA and (B) 25-800µM AC in the presence of 5 mM AA. The scan rate was 50 mVs^{-1}. Insets: Plots of subtracted peak currents obtained from linear sweep voltammograms versus AC concentration.

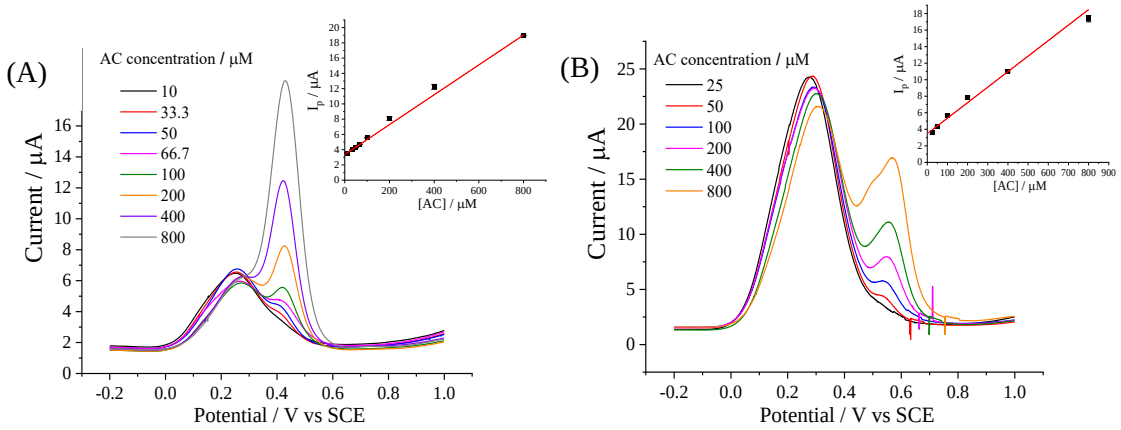


Figure B2. Square wave voltammetric responses of (A) 10-800µM AC in the presence of 1 mM AA and (B) 25-800µM AC in the presence of 5 mM AA. The frequency was 50 Hz, the step potential was 1 mV, the amplitude was 10 mV, and the scan rate was 50 mVs^{-1}. Insets: Plots of subtracted peak currents obtained from the square wave voltammograms versus AC concentration.

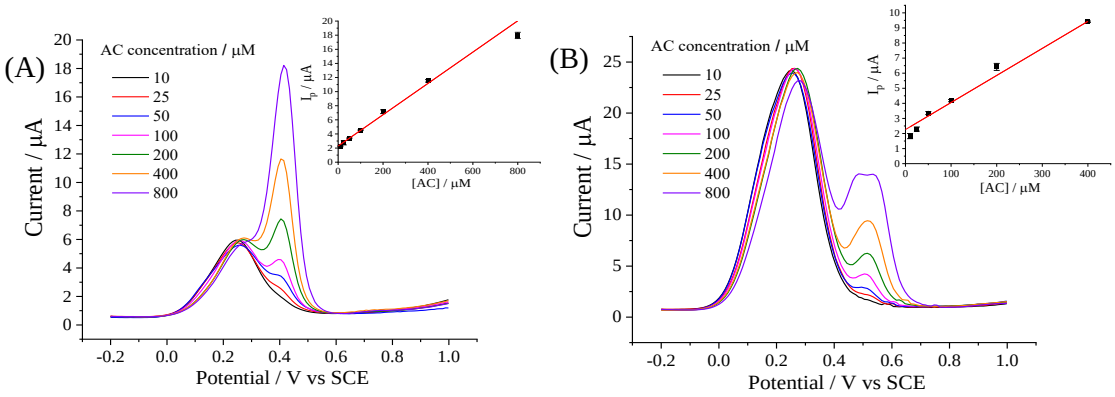


Figure B3. Differential pulse voltammetric responses of (A) 10-800µM AC in the presence of 1 mM AA and (B) 25-800µM AC in the presence of 5 mM AA. The step potential was 10 mV, the interval time was 0.2 s, the modulation amplitude was 25 mV, the modulation time was 50 ms, and the scan rate was 50 mVs^{-1}. Insets: Plots of subtracted peak currents obtained from differential pulse voltammograms versus AC concentration.

B2. Voltammograms Measured for the Hydroquinone/Catechol system

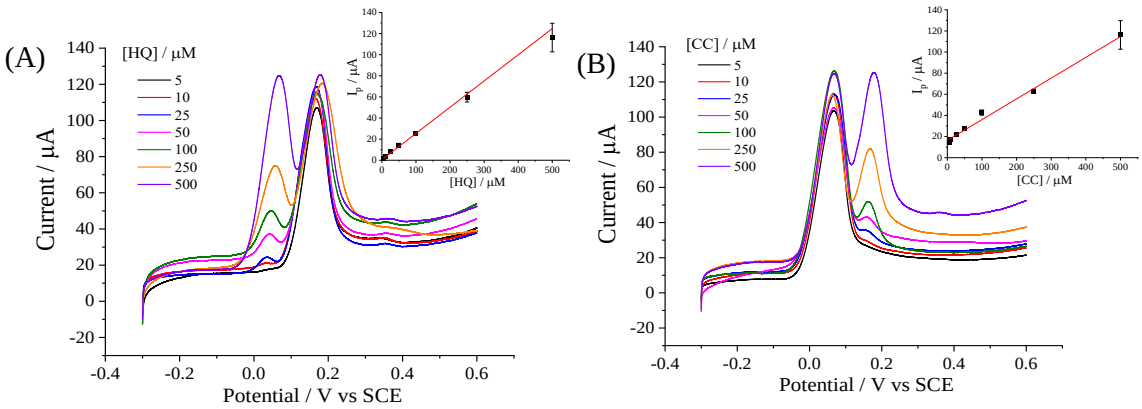


Figure B4. Linear voltammetric responses of (A) 5-500µM HQ in the presence of 500µM CC and (B) 5-500µM CC in the presence of 500µM HQ. The scan rate was 50 mVs^{-1}. Insets: Plots of subtracted peak currents obtained from linear sweep voltammograms versus (A) HQ and (B) CC concentration.

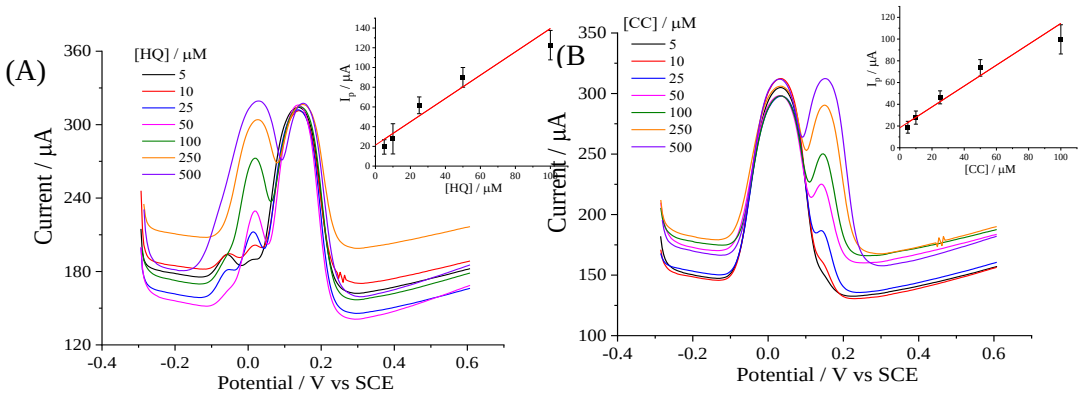


Figure B5. Differential pulse voltammetric responses of (A) 5-500µM HQ in the presence of 500µM CC and (B) 5-500µM CC in the presence of 500µM HQ. The step potential was 4 mV, the interval time was 80 ms, the modulation amplitude was 30 mV, the modulation time was 40 ms, and the scan rate was 50 mVs^{-1}. Insets: Plots of subtracted peak currents obtained from semi-circular voltammograms versus (A) HQ and (B) CC concentration in the linear range of 5-100 µM.

Appendix C

The Determination of the Acetaminophen Content in Real Samples

(A)

Paracetamol capsules	Measured concentration /μM	Recovery/%	Calculated AC content in each capsule /mg	Labelled amount of AC each capsule /mg
Sample	31.94 ± 0.57		479 ± 4.9	500
Sample + 50 μM AC	69.15 ± 0.05	109		
Sample + 100 μM AC	135.13 ± 0.62	103		
Sample + 200 μM AC	219.54 ± 0.15	93		

(B)

Beechams Sachet	Measured concentration /μM	Recovery/%	Calculated AC content in each sachet /mg	Labelled amount of AC each capsule /mg
Sample	59.00 ± 0.61		1044 ± 10.8	1000
Sample + 50 μM AC	114.05 ± 0.66	110		
Sample + 100 μM AC	155.15 ± 0.25	96		
Sample + 200 μM AC	256.19± 0.99	99		

(C)

Efferalgan + Vitamin C Effervescent Tablets	Measured concentration /μM	Recovery/%	Calculated AC content in each tablet /mg	Labelled amount of AC each capsule /mg
Sample	35.41 ± 0.80		531 ± 12.0	500
Sample + 50 μM AC	87.20 ± 0.78	104		
Sample + 100 μM AC	133.58± 0.73	98		
Sample + 200μM M AC	234.33± 2.13	99		

Table C1. Detected AC contents and concentrations analysed by calibration curves in insets of Figure 5(A) extract, extracts added with standard solutions and the corresponding recoveries of (A) Paracetamol Capsules, (B) Beechams Sachet, (C) Efferalgan + Vitamin C Effervescent Tablets.

Appendix D

D1. Calculations of the Volumes of MWCNT Suspensions Used for Dropcasting to Make MWCNT/GC Electrodes Used in Chapter 7

The mass of MWCNTs used in the 20 μL suspension was 20 μg.

The MWCNT are assumed to be cylinders of length 20 μm and diameter 30 ±15 nm, which were stated by the manufactures and confirmed in the previous work[1]. Taking a density value of 1.54 g cm^{-3} [2] and assuming the MWCNT in the dropcast was uniformly deposited onto the GC electrode in the close-packed manner, the total volume of the MWCNT layer on the electrode can be estimated as 1.30×10^{-11} m^3.

Assuming the dropcasted MWCNT layer covered exactly the whole geometric area of GC electrode, the thickness of the MWCNT layer can be estimated to be 1.8 μm.

D2. Calculations of Geometric Electrode Areas, and the MWCNTs and GNPs Surface Areas Used in Chapter 8

Geometric area of GC, BPPG and EPPG electrodes:

The geometric electrode surface area of GC, BPPG, and EPPG electrode can be calculated from: $A = \pi(d/2)^2$, where A is the geometric surface area and d is the diameter of GC, BPPG and EPPG electrode which is 3 mm, 4.9 mm and 4.3mm, respectively.

The obtained geometric surface area is 0.0707, 0.189 and 0.145 for GC, BPPG and EPPG electrode, respectively.

Surface area of MWCNTs:

The surface areas of MWCNTs were calculated using the specific surface area (SSA) provided by the supplier, Nanolab (Brighton, MA, USA) as 200-400 m^2/g

The total area of the given amount of MWCNTs dropcasted on electrode, $S_{dropcast}$ can be calculated by $A_{MWCNTs} = S_{SSA}\ m_{dropcast}$, where $m_{dropcast}$ is the mass of the MWCNTs dropcasted and S_{SSA} is stated as above.

For 5, 7.5, 10, 20 and 30 μg MWCNT, the total surface area A_{MWCNTs} was calculated as10–20, 15–30, 20–40, 40–80, 60–120 cm^2, respectively.

The volume of a single MWCNT V_{MWCNT} was calculated by:

$$V_{MWCNT} = \pi r^2 h = (15\times10^{-9})^2\times2\times10^{-5}\times\pi\ m^3 = 1.4\times10^{20}\ m^3$$

The number of MWCNTs in 1g, N_{1g} can be calculated using a density of 1.54 g/cm^2 [2] by:

$$N_{1g} = \frac{V_{1g}}{V_{MWCNTs}} = \frac{\frac{1g}{1.54\ g/cm^2}}{1.4 \times 10^{-14}\ cm^3} = \ 4.59 \times 10^{13}$$

The average surface area of each MWCNT, $A_{single\text{-}MWCNT}$ was calculated by:

$$A_{single-MWCNT} = \frac{1 \times S_{SSA}}{N_{1g}} = \frac{200 \sim 400}{4.59 \times 10^{13}}\ m^2 = 4 \sim 9\ \mu m^2$$

Surface area of GNPs:

The surface area and the thickness of a single GNP was characterised to be 297±152 μm^2 and 7.1 ± 2 nm respectively from a previous SEM study[3]

Therefore the volume of a single GNP can be estimated as (2.11 ± 1.08) × 10^{-18} m^3. For 'loose' powders, the density of a single GNPs is assumed to be the same as graphite, 2.3 × 10^6 g/m^3 [4]. Hence the mass of a single GNPs can be estimated as (4.8 ± 2.4) × 10^{-9} mg.

For 10 μg GNPs, the total surface area can be calculated by:

$$A_{GNPs} = \frac{10 \times 10^{-3} mg}{(4.77 \pm 2.44) \times 10^{-9}} \times (2.97 \pm 1.52) \times 10^{-6} cm^2 = 6.2 \pm 3.2\ cm^2$$

Similarly, the total surface area of 2.5, 5, 15, 20 mg GNPs was calculated as (1.6 ± 0.8), (3.1 ± 1.6), (9.3 ± 4.8) and (18.7 ± 9.6) cm^2, respectively.

Bibliography

1. T.W.B. Lo , L. Aldous, R.G. Compton, *Sensors and Actuators B: Chemical*, 2012, **162**, 361-368.

2. A.T.Masheter, L. Xiao , G.G. Wildgoose, A. Crossley, J.H. Jones, R.G. Compton, *Journal of Materials Chemistry*, 2007, **17**, 3515-3524.
3. J. Poon, C. Batchelor-McAuley, K. Tschulik, R. G. Compton, *Chemical Science* 2015, **6**, 2869-2876.
4. E. Inc., Entegris Inc., Billerica, MA, **2013**.

Appendix E

Scan Rate Study for the Oxidation of Fipronil

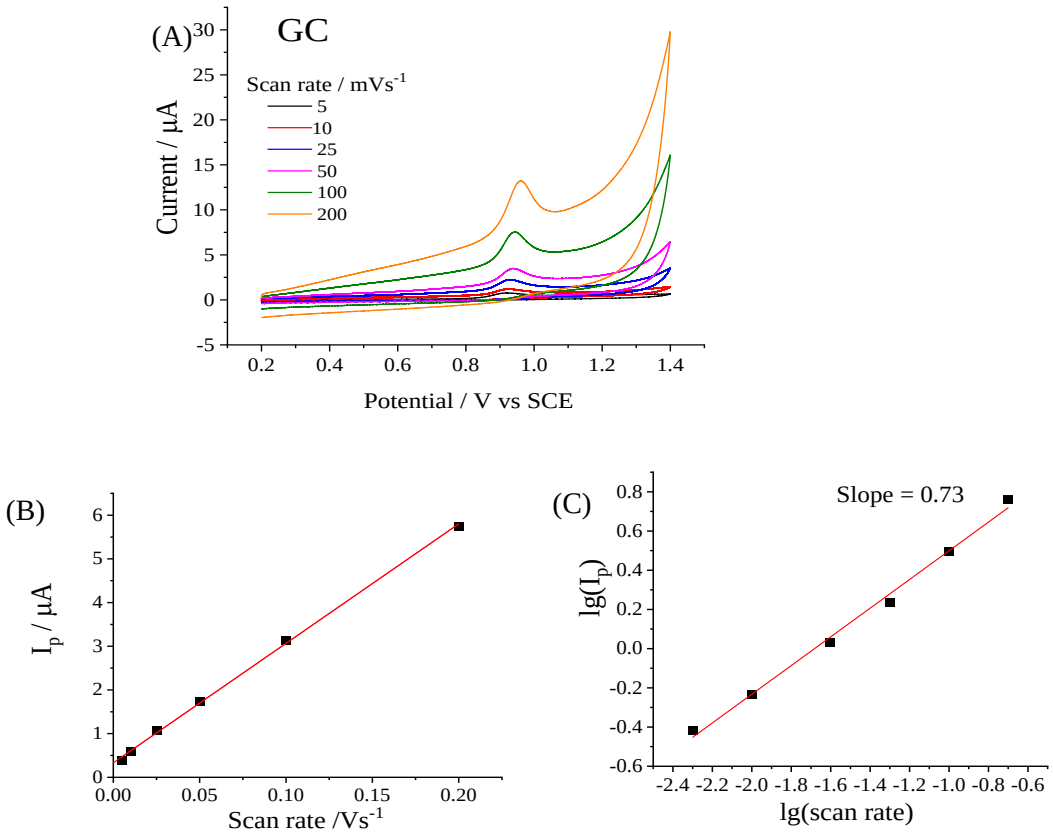
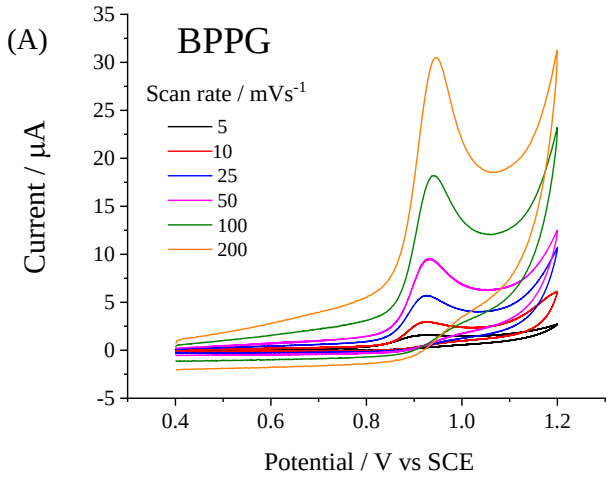


Figure E1. (A)Adsorptive stripping voltammetric responses 0.1 mM FIP at GC electrode recorded at varying scan rates of 5-200 mVs^{-1} (B) plot of peak current versus scan rate (C) log-log plot in scan rate range of 5-200 mVs^{-1}



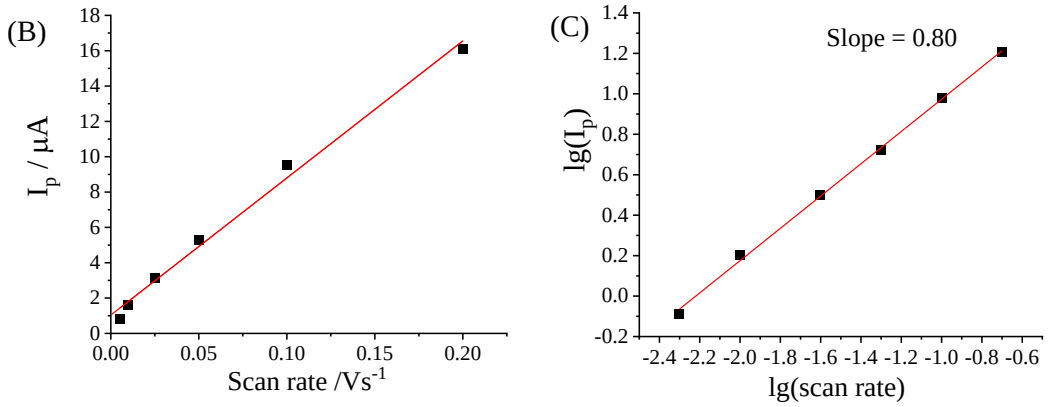


Figure E2. (A)Adsorptive stripping voltammetric responses 0.1 mM FIP at BPPG electrode recorded at varying scan rates of 5-200 mVs^{-1} (B) plot of peak current versus scan rate (C) log-log plot in scan rate range of 5-200 mVs^{-1}

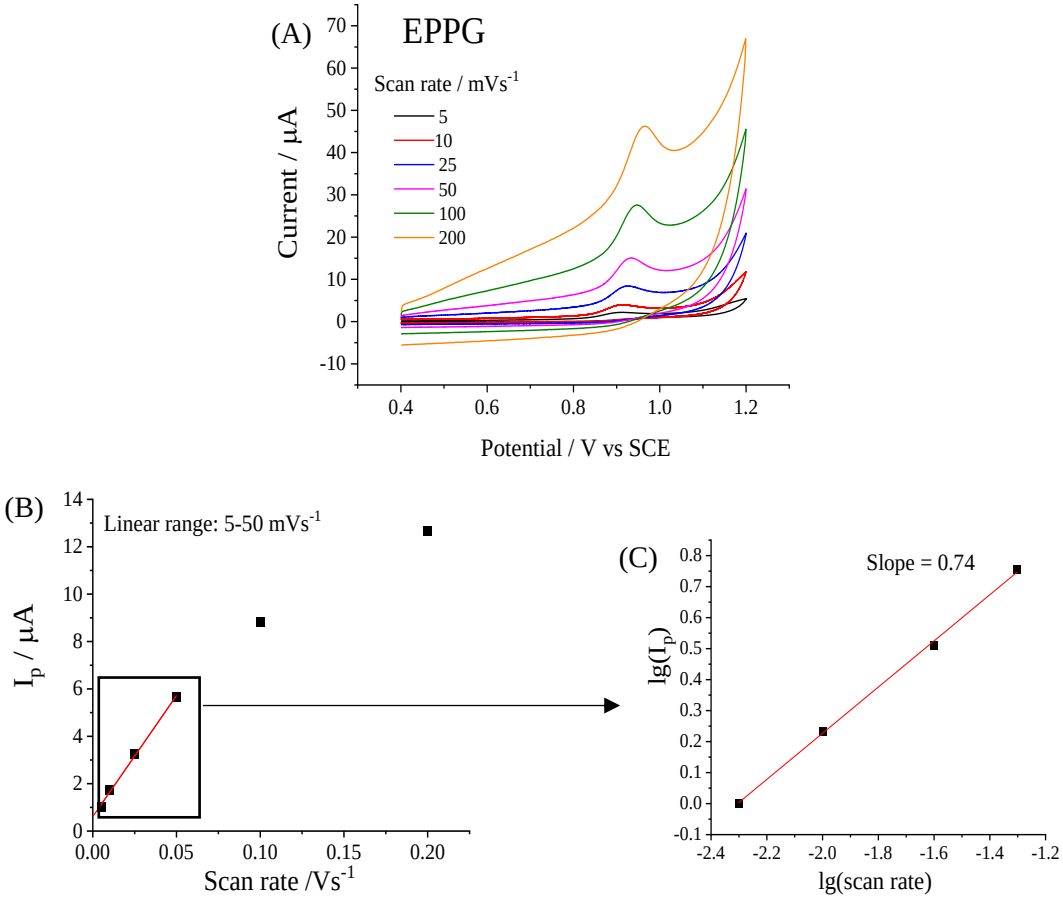


Figure E3. (A)Adsorptive stripping voltammetric responses 0.1 mM FIP at EPPG electrode recorded at varying scan rates of 5-200 mVs^{-1} (B) plot of peak current versus scan rate (C) log-log plot in scan rate range of 5-50 mVs^{-1}

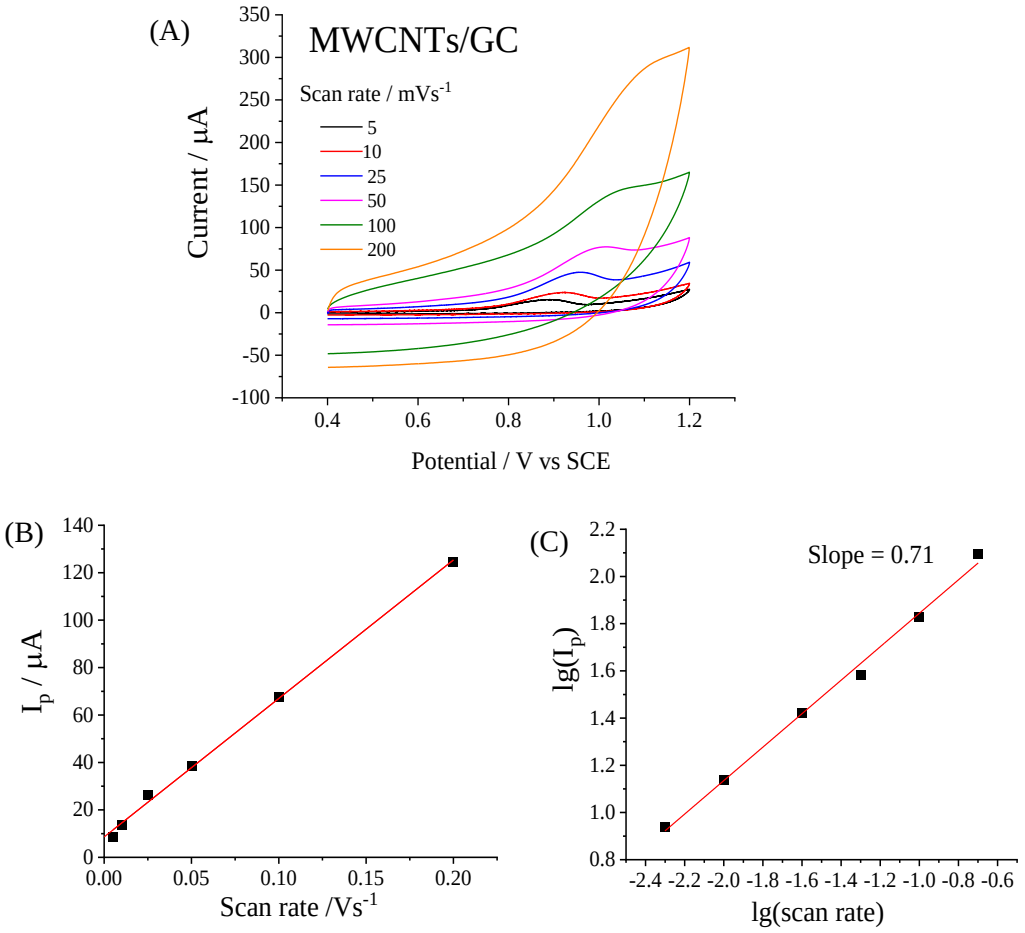
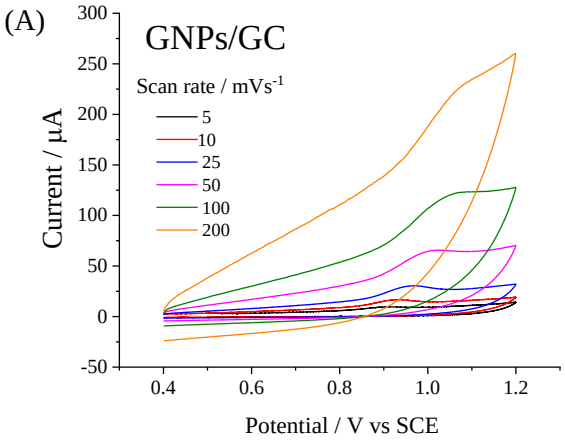


Figure E4. (A)Adsorptive stripping voltammetric responses 0.1 mM FIP at MWCNTs modified GC electrode (MWCNTs/GC) recorded at varying scan rates of 5-200 mVs^{-1} (B) plot of peak current versus scan rate (C) log-log plot in scan rate range of 5-200 mVs^{-1}



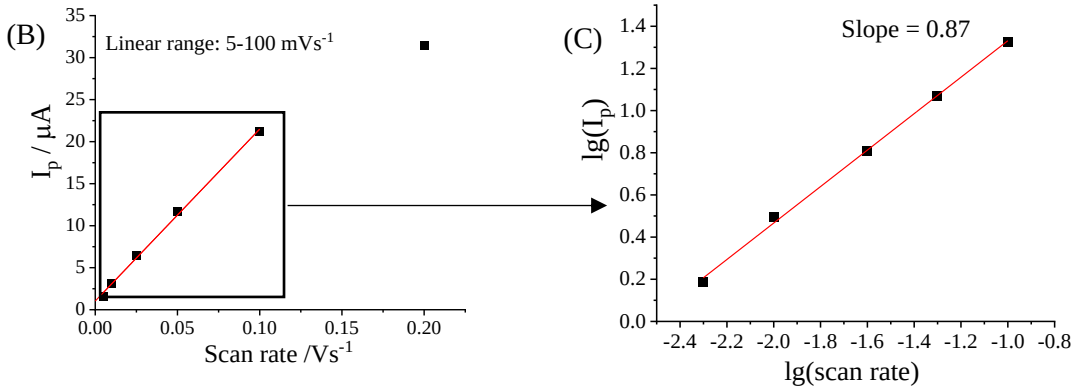


Figure E5. (A)Adsorptive stripping voltammetric responses 0.1 mM FIP at GNPs modified GC electrode (GNPs/GC) recorded at varying scan rates of 5-200 mVs^{-1} (B) plot of peak current versus scan rate (C) log-log plot in scan rate range of 5-100 mVs^{-1}

Appendix F

Langmuir Plots Measured at the Electrodes Used in Chapter 8

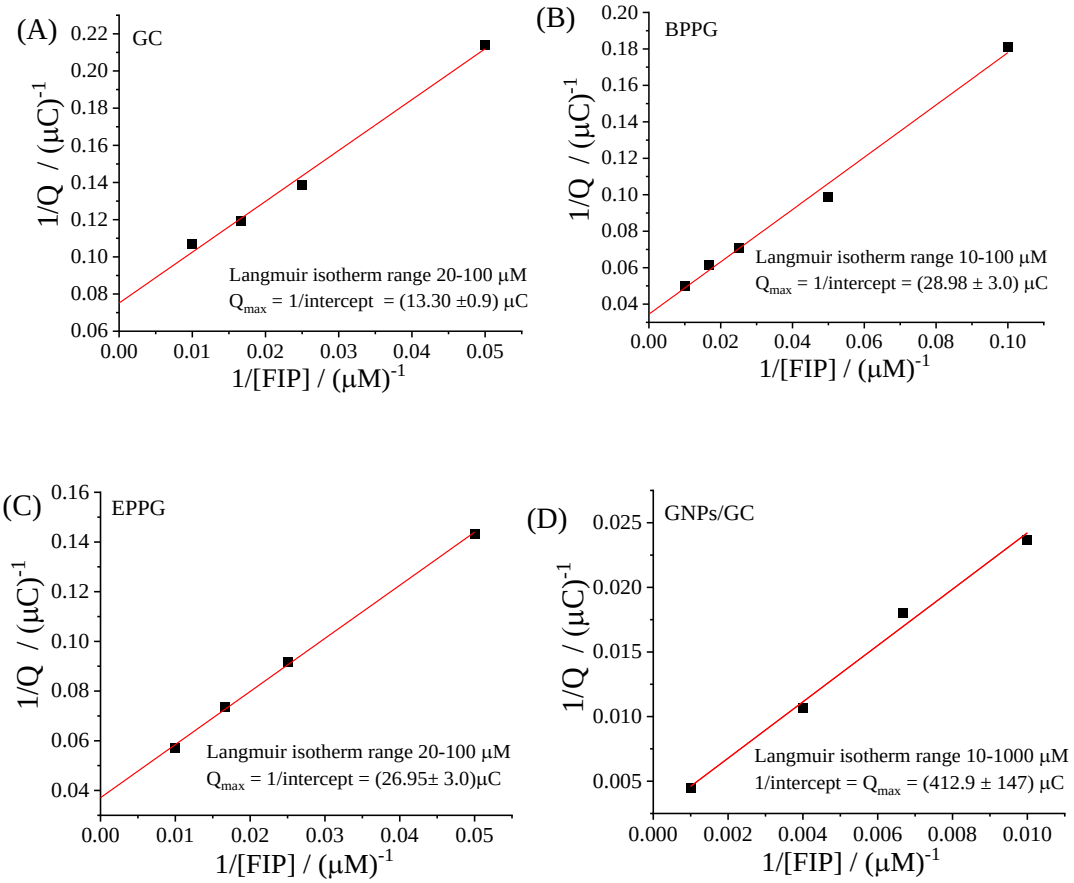
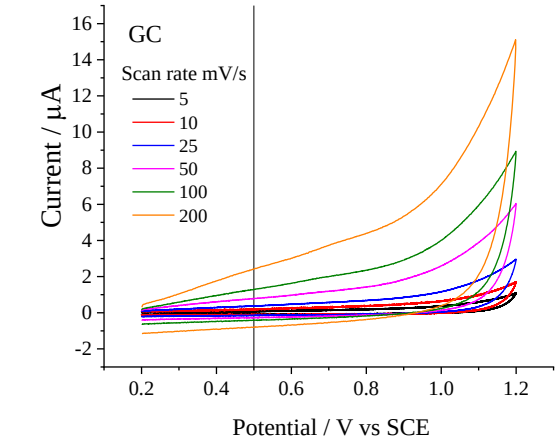
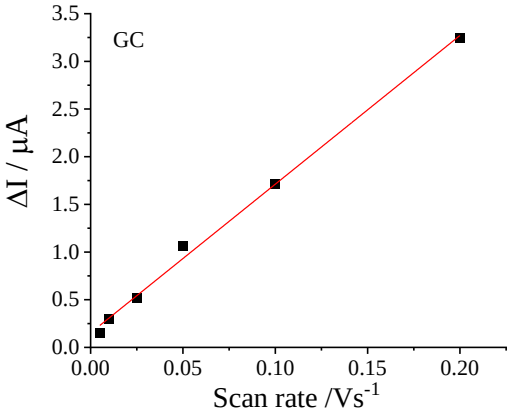


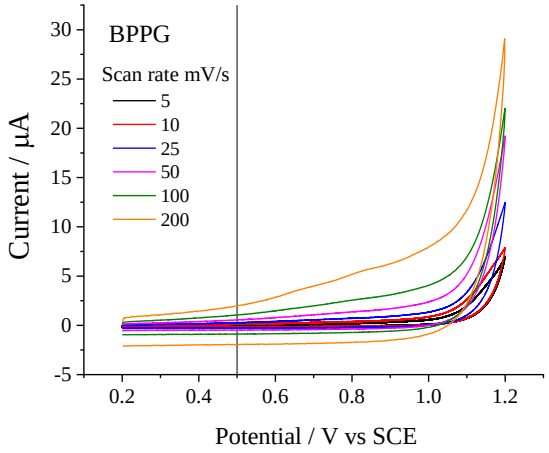
Figure F1. The Langmuir plots obtained from the adsorptive stripping voltammograms of 5-200 μM FIP at (A) GC (B) BPPG (C) EPPG (D) GNPs modified GC.

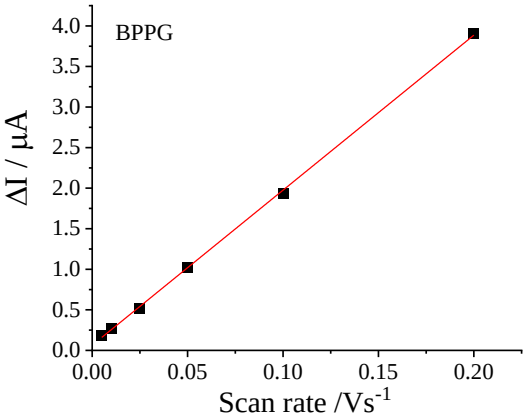
Appendix G

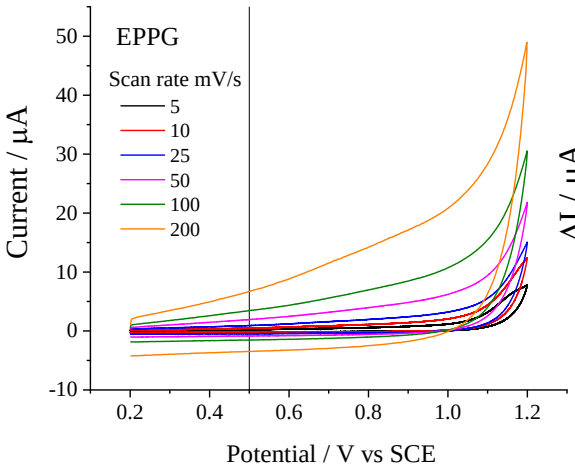
G1. Capacitance Measurements of the Electrode Surfaces Used in Chapter 8

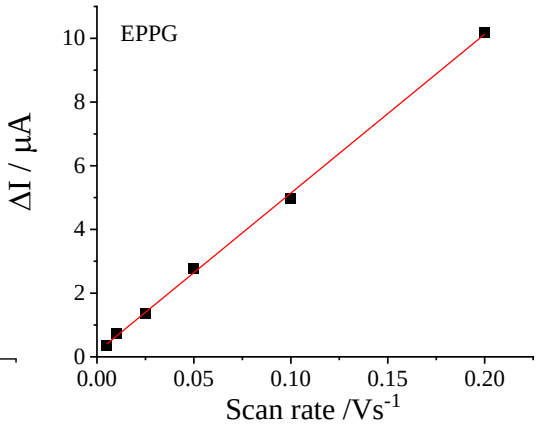












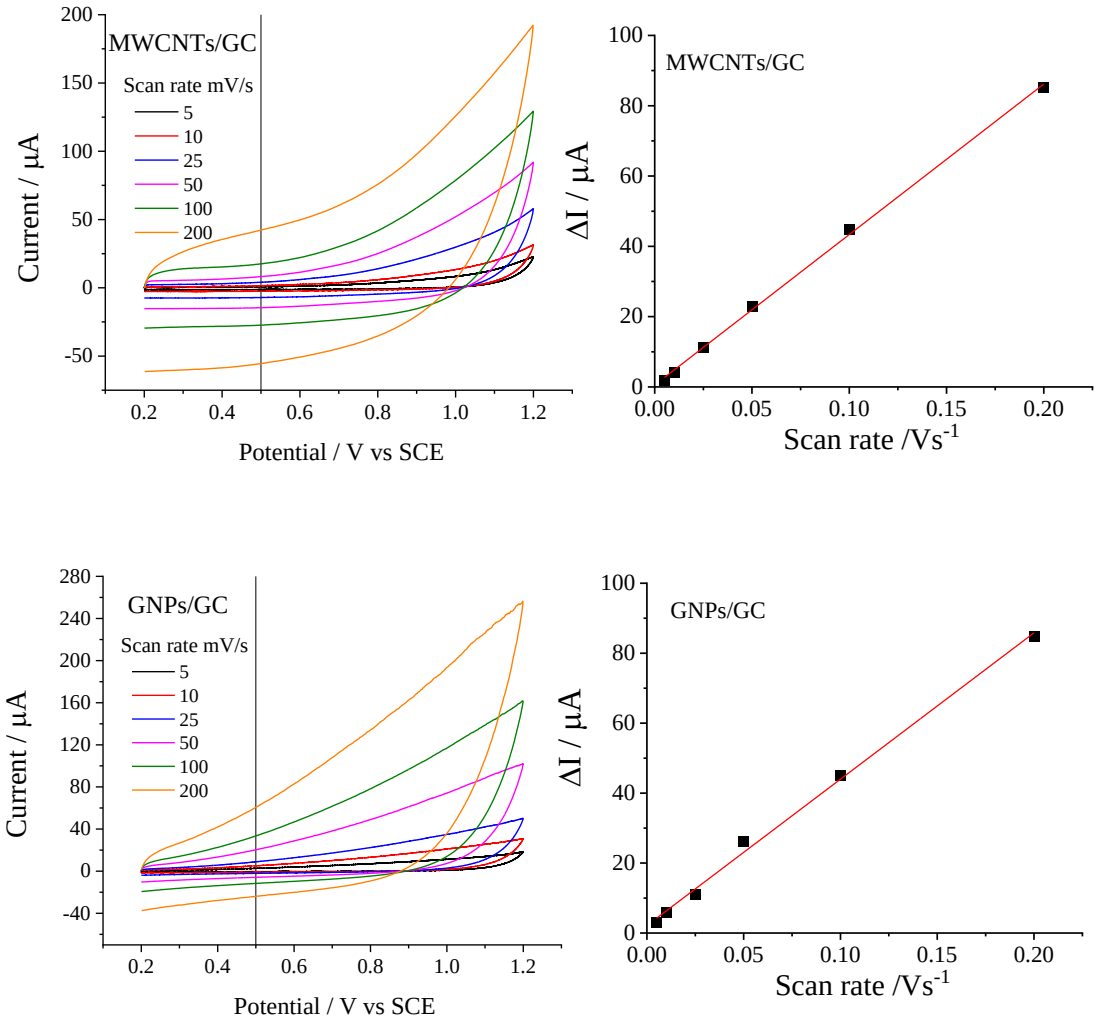


Figure G1. Cyclic voltammograms of the mixture of 60% pH 8.0 B-R buffer and 40% methanol blank solution recorded at varying scan rates at the studied electrode surfaces and the corresponding plots of the difference between the forward and backward current measured at 0.5 V vs SCE as a function of scan rate.

G2. Capacitance Currents at the Nano-particles Modified Electrodes Used in Chapter 8

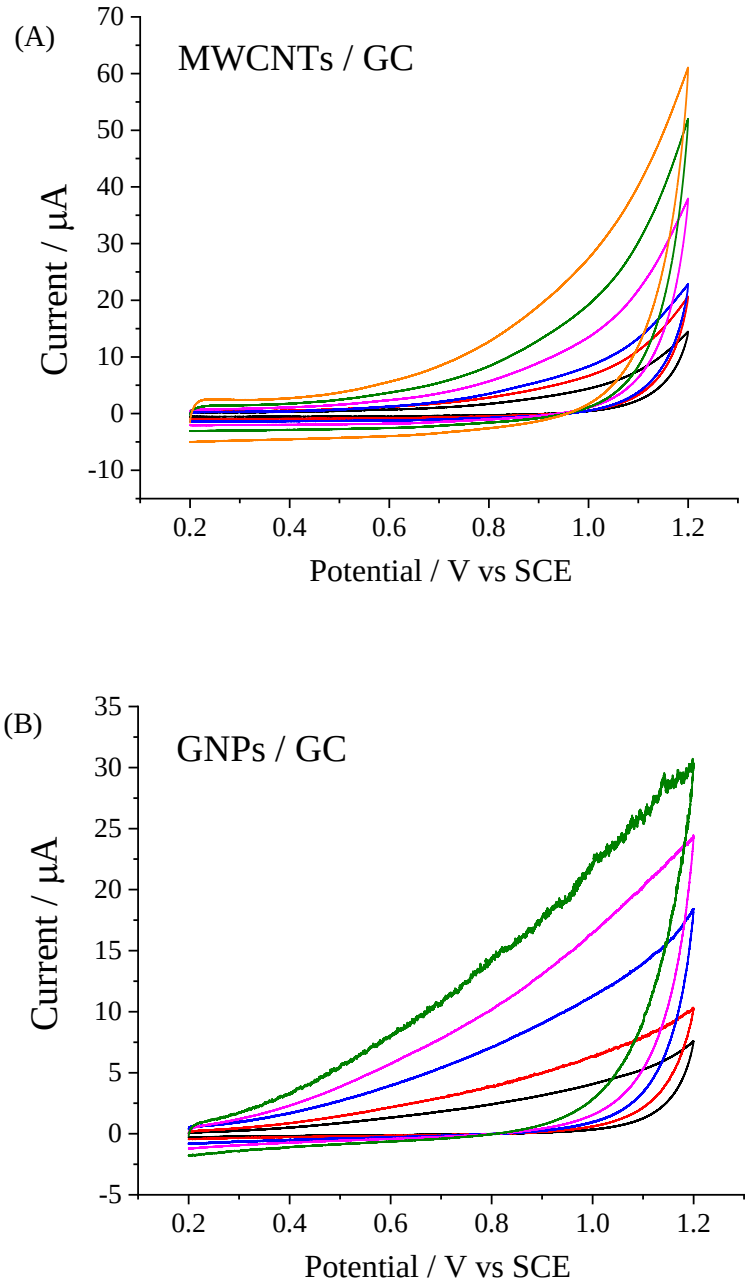


Figure G2. The background-subtracted adsorptive stripping voltammetric responses of the blank solution at (A) 5, 7.5, 10, 15,20 and 30 µg MWCNTs modified GC and (B) 2.5, 5, 10, 15 and 20 µg GNPs modified GC electrode.